Universitat Autònoma de Barcelona

ELECTRON MICROSCOPY STUDIES ON FUNCTIONAL CARBON NANOTUBES

Elzbieta Pach

Universitat Autònoma de Barcelona

ELECTRON MICROSCOPY STUDIES ON FUNCTIONAL CARBON NANOTUBES

Elzbieta Pach

Tesis Doctoral

Programa de Doctorado en Ciencia de Materiales

Directora: **Belén Ballesteros Pérez**

Tutor: **José Peral Pérez**

Departamento de Química

Facultad de Ciencias

2017

Institut Català de Nanociència I Nanotecnologia (ICN2)

Campus de la UAB

08193 Bellaterra (Barcelona)

Universidad Autónoma de Barcelona

Departamento de Química 08193 Bellaterra (Barcelona)

Memoria presentada para aspirar al Grado de Doctor por

Elzbieta Pach

Visto bueno de

Dra. Belén Ballesteros

Bellaterra, 1 de junio de 2017

Bellaterra, 1 de junio de 2017

Dra. Belén Ballesteros Pérez, líder del Departamento de Microscopía Electrónica de Institut Català de Nanociència i Nanotecnologia (ICN2), en calidad de directora de tesis y **Dr. José Peral Pérez**, profesor asociado en Departamento de Química de la Universidad Autónoma de Barcelona (UAB), en calidad de tutor de tesis.

CERTIFICAN:

Que Elzbieta Pach, licenciada en Química, ha realizado bajo su dirección el trabajo que lleva por título "*Electron microscopy studies on functional carbon nanotubes*", que se presenta en esta memoria para optar al grado de Doctor por la Universidad Autónoma de Barcelona.

Dra. Belén Ballesteros Pérez

Dr. José Peral Pérez

Acknowledgements

First, I would like to express my deep gratitude to Dr Belén Ballesteros for giving me the opportunity to learn and master my skills in the field of electron microscopy and materials science. Thank you for your guidance, trust and support as well as for your dedication especially in the final stage of writing of this dissertation. Also, I would like to acknowledge Dr José Peral for accepting to be my tutor.

To my past supervisor Prof. Miquel Salmeron from LBNL, ALS beamline scientist Dr Hendrik Bluhm and Dr Carlos Escudero from ALBA synchrotron, all of them were always convinced I "really should get that PhD", although at that time I was not convinced to pursue a scientific career. Thank you for believing in me, for you encouraging words and support.

This thesis was financed by Marie Curie Actions which are great initiatives because they bring scientific community of Europe closer together and this was the case of RADDEL, the project this thesis was based on. The leaders of this project: Dr Gerard Tobias (the coordinator), Dr Benjamin G. Davis, Dr Kostas Kostarelos, Dr Khuloud Al-Jamal, Dr Mauricio Prato, Dr Tatiana Da Ros, Dr Alberto Bianco, Dr Dimitris Emifietzoglou, Dr Martin Kalbáč, Jean-Claude Saccavini and Prof. Gustaaf Van Tendeloo, all of them shared their valuable knowledge with us, the RADDEL fellows. Dear fellows, I had a great time with you at our project meetings and at your stays in ICN2, we learned a lot from each other because each of us is specialized in different field. Magdalena Kierkowicz and Markus Martincic you were the closest to me, our collaboration on the project was essential for elaboration of this thesis. Thank you for providing me with numerous samples of purified and filled carbon nanotubes. Also many thanks to other fellows who provided samples of functional carbon nanotubes and made great investigations

from their part, especially to Agnieszka Gajewska, Aritz Pérez, Ana Santidrián, Cinzia Spinato, Rebecca Klippstein, Maxime Bourgognon, Jose Miguel Gonzalez-Dominguez, Reida Rutte, Sonia de Munari and Christopher Serpell. The collaboration with you resulted in publications we may be proud of. Not a part of RADDEL network, but thank you Houmam Kafa, Iris Marangon, Cécilia Ménard-Moyon, Ania Servant and Julie Tzu-Wen Wang for your samples of functional carbon nanotubes for the investigation on their interaction with cells. Thank you Dr. Jorge Pérez for being a supportive project manager.

To the other members of Gerard Tobias´s group especially Laura Cabana for her collaboration on lead iodide project. I really appreciate your friendship and the time we spent together. Also, would like to thank Stefania Sandoval for fruitful collaboration on filling of nanotubes with other tubes.

I would like to acknowledge the contribution of Dr. Riccardo Rurali (ICMAB) who optimized the structures of lutetium halides within DFT theory and generated the models of lutetium halide nanotubes of different chiralities and diameters. Thanks to Dr. Carlos Frontera (ICMAB) for acquisition and refinement of synchrotron-based XRDs of lutetium halides. Also, to Prof. Alfredo Segura (University of Valencia) for photoluminescence and Dr. Mathieu Kociak (CNRS) for cathodoluminescence results of lead iodide nanotubes. From the ICN2, I would like to recognize the work of Pablo Garcia on the acquisition of laboratory-based XRD spectra.

I am deeply grateful to Prof. Van Tendelo for allowing me to do a two month secondment in his group (EMAT) which allowed me to get to use aberration-corrected microscopes. Special thanks to Prof. Sara Bals for supervising my work there on the daily basis. To now Dr Mert Kurttepeli for being my kind guide at EMAT and welcoming me in the group, presenting me to everybody, showing me

around Antwerp as a friend and sitting with me during endless hours at the microscope, even if that meant Sunday. Your expertise in aberration-corrected STEM and tomography resulted in beautiful images presented in this work on lutetium halide and lead iodide nanotubes. To other EMAT members who treated me like a friend and shared their knowledge and time with me, especially Maria F., Maria M., Alex M, Antonis N. and Robert P.

Muchas gracias para mis súper-compis de la oficina! No podría haber pedido a mejores compañeros y a la vez amigos para compartir el día a día en la oficina. Marcos, los usuarios siempre te están buscando por tu profesionalidad y eficiencia (o esa sonrisa que siempre llevas!), de verdad creo que tendríamos que imprimir esas camisetas de "Keep calm and find Marcos" y repartirlas por el ICN2. Francisco, te has convertido en uno de mis mejores amigos durante estos años, valor mucho tu apoyo y tus ganas de escucharme cuando lo necesito. Siempre has estado allí trabajando duro puliendo y cortando y a la vez escuchando. Os voy a echar mucho de menos!

Muchas gracias a grupos de "lunch time" y "a muerte", tanto como los amigos de ICN2 e ICMAB por estar siempre allí, reírnos juntos, discutir sobre temas tan importantes como la ciencia, la política o el cambio climático a la vez que hablar sobre temas tan triviales (pero no menos importantes), como los fines de semana, la escalada o la jardinería. Esta pausa a mediodía era esencial para sentirse parte de una comunidad dentro del ámbito de trabajo y relajarse un poco tomando el sol y el café en "nuestro" césped bajo el árbol. Kumara: siempre serás una de mis mejores amigas, tus valores son admirables; James: valoro mucho nuestras conversaciones, he aprendido mucho de ti; Fede y Mateo: tan divertidos, me he reído mucho con vosotros; Gustau: siempre he valorado mucho tus consejos y aunque llegues tarde a la hora de comer, te esperaremos!; Fabián, Roque, Alex, Dyana, Bernimond, Bernhard, Bernat, Max, Blai, Juanlu, Roberto, Pablo y Laura,

sois geniales, me ha encantado compartir estos pequeños y grandes momentos con vosotros!

También quisiera agradecer a mis "viejos" amigos del barrio, los Carmelomanos! Ya hacen 10 años que nos conocemos, me lo he pasado siempre genial con vosotros, hay momentos que no sería capaz de olvidar nunca, como los míticos 40 años de Arantxa ☺ Os quiero: Arantxa, Alex, Carlos, Ramón, Miquel, Marta B, Marie, Marta S, Dani (Primo), Vanesa, Sergio. Aún nos quedan muchas aventuras por compartir!

Ashley, no tengo palabras para describir lo mucho que te agradezco todo este tiempo que hemos pasado juntos! Conocerte ha sido lo más bonito que me ha ocurrido. Me has impresionado con tu alegría, tus conocimientos, tu dedicación, tu manera de bailar y ese punto de pequeña locura que hace divertido cada día ☺ Escribir la tesis a la vez ha hecho que el proceso ha sido mucho más llevadero, gracias por tu apoyo, tu paciencia, tus sinceridad, tu amor tanto como por tus deliciosos platos de chef! KC

Moim najwspanialszym dziewczynom z grupy "Polish mafia" chcę podziękować za bezcenne pogaduchy, kawy, kolacje i imprezy, bez was to nie było by to samo! Nazbierało sie tych wspomnień, interesujących rozmów, zwierzeń i wyjść na miasto w ciągu tych ostatnich czterech lat. Będzie mi bardzo brakowało tych naszych babskich wieczorów, ale jestem pewna, że jeszcze nie raz się spotkamy. Pytanie tylko gdzie? Magdaleno, byłyśmy w tej historii razem od początku i obie wiemy jak było fajnie i ciężko zarazem, mam nadzieję, że znajdziesz jeszcze miejsce tak wspaniałe jak Cerdanyola ☺ Karolina, nigdy nie zapomnę naszych pogaduszek, historii oraz twoich przemian, ale przede wszystkim twojej siły i determinacji. Marianna, ty to jednak byłas największym zaskoczeniem dla mnie, z pozoru taka

niewinna, a jednak przebojowa. Uwielbiam nasze poranne przejażdżki pociągiem z kubkiem kawy w ręce ☺

Dziekuję moim rodzicom za opiekę i poświecenie. Wiem, że nie było łatwo wychować czworkę dzieci, szczególnie na początku, ale staraliście sie wychować nas najlepiej jak potrafiliście i za to jestem Wam bardzo wdzięczna. Karolina i Agnieszka, zawsze byłyscie dla mnie nie tylko siostrami, ale także najlepszymi przyjaciółkami, a to nie zawsze sie zdarza. Mam nadzieję, ze nasz kontakt będzie się tylko zaciskał z czasem, choć nie łatwo jest się często widywać mieszkając w trzech rożnych krajach ☺ Wojtuś, zawsze byłes naszym mały braciszkiem i zawsze nim będziesz. Życzę Ci odnalezienia właściwej dla Ciebie drogi, zawsze uważalam, że jesteś bystry i inteligentny, wykorzystaj to!

Abstract

The present PhD thesis focuses on the thorough study of functional carbon nanotubes by means of electron microscopy techniques. Functional carbon nanotubes (CNTs) are attracting an increased attention due to their potential use for biomedical applications, including in vivo imaging, tumour targeting and drug delivery systems. An intrinsic advantage of carbon nanotubes is that their inner cavity can be filled with a chosen payload whilst the outer surface can be modified to improve their dispersability and biocompatibility.

Being the envisaged application in the biomedical field, a detailed characterization of the samples in all the steps of the preparation process (namely purification, shortening, filling and external functionalization) is mandatory. To achieve this goal, in this PhD thesis we have employed already established analysis including high resolution transmission electron microscopy to study the structure of the filling material, or energy dispersive X-ray spectroscopy to assess their composition, but also we have explored the use of other techniques to expand the possibilities of characterization of the samples.

In this sense, we have optimized the conditions for the study of the lengths of as-purified single-walled CNTs by surface sensitive high resolution scanning electron microscopy (HRSEM). Besides, low voltage scanning transmission electron microscopy (STEM) has been demonstrated as a time-efficient technique for assessment of filling yield and purity. Indeed, the combination of high spatial resolution and low voltage operation of this technique has made it particularly suitable for the study of the interaction of functional carbon nanotubes with biological samples such as cells.

Some of the employed compounds with interest for biomedical applications have a layered structure in their bulk form. Layered materials are known to form

monolayers which may exert enhanced or novel properties due to confinement effects. CNTs may act as templates to guide those layered materials to form single-layered nanotubes. This is the case of lutetium halides and lead iodide. In this PhD thesis we have succeeded in the formation of lutetium halide subnanometer-sized nanotubes, and proved their tubular nature by aberration corrected STEM and image simulations. Additionally, high yield growth of PbI_2 nanotubes on the exterior of CNTs has been achieved. Thanks to aberration corrected HAADF STEM and electron tomography, the structure of the hybrids has been revealed. Remarkably, the optical properties of the hybrids differ from those of the bulk PbI_2. The blue shift observed by photoluminescence has been further confirmed by cathodoluminescence STEM analysis detected on individual PbI_2-CNT hybrids.

In conclusion, during this PhD project the range of electron microscopy techniques used for the study of functional CNTs has been expanded to get a thorough characterisation of the samples.

Resumen

La presente tesis doctoral se centra en el estudio exhaustivo de nanotubos de carbono funcionales por medio de técnicas de microscopía electrónica. Los nanotubos de carbono (CNTs) funcionales están atrayendo una atención creciente debido a su potencial uso para aplicaciones biomédicas, incluyendo la adquisición de imágenes *in vivo*, acumulación selectiva en tumores y sistemas de administración de fármacos. Una ventaja intrínseca de los nanotubos de carbono es que su cavidad interna puede llenarse con una carga útil de interés mientras que la superficie externa puede modificarse para mejorar su dispersabilidad y biocompatibilidad.

Debido a su potencial aplicación en el campo biomédico, es esencial una caracterización detallada de las muestras en todas las etapas de su proceso de preparación (purificación, acortamiento, llenado y funcionalización externa). Para lograr este objetivo, en esta tesis doctoral hemos empleado tanto análisis ya establecidos como microscopía electrónica de transmisión de alta resolución para estudiar la estructura del material de relleno o espectroscopía de dispersión de energía de rayos X para evaluar su composición, pero también hemos explorado el uso de otras técnicas para ampliar las posibilidades de caracterización de las muestras.

En este sentido, hemos optimizado las condiciones para el estudio de las longitudes de CNTs monocapa purificados por microscopía electrónica de barrido de alta resolución (HRSEM) con sensibilidad superficial. Además, la microscopía electrónica de transmisión y barrido (STEM) a bajos voltajes se ha demostrado como una técnica eficiente y rápida para evaluar el rendimiento del rellenado y la pureza del material. De hecho, la combinación de alta resolución espacial y el trabajo a bajos voltajes de esta técnica la ha hecho particularmente adecuada para el estudio de la interacción de nanotubos de carbono funcionales con muestras biológicas, como por ejemplo células.

Algunos de los compuestos con interés para aplicaciones biomédicas empleados en este trabajo tienen una estructura laminar. Se sabe que los materiales laminares forman monocapas que pueden tener propiedades mejoradas o nuevas debido a efectos de confinamiento. Los CNT pueden actuar como plantillas para guiar los materiales laminares a formar nanotubos monocapa. Este es el caso de los haluros de lutecio y el yoduro de plomo. En esta tesis de doctorado hemos conseguido la formación de nanotubos de haluros de lutecio de tamaño subnanométrico, y su naturaleza tubular se ha demostrado mediante STEM con corrector de aberraciones y simulaciones de imagen. Además, se ha logrado el crecimiento con alto rendimiento de nanotubos de PbI_2 en el exterior de CNTs. La estructura de los híbridos se ha revelado mediante STEM con aberración corregida y tomografía electrónica. Cabe destacar que las propiedades ópticas de los híbridos difieren de las del PbI_2 en masa. El desplazamiento azul observado por fotoluminiscencia se ha confirmado mediante análisis en híbridos PbI_2-CNT individuales por catodoluminiscencia-STEM.

En conclusión, durante este proyecto de doctorado la gama de técnicas de microscopía electrónica utilizadas para el estudio de CNT funcionales se ha ampliado para obtener una caracterización exhaustiva de las muestras.

Table of Contents

List of figures

1 Introduction

In this chapter the introduction into general aspects of carbon nanotubes and functional carbon nanotubes is presented. Additionally, the characterization strategies and possible applications of functional carbon nanotubes will be discussed.

1.1 Carbon nanotubes

1.1.1 General aspects of carbon nanotubes

Carbon is the 15th most abundant element in the Earth's crust, the fourth most abundant element in the universe by mass and the second most abundant element in the human body (about 18.5%). The atoms of carbon can be bonded together in diverse ways, forming different allotropes of carbon with dissimilar physical properties. The most commonly known allotropes are graphite, diamond, and amorphous carbon. Their physical properties vary depending on their structure. For example graphite is opaque and black while diamond is highly transparent. Moreover, graphite is soft enough to form a line on paper while diamond is the hardest naturally-occurring material. Even more, graphite is a good electrical conductor while diamond has a low electrical conductivity. Moreover, it was not until the discovery of fullerenes in 1985 [1], this family started to expand. Indeed, the synthesis of molecular carbon structures in the form of C60 (Buckminsterfullerene) and other fullerenes (buckyballs) has stimulated intense interest in the structures accessible to graphitic carbon sheets. These investigations lead to the discovery of carbon nanotubes, also called cylindrical fullerenes or buckytubes, first described by Iijima in 1991 [2]. The structure of carbon nanotubes may be thought as a flat sheet of graphene wrapped along one of its axis to form a tube with at least one end capped with a hemisphere of the fullerene structure. Depending on the number of graphene sheets enrolled around the same axis either single-walled carbon nanotubes (one layer of graphene, SWCNTs) or multi-walled carbon nanotubes (multiple layers of graphene, MWCNTs) are obtained (**Figure 1.1**).

Carbon nanotubes (CNTs) have relatively well defined diameters and controllable lengths. Their large length (up to several microns) and small diameters (a few nanometers) result in large aspect ratio and hence CNTs may be seen as nearly

one-dimensional structures. MWCNTs generally have larger outer diameters (2.5 – 100 nm) than SWCNTs (1.0 – 2.4 nm) and consist of a varying number of concentric SWCNT layers, with an interlayer spacing of about 0.34 nm.

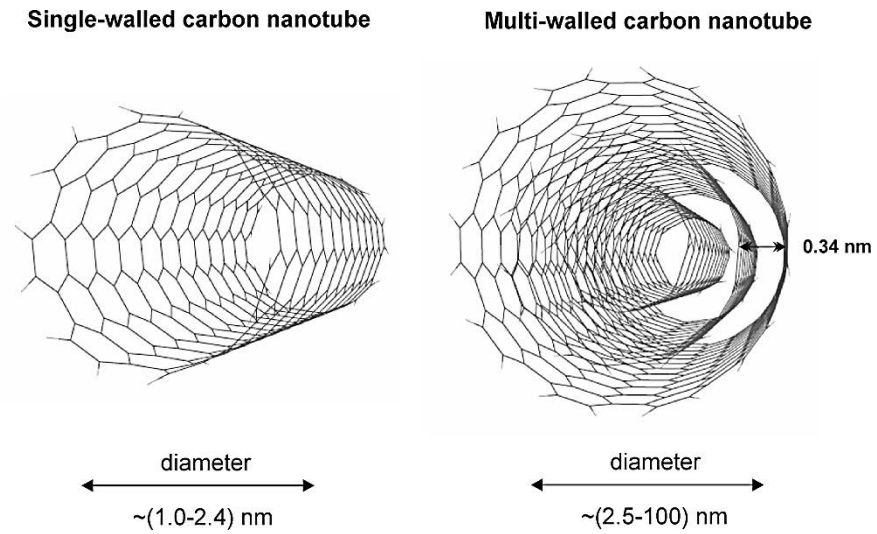

Figure 1.1 Schematic illustration of single-walled carbon nanotube (left) and multi-walled carbon nanotube (right).

There are different ways of wrapping a graphene sheet into a cylindrical nanotube. The three basic ways are yielding to zig-zag, armchair or chiral configurations (**Figure 1.2**). Chirality of a SWCNT is obtained from its chiral vector (C_h), defined by a pair of integers (n, m) obtained from the arrangement of the graphene hexagons with respect to the CNT axis. The zig-zag configuration is characterized by vectors (n, 0) and has a V-shape perpendicular to the tube axis while the armchair configuration with chiral vectors (n=m) is characterized by the shape of a chair. All other vector compositions ($n \neq m \neq 0$) are described as chiral. The chiral vector may be expressed as:

$$C_h = na + mb,$$

where **a** and **b** are unit cell base vectors of the graphene sheet and each (n, m) integer represents a possible tube structure.

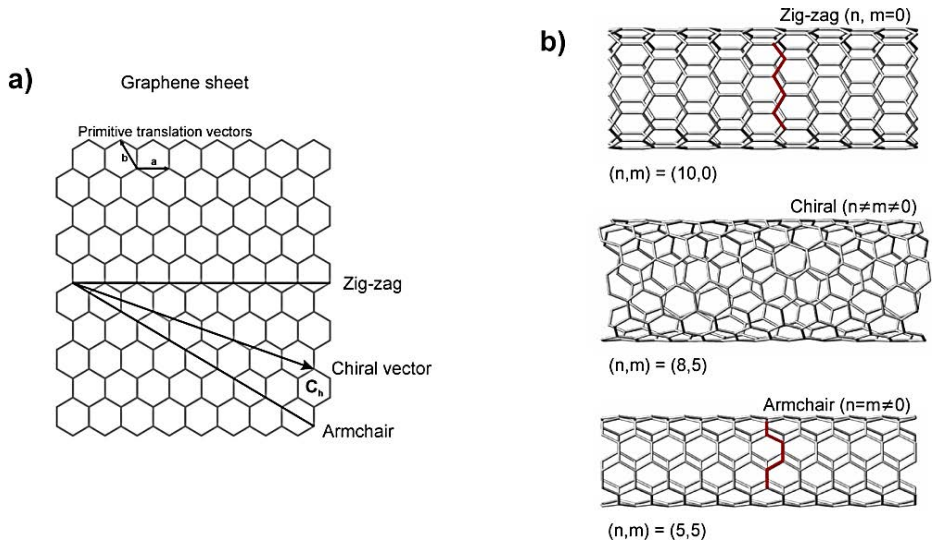

Figure 1.2 Schematic representation of (a) formation of single-walled carbon nanotubes by rolling of a graphene sheet along lattice vectors which leads to armchair, zigzag, and chiral tubes and (b) the three types of carbon nanotubes

Although the first reported carbon nanotubes were made in an arc-discharge experiment, nowadays there are other techniques available for their synthesis. The most common are chemical vapour deposition (CVD) and laser ablation. CVD technique consists of using plasma or a resistively heated coil to break up carbon containing gas molecules (methane, carbon monoxide, acetylene) into reactive atomic carbon. Carbon diffuses towards the substrate coated with nanoparticles (usually Ni, Fe or Co) where it binds, forming CNTs. CVD works the best to produce SWCNTs of controlled diameters governed by the catalyst nanoparticle´s size [3]. In the laser ablation synthesis, the carbon-rich feedstock gas (methane or carbon monoxide) is hit by a high-power laser beam yielding primarily SWCNTs [4]. In the arc-discharge method the nanotubes self-assemble from the carbon vapour generated by an arc discharge created between two carbon electrodes. This process may occur with or without the presence of catalytic nanoparticles and depending on the conditions SWCNTs or MWCNTs may be grown selectively [5].

Depending on the technique of preparation CNTs may end up open- or close-ended.

1.1.2 Physical properties of carbon nanotubes

The electronic, molecular and structural properties of carbon nanotubes are determined to a large extend by their nearly one-dimensional structure, high surface to volume ratio and low atomic weight.

Mechanical properties

Carbon nanotubes are characterized by large Young modulus in the axial direction, reaching average values around 1.8 TPa for MWCNTs and 1.25 TPa for SWCNTs, originated from the presence of strong C=C bonds [6, 7]. Subsequently, multi-layered CNTs are mechanically much stronger than conventional carbon fibres[6], and are extraordinarily flexible when subjected to large strain [8]. MWCNTs are difficult to stretch axially but easy to bend laterally and they can withstand large lateral distortions reversibly, which practically means nanotubes will rather buckle than distort or break when they are bent [9]. Their high stiffness and low density make them potential fibres in strong, lightweight composite materials that need anisotropic properties [10]. However, the mechanical strength of CNTs varies with the presence of structural defects.

Electronic properties

In the early 1990s, first calculations predicting that single-walled carbon nanotubes are metallic or semiconducting depending on their chirality and diameter were conducted [11, 12]. Later on, these predictions were experimentally confirmed to be true [13, 14]. Additionally, few other reports revealed the electronic properties of nanotubes are extremely sensitive to the degree of graphitization, chirality and diameter [15-17]. The differences in the conducting properties are caused by dissimilar band structures resulting in diverse band gaps. Generally, when the n

and m integers are equal, the nanotube will be metallic. Therefore, all armchair tubules are metallic, as well as zigzag cylinders exhibiting values of n, m multiples of three (**Figure 1.3**).

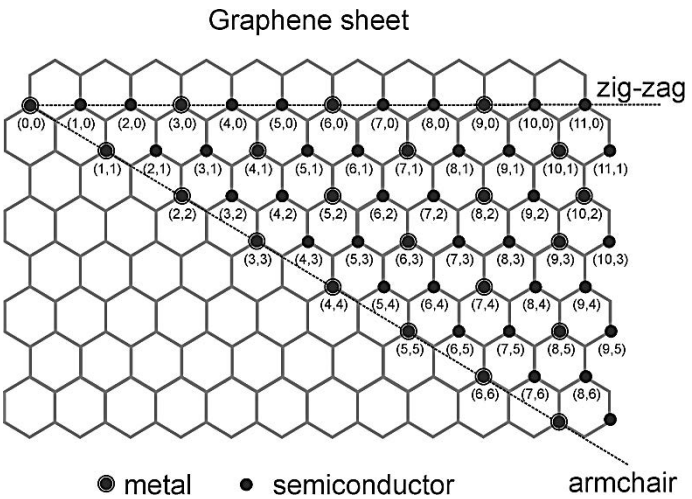

Figure 1.3 Graphene sheet and different ways of rolling it up into metallic or semiconducting carbon nanotube.

In summary, the metallic transport condition for these tubular structures can be expressed as:

$$\frac{(2m+n)}{3} = i$$

where *i* is an integrer. The rest of the nanotubes are semiconducting, with the band gap depending on the nanotube diameter. Moreover, it was shown that the resistance to conduction is determined by quantum mechanics and is independent of the nanotube length [10].

During the production of SWCNTs, metallic and semiconducting tubes are grown at the same time, yielding a mixed sample. Double-walled CNTs (DWCNTs) are semiconducting or metallic depending on the chirality of both the inner and the outer wall [18]. In the case of MWCNTs, it has been shown that each individual

nanotube exhibits unique conductivity properties that can lead to both metallic or semiconducting behaviour [16, 17]. The electronic properties are important since semiconducting CNTs perform better in applications that involve charge transfer processes, including sensors, field emission devices, and photocatalytic applications, while metallic CNTs are preferred as interconnect in electronic devices or as conductive filler in CNT-composites. Therefore, efforts have been put into development of procedures of sorting of nanotubes in function of their electronic properties. In consequence, nowadays, it is possible to sort CNTs with the most common technique being the density gradient ultracentrifugation [19].

Optical properties

Optical properties of SWCNTs are found to strongly depend on the chirality of the individual tube [20, 21]. The investigations of the structure and one-dimensional excitonic nature of CNTs were revealed through absorption, photoluminescence (PL), Raman and ultra-fast optical spectroscopies [21, 22].

It was shown that SWCNTs of different chiralities show unique set of absorption peaks depending on the chiral vectors (n, m). For the CNTs with more than one wall the absorption features are less defined due to wall-to-wall electronic coupling and spectral overlapping in a heterogeneous mixture [23]. Hence, MWCNTs are characterized by smooth exponential decay like absorption curves.

On the one hand, semiconducting SWCNTs display interesting fluorescence properties with a quantum yield reaching 8 % for individual SWCNT but being strongly dependent on the chirality of the tube and environment [24]. From the other hand, DWCNTs have been shown to fluoresce from their inner walls but the majority of PL is quenched by the outer wall. It was described that only inner walls with a diameter of ~0.93 nm and a high chiral angle are able to produce measurable PL signal [25]. Finally, MWCNTs do not emit any PL signal because the excitons are easily quenched by other concentric walls.

The origin of optical properties emerging from CNTs was assigned to excitons (electron-hole pairs) by Ando, in his theoretical work [26]. Unlike most other semiconducting materials, CNTs are characterized by large exciton binding energies, up to ~1 eV. Thus, the excitonic nature of CNTs is a key characteristic for developing nanotube-based optoelectronic devices.

Similar to absorption and PL spectroscopy, Raman spectroscopy is a useful technique for studying the optical properties of CNTs. Although metallic nanotubes do not fluoresce they possess absorption maxima corresponding to inter-band electronic transitions. Features in the Raman spectrum that are distinct for particular (n, m) nanotubes couple to these transitions as the probing laser energy becomes commensurate with the transition energy. By looking at the intensity profile of the Raman spectrum through a range of closely spaced excitation energies, these features can be correlated and assigned to (n, m) nanotubes [27].

Thermal properties

Although the thermal properties of CNTs are the least studied, they include very interesting results of theoretical and experimental work on specific heat and thermal conductivity of CNTs. The specific heat and thermal conductivity of CNTs are generally dominated by phonon contribution and are dependent on temperature [28]. While at high temperature, the specific heat of carbon nanotubes should be similar to that of graphene, at low temperatures (below 100 K) it would differ substantially. For MWCNTs of a few tens nm diameter a strikingly linear temperature-dependent specific heat was measured, over the entire temperature range ~10–300 K [29].

The thermal conductivity of carbon nanotubes is predicted to be superior to other materials, and indeed the experimental data confirmed that. For example, a metallic SWCNT of 1.7 nm in diameter and 2.6 μm in length gave a value of ~3500 Wm^{-}

$^{1}K^{-1}$ at room temperature [30]. This is considerably greater than theoretical calculations for the thermal conductivity of diamond, graphite and few-layer graphene. The theoretical calculation predicted to almost double that value for (10,10) SWCNT [31]. Unfortunately, it has not been experimentally confirmed yet. However, for individually measured DWCNT and MWCNT, thermal resistance experiments have shown a substantial decrease in the thermal conductivity, namely ~600 $Wm^{-1}K^{-1}$ for DWCNT and 42–343 $Wm^{-1}K^{-1}$ for MWCNT [32].

1.1.3 Purification and dispersion of carbon nanotubes

Pristine carbon nanotubes are a mixture of CNTs, amorphous carbon, graphitic nanoparticles and often catalyst nanoparticles used in the synthesis process. These impurities significantly influence the CNTs properties and limit their applications. Consequently, prior to any functionalization process they are purified in order to obtain "clean" carbon nanotubes. The most common approach is based on two steps. In the first step, a thermal or oxidative (acid or steam) treatment removes amorphous carbon and graphitic layers surrounding metal catalyst nanoparticles (namely Fe, Co or Ni) [33-37]. The second step consists in washing off the metallic nanoparticles with an acid [36, 38]. This is possible only for the "naked" nanoparticles, with no remaining graphitic shells around them. There are other efficient techniques that may be used to purify pristine CNTs such as magnetic filtration, microwave irradiation, electrochemical oxidation, surfactant assisted purification and $C_2H_2F_4$ or SF_6 treatment [39-42]. However, the technique based on steam treatment combined with subsequent HCl washing is preferred over all of the mentioned above. This is because it was reported to yield clean carbon nanotubes with no damage made to tubular structure even after prolonged treatment with steam [36]. It was even shown in the recent years by Raman spectroscopy that steam treatment may result in less defective nanotubes [43].

An important aspect of carbon nanotubes is their dispersibility. Pristine and purified carbon nanotubes are known to strongly aggregate into bundles as a result

of strong π-π stacking interactions between neighbouring nanotubes. This makes them hard to disperse in water and organic solvents. However, the dispersibility of CNTs is crucial for the preparation of functional carbon nanotubes and has to be addressed beforehand. There are two main strategies to improve the solubility based either on covalent functionalization [42] of the sidewalls or non-covalent modification with guest molecules [44-47]. In the former, usually carboxylic and carbonyl groups are introduced disrupting the electronic structure of CNTs. In the latter, CNTs are non-covalently wrapped by molecules such as DNA, polymers or aromatic molecules and thus do not modify the electronic structure of CNTs.

1.2 Functional carbon nanotubes

The intrinsic properties of carbon nanotubes (CNTs), such as excellent electric and thermal conductivity, mechanical strength, thermal and chemical stability, high aspect ratio and large surface area have generated a tremendous interest for both fundamental and applied research. Their performance as well as the number of potential applications can be further increased by combining CNTs with a second (and third, etc.) functional material. This can be achieved in two ways. One of them is a random mixing of CNTs with a second material to form a composite. Such nanocomposites are usually produced by mechanical mixing of carbon nanotubes into a matrix material (e.g. polymer, ceramic), which can result in a heterogeneous distribution of the filler and consequently in non-uniform properties. The resulting nanocomposite typically displays the intrinsic properties of the individual components, such as the high electrical conductivity of CNTs to create a conducting polymer, or the mechanical properties to reinforce metals and ceramics. The second way of producing functional CNTs is the designed interaction of CNTs with a second material to form a hybrid (**Figure 1.4**). This might be done by designed coating of the hybrid component onto the nanotube (sidewall functionalization) or by the encapsulation of the functional component

within the nanotube (filling of the interior cavity). As a consequence of functionalization, either external or internal, or both, new constructs with novel or enhanced physicochemical properties are created.

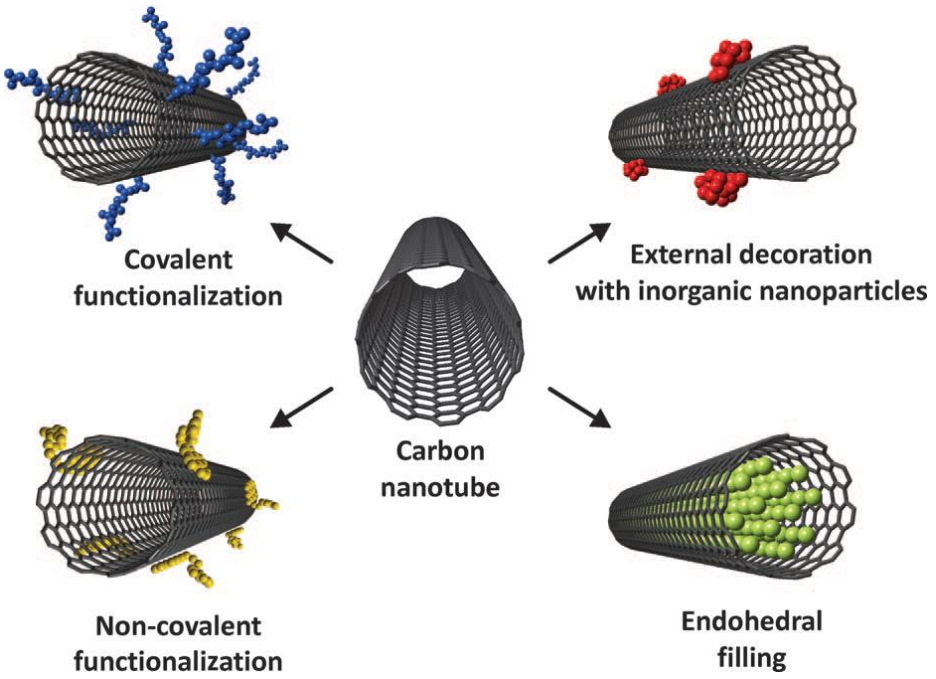

Figure 1.4 Scheme of possible modifications of carbon nanotubes from Tobias and Flahaut [48].

In the endohedral modification of carbon nanotubes organic molecules or inorganic crystals may be introduced in the interior cavity forming a functional hybrid material of unique properties. The choice of the payload depends on the application of the final product. In the case of exohedral functionalization different strategies may be adapted. Molecules of interest may be attached to the side walls of CNTs by covalent bonding, non-covalent interactions (van der Waals, π–π interactions, hydrogen bonding) or external wall decoration. Each of the functionalization strategies has its own purpose depending on the targeted application.

1.2.1 Endohedral functionalization of carbon nanotubes

Endohedral functionalization of carbon nanotubes is based on filling their inner cavities with a payload of interest. Consequently, CNTs may be filled with metals, semiconductors, salts or organic materials. There are two main ways of preparation of such hybrids, either during the CNTs synthesis process (*in-situ* filling) or through opening of the ends of CNTs and subsequent filling of the nanotube (*ex-situ* filling). The *in-situ* synthesis [49, 50] occurs during arc discharge or CVD growth of CNTs and has the advantage that the CNT integrity remains intact and the encapsulated material is completely protected from the post-synthesis atmosphere. However, the choice of materials is restricted to those that can be used as catalysts for the CNTs growth (Fe, Co, Ni, etc).

The mechanism of the *in-situ* filling (**Figure 1.5**) was debated to be based on either *open-tip growth* [51] where in a first stage the catalyst detaches from the substrate with the hydrocarbon initiating the formation of the wall followed by the catalyst falling on top of the already initiated and growing tube becoming thus a new site for nucleation and growth; or *base growth* [52] where the filling results from the building-up of catalyst nanoclusters that fall on the open tip and, if the diameter allows, diffuse inside the inner volume of the tube itself. A combined approach based on the two previously described mechanisms has also been proposed [53]. It has been suggested by Kunadian et al., that the initial stage of filling is characterized by *base-growth* and followed by *tip-growth* mechanism (assuming that catalyst particles are floating). Indeed, this approach can appropriately describe the synthesis of metal-filled carbon nanotubes. Moreover, it also offers some insight into the spatial distribution of metal particles and wires inside the CNT and the occurrence of unexpected features such as kinks and branches, often observed in these cases [54, 55].

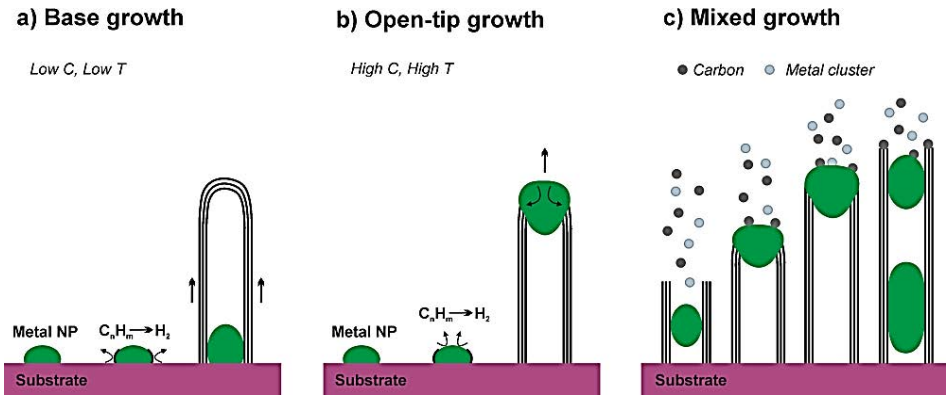

Figure 1.5 *In-situ* filling of carbon nanotubes through base growth (a), open-tip growth (b) and mixed growth (c) mechanisms. Substrate is in purple, metal nanoparticles in green, C means carbon species and T means temperature.

Generally for the *ex-situ* filling carbon nanotube tips should be opened before or during the encapsulation process allowing the diffusion of the payload material into their internal cavities. This may be achieved beforehand mainly by thermal treatment in oxidizing environment (air or oxygen) or chemically, by using acids capable of oxidizing poly-aromatic carbon [56, 57]. However, usually before the filling process CNTs are purified by one of the methods described before leading to open-ended nanotubes with no need of further processing before encapsulation. As already mentioned before, there are various methods available for the encapsulation of the materials inside carbon nanotubes [58-60], the main ones being the gas, liquid and solid phase [61]. Thus many physical properties have to be considered, such as solubility, melting point, surface tension, boiling point, viscosity, and decomposition temperature.

In the gas phase filling strategy, the vapour of the filling material is introduced in a sealed evacuated flask and heated up at the temperature of vaporization or sublimation of the filling material. In conditions of high partial pressure, the vapour starts to condense and upon cooling down it tends to diffuse towards the inner cavity of CNT due to the capillary forces. This route is an easy way for the

fabrication of filled CNTs, with the potential for a high-filling rate, high-purity and homogeneity of the filling material. There are many literature reports on gas phase filling of SWCNTs but very little on MWCNTs [62-64]. It should be noted, the gas phase route is limited to materials that vaporize or sublime without decomposing.

One of the liquid phase filling strategies is based on adding the nanotubes to the liquid solution of a chosen material (solution filling). This process is extremely dependent on the physical interaction between the filling liquid and the hosting tube, usually governed via the Young–Laplace law for capillary wetting. Another important parameter to have in consideration is the viscosity of the liquid. For example, in case of magnetic cobalt nanoparticles encapsulated in the interior of MWCNTs, a high filling yield was easily achieved by dispersing CNTs in a suspension of oleic acid and cobalt stearate complex, and subsequently bringing the entire mixture to thermal decomposition [65]. Another approach of liquid phase filling is to heat a material of interest above the melting point when mixed with carbon nanotubes. When the solid is melted it becomes a liquid and enters the internal cavities of CNTs through capillary wetting force. For example, in the molten phase capillary wetting process SWCNTs were filled with $CoBr_2$ nanowires [66] and MWCNTs with PbI_2 nanotubes [67].

The most challenging materials to fill in the CNTs are semiconducting or insulating nanostructures, as these materials have high melting points and do not easily dissolve in solvents. Hence, the syntheses and investigations of such nanostructures are rather limited. However, Keller et al reported the inclusion of magnetic $CoFe_2O_4$ nanowires into CNTs. The synthesis which consisted on filling of MWCNTs by aqueous solution, containing cobalt and iron nitrates, was accomplished under relatively mild conditions (100 ℃ and atmospheric pressure) with high filling yield (around 70 %) [68].

A totally different approach is based on coating of semiconducting nanowires with graphitic carbon layers, yielding as a final product filled CNTs. This has been

achieved, for instance, inside a transmission electron microscope (TEM) for Ge and GaN nanowires [69, 70].

1.2.2 Exohedral functionalization of carbon nanotubes

Pristine carbon nanotubes are hardly soluble in any solvent what makes them difficult to separate into individual nanotubes. The dispersibility of CNTs is especially important for the biomedical applications where solubility in water is essential to integrate nanotubes in the biological milieu. Dispersion is usually achieved by eliminating the van der Waals forces between individual tubes or bundles of CNTs by introducing functional groups on their surfaces [71]. There are many strategies leading to functionalization of the external walls of CNTs that may be divided into two main groups: covalent and non-covalent. Additionally, external walls decoration with an inorganic material may be treated as a third modification strategy. The procedure of non-covalent functionalization consists on the addition of surfactants, nucleic acids, peptides or oligomers. This procedure allows the dispersion of CNTs in solution while preserving their aromatic structure and therefore their electronic characteristics. Covalent functionalization often implies oxidation treatments prior to the attachment of chosen hydrophilic molecules. Alternatively, external walls may be directly functionalized by addition reactions.

1.2.2.1 Covalent functionalization

Covalent functionalization is an effective way of modifying carbon nanotubes in order to obtain new CNT-based conjugates with better dispersibility and tailored properties often designed for specific applications. In the process of forming strong covalent bonds with organic moieties the aromatic sp^2 structure characteristic to carbon nanotubes gets disrupted what may cause changes in their intrinsic properties. The most important and common reactions leading to the covalent functionalization of CNTs are described in literature [72] and represented schematically on **Figure 1.6**.

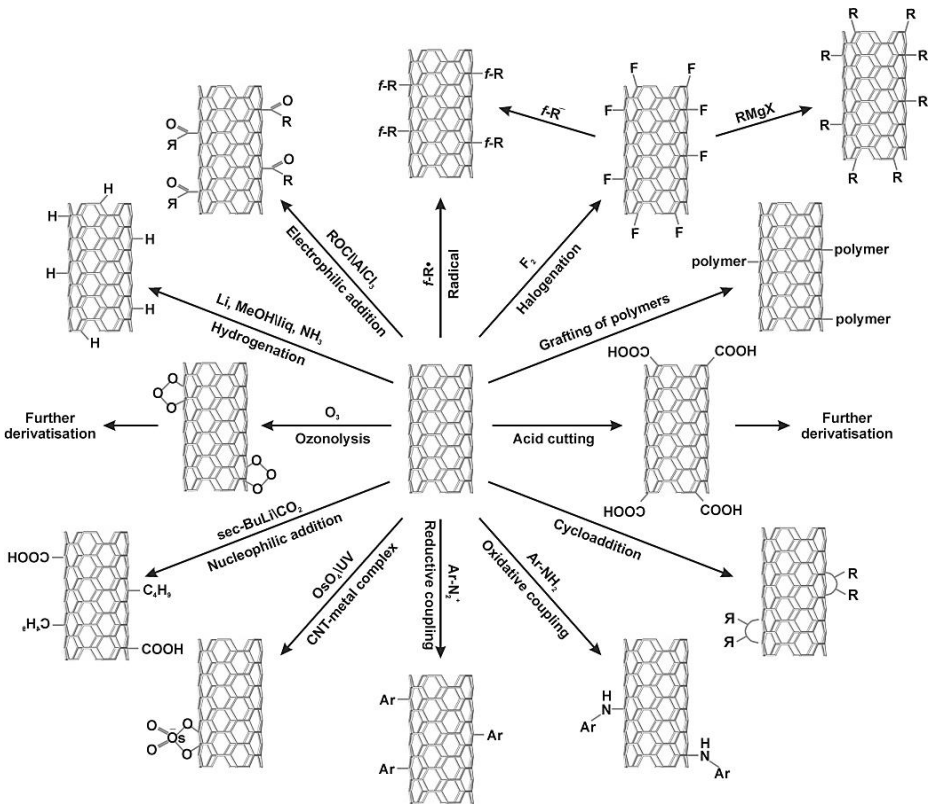

Figure 1.6 Covalent functionalization of carbon nanotubes.

There are two main mechanisms employed in the modification, based on either sidewall or defect site functionalization. As a name suggests the sidewall mechanism occurs on the walls of CNTs while the defect site mechanism is focused on the defects mostly present on the opened tips. The defects may be introduced either in the synthesis of nanotubes consisting of the introduction of pentagons and heptagons in the hexagon-based structure or by post-synthesis treatments. Usually, before functionalization of any kind, carbon nanotubes are purified in order to remove the catalytic nanoparticles and amorphous carbon through oxidative methods. In general in these processes some defects are created on the external walls and the closed ends are transformed into defect-rich open tips (usually carboxylic groups) [73, 74].

Among many processes there are some with special importance, for example the halogenation and cycloaddition reactions. Direct sidewall functionalization of CNTs through cycloaddition is based on reactive species such as nitrenes and carbenes [75]. Another important method is halogenation of CNTs [76, 77]. Particularly halogenation by fluorine, which may be covalently attached to the sidewalls of CNTs in a wide range of temperatures (from room temperature to 600 ℃) [78]. The fluorination is particularly useful because fluor is easily substituted by other organic groups such as alkyl or organometallic groups [79, 80]. Thermal and photochemical methods have also been applied to the successful covalent functionalization of CNTs with radicals. Thermal decomposition of alkyl or aryl peroxides results in radicals' formation that might be added to the graphitic network [10, 81]. Electrophilic [82] and nucleophilic [83] addition reactions, CNTs´ diameter dependent ozonolysis [84] and other strategies result in covalent bond formation between carbon nanotube body and organic moiety of choice. Polymers play very important role in the design of biologically suitable constructs and may be in contact with CNTs through covalent bond formation or non-covalent interactions (discussed in next section). When a covalent bond is formed long polymer chains help to solubilise the nanotubes even at low degree of functionalization. There are two main methods for the covalent attachment of polymers to CNTs, which are defined as "grafting to" [85-87] and "grafting from" [88-90] methods.

1.2.2.2 Non-covalent functionalization

Non-covalent bonding (physical adsorption) to CNTs is based on π-π stacking, Van der Waals or charge-transfer interactions. Wrapping around of organic molecules is advantageous over the covalent bonding in the cases when the structure preservation of carbon nanotubes and/or organic molecules is of importance. Moreover, the reaction conditions are not as harsh as in the covalent functionalization strategies. Furthermore, carbon nanotube bundles get separated into individual nanotubes [91]. This is mostly achieved by the addition of

surfactants into a solution of carbon nanotubes. The hydrophobic parts of organic molecules are adsorbed on the surface of carbon nanotubes while the hydrophilic parts interact with the solvent [92]. Although surfactants are efficient for solubilisation of carbon nanotubes, they have a drawback of a toxicity profile what limits their biomedical usability [93].

Biologically important molecules such as DNA, (poly-) saccharides, (poly-) peptides, nucleic acids, phospholipids and polymers wrap around carbon nanotubes [94-97]. Other organic species non-covalently interacting with CNTs are amines, aniline and proteins [98-100]. All of them may be used to introduce new CNT-based constructs into biomedical applications. For example, self-assembly processes similar to k-k interactions typical of double-stranded DNA may be exploited for the dispersion of CNTs. Studies of dispersion of CNTs by sonication in the presence of single-stranded DNA have already shown enhanced solubility of nanotubes [44]. The same was seen for amphiphilic peptides which ease CNTs dispersion in aqueous solution due to the presence of amino acids such tryptophan, phenylalanine, tyrosine and histidine built in the sequence [101]. In the case of polymers, their use as a drug delivery molecular carrier is studied [102].

1.2.3 External decoration of carbon nanotubes with inorganic materials

External decoration of carbon nanotubes with inorganic materials [103] is an emerging field where two strategies are common: the *in-situ* approach where CNTs are directly decorated by growing of nanoparticles on top of nanotubes or *ex-situ* approach consisting of prior synthesis of nanoparticles and then deposition of those on the sidewalls of carbon nanotubes *a posteriori*. These hybrids are often characterized by unique physical and chemical properties emerging from both, carbon nanotubes and inorganic nanoparticles and/or the interaction between both. Thus, they find applications in many fields as catalysis, sensors and devices [104].

Inorganic crystals may be connected to the surface of carbon nanotubes in different ways; this is through covalent bonding [105], electrostatic interaction [106], π-π stacking [107], hydrophobic interaction, or hydrogen bonding [108].

1.2.3.1 *In-situ* decoration of CNTs

The mechanism of *in-situ* decoration of carbon nanotubes with inorganic nanocrystals is based on physical of chemical adsorption of the precursors on the outer walls of CNTs and successive reactions [109]. However, pristine CNTs lack of sufficient binding sites for the precursors and therefore there is a need of creating some defects and functional groups to allow the adsorption of the precursors and subsequent formation of nanocrystals. This may be achieved by acid treatment, ultrasonication, microwave irradiation or γ-ray irradiation [103, 110]. When defects and functional groups are formed they act as anchoring and nucleation sites for the deposition of NPs [111-113]. Sometimes functional groups may even act as reducing agents for metal nanocrystals formation on nanotubes.

Among many methods of *in-situ* deposition, the earliest approaches were based on evaporation [114, 115], sputtering [116] and thermal decomposition [117]. These methods have an advantage of preserving the structure and properties of pristine CNTs. Noble metals can be deposited on CNTs by transforming them into gas phase by thermal heating or sputtering. In this process CNTs act as nucleation templates allowing formation of nanocrystals on their walls. Other strategies are based on decomposition of organometallic compounds, atomic layer deposition (ALD) or chemical vapor deposition (CVD) yielding metallic or semiconducting nanoparticles [109, 118]. Other methods include: electro-less chemical deposition, electrochemical deposition, supercritical fluids method, sol-gel process along with hydrothermal and solvothermal methods [119-123].

Few interesting examples of using carbon nanotubes as platforms for the formation of inorganic nanotubes are reported in literature. These means CNTs are completely covered by inorganic material. After the formation of inorganic

nanotubes the carbon nanotube may be burned up leaving a free standing inorganic nanotube. For example, a layer by layer strategy was used to create porous In_2O_3 nanotubes [124]. Inorganic nanotubes were also formed in CVD and ALD processes using CNTs as templates [115]. C.N.R. Rao et al. reported formation of ZrO_2 nanotubes in a sol-gel process using metal alkoxide in combination with subsequent calcination [125]. Interestingly, in these routes carbon nanotube outer diameter determines the interior diameter of inorganic nanotube.

1.2.3.2 *Ex-situ* decoration of CNTs

Various nanocomposites based on carbon nanotubes have been prepared by *ex-situ* decoration method. The nanoparticles of choice are prepared in advance what enables a better control of size and shape of the crystals created by well-known synthetic strategies. However, the loading efficiency onto pristine CNTs is not very high. Therefore, in order to obtain a better loading efficiency the surface of CNTs has to be modified by functionalization with appropriate linking molecules. The type of linker molecule plays a key role in the interaction with nanocrystals. Consequently, the *ex-situ* approach usually involves many steps including: formation of nanoparticles, chemical modifications of both components and their connection. For example, a series of nanocomposites have been prepared via step-by-step self-assembly approach using pre-synthesized nanoparticles of TiO_2, Co_3O_4, Au and mixtures of TiO_2/Au, TiO_2/Co_3O_4 nanoparticles by either sonication or mechanical stirring [126].

1.3 Characterization of functional carbon nanotubes

There are various analytical tools used for characterization of pristine and functional carbon nanotubes and investigation of their unique properties. We have divided them into few groups depending on their principle and function, as a

matter of clarity. First of all, we will describe microscopic techniques, then spectroscopic, diffraction, magnetic measurements and finally we will finish with description of other useful techniques such as thermogravimetric analysis (TGA).

Microscopies

The standard procedure for characterization of functional carbon nanotubes includes its visualization and is often the first step in the characterization process. The visualization of the hybrids and composites at the micrometre, nanometre and atomic scale is crucial for many studies minding application of functional CNTs. Four main microscopic techniques are commonly used, including: scanning electron microscope (SEM), transmission electron microscope (TEM), atomic force microscope (AFM) and scanning tunnelling microscope (STM). All of them allow for investigation of the local structure of the CNTs at nanometer and sub-nanometer level.

Electron microscopy is an essential tool for characterization of any nanomaterial because it allows direct observation of its size, shape and structure. TEM and SEM are useful tools to check the exfoliation of bundles, dispersibility and the purity of carbon nanotubes, as well as filling yield in endohedrally filled CNTs. SEM is a technique employed mainly for imaging of functional carbon nanotubes to obtain information about their morphology (size, shape), topology (texture, general aspect) and purity of the sample at resolution down to a nanometer. The lengths and diameters of CNTs may be assessed in fast and relatively easy way along with the presence of contaminants. Low voltage scanning transmission electron microscopy (STEM) used in SEM provides valuable information of the filling yield and the presence of possible external impurities with low electron beam effect, especially advantageous for examination of beam sensitive samples.

TEM microscope is used when higher than 1 nm resolution is needed. It is mostly employed in investigations at the atomic level, for example to obtain the crystalline

structure of the payload material in case of filled CNTs or to assess the number of walls in MWCNTs and the state of the nanotube tips (opened/closed). Commonly it is used to assess the outer and inner radius of CNTs as well as the helicity and presence of bundles. The inter-layer spacing, chiral indices and helicity of CNTs are available commonly in high resolution bright field mode (HRTEM) [127]. Beside the HRTEM mode, scanning TEM mode (STEM) is available. In STEM imaging the contrast depends on the atomic number (Z) of the constituent elements and therefore enables to visualize and localize component elements spatially. This technique is mostly used for filled samples, to roughly asses the filling yield. However, with the attachment of heavy element tags to organic molecules, they may also be visualized by this technique [128].

Beside the SEM and TEM imaging tools, atomic force microscopy (AFM) can be used to provide real time image of the height profiles of non-conductive samples. Although AFM is generally used to measure lengths and diameters of CNTs it has other capabilities that electron microscopes usually do not have. For example, AFM experiment may be conducted in different environments such as air, inert gas, vacuum or even liquid. This may be beneficial for studies on stability of functional carbon nanotubes in different environments.

Finally, STM is a powerful technique used to obtain tree-dimensional images and electronic states of nanotubes. However, it is required to deposit the nanotubes on a flat and conducting substrate such as HOPG [129] or Au [130]. STM is capable of resolving the atomic structure and the electronic density of states (DOS) simultaneously [13]. Moreover, using atomically resolved STM images, the measured chiral angle (θ_{exp}) of nanotubes can be determined. This is done by measuring the angle between the tube axis and the (n,n) direction for $\theta_{exp} < 15°$. When $\theta_{exp} > 15°$, the angle θ_{ind} is measured between the tube axis and the (n,0) direction and the chiral angle is determined from the relation $\theta_{exp} = 30° - \theta_{ind}$ [131].

Spectroscopies

Energy dispersive X-Ray spectroscopy (EDX) is often coupled to TEM or SEM and offers elemental analysis of the structures [132]. In an EDX experiment a spectrum, elemental map or a linescan of individual functional carbon nanotube may be obtained. Chemical composition of inorganic nanostructures is easily accessed and may be spatially resolved. Organic molecules often contain in their structure elements such as oxygen, nitrogen, sulphur and phosphor all of which form distinguishable EDX peaks. Hence, the characterization of the elemental composition of functional carbon nanotubes and presence/absence of impurities may be assessed.

Another technique coupled to the TEM is electron energy loss spectroscopy (EELS) [133, 134] which apart of carrying information on the composition of materials (like EDX does), also carries the information on chemical bonding, valence and conduction bands of each of the composing elements of the CNT-based construct. It is particularly sensitive to light elements and thus is preferred for investigation of functionalities of organic nature composed of elements such as carbon, oxygen, nitrogen, sulphur, etc.

From X-ray photoelectron spectroscopy (XPS) investigation [135], elemental composition, the nature of chemical bonding and electronic structures of elements are offered in a simple experiment. It may be used for the investigation on the structure modification of CNTs due to chemical interaction with organic molecules or gases adsorption [136]. However it is not commonly used since it requires a specialized instrument and there is no control over the probed area. In contrast to that, EDX and EELS are often coupled to SEM or TEM and offer instantaneous image of probed structure or area of interest with resolution down to the atomic level.

X-ray absorption near-edge structure also called NEXAFS (near-edge X-ray absorption fine structure) exists in the energy level of 50 eV above the absorption edge. It includes the unoccupied part of band structure just above the Fermi level. Thus, certain aspects of electronic structure of detected element can be revealed. Accordingly, it provides detailed information on local bonding environments associated with different elements by monitoring the electron yield as a function of incident photon energy. Like EELS, NEXAFS spectra are characterized by distinctive absorption edges because of core-shell ionizations. Their detailed structure contains comprehensive structural information on the local bonding environment. However, the use of this technique is limited due to the need of a tuneable X-Ray source, typically a synchrotron, and the difficulty of deconvolution of lineshapes of elements.

Raman spectroscopy offers fast and non-destructive characterization of vibrational modes identified by measuring the energy of scattered photons generated from a sample exposed to intense laser light. Raman spectra of CNTs typically consist of following characteristic peaks: a low frequency peak < 200 cm^{-1} characteristic to SWCNTs assigned to a "breathing" mode, whose frequency depends on tube diameter (RBM); a large peak at 1340 cm^{-1} assigned to ill-organized graphite (D line (D standing for disorder) and a high frequency band (G band) spread between 1500 and 1600 cm^{-1} corresponding to a stretching mode of graphite. By determining the ratio between the D and the G bands ($A_D \backslash A_G$), a quantitative measure of defect density in the CNT sidewall can be determined. Furthermore, the D band shape and intensity is often correlated with the extent of nanotube sidewall functionalization. This is due to the disruption of sp^2 structure of CNTs forming more sp^3 hybridized carbons that substantially modify the electronic structure of CNTs, what gets reflected on Raman spectrum. Consequently, $I_D \backslash I_G$ band analysis can be used to obtain information regarding structural changes as a result of functionalization [137, 138].

Another efficient tool for the characterization of electronic structure of SWCNTs is near-infrared (NIR) spectroscopy [139]. SWCNTs are characterized by unique NIR peaks due to their inter-band transition of van Hove singularities in either semiconducting or metallic nanotubes. Therefore, this technique is useful to identify functional groups and the nature of their attachment to the CNT sidewalls [140]. Different groups absorb characteristic frequencies of IR irradiation giving distinctive peaks. However useful, it does not provide a quantitative measure of functional group concentration.

The discovery of fluorescence emerging from SWCNTs was first revealed upon exfoliation of nanotubes from bundles [20] and opened the door to quick determination of the structure distribution in bulk SWCNTs. This was facilitated by surfactant wrapping of individual nanotubes separating the semiconducting ones from metallic ones which quench the fluorescence signal of the former. The observed fluorescence of semiconducting SWCNTs makes them candidates for applications such as fluorescence tracking of single molecules *in vivo* [141], NIR sources of single photons for quantum optics [142] and nanoscale optoelectronic components [143]. The fluorescence changes depending on the solvent used for the dispersion of carbon nanotubes and was shown to be brighter for organic solvents when compared to water.

Important for dispersion characterization of carbon nanotubes is a technique based on UV-VIS spectroscopy [144]. From UV-VIS spectra the quantification of nanotube dispersion is possible by applying a light source on the suspension and correlating absorbed or scattered amount with particle size. Completely dispersed CNTs are highly active in the 200 – 1200 nm wavelength region. Therefore, this technique is used to detect individual nanotubes relating the intensity of absorption at a specific wavelength to the concentration of CNTs suspended in the solution through Beer-Lambert law [145]. MWCNTs show peak absorption at 253 nm while SWCNTs at 972 nm and 1710 nm. Moreover, UV-VIS spectra can be

characterized as a set of superimposed peaks for CNTs of different diameters and chiralities [146].

Photoluminescence spectroscopy (PL) emerges from the recombination of electron-hole pairs at the band gap of semiconductors. As already mentioned before, SWCNTs are either metallic or semiconducting, depending on the chirality of the tube. However, they are usually grouped in bundles where they interact with each other through Van der Waals force. Thus, photoluminescence of semiconducting tubes is relaxed and often results in no signal. In order to be able to observe the PL signal the bundles must be separated into individual tubes [147]. Then, the nature, the geometries and the diameters of individual SWCNTs may be accessed. Moreover, it was shown PL signal is sensitive to the presence of chemical defects and to the purity of the sample [148].

Diffraction

In order to identify the crystallographic structure of CNT hybrid constituents, a versatile and non-destructive X-Ray diffraction (XRD) experiment is often conducted [149]. A set of characteristic peaks reveals the crystal structure, interlayer spacing and presence of possible impurities. Diameters and chiralities distribution are also observed as well as various number of layers for MWCNTs. Therefore, statistical analysis and determination of sample purity may be performed on CNTs based on XRD spectra. A mean diameter of CNTs can be calculated based on the Debye-Scherrer relation on the (002) peak. However, systematic overestimation of tube diameters with respect to TEM analysis was reported.

Another method of obtaining the crystallographic information is the electron diffraction (ED) often used in the transmission electron microscope (TEM). The advantage of ED is the ability to probe a single nanoparticle or a single nanotube, while in the XRD we probe whole bulk. However, the common characteristic is

that both of them (XRD and ED) are useful for characterization of periodically arranged structures such nanotubes, nanoparticles, nanowires and polymers but not suitable for organic molecules. Moreover, electron diffraction solves one of the problems we may encounter in HRTEM analysis that comes from the projection of artefacts, which may prevent the resolution of structural features. This can be partially resolved by considering selective area electron diffraction (SAED), since any overlapping does not affect the characteristic lattice spacing in the diffraction pattern and information on the degree of ordering can be derived from the brightness and width of the diffraction pattern. Also, the chiral indices of CNTs can be measured by SAED technique performing semi-quantitative analysis of the diffraction pattern. It can be done up to the radii of 4 nm for both SW- and MW-CNTs [150].

Magnetic measurements

For measurement of the magnetic character of carbon nanotubes the most common technique used is superconducting quantum interference device (SQUID). Semiconducting and metallic pristine SWCNTs show a diamagnetic response in SQUID measurements. Ferromagnetic behaviour is seen for iron filled in metallic SWCNTs and paramagnetism for Fe-filled semiconducting nanotubes [151]. Therefore SQUID may give us an indication of the presence and the quantities of iron catalyst in various samples and hence assess their purity. It may also be used for other materials filled in carbon nanotubes, deposited on their outer walls or other nanocomposites based on CNTs to characterize their magnetic performance [152]. For example, magnetic properties of N-doped MWCNTs were studied showing temperature dependent decay of magnetization [153] and the distribution of MWCNTs in polymer matrix was correlated with electrical conductivity and magnetic field response [154].

Other techniques

Thermogravimetric analysis (TGA) is used to quantitatively determine the amount of carbon and other than carbon materials in bulk samples of pristine, purified and functional carbon nanotubes [155]. It also gives information about thermal stability and amount of catalyst impurities of the material under study. Due to higher decomposition temperature of CNTs in comparison with adsorbed molecules and amorphous carbon we may estimate the presence and concentration of organic molecules attached to their sidewalls based on TGA. In case of filled carbon nanotubes filling yield may be calculated based on the quantity of the TGA inorganic residue through a simple method [156].

1.4 Toxicity of pristine and functional carbon nanotubes

The toxicity of pristine and functional carbon nanotubes is of high importance due to the wide variety of CNT-based structures already applied or studied for applications ranging from electronic devices such as rechargeable batteries to biomedical uses, such as medical devices and drug delivery carriers. Thus, exposure to CNTs can occur intentionally or accidentally not only during innovative and manufacturing processes, but also during usage, disposal, recovery, and recycling processes of CNTs and their commercial products (**Figure 1.7**). The uptake of any nanomaterial into the human body may undergo through processes such as inhalation, ingestion or absorption. Therefore, a detailed understanding of the biological interactions of carbon nanotubes and carbon nanotube based hybrids and composites, is extremely important both from efficacy and safety point of view. The understanding of the accumulation, degradation and/or excretion processes of CNTs and functional CNTs in the human body is essential before their application, especially in biomedicine. The prevention-through-design is the best way of producing safe nanoproducts.

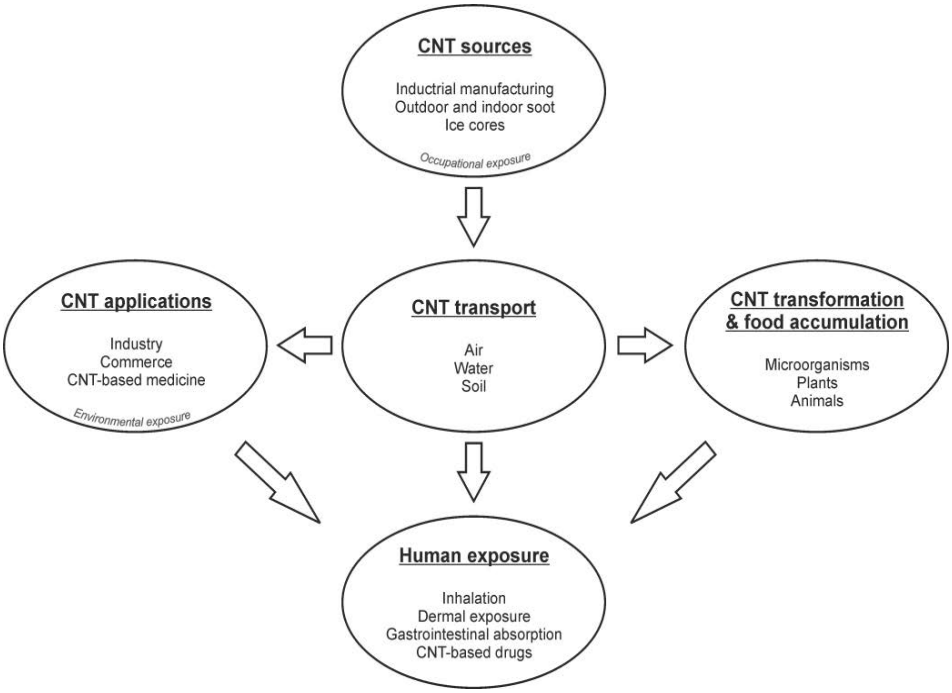

Figure 1.7 Human exposure to carbon nanotubes pathways.

When a designed CNT-based drug delivery nanocarrier is administrated a desirable effects may arise such as modulation of cell activity and *in-vitro* or *in-vivo* activation (**Figure 1.8**). However, if the immune system senses a CNT as a threat, some adverse effect as cytotoxicity or inflammation may emerge. The major exposure to CNTs is due to industrial manufacturing. Production of CNTs leads to occupational exposure, release to natural environment and potential accumulation in food. Exposure routes through inhalation, skin absorption, ingestion or as drug delivery systems are possible.

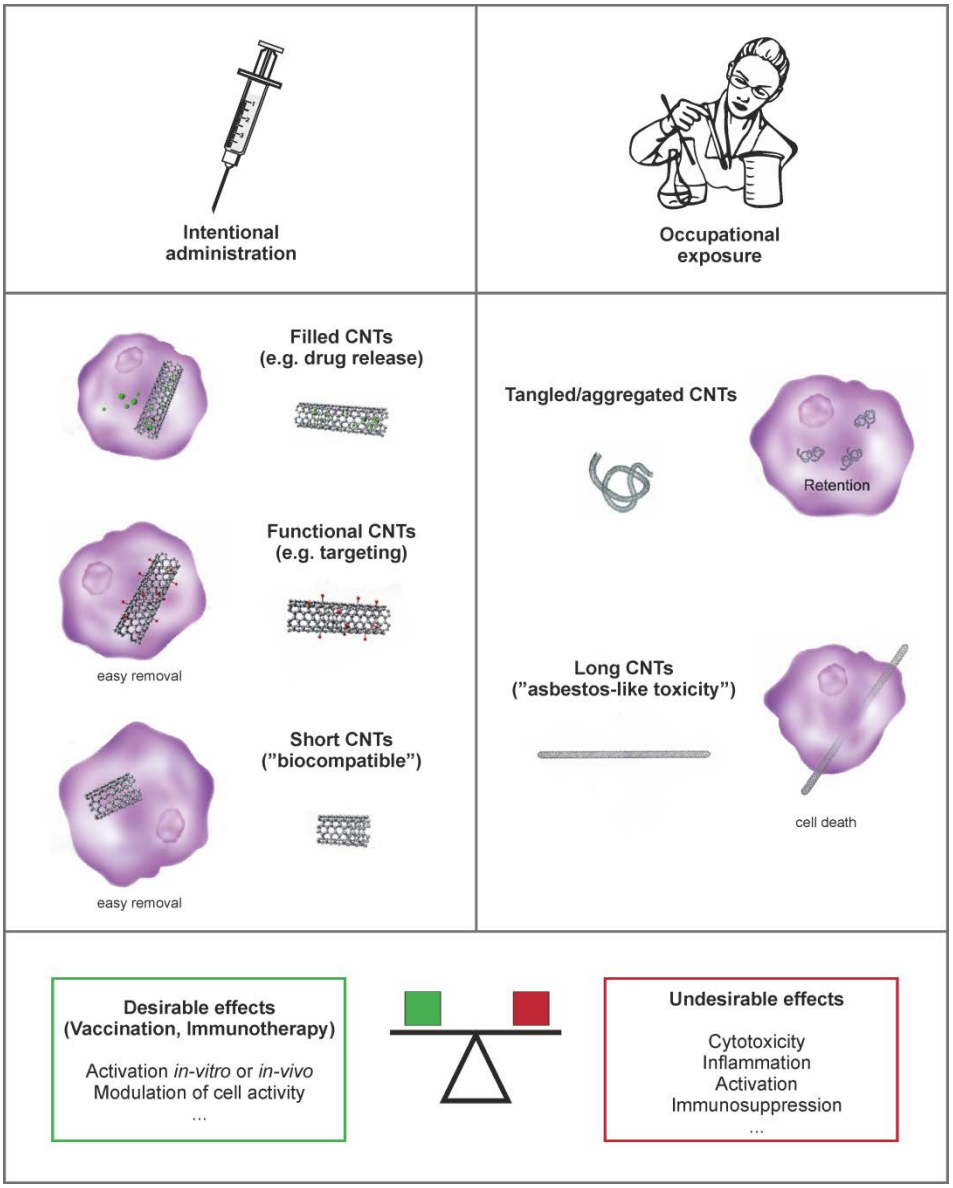

Figure 1.8 Balanced impact of CNTs on the immune system. The immune cells may encounter CNTs by intentional administration as drug delivery carriers or by occupational exposure. When engineered on purpose, they can generate desirable effects. However, if the immune system senses the CNTs as a threat, undesirable effects may occur.

The potential toxicity of carbon nanotubes has been extensively discussed in the last years, subject of many reports and reviews [157-161]. While some of the authors attributed similar to asbestos pathogenicity to the CNTs, caused by their fiber-like structure and biological perseverance [162, 163], it was shown later that lung inflammation caused by well dispersed SWCNTs was insignificant compared with asbestos. Moreover, other scientists have reported no toxicity effects in their investigations [164-168]. However, there is a wide range of functional carbon nanotubes showing dramatically different physicochemical properties when compared to pristine CNTs and to each other and hence each of them should be treated as a separate group. Indeed, in the recent years, the main characteristics affecting the biocompatibility of CNTs were pointed out, being their length, purity, aggregation state and surface properties.

The main aspect of pristine carbon nanotubes is their high aspect ratio, mainly due to the lengths ranging from few micrometers up to milimeters. Nonetheless, there are numerous known methods to shorten them down to few hundreds of nanometres what essentially improves their biocompatibility. As an example, it was shown that long and straight CNTs with lengths of ~5-20 μm, but not short and entangled CNTs (~1-5 μm), exhibit asbestos-like behaviour and induce mesothelial granulomatous inflammation upon injection into a mouse [163, 169]. Similar behaviour and conclusions were withdrawn from other studies on MWCNTs, were only long but not short tubes, induced pulmonary fibrosis [162, 170]. These results seem to be in good agreement with the asbestos definition and behaviour. Indeed, based on recent investigations on the pathogenicity, asbestos were defined as fibres of a length greater than 5 μm and an aspect ratio of 3:1-5:1 by World Health Organization (WHO), Occupational Safety and Health Administration (OSHA) and International Institute for Occupational Safety and Health (NIOSH) [171, 172].

Another issue regarding biocompatibility of pristine CNTs is emerging from the metallic content (catalytic nanoparticles) remaining after the synthesis. Metals, such as nickel and iron, affect some but not all of the toxicological properties of CNTs. For instance, the iron content of 26% in a SWCNTs sample was found to greater affect the production of reactive oxygen species called ROS ($O_2^{\bullet -}$, $^{\bullet}OH$, $RO_2^{\bullet}$, $RO^{\bullet}$), in contrast with SWCNTs with only 0.23% of iron [173]. A separate investigation showed that purified SWCNTs (Fe content of 0.23 %) were less cytotoxic to skin cells *in vitro* than their unpurified counterparts (Fe content, 30 %) [174]. Moreover, in a work from 2004 on SWCNTs, the iron content seemed not to affect the formation of granulomas in mice in a wide range of Fe content (0.53-26.9 %) [175].

Many concerns are raised due to the dispersibility of carbon nanotubes. Pristine CNTs tent to form agglomerates in form of fiber-like ropes, loose bundles or large size agglomerates. Such aggregation changes the dynamics of interaction with cells and molecules. Large agglomerates of CNTs are more difficult to be cleared off from the body than individual CNTs or small bundles. In addition, they tend to stimulate the formation of granulomas [176]. In a similar study, the agglomeration of CNTs was shown to stimulate macrophage engulfment of the nanotubes to prompt granulomatous inflammation [177]. Therefore, it seems to be important to obtain well dispersed nanotubes for medical and technological applications.

To sum up, most of the issues with biocompatibility emerging from carbon nanotubes´ physicochemical properties may be mediated through specific design and modification processes. The nanotubes may be shortened, purified and transformed into easily dispersible individual CNTs through surface modifications reducing substantially their toxicity and enhancing their biocompatibility. For instance, nitrogen-doped MWCNTs revealed significantly reduced toxicity and increased tolerance in exposed mice in comparison with undoped MWCNTs [178]. Ammonium-functionalized MWCNTs were rapidly eliminated from mouse´s body

and thus showed reduced toxicity [179]. DNA-coated CNTs resulted to be safe gene delivery carriers [167]. In another case, Pluronic-coated carbon nanotubes injected *in vivo* into animal brains did not induce degeneration of cortical neurons [180]. Not only the functionalization of carbon nanotubes with organic moieties brings a better biocompatibility and reduced toxicity, but also an inorganic functionalization was effective in that matter. In this case aluminium oxide coating of CNTs helped to reduce lung fibrosis in mice during *in vivo* studies [181].

The first step into creating biocompatible and safe carbon nanotubes for biomedical and other applications is a smart design of short, dispersible and functionalized CNTs. However, there is another issue that need to be studied. We should have in mind what happens when carbon nanotubes and functional CNTs interact with so-called bio-corona of proteins, lipids and other biomolecules present in our bodies. Especially, the enzymatic degradation of carbon nanotubes by immune system with the use of bio-corona has important implications for the medical use of carbon-based materials. First steps in understanding that process, have already been done showing the bio-corona may dictate the biodistribution and affect the cellular recognition and biodegradation of CNTs [160].

1.5 Applications of functional carbon nanotubes

As mentioned before in this chapter, carbon nanotubes are characterized by unique physicochemical properties and versatile structure which converts them in platforms for preparation of functional carbon nanocomposites and hybrids. The variety of possibilities of combining single- and multi-walled CNTs with organic molecules (polymers, DNA, proteins, surfactants etc.), inorganic crystalline structures (nanoparticles, nanotubes, nanowires) or both at the same time is enormous. Therefore, the possible applications of functional carbon nanotubes are growing and seem to be endless. Moreover, the production capacity of CNTs

exceeding several thousand tons per year enables the commercialization of many CNT-based materials [182].

1.5.1 Biomedical applications of functional carbon nanotubes

Carbon nanotubes are emerging as promising carriers for drug delivery due to their unique properties including high drug loading capacities, cell membrane penetrability and prolonged circulation times. Additionally, while their inner cavity may be filled with specific compound for drug and gene delivery, therapy or imaging, their external walls may be functionalized with specific molecules for dispersibility, biocompatibility and targeting. The Raman scattering, photoluminescence and strong NIR optical absorption of carbon nanotubes make them suitable candidates for biological tracking, detection and imaging.

As already mentioned before, in order to reduce the toxicity and enhance the biocompatibility of carbon nanotubes for biomedical applications, they have to be shortened, purified and dispersible in aqueous solutions through external functionalization. When all of these criteria are met, we may add a specific function by encapsulating particular material in the internal cavity and/or add some other functional groups such as targeting agents on their sidewalls.

Drug and gene delivery

The drug and gene delivery of functional carbon nanotubes has been studied extensively, mainly due to their versatility, as CNTs may be modified in several ways in order to create a drug delivery carrier. For example, in a model study, doxorubicin (a common drug) was loaded by noncovalent π-π stacking interactions onto CNTs [183]. The noncovalent interactions enable attachment of many molecules, mainly proteins and genes. Another way of loading a drug onto CNTs´ sidewalls is done by covalent bonding working best for amino acids, oligopeptides, genes and antibiotics. For example, covalently bounded cisplatin in combination with a targeting ligand (epidermal growth factor, EGF) resulted in a selective

delivery to head and neck epithelial carcinoma cells overexpressing EGF receptors *in vivo* and *in vitro* [184]. Targeted delivery of oligonucleotides to cancer cells and employment of NIR light induced extensive local heating of the CNTs and in consequence killed the cancer cells [185]. Lately, the exploration of using CNTs for targeted delivery of radioactivity is investigated by loading potentially radioactive materials in the interior cavities of nanotubes and closing their ends to prevent uncontrollable leakage of the payload [128] Many efforts have been put into investigations of CNTs in the field of gene delivery or delivery of small interfering RNA owing their known interaction with DNA [186, 187]. This field is taking an advantage of a needle-like shape of CNTs allowing them to pierce through the cell membrane [188].

Imaging

Carbon nanotubes show strong Raman scattering, photoluminescence in the NIR region and good laser-to-acoustic transferring capacity what makes them potential candidates for cancer detection and imaging [189]. Among all the techniques, fluorescence imaging is the most habitually implemented for CNTs imaging/detection. The *in vivo* tumor detection by CNTs is possible due to their NIR emission (1100-1400 nm) [190]. At the same time, CNTs conjugation with multiple fluorophores (i.e. quantum dots) with different emission wavelengths makes them suitable for fluorescence resonance energy transfer imaging (FRET) technique, as in the case of Fe_2O_3-filled CNTs conjugated with CdTe quantum dots designed for both imaging and magnetically driven targeted drug delivery [191]. Another possibility is to use CNTs in cancer imaging as ultrasound contrast agents or photoacoustic agents (US and PAI imaging). Double function of UC imaging and drug delivery was assigned to antibody conjugated MWCNTs [192]. SWCNTs conjugated with cyclic Arg-Gly-Asp (RGD) peptides were used as a contrast agent for PAI imaging of malignant glioma tumors in mice [193]. In another example, RDG-conjugated, silica-coated gold nanorods deposited on the surface of CNTs were used for targeted PAI imaging of gastric cancer [194].

Raman scattering has been used for imaging of live cells using functionalized with targeting ligands carbon nanotubes containing different isotopes (^{12}C or ^{13}C) and a single laser excitation [195]. Moreover, when CNTs are coated with noble metals (e.g. Au, Ag) they may be used for surface enhanced Raman scattering (SERS) imaging and photothermal therapy [196]. Other imaging techniques where the use of CNTs is being exploited include positron emission tomography (PET) [197], magnetic resonance imaging (MRI) [198], single photoemission computed tomography (SPECT) and multimodality imaging [199, 200].

Therapy

The electronic properties of CNTs can be exploited for therapeutic purposes via photothermal therapy [196]. This is possible due to the strong absorption of light by SWCNTs in NIR range (800–1600 nm). Functionalized CNTs resulted to be attractive nano-vehicles for the delivery of boron to tumor cells for an effective boron neutron capture therapy (BNCT) [201]. Many different constructs based on carbon nanotubes are under investigation for cancer therapy [202]. When diagnosis and therapy are combined in one material it is called "theranostic" [203]. Such materials allow precisely defining the location of the tumor and accordingly setting the optimal drug doses as well as therapeutic time frame determined by acquiring the real time drug distribution profile *in vivo*.

1.5.2 Other applications of functional carbon nanotubes

The field of applications of functional carbon nanotubes expands beyond biomedicine, ranging from catalysis to rechargeable batteries and solar cells.

In catalysis, carbon nanotubes are substituting other carbon based materials as a support for inorganic nanoparticles. This is due to the enhanced catalytic activity of CNTs-supported catalysts shown in various investigations on composites with nanoparticles composed of elements such as Pt, Au, Ag, Rh, Ru, Co and Ni [110, 204, 205]. For example, MWCNTs coated and filled with Fe_2O_3 nanoparticles were

used for study on Fischer-Tropsch reaction which converts CO and H_2 (syngas mixture) into hydrocarbons and showed selectivity towards longer chain hydrocarbons [206]. The implementation of CNTs in photocatalysis, based on the formation of CNT-TiO_2 hybrids, resulted in enhanced activity and was shown to be due to the high conductivity of carbon nanotubes [207]. Additionally, MWCNTs hybridization with graphitic carbon nitride (g-C_3N_4) exhibited superior photocatalytic performance of water splitting reaction leading to hydrogen production [208].

In energy storage, carbon nanotubes also play an important role. MWCNTs are widely used in lithium ion batteries, where they are mixed with active metals and binding polymers to provide increased electrical connectivity and mechanical integrity [209, 210]. In fuel cells, the use of CNTs as a catalyst support can potentially reduce platinum usage or even eliminate it [211, 212]. In general, CNT-metal nanoparticle materials show improved catalytic activity and reduced metal loading.

CNTs forming nanocomposites with semiconducting CdS, CdSe, TiO_2 and Cu_2S nanoparticles or polymers are employed in solar cells serving as photo-generation sites and charge carriers in collecting/transport layer of these energy conversion materials [213-216]. Usually, in these cases highly conductive CNTs act as electron acceptors and charge carriers while semiconductor nanoparticles as electron donors.

Besides all of the applications mentioned above, there are many others like the use of CNT in electronics [217-219], optics [220, 221], gas sensors [222, 223], memory switching devices [224], and hydrogen storage [225].

1.6 Objectives of the thesis

This Thesis is focused on the thorough characterization of functional carbon nanotubes with interest for biomedical and optical applications by electron microscopy techniques.

The following main objectives have been addressed, each of them constituting one thesis chapter:

Objective 1: Optimization of characterization methodology for each step of preparation of functional nanotubes, namely: (1) shortening and purification of carbon nanotubes, (2) filling of internal cavities of CNTs, (3) functionalization of external walls of CNTs and (4) investigation of functional carbon nanotubes interactions with biological cells. Besides conventional analysis usually employed for the study of this type of materials, we aim to:

i) Provide standard operating conditions for study of lengths of purified and shortened SWCNTs by low voltage surface sensitive HRSEM, optimizing parameters such as solvent, best support and suitable imaging conditions.

ii) Explore the use of low voltage HAADF STEM for the study of the filling yield and removal of external material efficiency in a myriad of as-filled samples, as well as the determination of the structure and composition of the filling materials.

iii) Assess the success of organic functionalization on the external walls of carbon nanotubes by visualizing heavy element tags using HAADF-STEM and spectroscopic techniques.

iv) Expand the use of low voltage STEM for the visualization of the interactions of functional carbon nanotubes with cells.

Objective 2: Study the formation of narrow diameter single-layered inorganic nanotubes enclosed in single-walled carbon nanotubes. The role of the anion size in the growth of these novel structures will be investigated by keeping the cation and changing the anion of the encapsulated halide.

Objective 3: Investigate the effect of the MWCNT template materials in the formation of inorganic nanotubes. The structure of the prepared hybrids, as well as their optical properties, will be analysed.

These objectives have motivated our research and the main results are presented in this Thesis dissertation.

2 Methods

In this chapter, the description of the experimental techniques used in this thesis dissertation for the characterization of shortened and functional carbon nanotubes will be described.

2.1 Electron microscopy and related techniques

Since its development Electron Microscopy (EM) capabilities have been growing to become essential tools in academics and industry for characterization of wide variety of materials, ranging from inorganic to biological. EM pushed the resolution limit placed by light microscope to the atomic level switching from photons to electrons. There are two basic instruments available: Scanning Electron Microscope (SEM) and Transmission Electron Microscope (TEM). SEM is usually used to get an insight into the morphology of a specimen (size, shape, surface roughness) through scanning across the sample surface with electron beam at relatively low voltages. There are few advantages of SEM over TEM: it is faster, less expensive and less destructive to beam sensitive specimens. However, the big advantage of TEM over SEM is the much higher resolution of the former, obtained mainly through higher voltage of electrons that enables structural characterization down to the atomic level. Moreover, great progress has been done in the last decades to further improve the resolution of the TEM leading to the development of specific correctors and monochromator that helped to solve problems of spherical and chromatic aberrations, introduced by imperfect lenses and polychromatic beams, respectively. This gave a rise to construction of higher resolution microscopes, called aberration-corrected TEMs. There is also a possibility of using scanning transmission electron microscopy (STEM) which is a combination of SEM and TEM, as it uses a scanning beam to form an image just like in an SEM but uses transmitted electrons to form an image. All of the EM techniques were essential for the research discussed in this manuscript and thus are the core of this chapter.

During the electron – sample interaction different types of signals are produced: secondary (SE), backscattered (BSE), and Auger electrons (AE) are created along with photons of visible light and characteristic X-rays (**Figure 2.1**). Additionally, when the sample is thin enough (<100 nm) the electrons can transmit through it

and are primarily used in TEM. All of these signals carry specific information about the sample. For thin samples, i.e. electron transparent, electrons go through it either without energy loss or losing energy in scattering events.

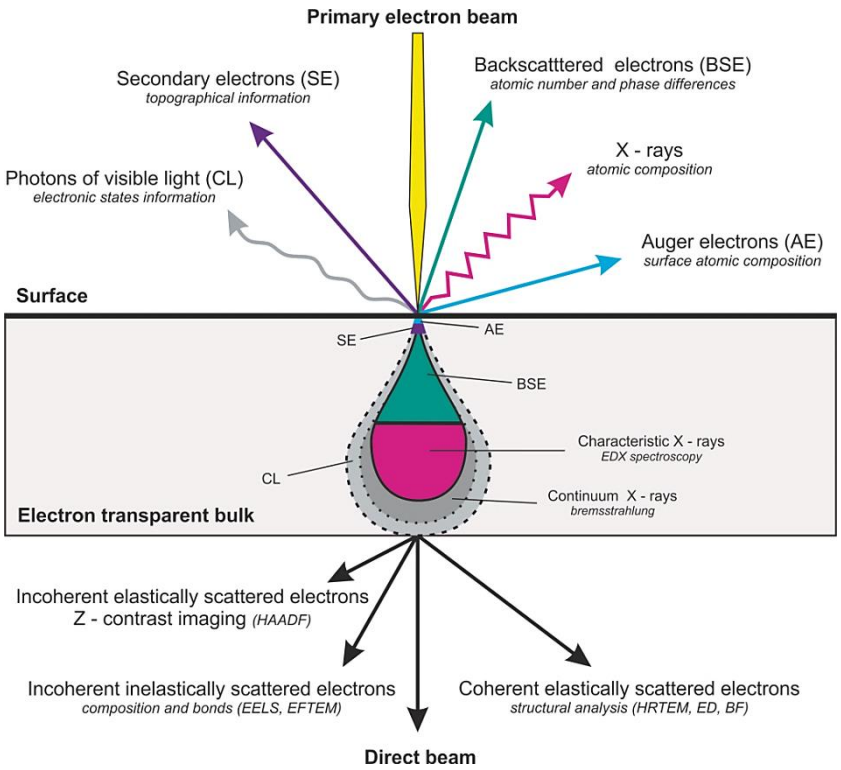

Figure 2.1 Signals generated when high-energy beam of electrons interacts with a thin specimen.

On **Figure 2.1**, a scheme of possible electron-matter interactions for an electron-transparent sample is displayed. When a primary electron beam hits the specimen many processes are occurring at the same time. With a dedicated detector, we may select a particular type of signal and collect it to extract specific information. In SEM mainly secondary electrons (SE) and backscattered electrons (BSE) are used to form an image while in TEM, coherent elastically scattered transmitted electrons (TE) are collected to form high resolution images in bright field (HRTEM) or incoherent elastically scattered TE to form STEM (or Z-contrast) images. We may

also take an advantage of ejected X-rays for spectroscopic characterization through Energy Dispersive X-Ray (EDX) spectroscopy and of incoherent, elastically scattered electrons through Electron Energy Loss Spectroscopy (EELS). Both of them provide valuable information on the composition of studied materials (EDX, EELS) as well as the thickness and oxidation states of involved elements (EELS). Auger Spectroscopy is referred as alternative technique to EDX and is characterized by its high surface sensitivity. Additionally, luminescence processes may occur for some materials and we may collect as created photons of light by Cathodoluminescence (CL) detector.

Other techniques complementary to EM techniques were employed in this thesis for characterization of specific samples when needed. Consequently, in this chapter we will also describe techniques such as: Photoluminescence (PL), X-Ray diffraction (XRD), Thermogravimetric Analysis (TGA), Raman Spectroscopy and Superconducting Quantum Interference (SQUID).

2.1.1 Scanning Electron Microscopy

A Scanning Electron Microscope is a powerful imaging tool capable of getting two-dimensional images of materials and surfaces at relatively high spatial resolution; this is down to ~1 nm [226-228]. Micrographs are acquired by swapping across the surface in a raster manner with a finely focused low energy beam (typically up to 30 kV) composed of electrons emitted from an electron source, accelerated and then focused on the sample by electromagnetic lenses (**Figure 2.2**). During electron-sample interaction different types of signals are produced (**Figure 2.1**). SEM images are formed either by SE or by BSE arising from inelastic collisions between the primary beam and loosely bound electrons of the conduction band or tightly bound valence electrons.

The principal reason for building the first SEM in 1965 was not achieving the highest spatial resolution (the first TEM was built in 1936) but the ability to image

bigger samples than in a TEM with higher resolution than in light microscopy. Before the first successful commercial SEM was built by Cambridge Scientific Instruments Company in 1965, the concept of SEM was described in work of Knoll (1935) [229, 230]. There are two other important great pioneers of scanning electron microscopy, Charles Oatley and Manfred von Ardenne. The latter, established the theoretical basis of scanning electron microscope and constructed an instrument which was primarily intended to overcome chromatic aberration when relatively thick specimens were examined by transmission but did not gain the acceptance of the community due to its poor resolution. Following his work, Charles Oatley was able to overcome that problem and consequently the first commercial SEM was built. He acknowledged the work of his predecessors in a review about the history of SEM in 1982 [231]. Nowadays, much improved SEMs are commercially built with resolutions reaching sub-nanometer level.

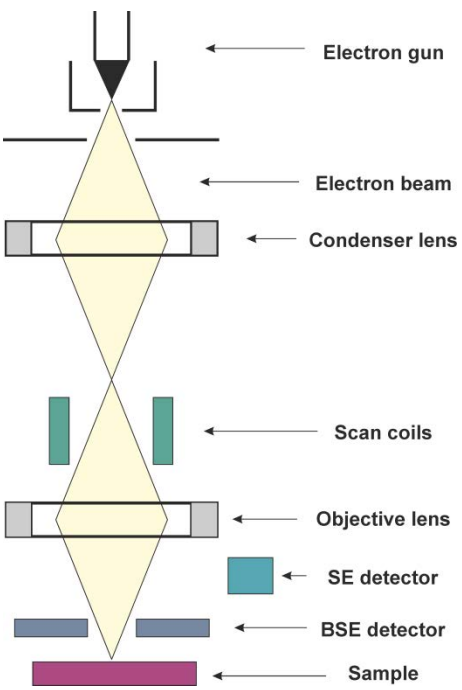

Figure 2.2 Schematic representation of Scanning Electron Microscope.

The most commonly used, secondary electrons are ejected from very close to the surface of the sample and hence offer topological information (**Figure 2.4 c**). The size and shape of nanomaterials are easily assessed due to the large depth of field that SEM offers. The SE detector may be mounted in different configuration in the SEM, the so called *out-lens*, *in-lens* or *semi-in-lens*. The most common configuration is the *out-lens* configuration where the detector is installed between objective lens and the specimen. The second type, the *in-lens* configuration places the detector above the objective lens what gives smaller lens aberrations and hence it is characterized by the best resolution. In the *semi-in-lens* configuration a specially designed objective lens is mounted and the detector can be either placed above the lens or in the lens. The advantage over the *in-lens* detector is that larger samples may be introduced.

On the other hand, backscattered electrons arise due to elastic interactions between the incoming electron and the nucleus of the target atom (i.e. Rutherford scattering) and therefore the higher the atomic number (Z) of the atom is, more BSE signal is emitted, being reflected on the micrograph as contrast variations (the higher the Z is, the higher the brightness of the pixel on the micrograph appears, **Figure 2.4 d**). Additionally, BSE are ejected from deeper regions within the sample than SE what compromises the resolution. When further combined with EDX spectroscopy BSE imaging becomes a powerful tool for elemental characterization of heterogeneous samples. Nevertheless, due to the availability of transmission mode in the SEM at the ICN2, this mode was not applied in our studies.

One of the SEM microscopes (FEI´s Magellan 400L XHR) used in our studies was additionally equipped with dedicated retractable STEM detector (**Figure 2.3**). This detector allowed acquiring Z-contrast images using specially designed specimen holder, capable of carrying up to six TEM grids carrying specimens.

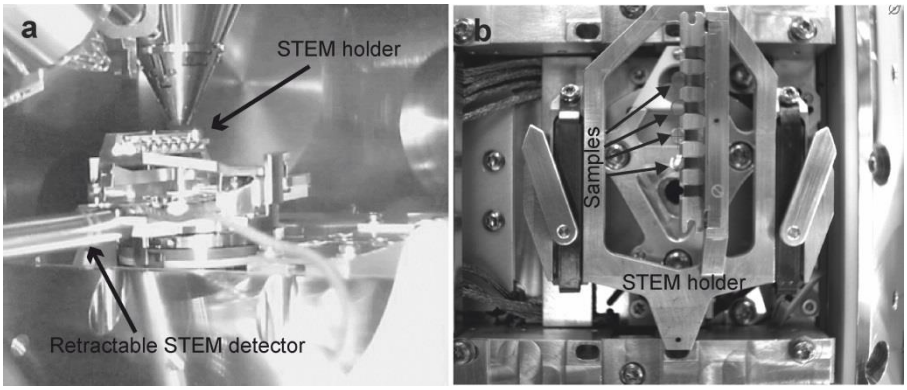

Figure 2.3 STEM imaging in SEM through dedicated retractable detector (a) and sample holder (b). Image acquired by CCD camera of the interior of SEM chamber with STEM holder and STEM detector inserted below it (a). Four TEM grids with samples deposited on top of them and clamped by the detector (b).

Additionally to SE, BSE (standard) and STEM (non-standard) detectors some of the microscopes include EDX detector to gather the X – rays formed during the interaction of the electron beam and the material under study. Apart of that, few of them are equipped with CL detector to study luminescence properties of materials. Because of their complexity, importance and versatility (may be used both in SEM and TEM), CL and EDX will be discussed separately, later in this chapter.

In this thesis focused on functional carbon nanotubes we have mainly used SE-SEM imaging in *through in lens* detector (TLD) configuration. For size distribution studies of shortened CNTs, evaluation of the cleanliness of purified and filled samples and the degree of aggregation/dispersion of pristine and functional CNTs samples we usually deposited them on top of Si chip or carbon covered TEM grid from ultrasonicated dispersion of CNTs in organic solvents or water. Furthermore, we used SEM in STEM mode concerning studies of filling yield of nanotubes, its post-synthetic purity and in investigation done on biological samples, namely cells, where low voltage permitted for visualization of the interaction between functional CNTs and cells but avoided possible damage of this beam-sensitive material. All of the abovementioned investigation was performed on FEI´s Magellan Xtreme High

Resolution microscope (**Figure 2.4 b**) operated in the range of 2-20 kV. Additionally, EDX elemental analyses were done when needed for purified, filled and functionalized CNTs. Elemental analysis was performed with EDAX super ultra-thin window (SUTW) X-ray detector with 136 eV resolution (chemical analysis down to Be) attached to FEI´s Quanta 650F SEM (**Figure 2.4 a**) operated at 10-20 kV.

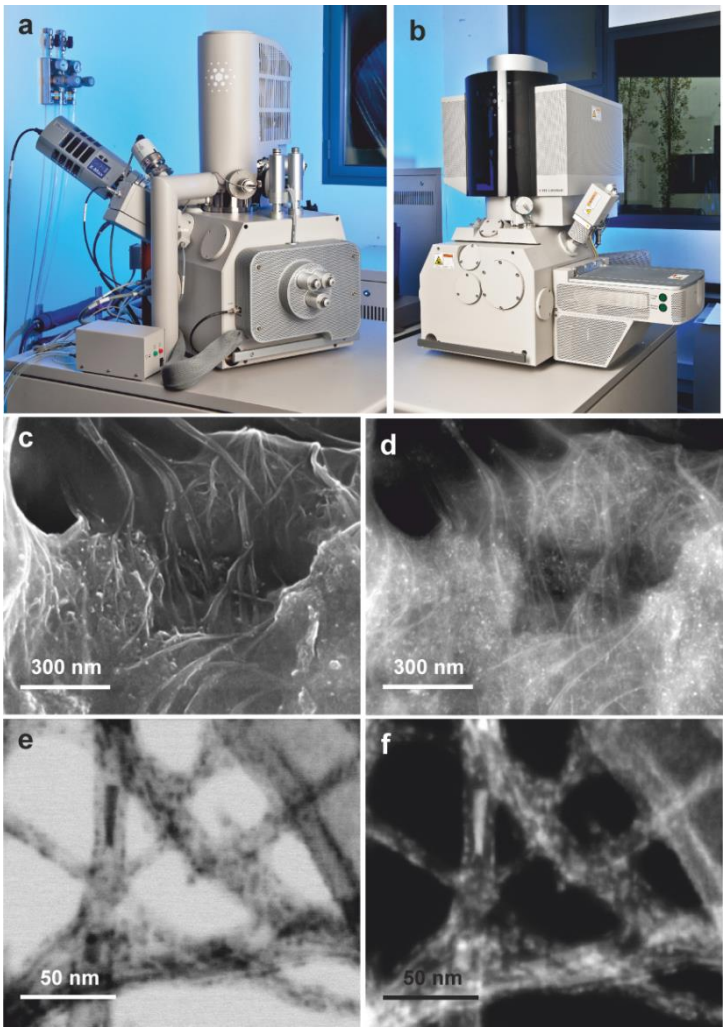

Figure 2.4 SEM equipment and imaging capabilities: a) FEI´s Quanta 650F SEM equipped with EDAX detector, b) FEI´s Magellan 400 L XHR SEM. SE (c) and

BSE (d) micrographs of sodium iodide filled in single-walled carbon nanotubes acquired with TLD configuration in Magellan at 5 kV. Bright field (BF) STEM image (e) and dark field (DF) STEM image (f), both acquired on the same area of lead iodide filled multi-walled carbon nanotubes sample in Magellan microscope (20 kV).

On **Figure 2.4**, both of the SEMs used in our investigation are displayed (**a, b**). In addition, SE (**c**) and BSE (**d**) micrographs of sodium iodide encapsulated inside single-walled carbon nanotubes are showed presenting the difference between the two detection modes. Consequently on the SE image, surface topology of the sample is seen while on the BSE image, the high brightness of iodide with high Z (53) contrasts with low brightness of carbon with low Z (6). Example micrographs acquired in STEM mode in Magellan 400L SEM are showed in bright field (**e**) and dark field (**f**) for multi-walled carbon nanotubes filled with lead iodide nanowires.

2.1.2 Transmission Electron Microscopy

TEM is a technique that provides information on the atomic arrangement of atoms due to its high spatial resolution (down to few angstroms for standard microscopes). Therefore, crystal structure of crystalline materials may be accessed directly from atomically resolved TEM images. Like in SEM the evaluation of size and shape of an object is available. Additionally, when coupled with EDX or EELS spectroscopes it is capable of elemental analysis of specimens with much higher resolution than EDX in SEM.

It was not a long time since Louis de Broglie (1925) theorized about the wave-like characteristics of an electron, that the first TEM microscope was built by Ruska and Knoll in 1930, for which achievement Ruska received a Nobel Prize in 1986. The basic concept arose from the fact that the wavelength of an electron is substantially lower than that of visible light, enabling to push the limits of spatial resolution to the atomic level. Nowadays, TEM is one of the most efficient and versatile tool used in academics and industry regardless of its high cost. Since the

first TEM many scientists have contributed to the progress of this technique and today highly specialized microscopes are available. There are dedicated TEMs for *in-situ* liquid, gas, heating, cooling (cryo), electric and magnetic experiments. This is mainly possible due to the development of new specialized holders. A major advance in TEM which has led to a leap in resolution (sub-angstrom) is the development of aberration correctors, which will be discussed later in this chapter.

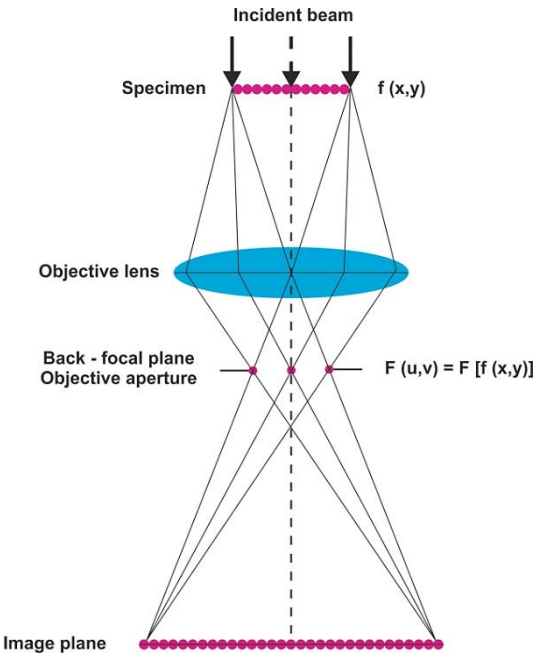

Figure 2.5 Image formation in ideal TEM.

For better understanding of the technique the basic principles of operation of a TEM need to be discussed [232]. Basically, a beam of highly energetic electrons is ejected from a gun placed on top of the microscope. They are focused and accelerated travelling down the column through a set of electromagnetic lenses and coils before hitting a specimen. When a plane wave of primary electrons hits the sample it is diffracted what leads to the creation of Bloch waves [233, 234]. The as-diffracted electrons are focused on the back focal plane of the objective lens (**Figure 2.5**). If the wave function of the exit plane of the object is given by f(x,y),

the diffracted amplitude of the beam is given by the Fourier transform of the object function F(u,v). These spherical waves interfere in the first image plane what leads to the formation of image in the image plane.

TEM image contrast may be formed in two ways. In the conventional micrographs the contrast is attributed to the change in the amplitude of either transmitted or diffracted beam. This leads to so called bright and dark field images. In the second case the contrast is formed by the differences in the phase of the electron wave and thus is called the phase contrast. This happens when a large objective aperture is selected allowing wider range of electrons with different phases to go through and form a high resolution image (HRTEM). A typical HRTEM micrograph contains information about the orientation of atoms and spacing between them through the lattice fringes.

In this thesis, HRTEM imaging of pristine, purified and functional carbon nanotubes was performed on FEI´s Tecnai G2 F20 microscope at 200 kV (**Figure 2.6** first from left). Also, TEM was used for investigation of CNTs interaction with biological cells on the same microscope but at lower voltage (120 kV) due to the delicate nature of samples. Investigation on the diameter and length of carbon nanotubes, their integrity, number of walls, opened/closed ends, filling yield and crystal structure of the payloads was carried out. Samples were usually deposited on copper TEM grids covered by lacey, holey or continuous carbon films from ultrasonicated dispersion of nanotubes in an organic solvent or water. HRTEM resulted also very useful for the studies on functionalized CNTs interacting with cells. In case of biological samples, they were prepared by cutting of resin-embedded cells/CNTs by ultramicrotone and depositing of these fine cuts (thickness below ~100 nm is required for TEM imaging) on top of a TEM grid. Combined with EDAX detector TEM provided information on the elemental composition of our carbon nanotube based samples and their purity. When the integrity of functionalized CNTs inside the cells was of interest we have employed EELS spectroscopy to confirm the CNT graphitic structure preservation.

Figure 2.6 TEM microscopes used for research focused on functional carbon nanotubes in this thesis. From left to right: FEI´s Tecnai G2 F20 (ICN2, Bellaterra, Spain), FEI´s (QU-Ant EM) Titan (EMAT, Antwerpen, Belgium) and FEI´s Tecnai OSIRIS (EMAT, Antwerpen, Belgium). All of them equipped with EDX and EELS spectrometers.

2.1.3 Scanning Transmission Electron Microscopy

In STEM, a focused electron beam rasters through a sample with a fixed beam direction. The need of having a fixed optical axis requires presence of scanning coils that tune the axis of the probe without tilting the optical axis. There are diverse STEM detectors that collect electrons scattered at different angles as shown on **Figure 2.7** (right). These are: high angle annular dark field (HAADF), dark field (DF) and bright field (BF). The highest image contrast is given when using HAADF, which collects incoherent electrons scattered at angles higher than 50 mrad. It is also called Z-contrast STEM owing high Z atoms scatter electrons to higher angles more strongly than lighter atoms. Essentially the intensity of HAADF image is proportional to Z^2. The BF gathers the elastically scattered coherent electrons with scattering angle below 10 mrad, while DF collects electrons scattered in angles between BF and HAADF range, typically between 10 and 50 mrad. The electron scattering is caused by Coulomb (electrostatic)

interactions between the primary electron beam and either electron cloud or nucleus of the atoms constituting the sample.

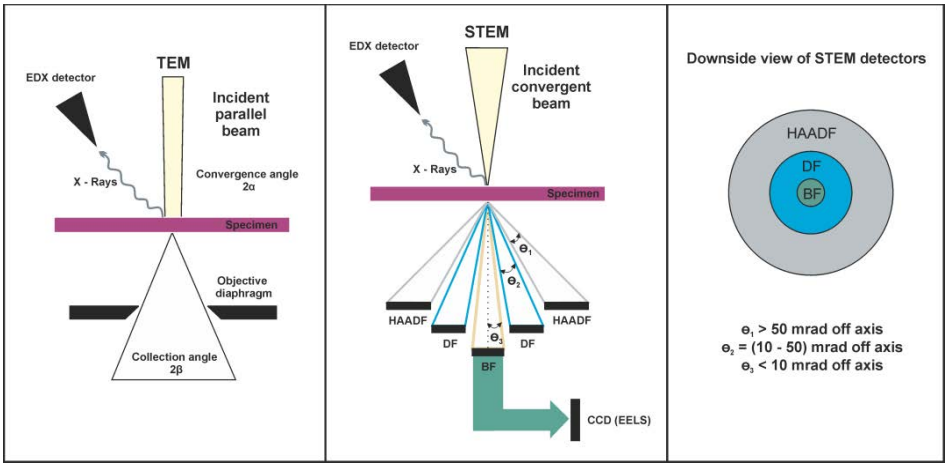

Figure 2.7 Configuration of TEM (left) and STEM (middle). Downside view of STEM detector segments (right). Additionally, characteristic X- rays may be collected by EDX after tilting the sample to face the detector (available in both TEM and STEM).

In the scope of our research CNTs were purified, filled with inorganic crystals composed of relatively heavy elements or functionalized with organic molecules bearing heavy elements in their structure and hence HAADF-STEM imaging resulted to be the most commonly used imaging tool. Usually, the first screening of our samples was done in STEM mode used in SEM at 20 kV (Magellan microscope). This is due to the fact that in this configuration few samples may be loaded at once and visualized in a fast manner (**Figure 2.3**). Hence, purified CNTs were imaged in HAADF-STEM in order to evaluate the cleaning efficiency in removing catalyst nanoparticles composed of iron. Additionally, all of the filled CNTs were visualized by this technique to provide an insight into the filling yield of the process and efficiency of post-synthetic washing step. STEM mode in SEM at low voltage (15 kV) was essential for studies on fine cuts of resin-embedded cells which are unstable under electron bombardment [235].

When higher resolution was of our interest we employed the Tecnai F20 microscope in HAADF-STEM mode at 200 kV (**Figure 2.6** first from left). In this case the difference between narrow inorganic nanowires and nanotubes was easily visualized. For CNTs functionalized with organic molecules bearing heavy element tags such as iodide and gadolinium it was possible to visualize groupings of atoms or even single atoms what enabled to assess the degree of functionalization. STEM in combination with EDX on the Tecnai F20 gave a confirmation of elemental composition of many samples while EELS provided a proof of carbon nanotubes integrity when crossing biological cells (study on cells conducted at 120 kV).

The Osiris microscope (**Figure 2.6**, third from left) is a state-of-the-art analytical instrument applied for fast chemical mapping in scanning transmission electron microscope configuration using EDX detector. This mode of operation was employed in the investigation on lutetium halide nanotubes encapsulated in SWCNTs and lead iodide single layer nanotubes deposited on top of MWCNTs for elemental mapping at 200 kV (**Chapters 4 and 5**). A dedicated STEM microscope, Vacuum Generator HB 501 fitted with a Cold FEG and operated at 100 kV, was used for CL measurments of lead iodide nanotubes (**Chapter 5**).

2.1.4 Aberration-corrected STEM

Unlike for the light microscope for which perfect glass lenses may be produced, the electron microscope uses electromagnetic lenses that are rather imperfect. Not much progress has been done in the matter of producing better lenses for the TEM, but fortunately dedicated correctors have been built to overcome those problems. Among the imperfections the most important for the performance (resolution) of TEM and STEM, besides stigmatism, are the spherical and chromatic aberrations (**Figure 2.8**) [236, 237].

The spherical aberration (**Figure 2.8 a**) emerges from the difference in the lens field for the off axis rays. After passing through point P representing a point in a

specimen, electrons travel down the column at different angles (θ) to the axis of the microscope and consequently are focused at different distances after crossing the lens. This causes a perfect point appear as a disc of the minimum radius at the plane of least confusion and a larger disk in the image plane at point P'. The higher the θ, the shorter the distance between P and P' becomes.

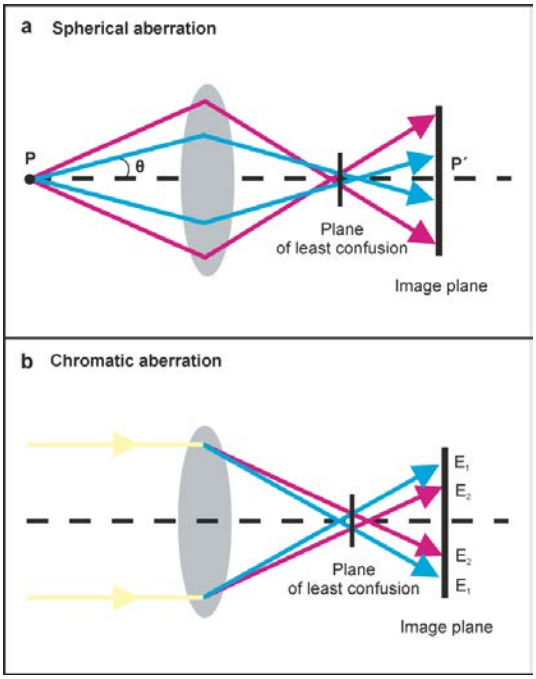

Figure 2.8 Spherical (a) and chromatic (b) aberrations.

The corrector for the spherical aberration (C_s corrector) pushed the resolution limit to the sub-angstrom regime [237]. It is composed of a number of magnetic multipole lenses, usually quadrupole–octupoles or hexapoles. The field of the multipoles varies with distance off the optic axis in the same way as spherical aberration does but with a rotational symmetry. The corrector uses the poles to distort the beam to compensate for the spherical aberration leaving an electron beam with a round shape. When C_s corrector is set up for STEM mode it needs to compensate for the condenser lens placed above the sample and thus the technique is called probe-corrected. On the contrary, if the corrector is set up for

HRTEM mode it compensates for the objective lens placed below the sample and is called image-corrected microscopy.

The chromatic aberration (C_c, **Figure 2.8 b**) is emerging from not fully monochromatic electron beam [236]. Depending on the electron source there is a different variation in energy spread in the beam which varies from 0.3 eV for cold FEG to ~ 1 eV for LaB_6 gun tip. This is a relatively small variation so the use of C_c corrector only makes sense if the microscope has a C_s corrector and a thin specimen so that the specimen–induced chromatic effects do not dominate the resolution. In general, the thicker the specimen is the more chromatic aberrations it will introduce.

The aberration–corrected HAADF-STEM microscopy was a valuable tool [238] for our studies on single – layered inorganic nanotubes of lutetium halides discussed in **Chapter 4** and for lead iodide single layers deposited on top of MWCNTs discussed in **Chapter 5**. The sub-angstrom resolution of Titan QU-Ant microscope (**Figure 2.6** middle) operated at 300 kV allowed for imaging of atomic arrays of single layer crystals.

2.1.5 Electron tomography

Standard TEM images are projections of three dimensional (3D) objects into two dimensions (2D) and therefore the real 3D structure may be misconstructed in the mind of the viewer. This is a fundamental limitation of TEM and STEM images. Although in most of the cases 2D images give sufficient information about the specimen sometimes it is crucial to get a 3D glimpse (tomography image) of our sample. The task consists of acquiring 2D images of the same object at successive tilt angles of as smallest as possible step and through a maximum possible angle range (**Figure 2.9**) proceeding with a 3D reconstruction of the object with help of dedicated software [239]. There are specially produced holders for tomography applications reaching around +/- 80°. However, there are some issues we need to

have in mind while acquiring a tomography series, like the stability of the sample, the shadowing effects and possible changes of focus, contrast and position of the object at each angle. In the case of functional carbon nanotubes the tomography experiment may bring on some difficulties due to the low stability of carbon atoms under high energy electron bombardment. The CNTs may undergo so-called knock-on damage for electron beams above 80 kV which may modify the structure during acquisition of the image series. Therefore, a low energy beam and short acquisition times are recommended to overcome this experimental difficulty.

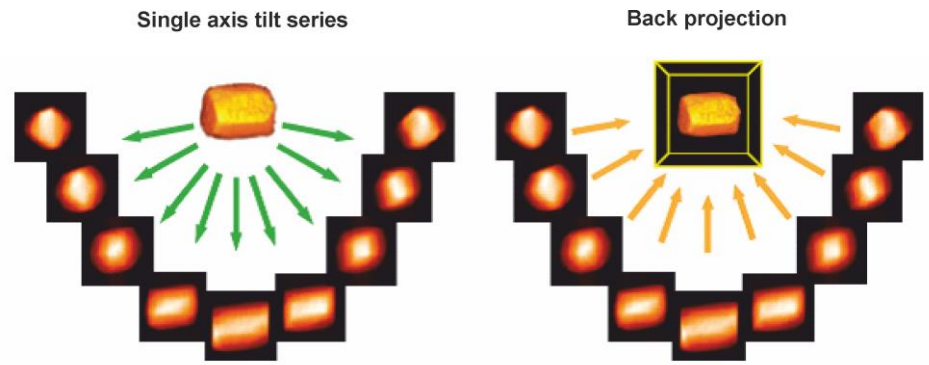

Figure 2.9 A scheme of tomography experiment by Midgley and Dunin-Borkowski [240].

In general, the resolution of a reconstructed tomogram is governed by the number of images in the tilt series and by the tilt range over which the series is recorded. Accordingly, a wide range of angles with a small step (1° - 2°) is required for a series of images in order to obtain a reliable 3D reconstruction. If there is a tilt range that cannot be achieved, the so-called "missing wedge" of information is created and therefore some artefacts may be introduced in the reconstruction. Typically tilt range of around +/- 75° is enough to reduce the artefacts to the minimum and obtain a reliable 3D image of an object. Another important aspect is to avoid the shadowing of our nano-object with the holder or other parts like the sample itself or the TEM grid.

In this thesis we used electron tomography for the 3D representation of lead iodide – MWCNT hybrids described in **Chapter 5**. These experiments were performed using Fischione 2020 single tilt holder over a range of -70° to +74° and -72° to +76° tilt every 4° operating in HAADF-STEM mode at 120 kV. The same set-up was used for acquisition of tilt series for lutetium triiodide single-layer nanotubes enclosed inside SWCNTs at 120 kV (**Chapter 4**). First hybrid was acquired in every 20° in range of +20° to -60° and the second one in small range of +10° to -10° every 10°.

2.1.6 Energy Dispersive X – Ray Spectroscopy

EDX is an analytical tool employed for the elemental analysis of specimens. It may be used as an accessory in both, SEM and TEM instruments. The technique was developed in the late 1960s and in few years has converted most of SEM and many TEMs in possible analytical tools. It is a fast and reliable technique that makes use of characteristic X – rays produced during the interaction of electrons from the beam and specimen [241]. When an electron beam with a sufficient energy hits an atom, it removes an electron from the inner shell. What is left behind is an ionized atom that fills the created hole with an electron from an outer shell emitting in this process an X – ray. We use the term characteristic X - ray because it is emitted with an energy that is exactly the difference between the two shell energies involved in the process. Therefore, it is characteristic to the specific element that has been hit.

It should be noted that depending on the energy of the incoming electron it may penetrate into the specimen to a different depth. The higher the energy the further the electron may travel inside the sample and thus an X – ray from a deeper region of the sample may be created. This is important for thick samples as those used in the SEM. As a rule of thumb the energy of the incoming electron has to be at least double the energy value of the X – ray we expect to see. Hence, depending on the

goal of our study, in a SEM we may change the operating voltage to obtain more surface sensitive or bulk sensitive data.

The EDX detector based on a semiconductor converts all of the created X – rays into a voltage of a proportional size. The quantity of electrons hitting the sample at each second is enormous and consequently the number of X – rays is too. So, in a matter of minutes or even seconds we are able to obtain a set of characteristic peaks offering qualitative identification of the elements and their quantitative distribution in the sample. The as-obtained spectra are plots of X-ray counts versus its energy and basically consist of a Gaussian – shaped peaks on a background. All possible EDX transitions for K, M, L, N and O lines are displayed on **Figure 2.10**.

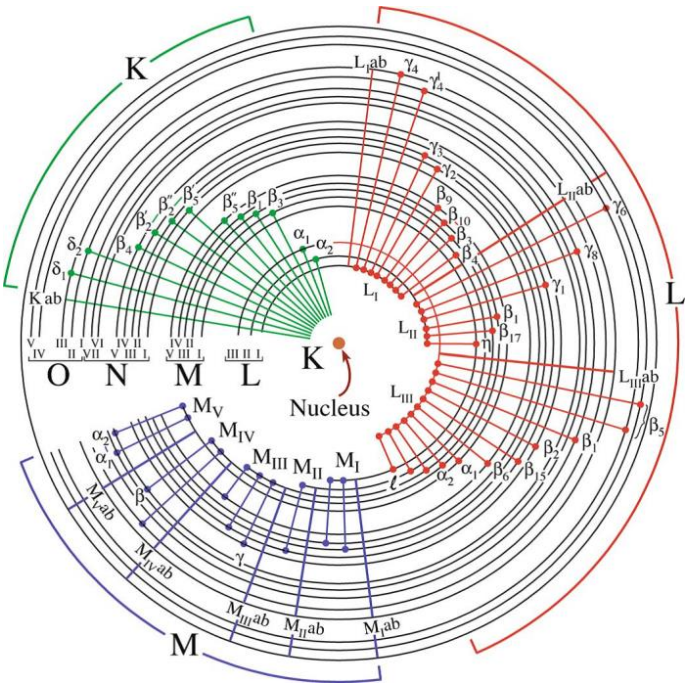

Figure 2.10 All possible electron transitions giving rise to characteristic K, L an M X – Rays [232].

We have used EDX in Tecnai (S)TEM for the evaluation of purity of steam treated pristine CNTs (presence and quantity of Fe), in order to confirm the composition

of a large variety of encapsulated payload materials and for the assessment of the functionalization when heavy element tags were attached to organic moieties. Standard analyses were performed at 200 kV, both in TEM and STEM modes.

Also, it has been useful for the study of single layer nanotubes composed of lutetium halides (**Chapter 4**) and for lead iodide enrolled on top of MWCNTs (**Chapter 5**) in mapping mode where each pixel of images is assigned to present elements. The EDX mapping was acquired on Tecnai Osiris D675 Analytical Twin TEM equipped with Super-X EDX system and operated at 120 kV in HAADF-STEM mode.

2.1.7 Electron Energy Loss Spectroscopy

Developed in 1944 by Hillier and Baker, EELS is offering valuable details on bonding, valence state, the nearest-neighbour atomic structure, electron density, the band gap and thickness of the specimen [242]. In comparison with EDX, EELS is better in analyzing light elements, has better spatial resolution and analytical sensitivity [232]. However, EELS acquisition and interpretation is much more challenging and requires a very thin specimen. The quantification based on EDX spectrum is far less complicated when compared with EELS spectrum where many parameters play a substantial role in the final result and few reliable quantification procedures are available. Often EDX and EELS are referred as complementary techniques since the detection of the high energy electron that ionized an atom is independent of whether the atom emits or not an X – ray.

EELS spectrum is a result of inelastically scattered electrons created during Coulomb interactions between the incident beam and the inner- or outer-shell electrons. Inner-shell electrons can only be excited when they absorb an amount of energy greater than their binding energy. As the total amount of energy must be conserved for each collision, the incident beam loses an equal amount of energy, which can be detected by EELS spectrometer. Single-electron excitations are also

possible in case of inelastic scattering by outer-shell electrons. Due to such scattering, in an insulator or a semiconductor material, a valence electron makes an inter-band transition across the energy gap, or a conduction electron of metal makes a transition to a higher state.

Basic EELS spectrum is divided in two main regions, the low-loss appearing just after the zero loss peak (ZLP) and the high-loss (**Figure 2.11**). ZLP is formed by collection of all electrons that have suffered inconsequential inelastical scattering and hence does not contain measurable spectroscopic information. However it is often used to determine the thickness of the sample [243]. Low-loss region (ZLP to 50 eV) contains information related to the interactions with outer-shell electrons and is related to optical properties of materials. The high-loss (also called core-loss, <100eV) region contains information from tightly bound core-shell electrons providing information on the chemistry of materials by elemental analysis, quantification and electronic structure by bonding and valence state analyses.

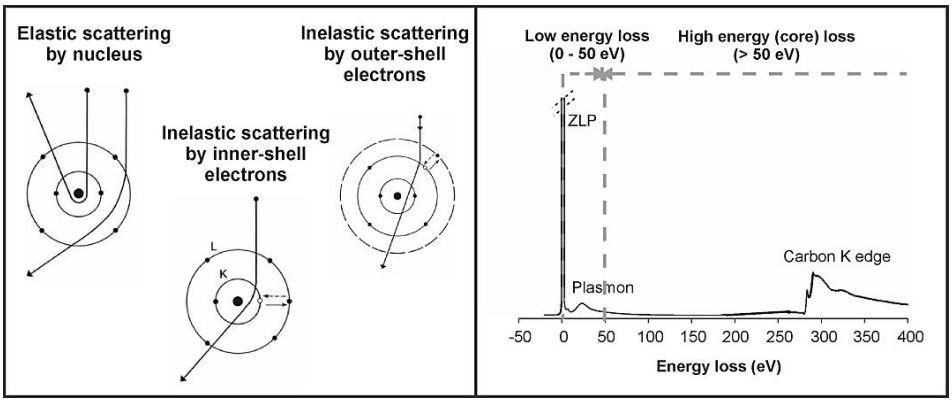

Figure 2.11 <u>On the left:</u> A classical view of electron scattering by a single atom (carbon), elastic scattering caused by Coulomb attraction by the nucleus (Zero Loss), inelastic scattering resulting from Coulomb repulsion by inner-, or outer-shell electrons, which are excited to a higher energy state (the reverse transitions (de-excitation) are shown by broken arrows). <u>On the right:</u> EELS spectrum of carbon nanotubes (the Zero Loss signal due to its high intensity was cut off for better visibility of the Carbon edge).

Energy loss (ΔE) of the inner-shell excitations is described by:

$$\Delta E \geq E_F - E_B,$$

where E_F is the Fermi level energy and E_B the binding energy of the inner shell (always negative). The result is a special feature in the energy-loss spectrum (inner shell loss edge). The threshold of the edge corresponds to the ionization energy of particular electron shell of the atom (K, L, M, N or O shell).

In this thesis we have used EELS in Nanoprobe mode with spot 6, condenser aperture of 60 μm, collection angle of 7.7 mrad and convergence angle of 12.7 mrad on Gatan Imaging Filter (GIF) Quantum SE 963 fitted with a 2k x 2k CCD camera attached to FEI´s Tecnai G2 F20 TEM microscope at 120 kV. We have focused on inner shell excitations of elements (high-loss) for chemical analysis of our CNT-based samples, mainly for the studies on graphitic structure preservation and identification of carbon nanotubes in studies concerning functionalized CNTs interacting with biological cells (**Chapter 3**).

2.1.8 Cathodoluminescence

Cathodoluminescence (CL) is a technique that provides information on luminescence properties of studied materials. When attached to an SEM or TEM it may be used with high spatial resolution on small objects.

Basically, luminescence process is based on release of photons of light following an excitation event. Depending on the source of excitation different names were adapted, for example photo-luminescence (photon excitation), electro-luminescence (excitation by electric field application), chemi-luminescence (energy from chemical reaction), and finally cathodo-luminescence (excitation by electrons or cathode rays). Accordingly, since in the electron microscope a source of highly energetic electrons is available, the study of the luminescent properties of materials is possible in both, SEM and TEM [244].

When an incoming beam of energetic electrons impacts on semiconducting specimen electrons and holes are created. In the process of radiative recombination of electron-hole pairs photons of light are emitted and may be detected by CL detector. The emitted photons have a frequency equal to the energy gap (E_G) of the material divided by Planck's constant (h). Since the wavelength of the emitted light depends on the bandgap energy and the allowed electronic transitions for a given material system it is sensitive to quantum confinement effects resulting from changes of dimension at the nanoscale.

The edge of the emission band arises fundamentally from conduction-band to valence-band transitions. If there is some variation in the energy gap (for instance due to temperature change, crystal structure in polymorphic materials, or high doping concentrations) this will be reflected on the CL spectrum.

Although, the CL-SEMs are more common, few dedicated CL-STEM instruments were built. They have an advantage of much higher spatial resolution. Therefore, they became a valuable tool for our studies of luminescence properties of single-layer lead iodide nanotubes formed on top of multi-walled carbon nanotubes discussed in **Chapter 5** of this manuscript. CL-STEM experiments were performed on a Vacuum Generator HB 501 fitted with a Cold FEG operated at 100 kV and a home-made nanoCL system. This microscope features high brightness and sub-nanometer spatial resolution. Experiments were performed in the spectral imaging mode. In this mode, the beam is scanned over the region of interest. At each scan position, a spectrum is recorded, along with the high-angle annular dark field (HAADF) signal. At the end of the scan, both a CL spectrum image (SI), that is, an image with a spectrum per pixel, and a HAADF image are available.

2.2 Other techniques

2.2.1 Photoluminescence

As already mentioned before, photoluminescence is a process of emitting visible light after absorption of electromagnetic radiation (photons) [245]. The relaxation processes involved in PL depend on the nature of studied material, either a direct or an indirect band gap semiconductor. The process of absorption and emission of light is schematically represented on **Figure 2.12**.

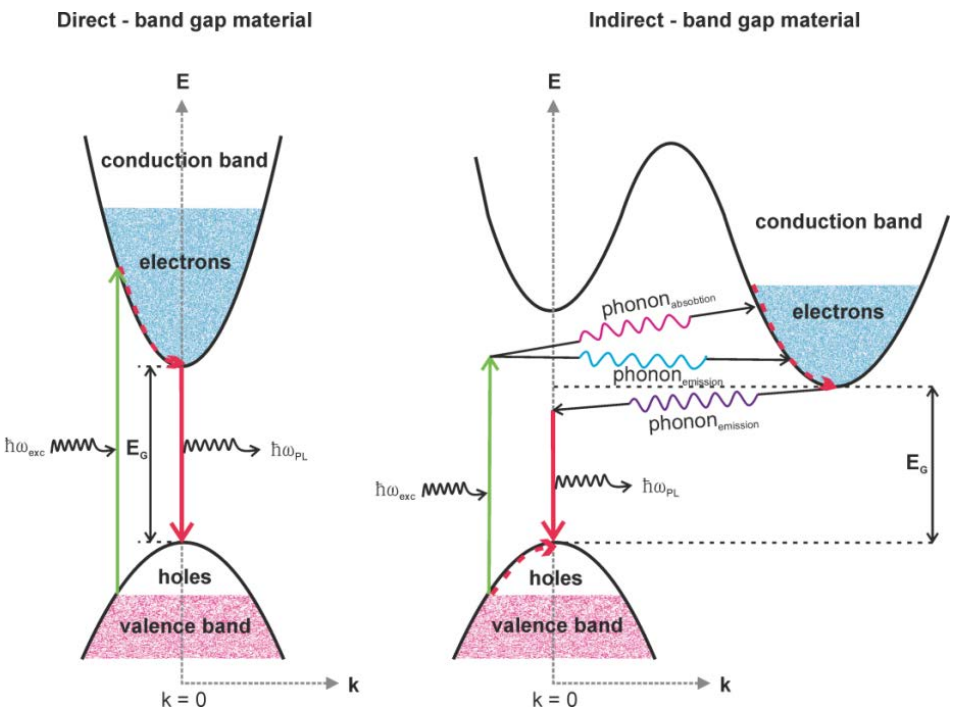

Figure 2.12 Photoluminescence mechanism for direct- and indirect- band gap semiconductors (E_G: band gap energy, k: momentum vector, $\hbar\omega_{exc}$: photon energy).

In the process of absorption of energy by luminescent material higher than its gap ($\hbar\omega_{exc} > E_G$) electrons in the conduction band and holes at the top of valence band are created. Transitions within the conduction and valence bands represent the rapid thermalization of the excited electrons and holes through phonon emission.

In a direct-band gap material (left), the conduction band minimum and the valence band maximum occur at the same wave factor (momentum vector, k). Both the photon absorption and emission (i.e. the electron-hole recombination) processes can conserve momentum without the assistance of phonons, since the momentum of the absorbed or emitted photon is negligible compared to the momentum of the electron. In an indirect-band gap material (right), the conduction band minimum and the valence band maximum occur at different k values. As a result, to conserve momentum, the photon absorption process must involve either absorption or emission of a phonon. Since the energy of a phonon is much smaller than the energy of the PL photon, for an indirect gap material, the peak energy of the PL roughly reflects its band gap.

It was discussed in literature that some layered materials undergo a change from direct to indirect-band gap when switching from single – to a multi – layer configuration [246]. Contrary to that, lead iodide undergoes a transition from direct to indirect-band gap when reducing its thickness to a single layer. This information is relevant for the discussion of PL results of our studies on single-layered lead iodide nanotubes deposited on the external walls of MWCNTs. Details of these results will be discussed in **Chapter 5**.

Photoluminescence measurements were carried out by exciting samples using 473 nm laser (diode pumped frequency doubled solid state CW laser) with 100 mW maximum power and 266 nm pulsed laser (diode pumped frequency quadrupled solid state laser, 10 ns pulses). The energy per pulse was 3 μJ, with peak power around 800-1000 W. Collecting optical fiber was composed of high quality fused silica with 600 μm diameter and optimized for UV-VIS-NIR spectral range (200-1400 nm). Spectrometer was an Ocean-Optics HR4000 multichannel spectrometer equipped with 4000 pixels Si CCD and a 1200tr/nm grating, an entrance slit of 25 mm, resulting in a spectral resolution below 1 nm.

2.2.2 Powder X-Ray Diffraction

Powder X-Ray allows obtaining information on the arrangement of atoms in crystalline material. The development of X-ray diffraction technique started in 1912 with the discovery of Max von Laue [247]. He discovered that crystalline substances act as three-dimensional diffraction gratings for X-ray wavelengths. Hence, X-ray diffraction is based on constructive interference of monochromatic X-rays and a crystalline sample. In XRD experiment, X-rays generated by a cathode tube or other source are filtered to produce monochromatic radiation, then collimated to focus, and finally directed towards the sample. When the conditions satisfy Bragg's Law ($n\lambda=2d\sin\theta$) the interaction of the incident rays with the sample produces a diffracted ray. Basically, Bragg's Law relates the wavelength of electromagnetic radiation to the diffraction angle and the lattice spacing in a crystalline sample. After the diffraction event the X-rays are detected, processed and counted. Importantly, the powder sample is composed of randomly oriented grains what allows to detect all possible diffraction directions while scanning the sample over a range of 2θ angles. Each crystalline material has its unique set of d – spacings and therefore the conversion of diffracted peaks to d values allows identifying the material composition, crystalline structure and chemical bonds through comparison with an established database.

The diffraction event is schematically described on **Figure 2.13**. The angle of incidence of two parallel rays is θ. The interplanar spacing, d, sets the difference in path length for the ray scattered from the top plane and the ray scattered from the bottom plane. This difference in path lengths is $2d\sin\theta$.

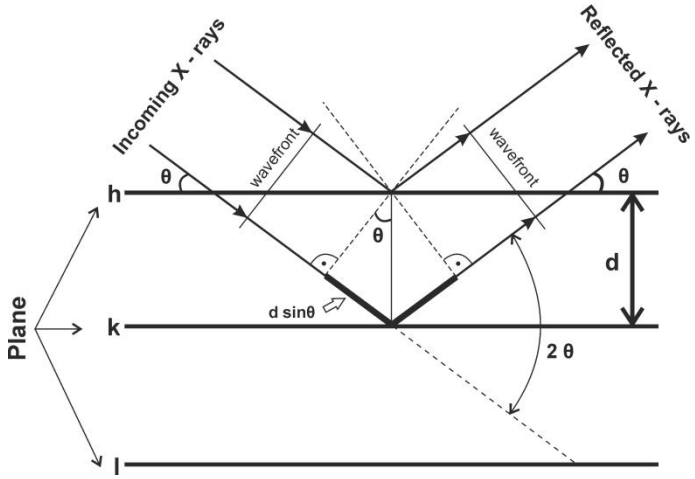

Figure 2.13 Principles of X – Ray Diffraction from crystals.

Resulting diffraction pattern is a spectrum of real space periodicities in a crystalline material. Atomic periodicities with long repeated distances cause diffraction at small angles, in contrary to short repeated distances which cause diffraction at high angles. Crystals with precise periodicities over long distances have sharp and clear diffraction peaks. Crystals with defects (impurities, dislocations, internal strains, etc.) are less precisely periodic in their atomic arrangements, but they still have distinct diffraction peaks. However, they are broadened, distorted, and weakened.

Synchrotron radiation is the single most powerful tool available to X-ray crystallographers. X-ray beams are generated in synchrotrons facilities designed and built to accelerate electrically charged particles, often electrons, to nearly the speed of light and confine them in a circular loop using magnetic fields. Although the use of synchrotron based X-rays gives exceptionally good diffraction patterns one needs to be careful with their interpretation since the intense ionizing radiation may cause radiation damage to samples. Very important advantage of synchrotron radiation is the user may select specific wavelengths to work with, allowing for anomalous scattering experiments which maximizes anomalous signal.

Laboratory-based XRD measurements on MWCNTs, lead iodide powder and lead iodide covered MWCNT hybrids were performed using PANalytical X`PERT PRO MPD (Multi-Purpose Diffractometer) system in θ angle range of 0° to 80° from their respective powders placed in capillaries (**Chapter 5**). The synchrotron based XRD was employed in the crystallographic characterization of starting materials, lutetium halide powders, used for the synthesis of lutetium halide ($LuCl_3$, $LuBr_3$, LuI_3) single-layer nanotubes in the interior of SWCNTs (**Chapter 4**) at ALBA synchrotron Materials Science and Powder Diffraction beamline (MSPD, BL04). The powder XRD patterns were obtained using Mythen® bank of detectors [248]. A short wavelength λ=0.62001Å, was used to lower absorption. Fine powder of each compound were inserted in ϕ=0.3mm borosilicate glass capillaries that were continuously rotated while measuring.

2.2.3 Thermogravimetric Analysis

There are many applications of TGA. We may determine temperature and weight change of decomposition reactions for quantitative composition analysis, determine water or residual solvents content in materials or study reactions with selected gases. It is also used for obtaining the Curie temperature values of magnetic transitions. These are just few examples of the possibilities TGA brings to scientific community.

The basic routine of TGA is to measure the change in weight of a material either as a function of increasing temperature or isothermally as a function of time. The experiment may be performed in vacuum or in gas atmosphere, such as argon, nitrogen, oxygen or any other gas of interest depending on the study. A wide range of materials can be studied such as metals, inorganic substances, polymers, plastics, composite materials, ceramics and more. The advantage of TGA is that a little amount of sample is required for precise measurement, the minimum being 1 mg but the higher the weight the better the precision.

In this manuscript TGA analysis was used mainly for determination of the amount of catalytic nanoparticle impurities in carbon nanotubes and the assessment of the filing yield (FY) of filled CNTs after burning the carbon in air at high temperature and quantification of the residue. The filling yield (FY) can be calculated knowing the amount of iron in starting, empty nanotubes based on following equations [249]:

$$FY\ (wt\%) = \frac{100 \times (R_2 - R_1)}{R_A - R_1}$$

Where R_1 and R_2 represent TGA residues of empty and filled carbon nanotubes respectively, while R_A can be calculated knowing the stoichiometry of the oxidative reaction which is taking place during the TGA analysis:

$$R_A = \frac{100 \times y \times M_B}{x \times M_A}$$

Where M_A and M_B are molecular weights of A and B, while x and y are the reaction stoichiometric constants.

We used TGA for investigation of the purity of steam treated carbon nanotubes and for assessing the filling yield of various CNT-filled samples (**Chapter 3**). Experiments were performed on 5-10 mg of powder under flowing air burning carbon from CNTs and measuring the quantity of the residue, either resulting from catalytic nanoparticles (Fe) or from a specific payload material. TGA analyses were performed on NETZSCH -STA 449 F1 Jupiter system at a heating rate of 10 °C/min until 900 °C.

2.2.4 Raman Spectroscopy

Raman Spectroscopy is a non-destructive chemical analysis technique providing detailed information about chemical structure, phase and polymorphy, crystallinity

and molecular interactions. It is based upon the interaction of light with chemical bonds within a material.

Raman is based on light scattering, whereby a molecule scatters incident light from a high intensity laser source. Most of the scattered light is at the same wavelength as the laser source and therefore does not provide useful information about the specimen, it is called Rayleigh scattering (**Figure 2.14**). However a small amount of light is inelastically scattered at different wavelengths which are depending on the chemical structure of the specimen, this phenomena is called Raman Scattering. When the frequency of incident radiation is higher than frequency of scattered radiation, Stokes lines appear in Raman spectrum. But when the frequency of incident radiation is lower than frequency of scattered radiation, anti-Stokes lines appear. Stokes shifted Raman bands involve the transitions from lower to higher energy vibrational levels and therefore, Stokes bands are more intense than anti-Stokes bands and hence are measured in conventional Raman spectroscopy while anti-Stokes bands are measured with fluorescing samples because fluorescence causes interference with Stokes bands.

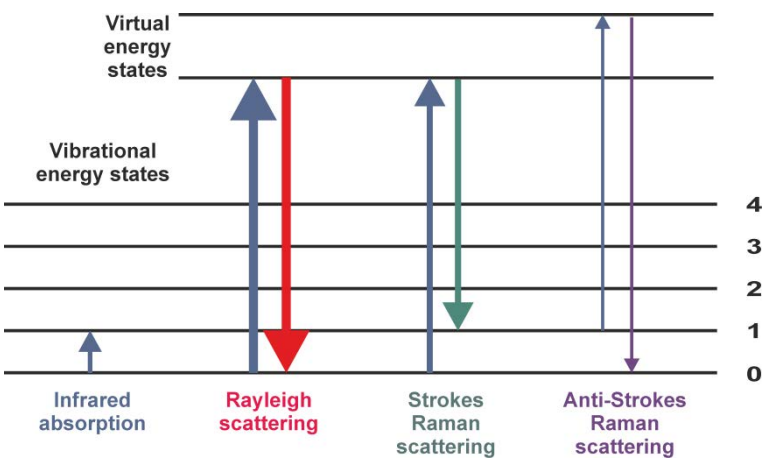

Figure 2.14 Energy level diagram showing the states involved in Raman signal.

Raman scattering allows following the changes in physical and chemical properties of CNTs. It is one of the most suitable techniques for studying the fundamental

properties of CNTs, since it is a non-destructive, contactless, quick technique with relatively simple or no preparation required [248, 249]. The Raman spectra of CNTs present several features, among which the most intense ones can be found in three spectral regions. First, the radial breathing mode (RBM), whose Raman shift (from 100 to 300 cm^{-1}) inversely depends on the CNTs diameter [250]. Second, the tangential mode (G-band) placed at 1588 cm^{-1}, containing an axial and a circumferential component, which can be used to distinguish between metallic and semiconducting CNTs by its line shape. And third, the second-order Raman mode is the G'-band (also known as the 2D-band), centred at around 2650 cm^{-1} [27]. Additionally, for samples containing structural defects, the disorder induced mode (D-band) is observed at around 1350 cm^{-1}. The D-band is a second-order Raman mode and is used to analyze the quality of the CNTs as it is sensitive to structural defects in the graphitic sp^2 network, like those induced by carbonaceous impurities [24]. Moreover, in order to study electronic structure and the physical properties of CNTs doping experiments can be performed. To induce doping, electrons or holes are introduced into the electronic structure of the CNTs either by chemical reactions (introducing donors [29, 30], or by electrochemical charging [251, 252]. The level of doping can be easily adjusted by applying potential. Electrochemical charging works as a double layer capacitor where the CNTs act as working electrode and the charge carriers are injected into the CNTs, while the electrolyte ions compensate the charge. In that way, extra electrons or holes are inserted in the CNTs causing changes in the electronic structure that can be followed by Raman spectroscopy. When the potential is changing, the charge transfer leads to a shift of the Fermi level, which can result in bleaching the Raman modes in the CNTs spectra. When the van Hove singularities are filled, the associated optical transitions become blocked [33, 34]. Therefore, Raman spectroelectrochemistry allows investigation of the changes in the physical properties of CNTs during charge transfer.

Raman spectra were acquired for steam-treated CNTs (**Chapter 3**) using a LabRAM HR Raman spectrometer (Horiba Jobin-Yvon), and laser excitation energies of 2.54 and 2.33 eV (488 and 532 nm, respectively, Ar/Kr laser, coherent) and of 1.96 eV (633 nm, He-Ne). A 50x objective was used with a laser spot of about 1 μm. The laser power was 1 mW and the spectral resolution was 1 cm^{-1}. Each sample was measured in multiple regions.

2.2.5 Superconducting Quantum Interference Device

SQUID is a very sensitive magnetometer used to measure extremely subtle magnetic field. In many cases, SQUID instrumentation offers the ability to make measurements where no other methodology is possible.

Magnetometers based on superconducting quantum interference devices (SQUIDs) are considered the most sensitive of all magnetometers. It consists of a closed loop made of a low temperature superconductor like NbTi or Nb_3Sn, with one or two Josephson junctions. A Josephson junction is a quantum mechanical device, which is made of two superconducting electrodes separated by a barrier (thin insulating tunnel barrier, normal metal, semiconductor, ferromagnet, etc.). The operation of a SQUID magnetometer is based on two fundamental physics principles: (1) the use of Josephson junctions as a means to create path differences (interference) in an otherwise coherent supercurrent persisting around the superconducting loop and (2) the fact that the magnetic flux trapped inside the area enclosed by the superconducting loop must be in integer units of a flux quantum, $\Phi_0 \equiv h/2e$. The supercurrent within the loop self-compensates to ensure that the flux through the loop is an integer multiple of Φ_0. For the detailed physics and design variations of the SQUID, refer to the review by Fagaly [253]. The fact that the SQUID is superconducting makes liquid He a requirement for operation.

In our studies magnetic measurements of purified (steam-treated) samples of carbon nanotubes (**Chapter 3**) were done to assess the quantity of Fe content in a

LOT-Quantum Design Iberia SQUID magnetometer. A diamagnetic gelatin capsule was filled with 3-4 mg of sample. Data was acquired with an applied field from -15.000 Oe to +15.000 Oe at 10 K to obtain the hysteresis loops. The sample holder contribution was subtracted in all the measurements. The amount of iron in each of the analyzed samples was determined by taking into account the magnetic saturation of the bulk material (Ms_{Fe} = 221.7 emu·g^{-1}).

PART I

NANOCAPSULES FOR IMAGING AND TARGETED DELIVERY

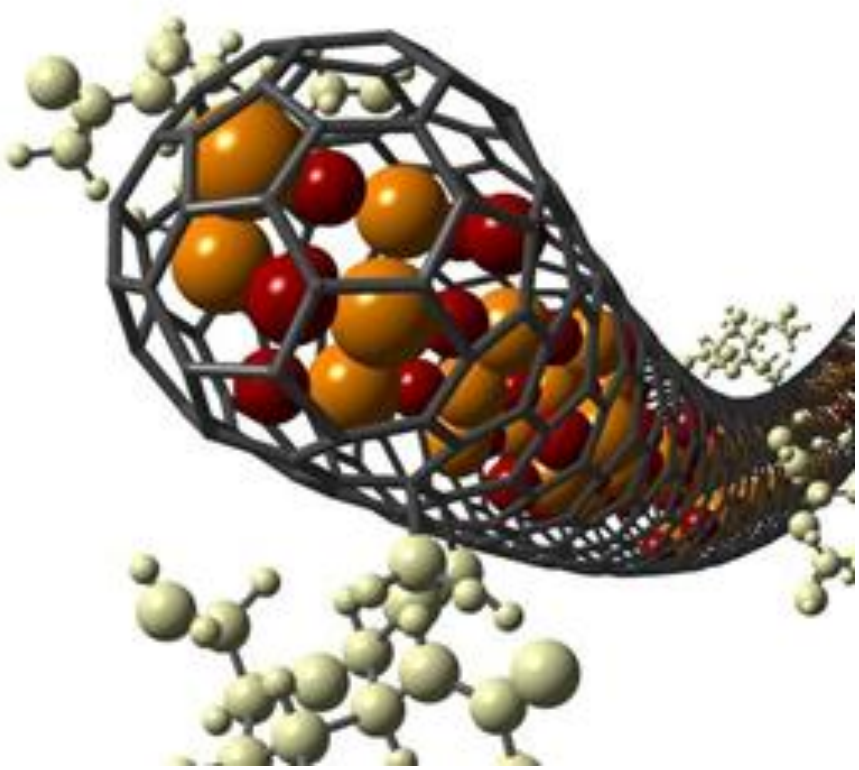

3 Characterization of functional carbon nanotubes with potential biomedical applications by electron microscopy

In this chapter we will present the optimum imaging and spectroscopic conditions for characterization of shortened, purified and functional carbon nanotubes, which are potential candidates for biomedical applications. Additionally, the best procedure for imaging and analysis of interaction between functional CNTs and cells will be addressed.

3.1 Purified and shortened carbon nanotubes

It has been long debated by scientific community if carbon nanotubes are the right material for medical applications [202, 254, 255]. Some reports compared the toxicity of carbon nanotubes with that of asbestos [256]. However, nowadays we know the toxicity in carbon nanotubes emerges from two main aspects, their length (typically from few hundred nanometres to micrometres) and the presence of toxic nanoparticles (residual catalyst composed of iron, cobalt or nickel). Although these characteristics are true for pristine material, currently post – synthetic strategies are able to overcome these obstacles and therefore improve the biocompatibility of carbon nanotubes.

First of all, let focus on the length of CNTs and how it affects the biocompatibility. Pristine CNTs have the lengths in a micrometre range. Therefore, during the years, many strategies were developed to make nanotubes shorter: oxidative chemical treatments [257], mechanical grinding [258], lithography [259], sonication [260], and electron-beam cutting [261]. Among them, strong acid treatments are the most frequently used [262-264]. Sulphuric and nitric acids and their mixtures are effective in cutting CNTs. However, during that process the structure gets disrupted changing the intrinsic properties of CNTs and creating defects that may facilitate the release of the payload, which makes them not recommended for use in biomedical applications.

Second of all, the biocompatible material should be free of any metallic nanoparticles which are often present in the sample. Fe, Ni or Co nanoparticles, toxic to the human body, are commonly used as catalysts in the growth of carbon nanotubes [265-267]. What is more, in the growth process part of the catalyst nanoparticles gets covered by graphitic shells that protect the metal from external agents.

Our approach to overcome both of the problems of biocompatibility in one step is a simple and effective strategy based on combined steam treatment and washing with hydrochloric acid (HCl) [36, 43]. Steam is a mild oxidizing agent but still capable of opening the ends and shortening of carbon nanotubes while removing amorphous carbon and the shells surrounding the catalytic nanoparticles (**Figure 3.1**). When exposed, metal nanoparticles are easily removed by washing with hydrochloric acid (HCl). This process was proved to be effective in shortening of single- and multi-walled carbon nanotubes and in removing the catalytic nanoparticles without disrupting the CNTs structure. Here, we describe the characterization methods and conditions useful for the studies on purified and shortened carbon nanotubes, to obtain information on their post-steam treatment length and their structural integrity.

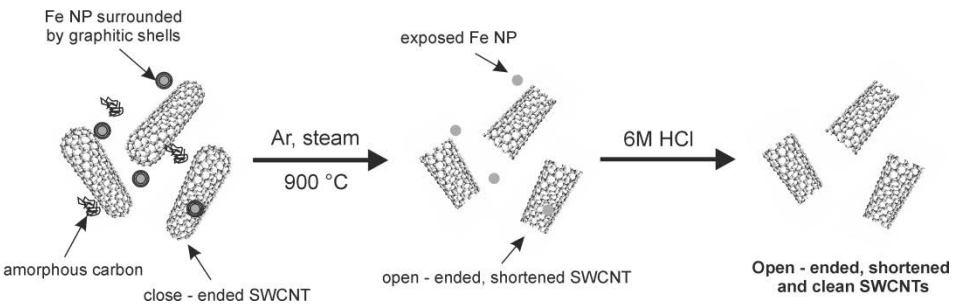

Figure 3.1 Diagram of steam purification and shortening of SWCNTs.

Our study shows that steam is able to effectively cut CNTs to tailored lengths controlled by the time "on steam" simultaneously removing graphitic shells covering catalytic (Fe) nanoparticles and amorphous carbon. The length distribution of as-prepared samples was determined by measuring the lengths of individual CNTs from electron micrographs.

However, before the characterization step, we had to establish an adequate protocol. The right conditions had to be selected including the solvent to disperse the nanotubes (water: H_2O, acetone: $(CH_3)_2CO$, chloroform: $CHCl_3$, hexane: C_6H_{14}, dichloromethane: CH_2Cl_2, pluronic acid and orthodichlorobenzene:

$C_6H_4Cl_2$), the support on which to deposit them (silicon chip, mica, polycarbonate membrane and holey/lacey/carbon coated TEM support grid) and the ideal imaging conditions (0.2 – 20 kV, type of detector). A series of solvent/support combinations was tested (see **Table 1**). As a result of the investigation orthodichlorobenzene ($C_6H_4Cl_2$) was found to be the best solvent for successful dispersion of CNTs while continuous carbon film supported on TEM Cu grid was chosen as the best support for the deposition and visualization by SEM. The best imaging conditions were selected, namely 2 kV of accelerating voltage and SE mode using TLD detector. To support our choice of conditions we show sample micrographs illustrating the problems encountered during the procedure of optimization (**Figure 3.2**).

Table 1 Choosing the best working conditions for SEM-based length distribution studies of carbon nanotubes.

Solvent /Support	H_2O	$(CH_3)_2CO$	$CHCl_3$	C_6H_{14}	CH_2Cl_2	Pluronic acid	**$C_6H_4Cl_2$**
Silicon chip	—	—	X	X	—	X	—
Mica	—	—	X	—	—	—	—
Teflon	—	X	—	—	—	—	—
Polycarbonate membrane	X	X	—	X	—	—	—
Holey/Lacey Carbon grid	X	—	—	X	X	—	—
Continuous Carbon grid	X	—	—	X	—	—	**OK**

X denotes the tested combinations of working conditions
OK denotes the chosen (best) condition
— combination not tested

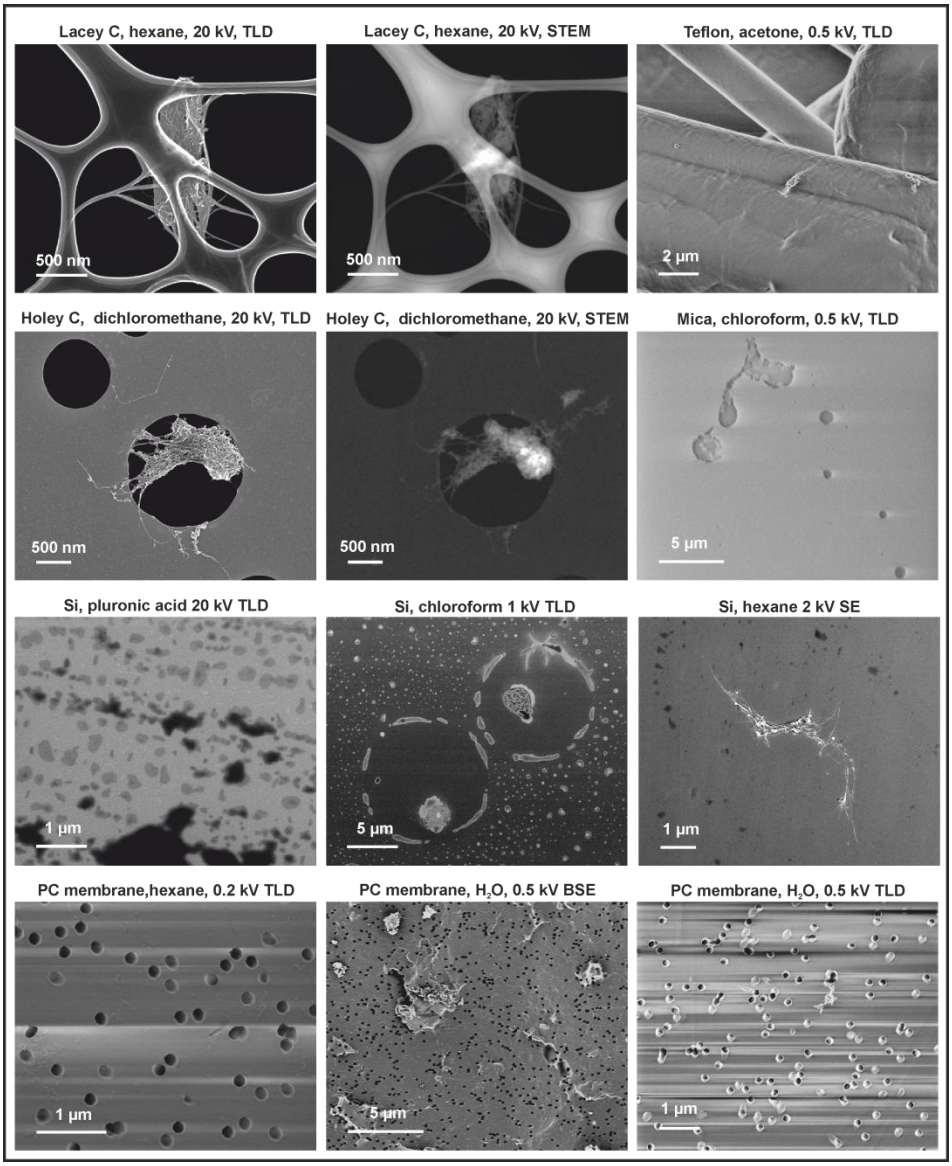

Figure 3.2 Choosing the best conditions for statistical analysis of length distribution of pristine and steam-treated SWCNTs.

Figure 3.2 is a summary of different conditions tested for the optimization of the study on length distribution of SWCNTs. During the process of searching for a suitable support, TEM grids with lacey/holey carbon film were tested. It was shown that the holes in both films are relatively large (~1 µm) and therefore short

nanotubes could easily pass through them and hence bring false results. Teflon was found to be a quite irregular surface so the small nanotubes were difficult to be distinguished from the support. Mica is a nonconductive material that charge under an electron beam irradiation even at low voltages. We tried to image SWCNTs on mica at 500 V (minimal charging) but then the resolution was too low to visualize them with precision. The same problem was found for polycarbonate membrane which was charging even at 200 V when imaged with TLD detector. In backscattered electrons mode at 500 V the image seemed to improve but the nanotubes did not appear with enough contrast. Additionally, the resolution is worse in BSE mode when compared with SE mode (used with TLD detector). In the matter of support, a Si chip seemed to be a good option due to its smooth surface and a good contrast with carbon nanotubes. However, it was found that when depositing a solution of SWCNTs on top of it, they would form aggregates in the time of evaporation of the solvent. All of the abovementioned problems emerging from support material were mediated when SWCNTs were deposited on continuous carbon film covering TEM grid. Its surface provided a smooth face, which offered a good contrast with carbon nanotubes in SE mode. Furthermore, high permeability of the film permitted the solvent to instantaneously pass through it allowing deposition of well dispersed individual carbon nanotubes when drop-casted from an orthodichlorobenzene solution.

Regarding the solvents, we found that orthodichlorobenzene provided a good dispersion and a quick evaporation making it suitable for this study. In other solvents we realized that either aggregates predominated over individual nanotubes (hexane, acetone, dichloromethane, water) or the solvent would leave a residue on top of the support making it hard to visualize individual nanotubes (chloroform, pluronic acid).

For the imaging conditions the equilibrium had to be found in terms of resolution and surface sensitivity. With an increasing accelerating voltage the resolution increases but the surface sensitivity decreases. SWCNTs are small objects with

diameters in range of few nanometers and thus high surface sensitivity is needed for the best contrast conditions in SEM. Hence, the best imaging conditions were found for 2 kV electron beam when using TLD detector, which provides the best resolution of all of the tested detectors in FEI's Magellan SEM microscope.

To sum up, SEM micrographs acquired in Secondary Electrons mode (SE) permitted the visualization of SWCNTs dissolved in orthodichlorobenzene, sonicated and deposited on top of thin carbon film coated Cu grids. The microscopy was conducted at 2 kV what allowed for surface sensitivity and through-in-lens detector (TLD) gave the best resolution conditions at this voltage (**Figure 3.3**). In contrast to TEM, we found that SEM came about as cost-effective and time-efficient for the analysis of the large amount of samples involved in this study. Moreover, TEM renders low contrast images of CNTs deposited on the surface of a TEM grid (most of them are covered with carbon film). This is due to the fact that in TEM, transmitted electrons are used to visualize the sample while in SEM secondary electrons are used giving a topological image of the studied material.

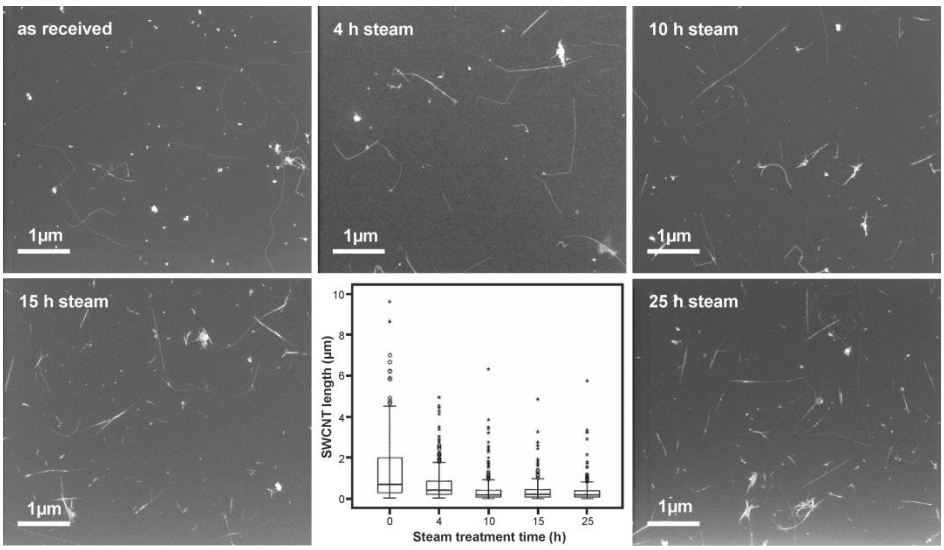

Figure 3.3 SEM images of as-received and steam treated SWCNTs. In the middle, box–plot analysis of the as-received and steam treated SWCNTs after HCl washing

step. Empty circles indicate outliers and asterisks far outliers. The lower and maximum adjacent observations are represented with horizontal lines at the end of the whiskers.

Statistical analysis of the length distribution based on SEM micrographs was performed with a sample size of 300 for each group, namely control group (as received) and treated groups (steam + HCl). Median lengths of as received, 4 h, 10 h, 15 h and 25 h steam shortened SWCNTs are as follows: 711 nm, 420 nm, 198 nm, 223 nm and 191 nm, respectively. It was shown that with the time on steam experiment the length decreased substantially reaching lengths below 200 nm after 10 h. Interestingly, after periods of time longer than 10 h, the length of SWCNTs would not undergo any important change.

SWCNTs are known to form bundles and aggregates, and thus were not easy to disperse in the solution. However, 30 to 45 minutes of sonicating bath permitted to obtain a good dispersion and therefore to get most of the nanotubes to be deposited individually on the support. However, before obtaining and using the optimum conditions it was common to detect many small and big aggregates (**Figure 3.4**).

In order to be confident that the length measurements were done on individual nanotubes, we checked the same grids used for the SEM study by high resolution TEM. Consequently, we could confirm our measurements to be trust for, finding the individual nanotubes had varying diameters but they were consistent with the diameters measured by SEM for individual CNTs. As an example, single-walled CNT (1W) along with double- (2W) and triple- (3W) walled carbon nanotubes were found on the grids with diameters of 2.0 nm, 1.8 nm and 3.3 nm, respectively, matching the diameters obtained by SEM (**Figure 3.5**).

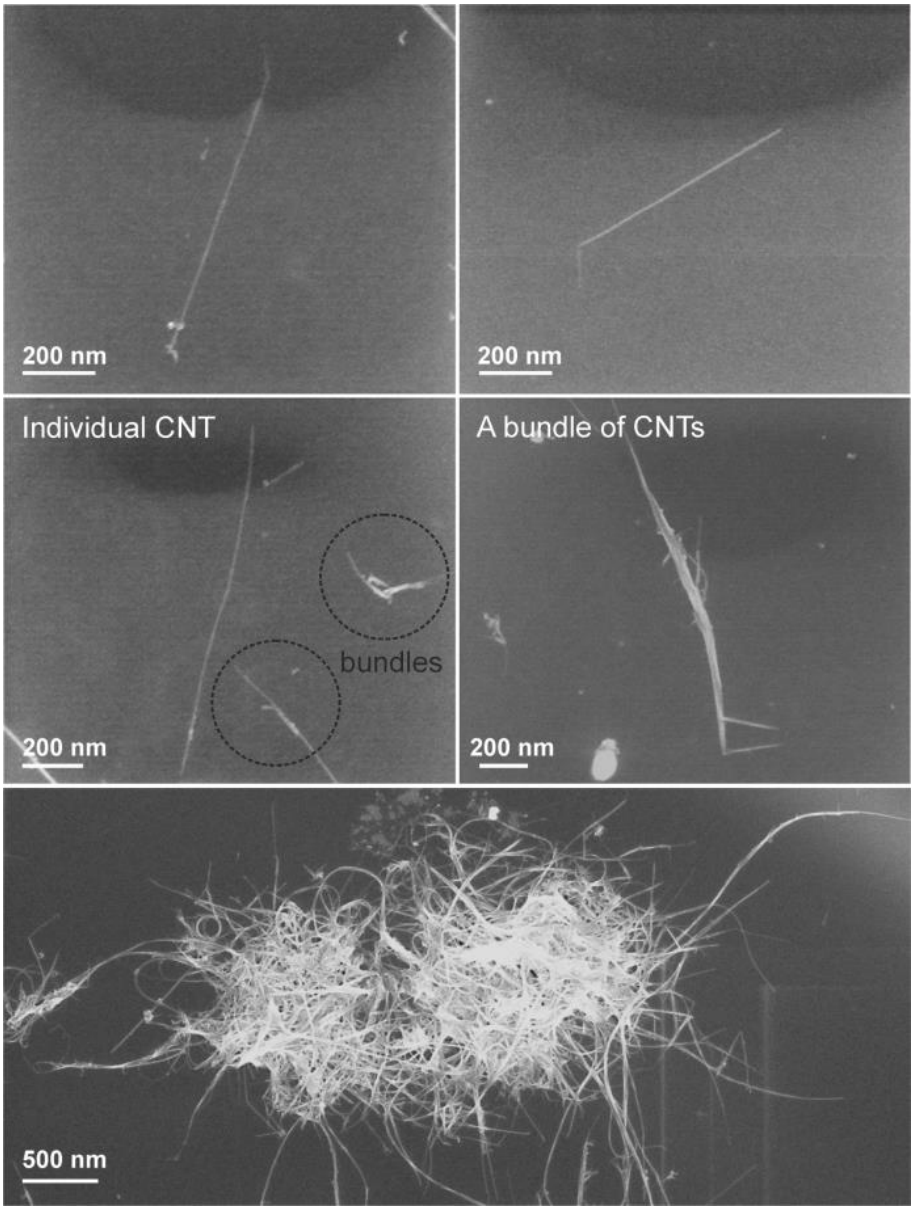

Figure 3.4 SEM images of a-b) individual nanotubes, c) individual SWCNT in the presence of small bundles, d) bundle of SWCNTs, e) big aggregate of SWCNTs in not properly dispersed sample.

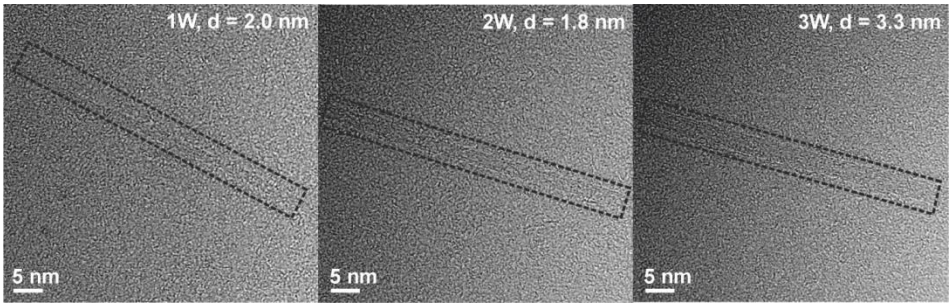

Figure 3.5 HRTEM images showing individual CNTs with few nanometers in diameter. The nanotubes are indicated by black rectangles for clarity. Low contrast of images is due to similar chemical nature of CNTs and carbon film supported on the Cu TEM grid.

After the SEM analysis of the length distribution, we were interested in discovering if the steam process somehow affected the CNTs structure. The structure preservation of SWCNTs after steam process is of importance for their biomedical application. For example, if we intend to fill the interior cavities of CNTs with a radioactive payload for radiotherapy, we have to guarantee that the material is safely sealed inside. Possible defects or breakage of CNTs in the process would cause the leakage and impede usage of filled carbon nanotubes in for this purpose. Hence, high resolution TEM imaging of the samples was performed enabling the visualization of the integrity of the graphitic walls. As an example HRTEM images of as – received and steam treated (25 h) nanotubes are presented (**Figure 3.6**). Fortunately, no visible differences in the structure of CNTs were noticed based on HRTEM micrographs.

Although HRTEM images gave a good indication of the structure preservation of the samples after steam, the more reliable proof was brought by Raman spectroscopy. Remarkably, the steam treated samples presented a continuous decrease in the ratio between D and G bands (the A_D/A_G ratio), being an indication of the removal of more defective nanotubes and amorphous carbon (**Figure 3.7 A**). As a result, according to Raman Spectroscopy we ended up with

less defective nanotubes after steam treatment, which makes them more suitable for biological applications than as-received CNTs.

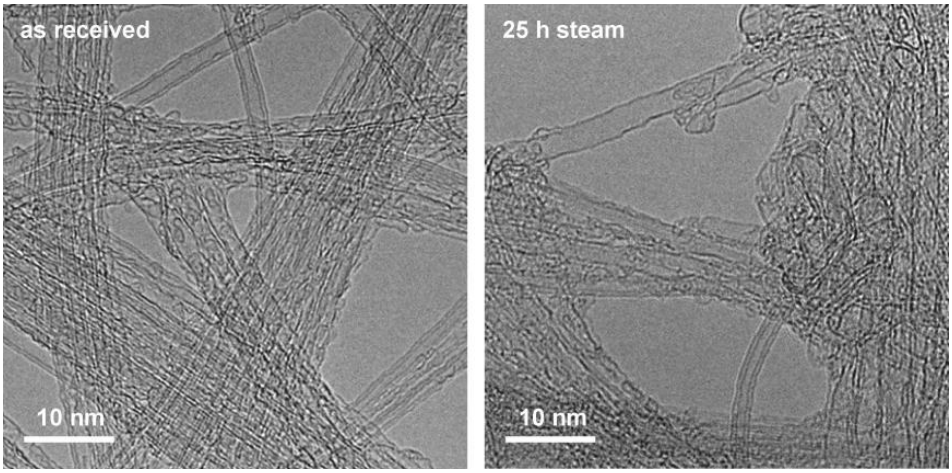

Figure 3.6 HRTEM images of as-received SWCNTs (left) and after 25 h of steam treatment with subsequent HCl washing.

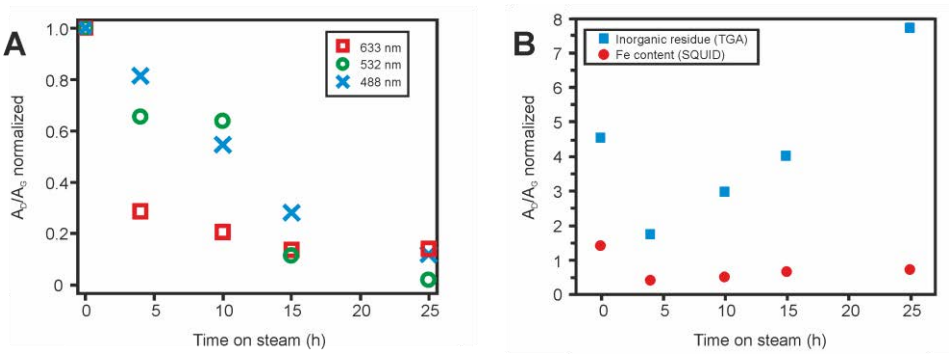

Figure 3.7 (A) A_D/A_G ratio of as-received (0 h) and steam processed and HCl washed SWCNTs. The samples were excited using 1.96 eV (red squares), 2.33 eV (green circles) and 2.54 eV (blue crosses) laser energies. (B) TGA and SQUID results of as-received (0 h) SWCNTs and steam treated SWCNTs for different amounts of time.

Following these conclusions, the last step of the characterization process was focused on the assessment of the amount of the catalyst present in all of the purified samples in comparison with the pristine material. Consequently, TGA

analyses were performed and are plotted on **Figure 3.7 B** as blue squares and as a function of time on steam. TGA analysis of the amount of inorganic residue for each sample was assessed by burning of the sample composed of SWCNTs in air. In this process all of the carbonaceous species (CNTs, graphitic shells surrounding the Fe nanoparticles and amorphous carbon) were burned out and evacuated as carbon dioxide. The leftover residue contained the oxidized inorganic compounds (Fe_2O_3 from the catalyst, **Figure 3.9 b**). It was expected that the TGA residue would drop as a function of time on steam but this was not the case. It is shown on the graph that the inorganic residue dropped when shifting from as-received SWCNTs to the sample of 4 h on steam but then it raised again for longer steam treatments. These surprising results were explained with the help of EDX analyses acquired at 20 kV on FEI Quanta 650F SEM (**Figure 3.8**) of the TGA residues which showed not only the expected presence of iron but also some quantity of silicon (Cu and C peaks emerge from the support TEM grid).

The respective contribution of Fe and Si cannot be correctly calculated from the TGA residue and thus the help of another technique such as superconducting quantum interference device (SQUID) was required. From the SQUID data the exact amount of metallic iron could be extracted after converting the Fe_2O_3 amount to pure Fe content. Based on the graph, (**Figure 3.7 B** red dots) the amount of Fe decreased from ~ 1.5 weight % for the as received sample down to ~ 0.4 weight % in the steam treated and HCl washed samples (almost identical for all of the samples treated with steam).

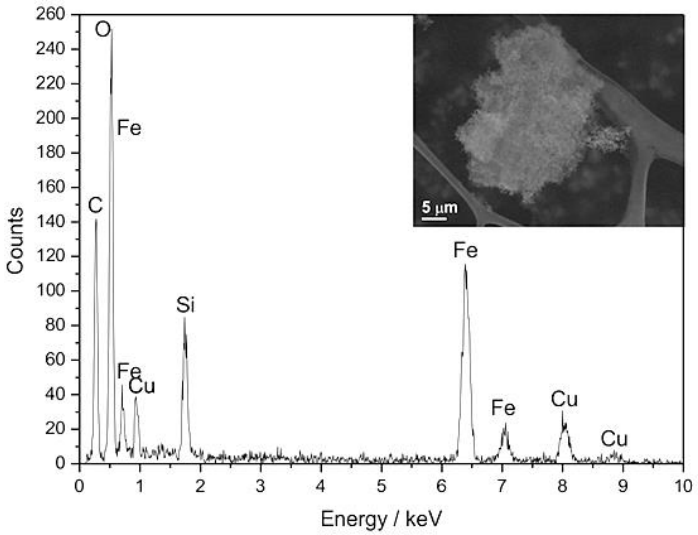

Figure 3.8 Energy dispersive X-ray spectroscopy (EDX) of the TGA residue obtained after the complete combustion of as-received CNTs. The inset shows the scanning electron microscopy (SEM) image of the analysed area.

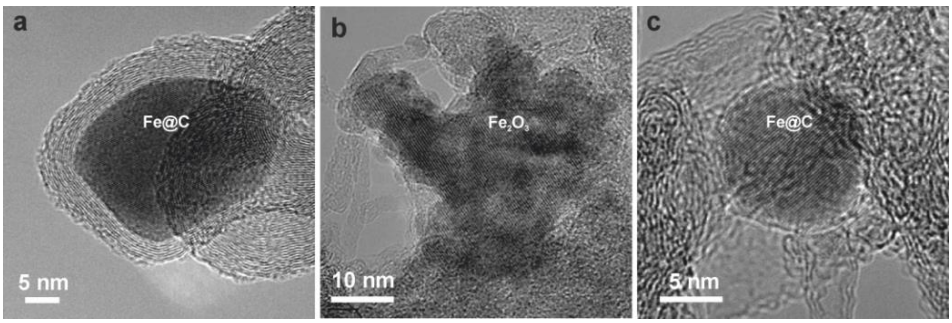

Figure 3.9 Removal of the catalyst nanoparticles by steam: a) Fe nanoparticle covered with many graphitic layers, b) Fe_2O_3 after the steam process but before HCl washing step, c) Fe NP covered by a monolayer of carbon after steam.

On **Figure 3.9 (a)**, single catalytic nanoparticle composed of iron is displayed covered by many layers of graphitic carbon. These graphitic layers were shown to protect metallic nanoparticles from oxidation and therefore from their removal. Steam acting as mild oxidizing agent eliminates the graphitic layers surrounding Fe and facilitates its oxidation in air leading to Fe_2O_3 (**Figure 3.9 b**), which is easily

removed from the sample by washing with HCl. It should be noted however that depending on time on steam not all of the graphitic layers are removed, leaving some quantity of Fe nanoparticles still protected from oxidation and hence present in the sample post-steam (**Figure 3.9 c**).

As a result of the above studies we have obtained a reliable method of preparation of more biocompatible SWCNTs and their characterization. This means: shorter, less defective and less toxic (lower Fe content) carbon nanotubes. The electron microscopy techniques combined with other complementary techniques allowed to fully characterize purified and shortened CNTs. Therefore, as prepared SWCNTs proved to be ready for further functionalization, being it internal, external or both depending on the desired application. For further details on steam shortening of SWCNTs please refer to our publication [43].

3.2 Endohedral functionalization of carbon nanotubes

Carbon nanotubes are widely studied for a range of applications due to their versatile structure. The possibility of endohedral and/or exohedral functionalization with different materials converts them into perfect hosts, resulting in extensive investigations in the fields of science, technology and medicine [268-271]. For instance, they are studied for magnetoelectronics [272], molecular electronics [273], nanothermometry [274] and controlled growth of layered materials [67]. Nevertheless, in this chapter we will only focus on characterization of carbon nanotubes filled with materials with potential applications in biomedicine [275-277]. Independently of their application, the characterization methodology of filled carbon nanotubes by electron microscopy and other techniques may be treated as a standard procedure.

The goal of our studies was motivated by using carbon nanotubes as carriers of radionuclides, either for imaging or therapeutic use. However, not many studies on

that matter were published until today. Few examples include CNT radioimmuno-carriers that have been reported to combine CNTs delivery properties with targeted antibodies and radionuclides, such as ^{86}Y [278], ^{125}I [128, 279], or ^{64}Cu [280-282], enabling radioimaging, tracking and anticancer therapy.

The selection of potential radionuclides for tumor imaging and radiotherapy depends on half-life, decay mode and their emission properties. Gamma emitters with energy in the 150 keV range can be used for gamma imaging or single photon-emission tomography (SPECT) while high energy positron emitters (β^+) with energy at 511 keV can be applied for positron-emission tomography (PET) [283, 284]. For targeted radiotherapy applications, high and low energy β^- emitters are ideal radioisotopes. They are employed in treatment of small to large-sized clusters of tumor cells. Alpha-emitters, from the other hand, hold great promise as therapeutics but only for small cancer lesions and micrometastatic cancers due to the tissue penetration range of 50-100 μm. Auger electrons have an energy of <30 keV and subcellular path-length of 2-12 μm and thus they can exert their radiotoxic effects on cells exclusively when internalized into the cytoplasm [285, 286].

In our work, we have selected few of the useful radionuclides for filling into the internal cavities of carbon nanotubes in form of their salts. They are listed in **Table 2,** where their essential properties (type of decay, half-life) and application possibilities are summarized.

The most commonly used therapeutic radionuclide is iodine-131 labelled sodium iodide in form of capsule or liquid. The treatment is known as radioactive iodine therapy (RAI) and uses ^{131}I to treat thyroid-related diseases such Graves' disease, solitary hyper-functioning nodule, and toxic multinodular goiter [287, 288]. It may also be used in patients with hyperthyroidism, particularly in patients with cardiac risk. Our interest in iodine was further encouraged by an article from 2010, where successful encapsulation of sodium iodide-125 in the hollow cavity of CNTs was

described [128]. The subsequent glycosylation enhanced the dispersibility and biocompatibility of the hybrid, which showed different biodistribution profile in mice compared to free ^{125}I, examined by SPECT/CT imaging. Hence, the localized safe delivery of radiodosage was first proven. Based on these findings, we chose few iodides suitable to be filled into SW- and MW- CNTs. In this context, SWCNTs were filled with LuI_3, NaI, PbI_2 and CuI and MWCNTs with KI, NaI, PbI_2, CeI_3 and ZnI_2. A few of them contain both iodine and a radioactivable cation such as Lu, Cu and Ce.

Table 2 Selected radionuclides for filling into carbon nanotubes.

Isotope	Type of decay	Half-life	Application
^{123}I	Auger, γ	13.20 hours	- imaging (SPECT)
^{125}I	γ, β^-	8.02 days	- biological assays - imaging (PET, SPECT) -targeted radiotherapy
^{131}I	γ, β^-	8.00 days	- imaging (PET, SPECT) - targeted radiotherapy
^{64}Cu	β^+	12.70 hours	- imaging (PET, NIRF)
^{67}Cu	β^-	2.60 days	-targeted radiotherapy
^{177}Lu	γ, β-	6.73 days	- imaging (SPECT) -targeted radiotherapy
^{160}Gd	β^- β^-	Stable	- imaging (MRI, PET)
^{153}Sm	γ, β^-	46.50 h	- targeted radiotherapy
^{152}Eu	γ, β^-, β^+	13.55 years	- imaging (SPECT) - targeted radiotherapy
^{141}Ce	γ, β^-	32.53 days	- imaging (SPECT)

Since the encapsulation of LuI_3, NaI, PbI_2 and CuI into CNTs resulted successful we expanded our choice of radioactivable elements to gadolinium, samarium, europium, lutetium and cerium.

Filling of gadolinium salts in CNTs is attracting much interest for future application in medical diagnostics. In a review from 2012, the application of the gadonanotubes (as they are called) as high-performance magnetic resonance imaging (MRI) contrast agents was discussed [289]. Gadonanotubes indicated a higher relaxivity when compared to other gadolinium-based contrast agents. In another study, nanocomposites of gadonanotubes with poly(lactic-co-glycolic acid) were employed for tracking biodegradation, release and biodistribution of gadonanotubes by T_2-weighted MRI [290, 291].

On the other hand, Samarium is the active component in samarium lexidronam, a chelated complex of radioactive ^{153}Sm used in osteoblastic bone metastases and osteosarcoma treatment [292].

Europium-chelate-based silica nanoparticles have been advocated as convenient multimodal platforms for applications in materials (tracers, counterfeiting, sensors of ground pollutant agents) and/or for *in vitro*, *in vivo* biological labelling (biophotonics or phototherapy). It was shown Eu inclusion into silica nanoparticles leads to materials with higher stability (shielding of the lanthanide ions from their environment and prevention of non-radiative deactivation processes) and to improved photo-stability and imaging [293-295]. In 2000, $EuCl_3$ was used as one of the payloads in the synthesis of filled SWCNTs [296].

^{177}Lu radioisotope in the form of halides (LuX_3, X = Cl, I, Br) has found extended use for treatment of several cancer types including neuroendocrine tumours [276, 297, 298].

Cerium oxide nanoparticles (CONPs) have demonstrated protection properties against oxidation in various cells and tissues [299, 300]. Yang et al. radiolabelled

CONPs with beta emitting ^{141}Ce in order to obtain a multifunctional nanoparticle platform combining dual imaging components (Single Photon Emission Computed Tomography/Optical Imaging, SPECT/OI) in one nanoparticle [301].

Based on the literature mentioned above focused on important radionuclides in the field of biomedicine, we have been motivated to undergo the experiments of filling of single – and multi – walled carbon nanotubes with different radioactivable inorganic materials. We have chosen non-radioactive forms of iodine, samarium, lutetium, europium, gadolinium, copper and cerium with the aim to proof the concept and be able to follow in the future with studies on their radioactive counterparts for the application in the field of anticancer therapy and imaging. The molten phase capillary wetting was selected as the synthetic strategy for the endohedral filling with "cold" salts (non-radioactive). The choice of salts was as follows: $GdCl_3$, $SmCl_3$, $EuCl_3$, $LuCl_3$ and $LuBr_3$ to seal into SWCNTs and $GdCl_3$, $SmCl_3$, $EuCl_3$ and $CeCl_3$ into MWCNTs. Prior to the encapsulation of the chosen payloads, the CNTs were purified and shortened following the steam process described in the previous section of this chapter. The post-encapsulation functionalization of such nanocapsules with appropriate organic moieties will provide safe biocompatible nanocapsules able to target a specific organ/tissue.

The standard procedure of filling of CNTs with a selected payload is based on molten phase capillary filling method. The general procedure is as follows. In the first step, purified, shortened and open – ended CNTs are finely ground in an inert atmosphere (Ar, glove-box) with a chosen payload. When the homogenous mixture is obtained the powder is placed in a silica ampule and then sealed under vacuum. After that, the ampoule is placed in a tubular furnace and heated at the rate of 5 °C/min until reaching a temperature about 50-100 °C above the melting point of the selected inorganic salt and dwelled at this temperature for few hours. After this time the sample is allowed to slowly cool-down to the room temperature permitting slow crystallization of the salt inside CNTs. Finally, the sample is collected resulting in close-ended filled CNTs. The subsequent washing step is

necessary for the removal of the non-encapsulated material remaining in the sample. Depending on the compound different washing procedure is applied.

The first step in the characterization of filled carbon nanotubes is to assess if the washing of the crystalline material external to the CNTs was effective. In the synthesis process the excess of the payload was used to ensure the maximum filling yield. A succeeding washing step was employed to remove the remaining, unreacted material present on the outside walls of carbon nanotubes. However, the washing procedure is not always effective and has to be repeated until all of the external material is removed resulting in a clean sample of filled CNTs. The washing efficacy of all of the samples was checked by HAADF-STEM examination conducted in a fast and simple way in the SEM. The principle of *Z*-contrast STEM is that the image is strongly dependent on the atomic number (*Z*) of the observed atoms, thus heavy elements appear with higher intensity as compared to carbon nanotubes. For example, samarium chloride ($SmCl_3$) encapsulated into SWCNTs gives a bright intensity when compared to carbon (Z = 6) due to the presence of Sm (Z = 62) [302].

First, we studied the post-washing protocol for obtaining clean $SmCl_3$@SWCNT nanocapsules, which consisted of stirring and sonicating of the sample in water. The cleaning filtrate was monitored by UV-Vis spectroscopy for each condition tested. Chrome azurol S was employed to assess the bulk removal of external $SmCl_3$ from the filtrate. Chrome azurol S is of interest since it can be used to quantify a large variety of materials in a fast, accurate and reliable manner. The parameters that control the cleaning process were optimized, including the time of stirring (1 h), temperature (80 °C), volume of water (50 ml) and sonication time (5 min), to achieve a fast and complete removal of the external material of 150 mg sample [303].

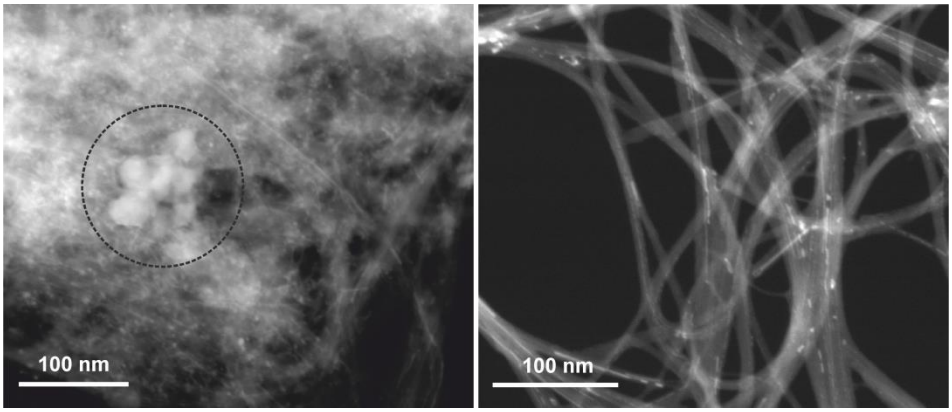

Figure 3.10 HAADF-STEM images of $SmCl_3$@SWCNTs before (left) and after (right) an effective washing.

On **Figure 3.10** images of $SmCl_3$@SWCNTs before (left) and after an effective washing (right) are displayed. On the left-handed micrograph big aggregates of unreacted $SmCl_3$ mixed with filled carbon nanotubes are present and marked with a black circle. In contrast to that, the right-handed micrograph shows clean samarium chloride filled nanotubes.

The possibility to assess the efficiency of the washing step in a reliable and rapid manner by HAADF-STEM allowed us to establish an optimized protocol for the removal of external non-encapsulated material of other payloads. Hence, in another study we compared different cleaning protocols for $LuCl_3$- filled SWCNTs, namely: sonication and filtration, sonication and dialysis, sonication and centrifugation, soxhlet with cellulose thimble and soxhlet with dialysis sack [304]. In all of the washing protocols large and equal amounts (480 mg) of $LuCl_3$@SWCNTs, collected after the filling experiment were processed. All treatments were repeated for up to six days unless a clean sample was already achieved at an earlier stage. Hot water used in the protocols was in range of 70-90 ºC. The best method was found to be based on a synergistic combination of both Soxhlet and dialysis which allows the efficient removal of the large excess of non-encapsulated material present after filling of carbon nanotubes. Although the

cleaning protocol was tested on $LuCl_3$@SWCNTs it can be employed for other non-encapsulated materials. Hence, we have developed a sustainable system to process samples of filled SWCNTs with poor water soluble materials.

Another use of HAADF-STEM imaging in the SEM is the rough evaluation of the filling yield. Scanning of the grid with deposited sample and observing the bright lines corresponding to the inorganic payload surrounded by light grey halo representing carbon nanotubes, gives us an indication of how successful the encapsulation process resulted. We have chosen this mode over the standard HRTEM imaging due to the low contrast of the latter, in which filling material is not as easily visible, especially in the case of bundles of nanotubes (**Figure 3.11**). In contrast to that, the high atomic number of the payloads we chose for filling into CNTs gives high contrast in HAADF-STEM images.

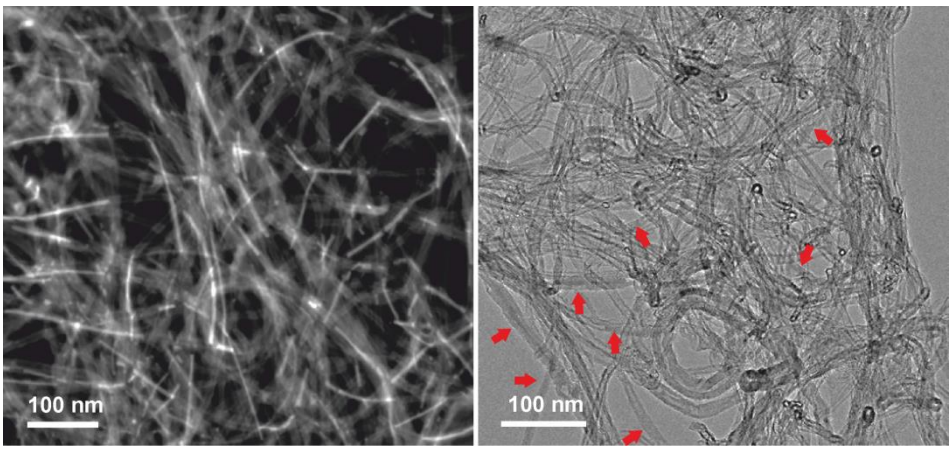

Figure 3.11 $EuCl_3$@MWCNTs visualized in two modes: HAADF-STEM (left) and TEM (right), both acquired on FEI´s Tecnai microscope operated at 200 kV.*Red arrows on TEM micrograph show the few visible filled CNTs.

The difference in the visualization of the filling yield may be clearly seen on **Figure 3.11**, where both, HAADF-STEM and HRTEM micrographs of the same sample are displayed. The sample consisted of MWCNTs filled with europium trichloride ($EuCl_3$@MWCNTs) and was characterized by a high filling yield. This conclusion

was clearly withdrawn from HAADF-STEM micrographs (left-handed image) but was not so obvious when exploring it in HRTEM mode (right-handed image). The red arrows on the TEM image point to some of the $EuCl_3$@MWCNTs. The example presented here is based on MWCNTs but the same conclusion is valid for samples of filled SWCNTs. Moreover, it results even more difficult to distinguish filled SWCNTs from non-filled ones due to their narrow diameters and their susceptibility of forming bundles. Hence, high contrast of STEM mode once again was proven to be a valuable tool when characterizing filled carbon nanotubes. More examples of HAADF-STEM images of filled CNTs are displayed on **Figure 3.12** for multi-walled nanocapsules and **Figure 3.13** for single-walled nanocapsules.

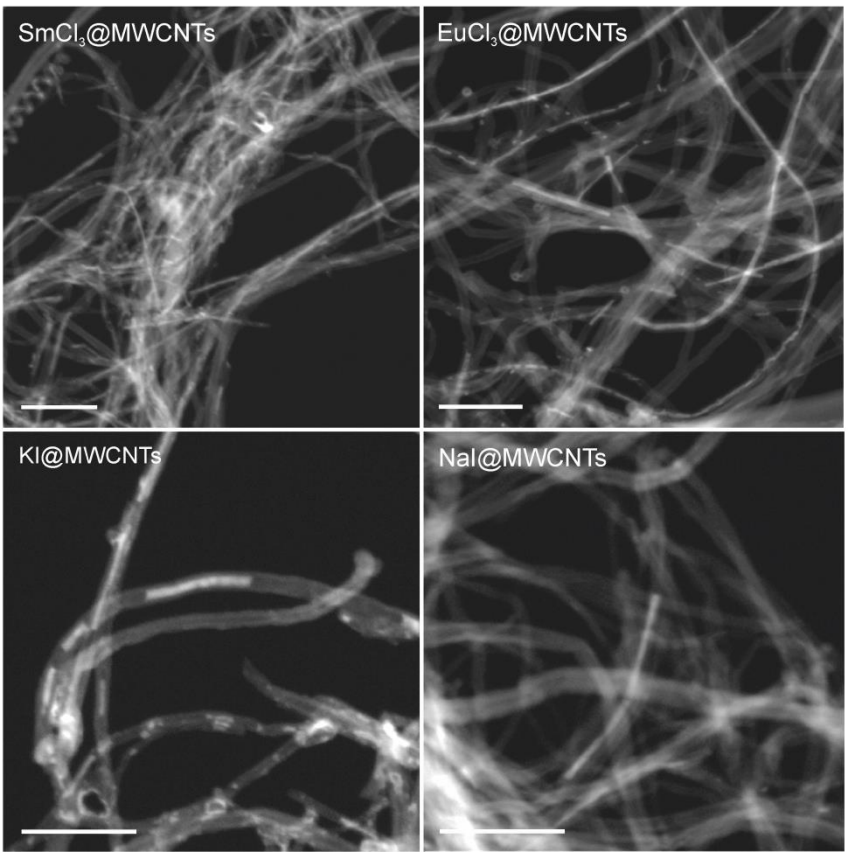

Figure 3.12 HAADF-STEM imaging in SEM microscope of filled MWCNTs. All scale bars are 100 nm.

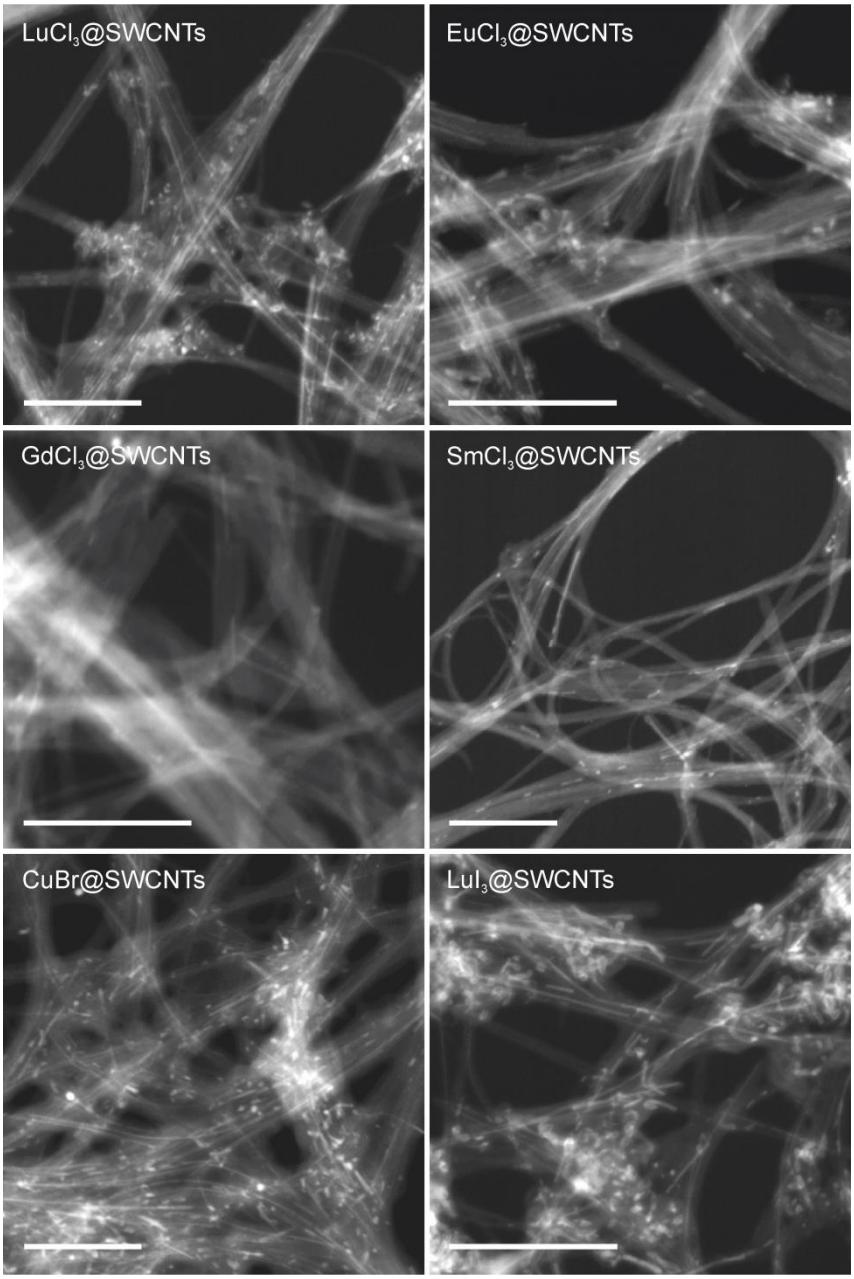

Figure 3.13 HAADF-STEM images acquired by FEI´s Magellan XHR SEM of filled SWCNTs. All scale bars are 100 nm.

The next step in the characterization of our nanocapsules was to confirm the crystallographic structure of the payloads. This was provided by high resolution capabilities enclosed in the TEM. A high energy beam passing through a set of lenses and apertures is able to interact with a thin specimen and resolve its structure at the atomic level. As a result, HRTEM micrographs enabled us to visualize the atomic columns of inorganic crystals present inside CNTs and resolve/confirm their structure. HRTEM images of the crystal-CNT hybrids are displayed on **Figure 3.14** for SWCNTs and **Figure 3.15** for MWCNTs.

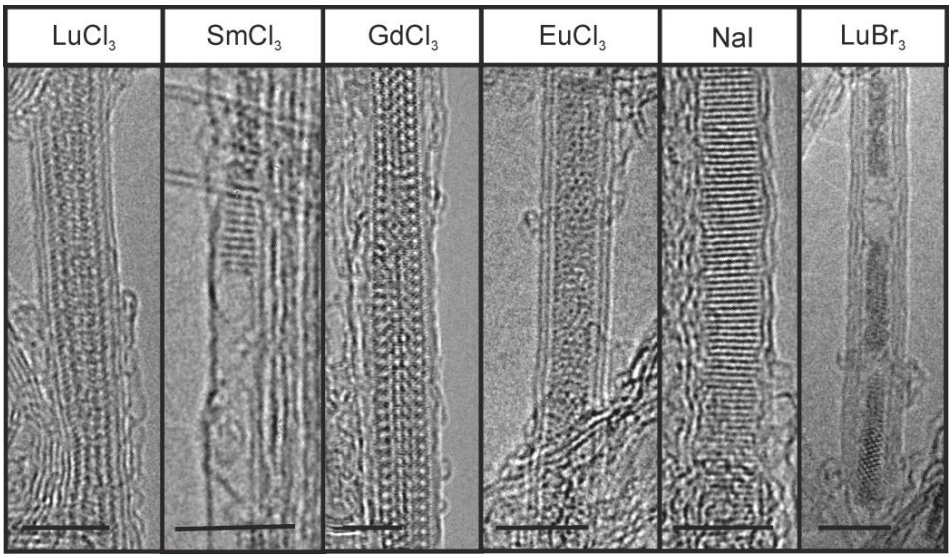

Figure 3.14 High resolution TEM micrographs of SWCNTs and DWCNTs filled with the following inorganic materials (from left to right): $LuCl_3$, $SmCl_3$, $GdCl_3$, $EuCl_3$, NaI and $LuBr_3$. The scale bars represent 5 nm.

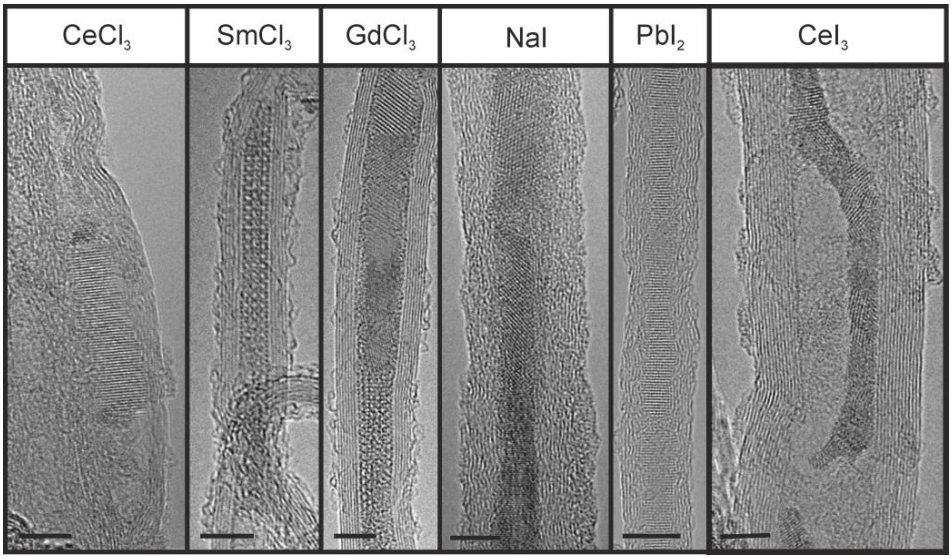

Figure 3.15 High resolution TEM micrographs of MWCNTs filled with the following inorganic materials (from left to right): $CeCl_3$, $SmCl_3$, $GdCl_3$, NaI, PbI_2 and CeI_3. The scale bars represent 5 nm.

The typical procedure, based on HRTEM images, involves a Fourier Transform of a part of a nanowire and performing inverse Fourier Transform on the masked reflections yielding filtered images of the crystals, as in the case of $SmCl_3$ and $LuCl_3$ enclosed inside SWCNT and DWCNT, respectively (**Figure 3.16**). Nonetheless, the lattice spacing can also be directly measured on the HRTEM image. As an example, we measured the lattice spacing of a $SmCl_3$ structure from its HRTEM image and obtained a value fitting the (200) – hkl reflection, in good agreement with the literature and corresponding to hexagonal $P\ 6_3/m$ space group. For the $LuCl_3$ we obtained a full set of reflections due to the crystal orientation perpendicular to the beam axis. After measuring the d-spacing values from the image it was revealed that the crystal was oriented along the [001] zone axis of monoclinic $LuCl_3$ crystal of $C\ 2/m$ space group. This procedure was repeated for most of the samples of filled CNTs, to assess and confirm if the payload preserved its structure once encapsulated within the CNTs.

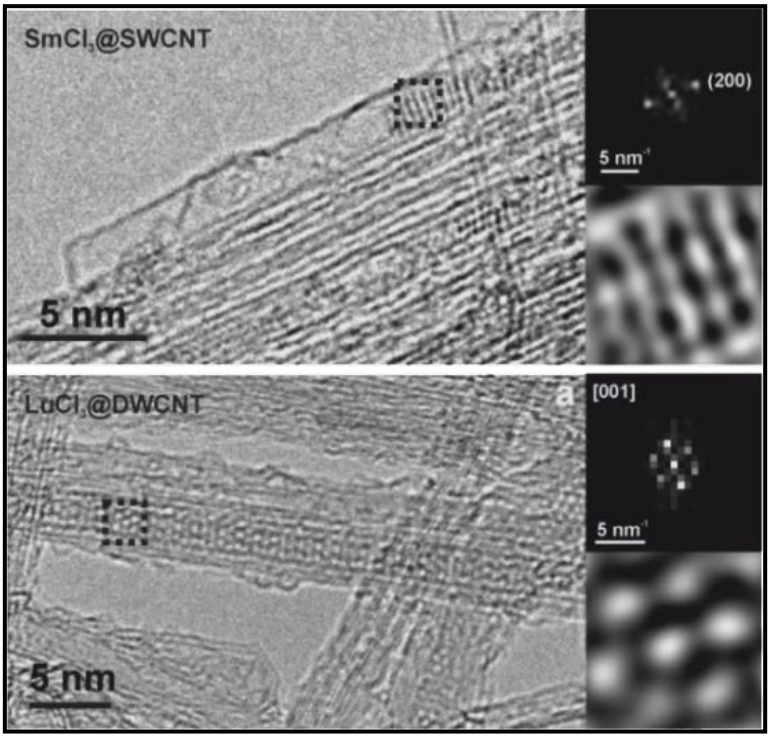

Figure 3.16 HRTEM, Fourier Transform of dotted square and inverse Fourier Transform of $SmCl_3$@SWCNT (above) and $LuCl_3$@DWCNT (below).

The combination of both, HAADF-STEM in the SEM and HRTEM imaging gives us essential information on the estimation of the filling yield, the purity of the sample and the crystalline structure of the payload. Moreover, in the case of some materials, which present a layered structure in the bulk (PbI_2, LuX_3, ZnI_2, $GdCl_3$, CeI_3), we may end up with carbon nanocapsules filled not exclusively with nanowires of selected material but also with inorganic nanotubes. These materials are characterized by weak interlayer Van der Waals interactions, the reason for which single layers are easily peeled off and may crystalize in form of nanotubes. In this particular case, the best visualization is provided by high resolution STEM imaging. The high resolution and high contrast of the image based on the atomic number of the present elements helped us to identify this type of structure in a fast

and almost unmistakable manner. Some examples of crystallization in form of nanotubes are shown on **Figure 3.17**.

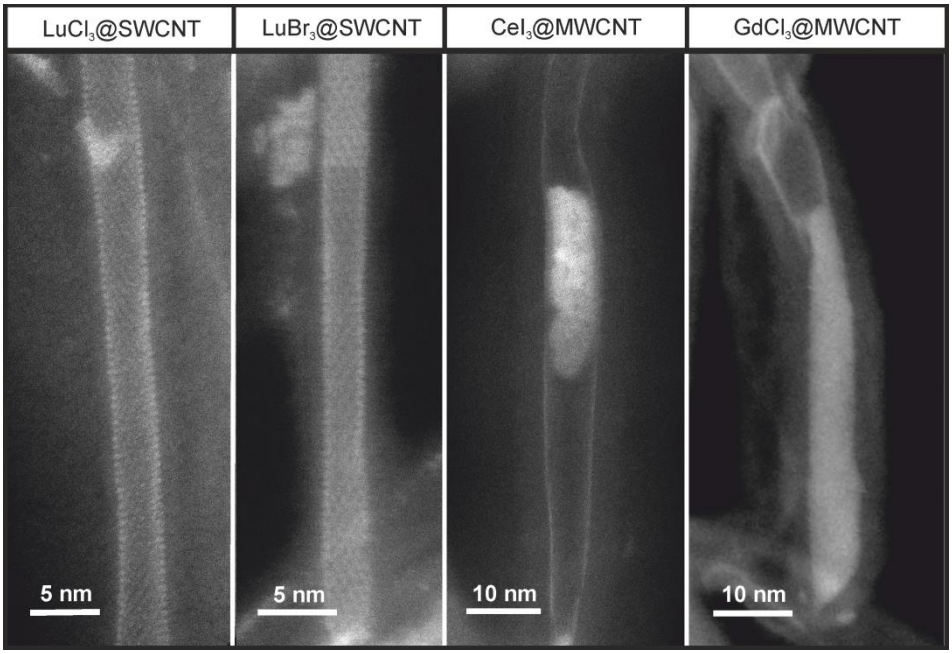

Figure 3.17 HAADF-STEM micrographs of inorganic nanotubes of $LuCl_3$ and $LuBr_3$ filled inside SWCNTs and CeI_3 and $GdCl_3$ filled in MWCNTs.

Unlike nanowires, nanotubes of inorganic payloads are characterized by bright edges and darker interiors following the shape of carbon nanotubes. In the case of any doubt the intensity profile may be drawn perpendicular to the nanotube long axis showing the expected change, as in the case of CeI_3@MWCNTs (**Figure 3.18**). It is common that a transition from nanotube to nanowire and then back to nanotube is happening along a single nanocapsule. For instance, this is observed in case of CeI_3@SWCNT displayed on **Figure 3.18 d**, where intensity profiles drawn perpendicular to the nanocapsule axis for nanowire (**B**) and nanotube (**A**) are shown and exhibit typical behaviour.

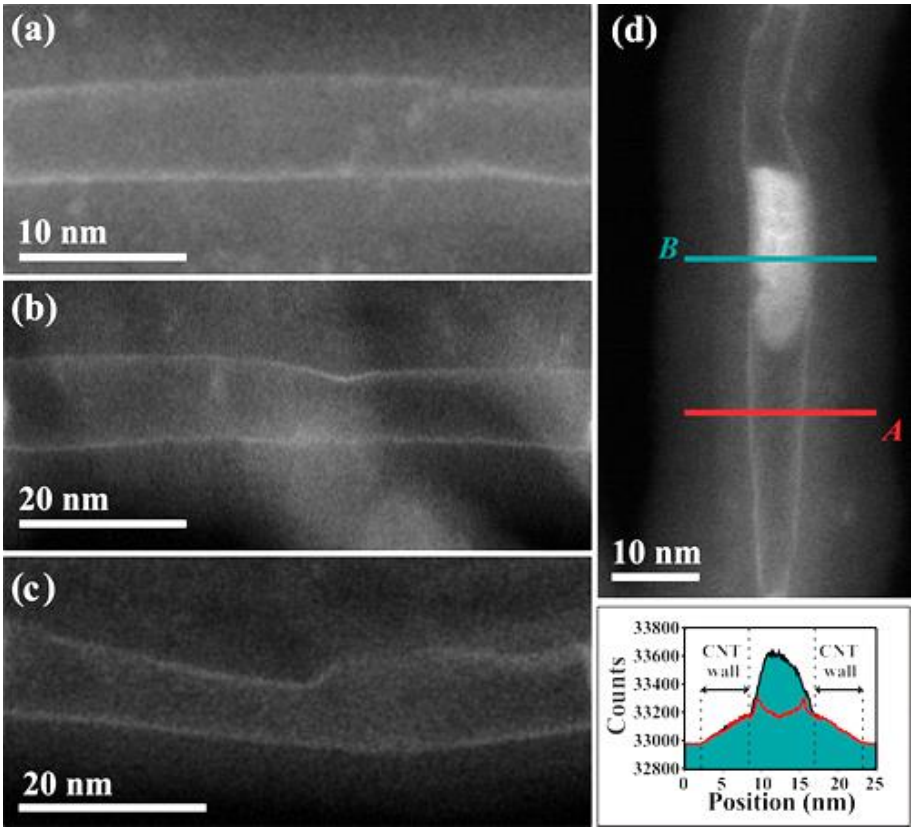

Figure 3.18 HAADF STEM images of (a-c) CeI_3 inorganic single-layered nanotubes confined within MWCNTs and (d) intensity profiles of two segments of a MWCNT containing a nanotube (A, red line) and a nanorod (B, green line) of CeI_3.

Apart from nanowires and nanotubes, we have noticed the formation of other types of structures inside CNTs, namely nanoparticles and "nanosnakes", characterized by a "snake-like shape". The four structures (nanowire, nanotube, nanoparticles and nanosnake), are presented on **Figure 3.19**, imaged by HRTEM on Tecnai F20 TEM at 200 kV. The selective formation of these structures depends on the encapsulated material but also on the conditions used for the synthesis. For instance, we observed that the growth of encapsulated single – layered metal halide nanotubes is enhanced with increasing synthesis temperature.

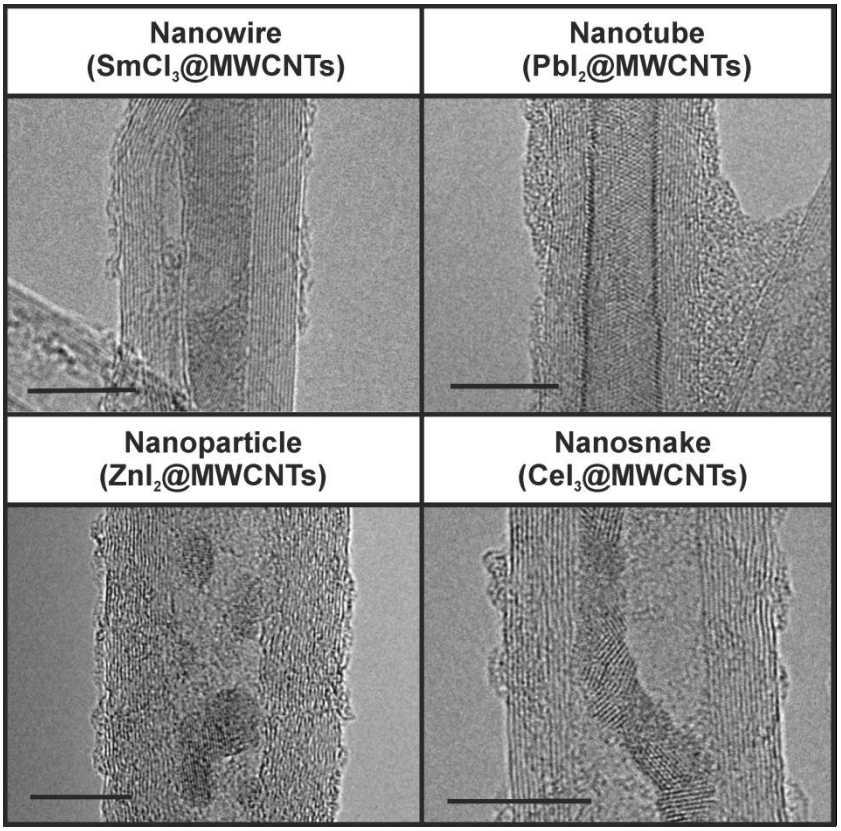

Figure 3.19 The main types of filling structures present in carbon nanotubes: a nanowire composed of $SmCl_3$, a nanotube of PbI_2, nanoparticles of ZnI_2 and a nanosnake of CeI_3. All the scale bars are 10 nm.

Until now, we were able to extract valuable information based on electron microscopy, but still there is more to do. With the help of an energy dispersive X-Ray detector (EDX), often coupled to an SEM or TEM, we are able to obtain a spectrum of all of the elements contained in the samples. This is especially useful when assessing the presence of possible contaminants. For that reason, it is one of the crucial steps in the study of nanocapsules for biomedical applications. Additionally, the quantification provided by such analysis gives us an opportunity to calculate the filling yield but this may only be done for carbon nanotubes when deposited on carbon-free support. As an example the EDX spectra of

$LuCl_3$@SWCNTs and $SmCl_3$@SWCNTs acquired from the region shown on the corresponding HAADF-STEM images (**Figure 3.20**).

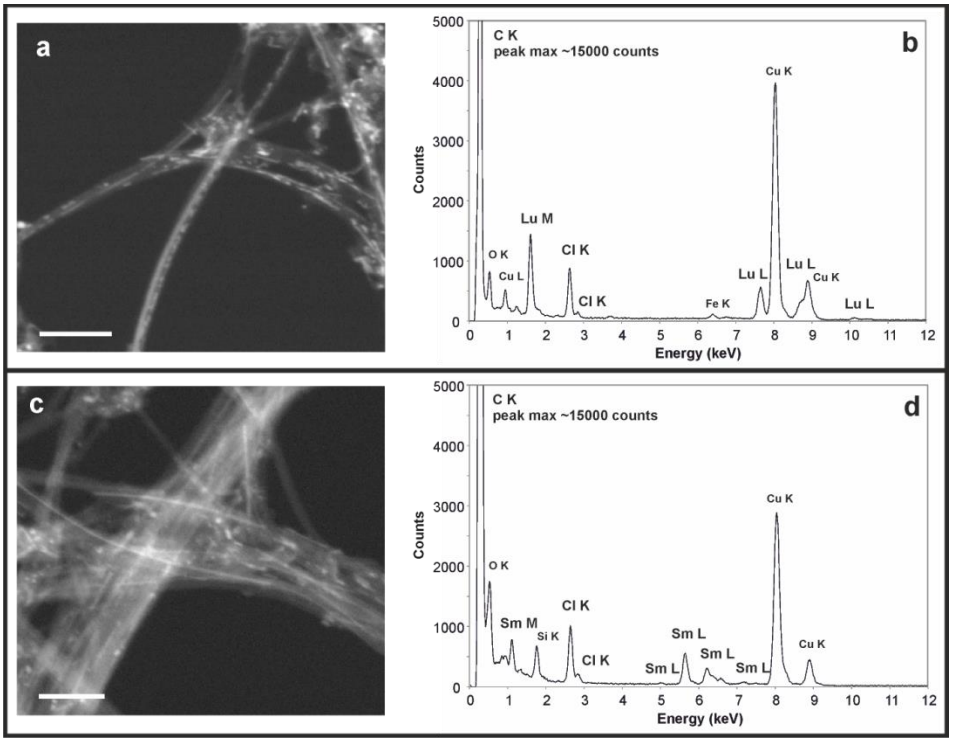

Figure 3.20 HAADF–STEM images of: $LuCl_3$@SWCNTs (a) and $SmCl_3$@SWCNTs (c) and corresponding EDX spectra of $LuCl_3$@SWCNTs (b) and $SmCl_3$@SWCNTs (d). The scale bars are 50 nm.

On the EDX spectra there is a clear evidence of the presence of chlorine (both samples) and lutetium or samarium depending on the material. The X-ray signals corresponding to Cl (K shell), Lu (M and L shells) and Sm (M and L shells) are revealed. In the lutetium filled sample a trace amount of iron was discovered, it was linked to the residual catalyst that could not be removed in the steam process and successive HCl washing. Both EDX spectra show the copper peaks that are associated with the supporting TEM grid. The additional Si peak appearing on $SmCl_3$@SWCNTs spectrum is linked to self-emissions of the Si-based X-ray detector.

Although we may confirm the elemental composition of the samples from EDX spectroscopy and the successful filling of SWCNTs from HAADF-STEM imaging, information on the filling yield is still missing. Quantification based on the EDX spectral analysis is possible provided that the sample is deposited onto a carbon-free support but in the previous example the carbon peak is originating not only from the carbon nanotubes but also from the supporting lacey carbon film thus making it impossible to assess the quantity of carbon corresponding only to CNTs. However, quantification of carbon nanocapsules can be obtained by acquiring an EDX of a sample deposited on top of carbon-free support. This can be done by depositing the sample onto a Si chip and analysing it by EDX on the SEM (**Figure 3.21**).

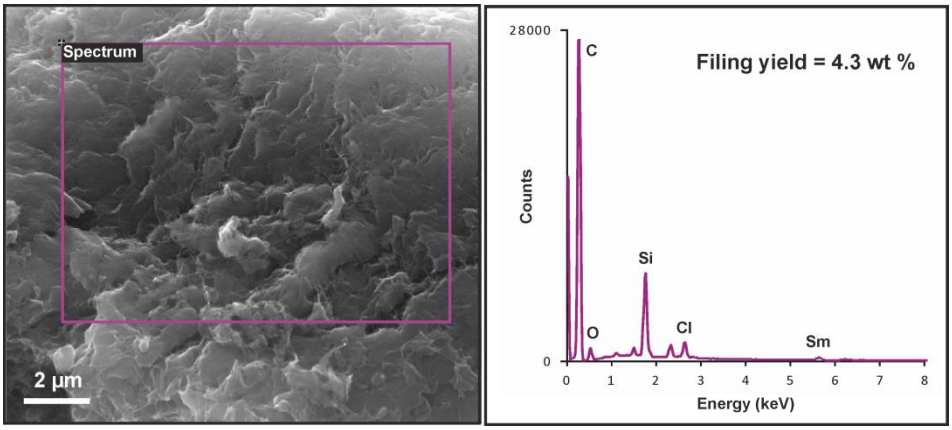

Figure 3.21 EDX acquired in SEM of $SmCl_3$@SWCNTs deposited on Si chip. The spectrum was acquired from the area marked as a purpule square on the left-handed image.

As an example, we show EDX analysis of a $SmCl_3$@SWCNTs sample acquired on FEI´s Quanta 650F SEM microscope equipped with EDAX detector at 20 kV. The quantification of the filling degree of $SmCl_3$-filled nanotubes was done using INCA software based on analysis of several areas of aggregates of few micrometres and resulted in 4.3 wt%. Due to the high intensity of carbon peak, the Sm and Cl peaks are barely visible.

In this part we have discussed the preparation of filled carbon nanotubes and their full characterization with the help of electron microscopy and related spectroscopic techniques. The crystals used here were the "cold" versions of potentially radioactive elements. These filled carbon nanotubes are intended to be studied in the near future for the creation of specialized nanocapsules for targeted delivery of radioactivity.

3.3 Exohedral functionalization of carbon nanotubes

Previously in this chapter we have introduced the topic of shortening and purification of carbon nanotubes as an important step to make nanotubes biocompatible and therefore suitable for clinical applications. After that, we have presented the subject of enclosing of possible radioactivable elements such as Sm, Lu, Gd, I, Eu, Ce and Cu in the interior of CNTs, which could be used for radiotherapy and imaging in cancer diagnosis and treatment. However, such purified, shortened and filled carbon nanocapsules would need to be dispersible in water in order to be injected intravenously, the easiest and fastest way of introducing medicines into our bodies. However, pristine carbon nanotubes are insoluble in water. This may be fixed by attaching suitable organic molecules on the external walls of carbon nanotubes which would render them dispersible and consequently compatible with intravenous injection. Additionally, organic molecules may bare metal components, such as gadolinium, which can be applied as an MRI contrast agent.

In this part we will describe the characterization of functionalized and Gd-chelated multi-walled carbon nanotubes. In the studies presented here Gd cations were chelated by diethylene triamine pentaacetic acid (DTPA) molecules attached covalently to the surface of MWCNTs [305, 306]. These structures were developed with the aim of preparing contrast agents for Magnetic Resonance Imaging (MRI). This subchapter is divided into two parts for clarity (two separate investigations),

both focused on MWCNTs functionalized with DTPA chelating Gd^{3+} ions. We will call the compounds Gd-DTPA-MWCNTs-1 and Gd-DTPA-MWCNTs-2 with the aim of simplification.

There are few limiting factors for the use of carbon nanotubes in biomedicine. As already mentioned, the length and presence of toxic nanoparticles is one of them, but it may be fixed by steam purification and shortening process. Another problem is the dispersibility of CNTs in aqueous solutions which may be mediated through functionalization of the walls of CNTs with organic molecules. An additional factor is the limited range of methods available to study carbon-based materials in biological environments [307]. Among non-invasive imaging methods, MRI appears as particularly advantageous because of its excellent spatial resolution and soft tissue contrast. To date there have only been few reports on the use of MRI for visualization of CNTs due to their poor MR contrast. Therefore, the addition of paramagnetic gadolinium overcomes that problem giving an efficient MR contrast and enabling to track the CNTs in biological media, as described in the recent years [308, 309].

Although carbon nanotubes are composed only of carbon atoms ($Z = 6$), they are arranged in a periodic crystal structure which allows their visualization by HRTEM. Organic molecules are also composed of elements of low atomic number, such carbon, oxygen, nitrogen and sulphur but with no periodicity. In consequence, they present none or very little contrast in HRTEM/STEM. With the intention of making the organic molecules visible, the attachment of heavy atoms is required (so-called "heavy element tagging") and Gd is perfectly suitable for that purpose with its atomic number of 64.

The detailed characterization of Gd-DTPA-MWCNTs-1 and Gd-DTPA-MWCNTs-2 was conducted in our work by electron microscopy techniques. The combination of HRTEM and Z-contrast HAADF-STEM imaging coupled to

EDX spectroscopy resulted suitable for characterization of samples of the nature described here.

3.3.1 Gd-DTPA-MWCNTs-1

In this first part, we will describe the preparation and characterization of covalently functionalized oxidized MWCNTs with DTPA for chelation of Gd^{3+} (Gd-DTPA-MWCNTs-1), intended for studies on intravenous administration into mice.

The Gd-DTPA-MWCNT-1 was prepared as follows. First, MWCNTs were oxidized in acidic conditions to shorten the nanotubes to lengths around 400 nm and to introduce carboxylic (COOH) groups making them dispersible in aqueous solutions. Then, the carboxylic acids were activated using oxalyl chloride. The corresponding acyl chloride groups were coupled to diethylene triamine pentaacetic acid (DTPA) derivative bearing a free amine function. The *tert*-butyl ester moieties were subsequently hydrolysed using trifluoroacetic acid (TFA). Finally, chelation of Gd^{3+} was achieved by dispersing the DTPA-MWCNTs in an aqueous solution of gadolinium(III) perchlorate, followed by dialysis against water to remove free gadolinium. Further details on the synthesis procedure are enclosed in the experimental section of our article [305]. The schematic representation of the process is showed on **Figure 3.22**.

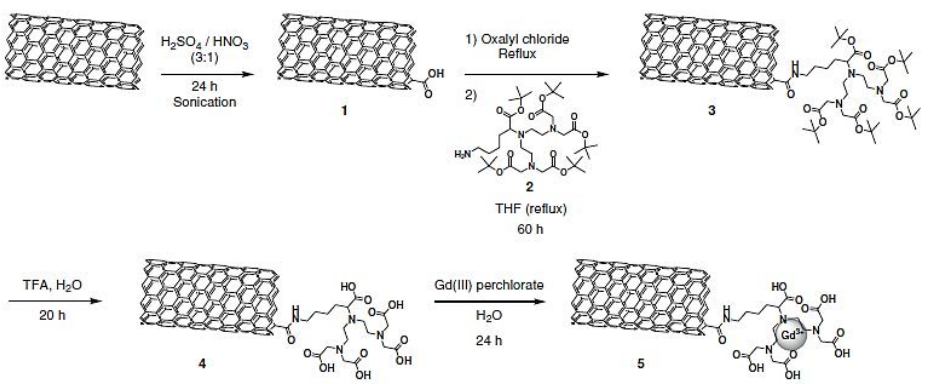

Figure 3.22 Synthesis of Gd-DTPA-MWCNTs-1.

Successful functionalization of the MWCNTs was initially confirmed by TGA analyses of the samples (1-5), namely oxidized MWCNTs (ox-MWCNTs), DTPA-functionalized MWCNTs (DTPA-MWCNTs) and pristine MWCNTs. TGA showed an increasing weight loss for modified MWCNTs, confirming the efficiency of functionalization (**Figure 3.23 a**). The weight loss corresponding to the drop at 500 °C between ox-MWCNTs and DTPA-MWCNTs provided the assessment of the level of functionalization. It has been estimated that 540 μmol of DTPA per gram of MWCNTs were introduced.

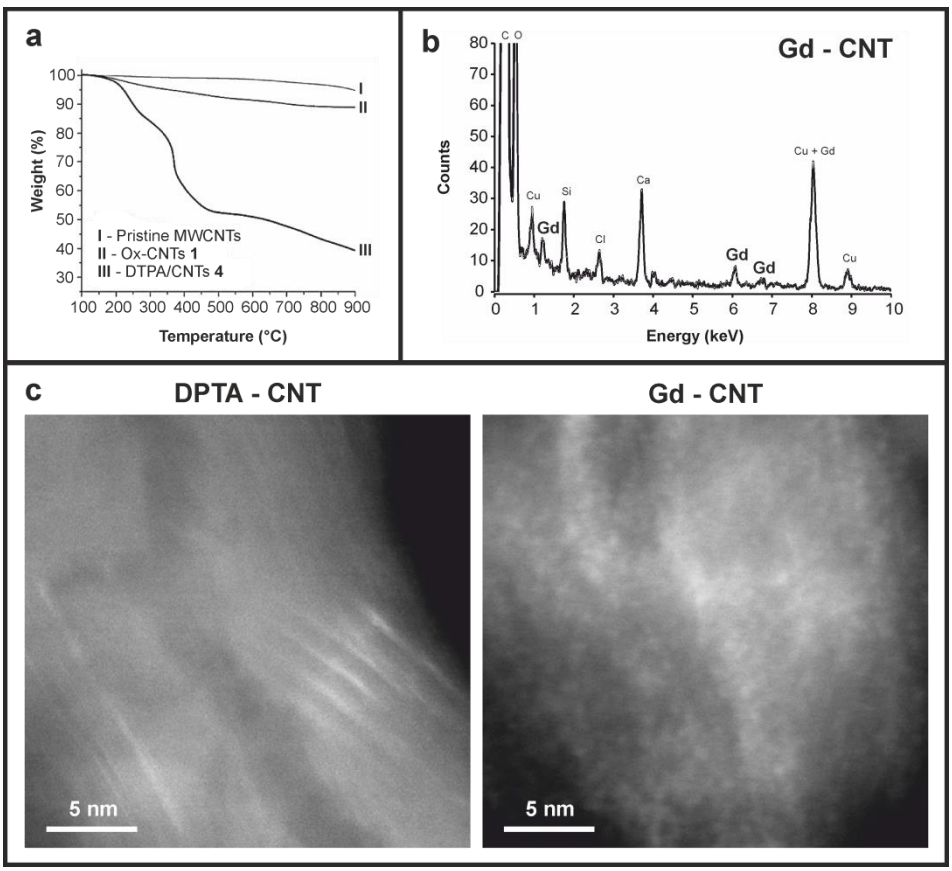

Figure 3.23 a) Thermogravimetric analysis of pristine, oxidized and DTPA-functionalized MWCNTs; b) EDX spectrum of Gd-DTPA-MWCNTs; c) HAADF-STEM images of DTPA-MWCNT and Gd-DTPA-MWCNT.

Gadolinum ions chelated by DTPA played a double role of acting as MRI contrast agents and as heavy element tags for STEM visualization. This is due to the high atomic number of Gd which allows for Z–contrast STEM. HAADF-STEM imaging at high resolution was essential to assess the degree of functionalization of MWCNTs by direct visualization of Gd atoms appearing as groupings of small bright dots on top of the external walls of CNTs (**Figure 3.23 c**). In contrast to that, no bright spots were present on the walls of the analogous DTPA functionalized sample. The fact that the Gd atoms are visible on the walls of carbon nanotubes is only possible provided the previous synthetic steps were effective. Therefore, the HAADF-STEM micrographs clearly demonstrated the successful oxidation of pristine MWCNTs, subsequent DTPA attachment and the chelation of Gd^{3+} ions in the last step.

Another confirmation of the formation of Gd-DTPA-MWCNTs came from the EDX analysis. A spectrum is showed on the **Figure 3.23 b** which represents the Gd-DTPA-functionalized CNTs. The presence of Gd was confirmed by the appearance of characteristic Gd X-ray lines. Additionally, C peak emerging mostly from carbon nanotubes and Cu and O from the TEM grid are present. The Ca and Si peaks are due to impurities probably emerging from the preparation procedure.

The purpose of preparing the Gd-DTPA-MWCNTs-1 was to provide an efficient contrast agent for Magnetic Resonance Imaging (MRI) and to study its application to follow the CNTs distribution when administrated intravenously to mice. The uptake of Gd-DTPA-MWCNTs-1 in liver and spleen was successfully assessed using in-vivo MRI imaging owing to the preserved capacity of the material to generate signal enhancement after cellular internalization (**Figure 3.24**).

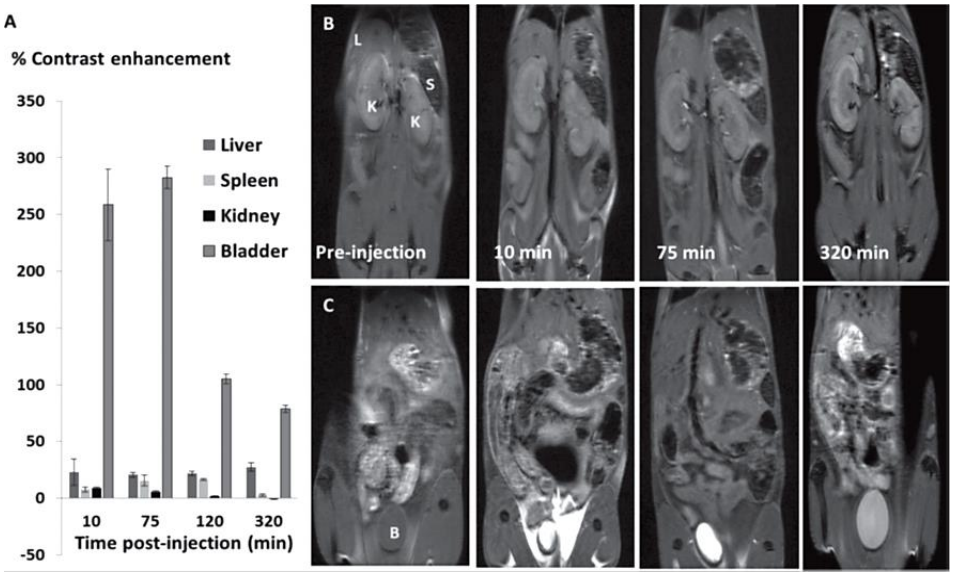

Figure 3.24 A) MRI contrast enhancement in liver, spleen, kidneys and bladder following intravenous injection of Gd-CNT (5 mg/mL, 100 μL) in comparison to the signal prior injection. Standard deviations are deduced from three independent measurements. B, C) Example of MR slices showing liver (*L*), spleen (*S*) and kidney (*K*) (B) or bladder (*B*) (C) at different-time points before and after injection of Gd-CNTs.

Overall, this study represents the first success in monitoring the CNT distribution with functionalized tubes used to generate a T_1 positive MR contrast after intravenous injection. This work shows that combining the properties of Gd^{3+} and CNTs allows performing MRI *in vivo* and resulted in a publication in Advanced Functional Materials [305].

3.3.2 Gd-DTPA-MWCNTs-2

In the following part of this chapter we will describe the synthesis strategy and full characterization of Gd-DTPA-MWCNTs-2, the second example of Gd-chelated DTPA-functionalized and oxidized MWCNTs. Similarly to the first construct, the Gd-DTPA-MWCNTs-2 was also developed as a T_1-weightened contrast agent for MRI. However, here the research on the MRI efficiency and the ability of CNTs to

translocate the cell membrane was conducted on Human Umbilical Vein Endothelial (HUVEC) cells. In this thesis dissertation we will focus mainly on the characterization of the Gd-DTPA-MWCNT-2 by electron microscopy.

The synthesis strategy of studied nanostructure Gd-DTPA-MWCNTs-2 was as follows (**Figure 3.25**). First, MWCNTs were oxidized by acid treatment in order to obtain structure **1**. After that, the 1,3-dipolar cycloaddition reaction of attaching the amine functionalities was performed yielding structure **2**. Following that, the attachment of DTPA molecules was facilitated and resulted in structure **3**, which was recovered by centrifugation, washing with water and re-precipitated from MeOH/diethyl ether. The recovered product **3** (DTPA-MWCNTs-2) was dispersed in water and at a concentration of 0.5 mg/ml mixed with $GdCl_3$ at different molar equivalents. The solutions were allowed to incubate for 1.5 h, washed tree times with water and centrifuged in order to collect the final Gd-DTPA-MWCNT-2 product.

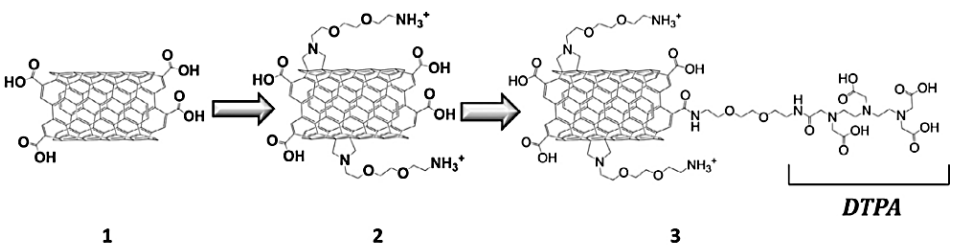

Figure 3.25 Preparation of DTPA-functionalized carbon nanotubes (structure 3).

After the synthetic process resulted in the formation of Gd-DTPA-MWCNTs-2 the characterization of that product was carried out. First, the morphology of the Gd-labelled carbon nanotubes was compared with that of their unlabelled counterparts by HRSEM. Resulting images are displayed on **Figure 3.26** (**first row**). Based on the micrographs no morphological change between the samples was evident.

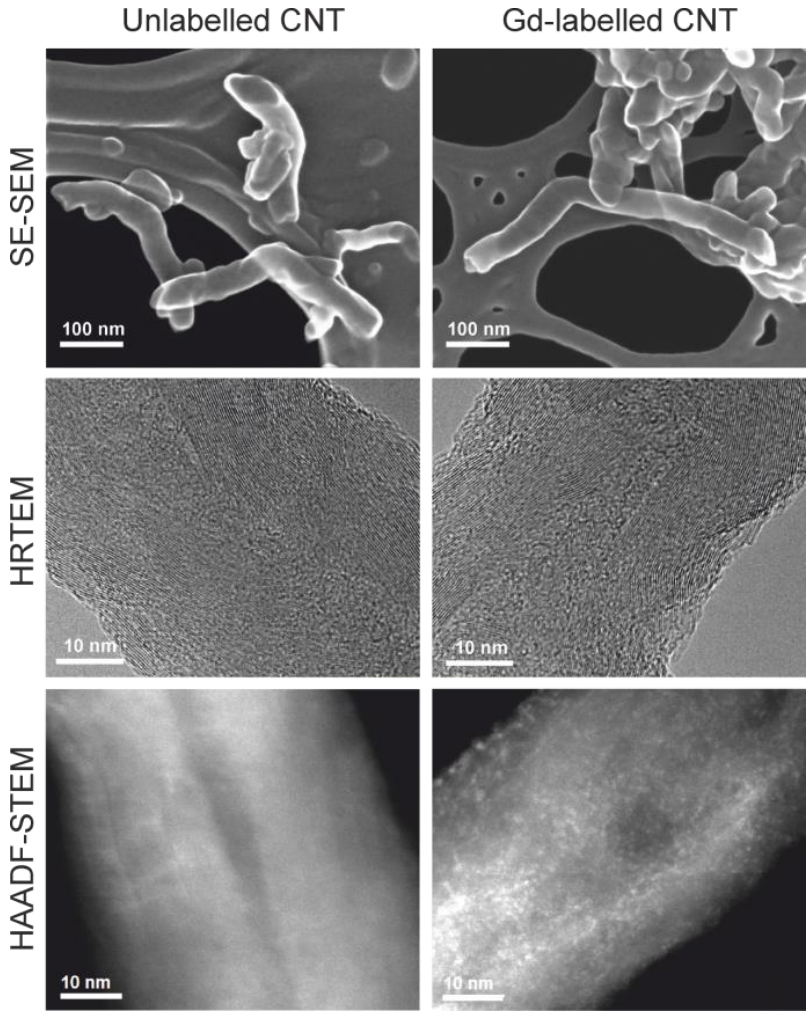

Figure 3.26 Electron microscopy characterization of unlabelled (left column) and Gd-labelled (right column) MWCNTs. First row: SEM images in Secondary Electrons mode; second row: HRTEM; third row: STEM in HAADF mode.

In order to confirm the preservation of the integrity of graphitic structure of functionalized CNTs, HRTEM imaging was conducted. The images of individual unlabelled and Gd-labelled MWCNTs are shown in the second row of **Figure 3.26**. No difference in the structure could be noticed based on HRTEM images. Moreover, no indication of the Gd attachment on the Gd-labelled nanotubes was perceived. As seen in the previous section, the best tool for the visualization of

individual Gd atoms attached to the walls of MWCNTs through DTPA chelating agent was HAADF-STEM imaging (**Figure 3.26 third row**). The high brightness dots visible on the exterior of the Gd-labelled MWCNT were associated with Gd atoms. In contrast to its labelled counterpart, the unlabelled MWCNT looked smooth.

In order to confirm these results, EDX spectroscopy in TEM mode was performed at 200 kV from aggregates of nanotubes with and without Gd. Results of the EDX analyses are displayed on **Figure 3.27**.

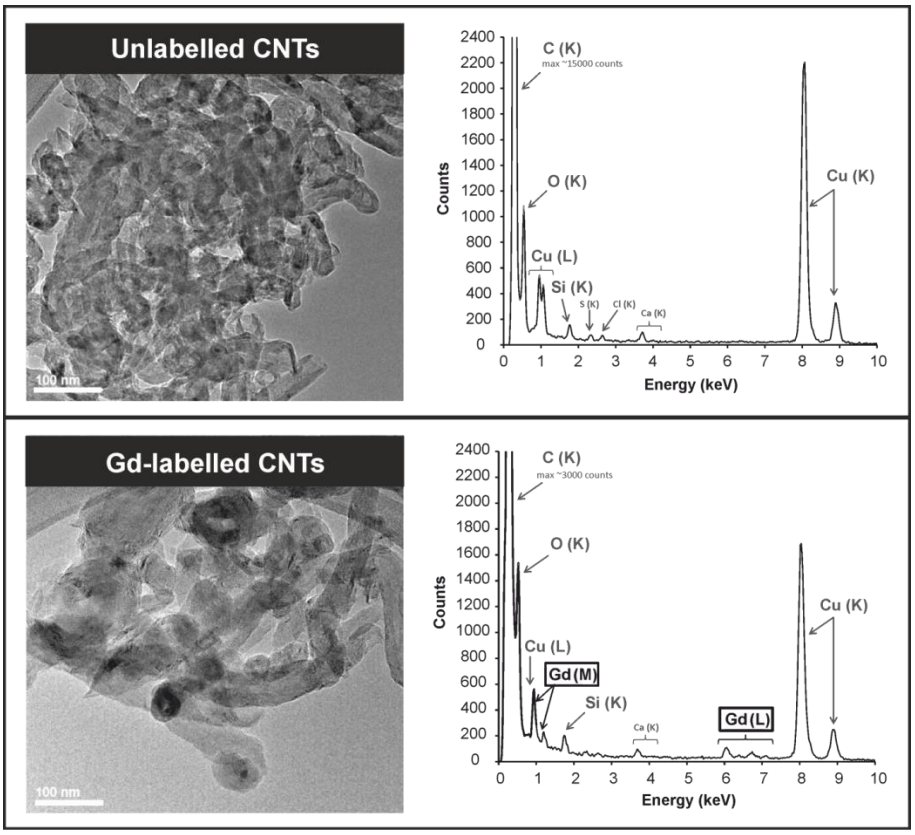

Figure 3.27 Energy dispersive X-Ray Spectroscopy of unlabelled (top) and Gd-labelled (bottom) CNTs of corresponding areas from HRTEM micrographs (left).

On both of the spectra we identified few common peaks. Carbon K edge is a sum up of the signals corresponding to the nanotubes, organic molecules and lacey carbon film on which the sample was deposited. Oxygen K edge peak corresponds to the oxygen containing organic functionalities, Copper L and K edge peaks are originating from the TEM grid made out of this metal. The Si K edge signal is most probably due to the self-excitation of Si-based EDX detector. Trace amounts of Cl, S and Ca are attributed to impurities from the solvents used at different steps of synthesis such as water and methanol. However, the most important feature of the spectra is the presence of Gd characteristic X-ray M and L peaks, existing only in the Gd-labelled MWCNTs.

After the full characterization was conducted, the Gd-DTPA-MWCNTs-2 were studied as a T_1 contrast agent for MRI cell labelling and tracking [306]. The r_1 relaxivity of the construct was found to be 3-fold higher than clinically approved Magnevist at a magnetic field strength of 7 T. The contrast efficiency, expressed as r_1 relaxivity, in Human Umbilical Vein Endothelial cells (HUVEC) was found to be 6.6 $mM^{-1}s^{-1}$. No reduction in efficiency was found post internalization in HUVECs, which was imparted to the ability of CNTs to translocate through the cell membrane.

The studies of Gd-DTPA-MWCNT-2 construct as a MRI contrast agent demonstrated the great potential of using MWCNTs as efficient cell probes for MRI. Further details are available in the article published in collaboration in Carbon [306].

3.4 Simultaneously endo- and exo- hedrally functionalized carbon nanotubes

Results presented above referred to one of the type of functionalization at a time (either endohedral or exohedral). In the following part we will combine these two functionalization types into one functional carbon nanotube construct.

3.4.1 Externally functionalized multi-walled carbon nanotubes filled with samarium trichloride and gadolinium trichloride

Filling of samarium and gadolinium salts into MWCNTs is attracting much interest for future application in medical diagnostic, as was described before in this chapter. Here we will describe simultaneously filled and functionalized multi-walled carbon nanotubes forming biocompatible nanocapsules.

As a first step, the successful filling of MWCNTs with $SmCl_3$ and $GdCl_3$ achieved by molten phase capillary wetting was confirmed by HAADF-STEM and HRTEM imaging, where the crystalline structure was revealed for $GdCl_3$ (**Figure 3.29**) and $SmCl_3$ (**Figure 3.30**). After that, we introduced specific linkers on the surface of CNTs to increase the solubility and biocompatibility of the carbon scaffold.

The most common linkers are so far poly(ethylene glycol) (PEG) and linear polymers, such as poly(vinyl alcohol) [310]. In recent years, branched polymers have become more popular, among these dendrimers [311] and dendrons [312]. In the case of application of carbon nanotubes for drug delivery, the linker and drug conjugation is usually based on cleavable bond like disulfide [313], ester [314], carbamate [315] and amide [315]. The reason is to create a bond that is biologically cleaved in the cell to deliver the active molecule. Our approach was to design a linker to provide solubility to the system, and create a flexible platform, with free amine groups, for an eventual further binding of targeting molecules.

The reaction was performed through *in situ* generation of diazonium salt from aniline precursors on the linker (**Figure 3.28**).

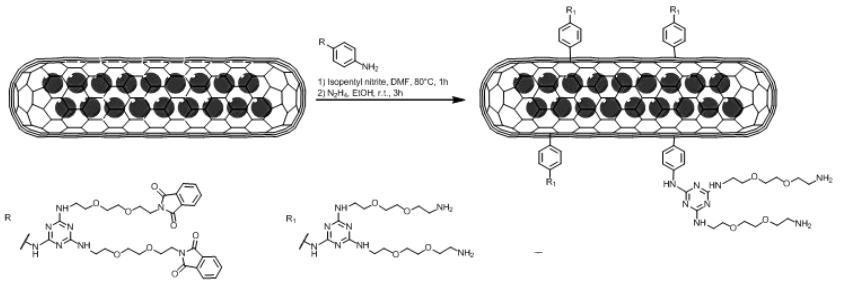

Figure 3.28 Functionalization of $GdCl_3$@MWCNTs and $SmCl_3$@MWCNTs.

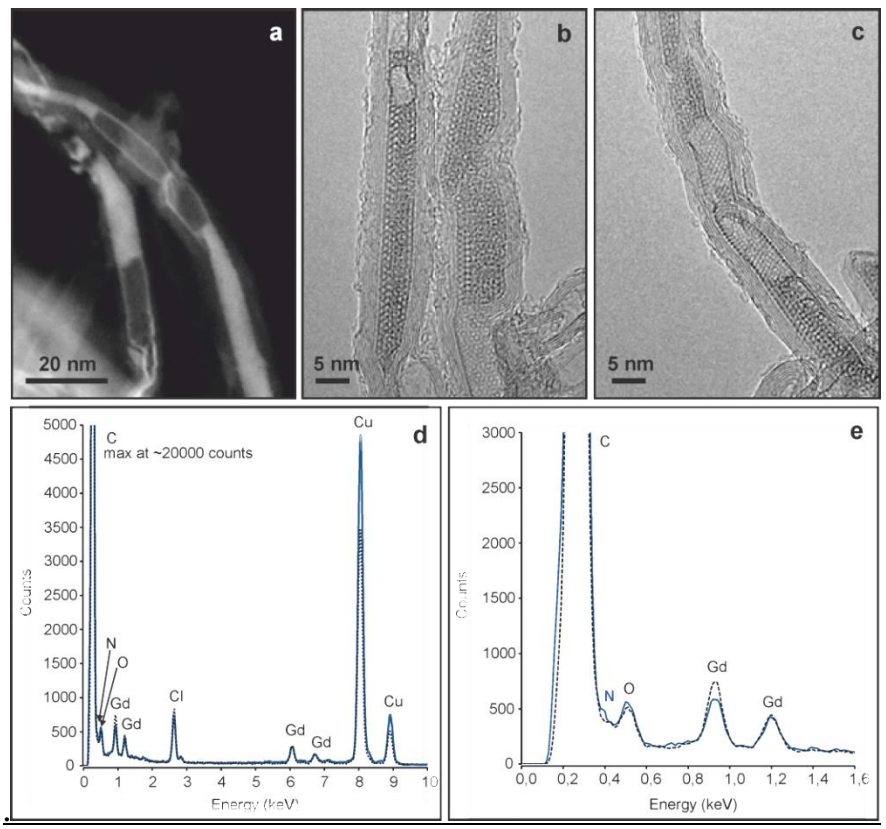

Figure 3.29 MWCNTs filled with $GdCl_3$ inorganic crystal and functionalized with organic molecules: a) HAADF-STEM image; b, c) HRTEM micrographs; d) EDX spectrum; e) zoom in into the N signal of d.

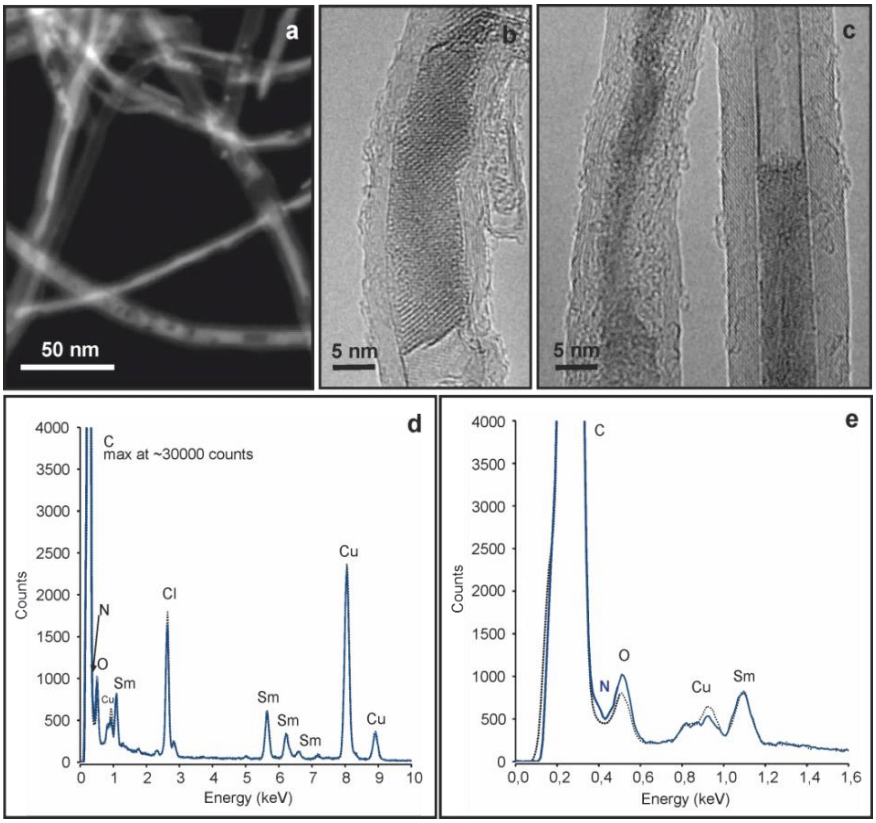

Figure 3.30 MWCNT filled with $SmCl_3$ and functionalized with organic molecules with nitrogen content: a) HAADF-STEM image; b, c) HRTEM micrographs; d) EDX spectrum; e) zoom in into the N signal of d.

Based on the **a-c** images of **Figure 3.29** and **Figure 3.30**, we concluded that two types of structures were present for both $GdCl_3$ and $SmCl_3$ samples; these are nanowires and nanotubes. The corresponding inorganic nanotubes are visible as bright edges following the carbon nanotube shapes in HAADF-STEM images while on HRTEM images they appear as dark lines in the interior of MWCNTs. As opposed to that, the $SmCl_3$ and $GdCl_3$ nanowires are clearly visible as bright (STEM) or dark (HRTEM) rods with evidently distinguishable crystalline structures. Due to the high resolution of the micrographs, high crystallinity of the structures (**Figure 3.29 b, c** and **Figure 3.30 b**) was established.

In order to confirm the presence of the linkers attached to the walls of MWCNTs, EDX spectra were acquired at 200 kV (**Figure 3.29 d, e** for $GdCl_3$ and **Figure 3.30 d, e** for $SmCl_3$). Elemental analyses for functionalized samples (blue lines) were compared with those before functionalization step (black dotted lines), i.e. filled MWCNTs. It is worth to notice that the EDX spectra present clear peaks of gadolinium and samarium, respectively, as well as the expected chlorine, confirming the composition of the respective payloads and carbon corresponding to the combined signal from CNTs, the organic molecules for functionalized sample and carbon coated grid. Additionally, copper signal is present as a consequence of the composition of the support TEM grid.

As it was expected the overlapping of carbon and nitrogen edge resulted in a hardly detectable nitrogen peak. However, a slight change in the spectra was observed in the functionalized samples as compared to the sample before the attachment of the linker (blue lines on **Figure 3.29 e** and **Figure 3.30 e**). This is an indication of the successful attachment of the nitrogen-rich linker to the MWCNTs walls.

To conclude, $GdCl_3$- and $SmCl_3$-filled and functionalized multi-walled carbon nanotubes were characterized by HRTEM, HAADF-STEM imaging and EDX spectroscopy, which confirmed the attachment of the linker by a weak N signal appearing as a shoulder on the C peak.

3.4.2 Externally functionalized single-walled carbon nanotubes filled with samarium trichloride

Here, we will describe a steam-purified SWCNTs filled with radioactive analogue ("cold" $SmCl_3$) by high temperature treatment and externally functionalized by nitrene cycloaddition reaction in order to subsequently attach an antibody called Cetuximab. The aim of preparing these functional carbon nanotubes was to test them for selective targeting of a specific receptor in cancer cells. The

functionalization of $SmCl_3$-filled SWCNTs was done on the same sample which preparation and full characterization was described in this chapter in the part entitled "Endohedral functionalization of carbon nanotubes" (subchapter 3.2). Hence, here we will only focus on the functionalization part and characterization of the final products.

As mentioned before, the choice of the filling radionuclide allows tailoring a specific radiation, cancer type and therapy. In parallel, the functionalization of the external surface of CNTs offers the versatility towards the attachment of targeting functionalities, thus enabling to modulate the biodistribution of the carrier. In the case presented here, the monoclonal antibody (mAb) Cetuximab (Erbitux®) was selected as targeting agent for the functionalization of samarium(III) chloride filled single-walled carbon nanotubes. This antibody has shown the efficiency in targeting and inhibiting the epidermal growth factor receptor (EGFR), a membrane receptor regulating multiple cellular processes and overexpressed in many cancer types [316]. In the clinical environment the Cetuximab has been approved for the treatment of various cancer types as colorectal cancer, non-small-cell lung cancer, and head and neck cancer [317-320]. A few examples of Cetuximab-CNTs conjugates have been already published in literature showing good targeting properties towards EGFR-overexpressing cells [320, 321]. However, no reports of radioactivity delivery by CNTs conjugated with Cetuximab have been found. Therefore, it seemed an interesting task to build a targeting agent composed of mAb-functionalized and $SmCl_3$-filled SWCNTs to target cancer cells. As before, this investigation was conducted as a proof of concept using non-radioactive materials, with the aim of translating the whole process to radioactively filled CNTs in the second phase.

A simple and quick protocol of preparation of $SmCl_3$@SWCNTs-mAb was conducted in order to minimize the time of preparation and simultaneously preserve the structure integrity of the nanotubes, preventing the leakage of the payload. The functionalization of the external walls of CNTs was done by initial

cycloaddition reaction to attach a suitable linker. The functionalization steps are displayed on **Figure 3.31** and **Figure 3.32**.

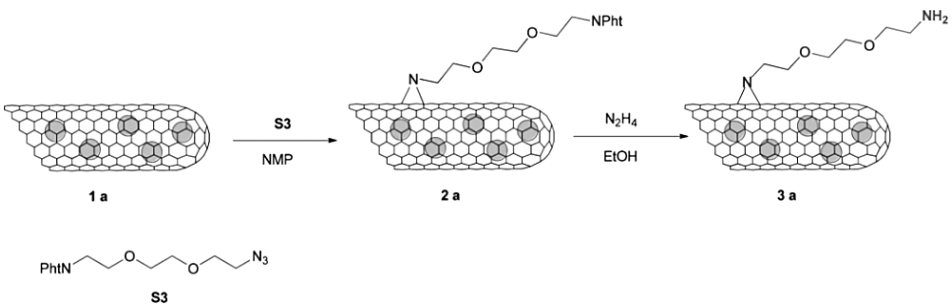

Figure 3.31 Nitrene reaction on $SmCl_3$@SWCNTs (1a) and cleavage of the phthalimide group to afford the amino functionalized $SmCl_3$@SWCNTs-NH_2 (3a).

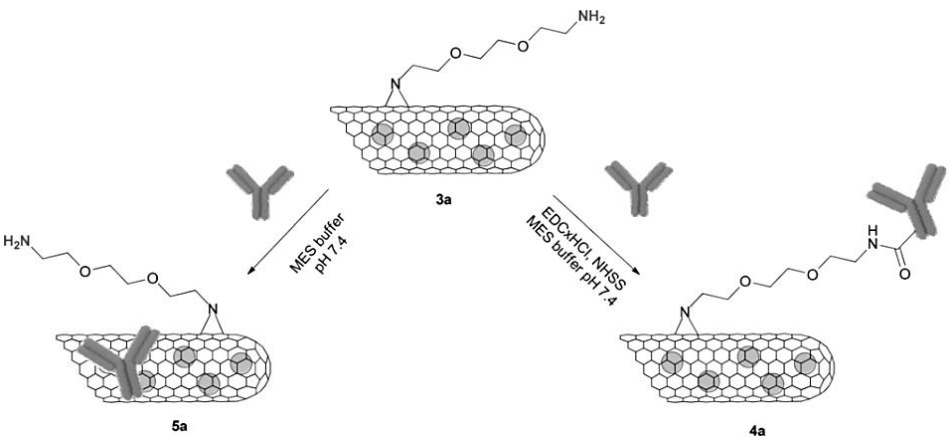

Figure 3.32 Covalent derivatization of $SmCl_3$@SWCNTs-NH_2 (3a) with Cetuximab forming $SmCl_3$@SWCNTs-mAb (4a) and control reaction in the absence of coupling reagents forming the non-covalent complex $SmCl_3$@SWCNTs/mAb (5a).

The successful synthesis of amino-functionalized $SmCl_3$@SWCNTs and successive attachment of the Cetuximab to $SmCl_3$@SWCNTs-NH_2 was initially evaluated by thermogravimetric analysis (**Figure 3.33**). Amino-functionalized CNTs ($SmCl_3$@SWCNTs-NH_2) were compared with pristine material ($SmCl_3$@SWCNTs), while covalently functionalized sample with Cetuximab ($SmCl_3$@SWCNTs-mAb) was compared to its analogue with non-covalently

attached Cetuximab ($SmCl_3$@SWCNTs/mAb). By comparing the TGA curves of the NH_2-functionalized nanotubes (blue curve) with the pristine material (black curve) the first ones lost 10 % more weight which confirmed the effective attachment of amino groups. Moreover, by comparing the weight loss of $SmCl_3$@SWCNT-mAb (**4a**) to that of the precursor (**3a**), we estimated that the loading of the antibody on SWCNTs was 250 mg/g (407 mg per g of C, taking into account the filling yield). However, the TGA curve of the non-covalent conjugate $SmCl_3$@SWCNT/mAb (**5a**) also displayed a significant weight loss, which corresponds to a loading of mAb of 200 mg/g (305 mg per g of C). This result suggests that a non-negligible amount of antibody was adsorbed onto the nanotubes and could not be removed despite the thorough washing and dialysis steps.

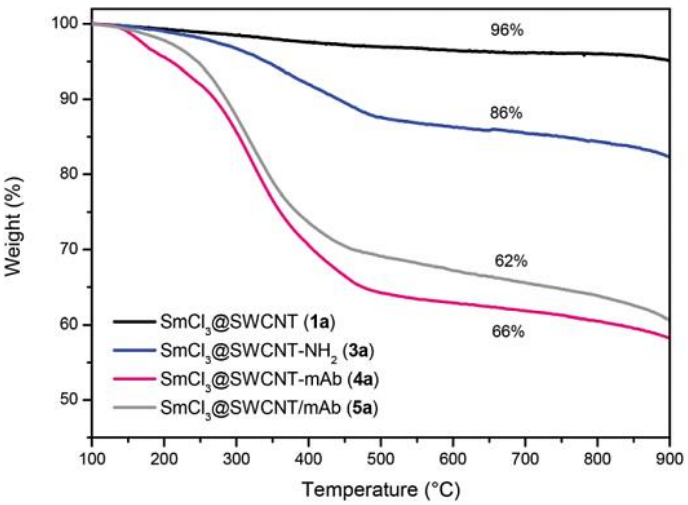

Figure 3.33 TGA curves of $SmCl_3$@SWCNTs (1a) and following conjugates: $SmCl_3$@SWCNTs-NH_2 (3a), $SmCl_3$@SWCNTs-mAb (4a) and $SmCl_3$@SWCNTs/mAb (5a). The percentages correspond to the weight losses observed at 650 °C.

In order to have a proof of the presence of free amines on the $SmCl_3$@SWCNT-NH_2 and of their availability for further derivatization, the amino-functionalized

CNTs **3a** were coupled with a 2,3,5-triiodophenyl tagging motif (**Figure 3.34**). This was achieved by EDC-assisted amidation with 2,3,4-triiodobenzoic acid.

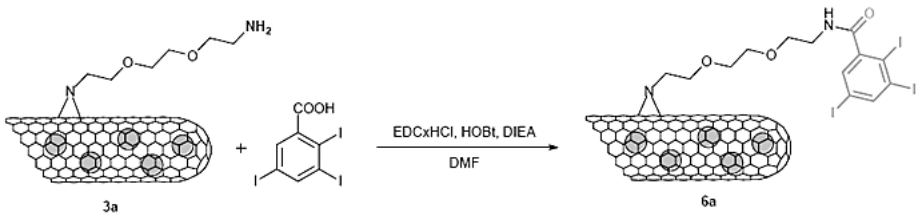

Figure 3.34 Tagging of the amino groups of $SmCl_3$@SWCNTs-NH_2 (3a) with the 2,3,4-triiodophenyl motif.

By microscopy imaging (**Figure 3.35**) it was possible to visualize many randomly distributed bright dots along the CNT sidewalls, which were not observed in the amino-functionalized CNT precursor (**3a**).

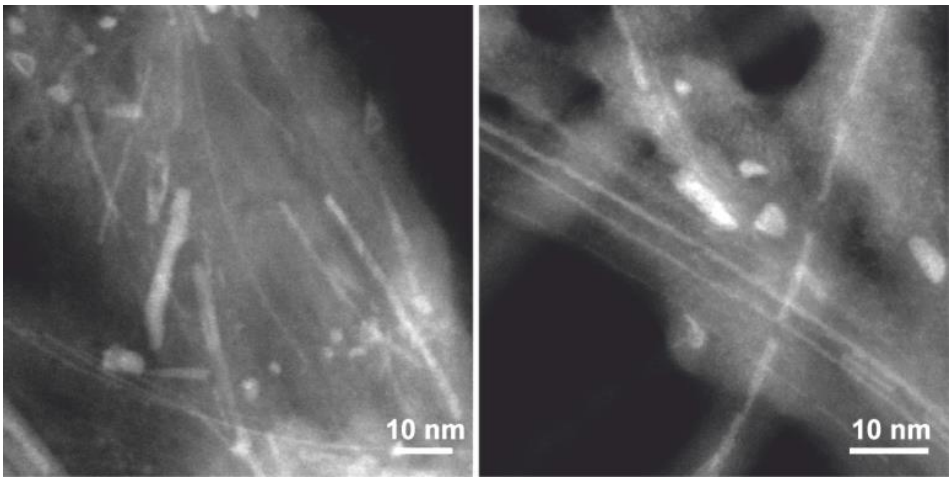

Figure 3.35 Simultaneous detection of filling and functionalization by Z-contrast HAADF-STEM of $SmCl_3$@SWCNTs-NH_2 (left) and $SmCl_3$@SWCNTs-I (right). The bright nanowires correspond to the filling material ($SmCl_3$) while the tiny bright dots on the right image are generated by iodine atoms.

On both of the micrographs displayed on **Figure 3.35** the $SmCl_3$ filling appears as bright lines following the shape of the CNTs. Additionally, on the right image, bright dots are visible and are attributed to the iodine atoms of the tag molecule.

EDX detector coupled to STEM allowed obtaining the elemental composition of the imaged area, providing a further characterization proof of the attachment of amino groups through the presence of iodine (**Figure 3.36**). As expected, Sm, Cl and N were detected in both of the amino-functionalized samples. The confirmation of the functionalization was given by the tagging motif, namely Iodine-rich molecules that appeared on the EDX spectrum as characteristic I peaks (below).

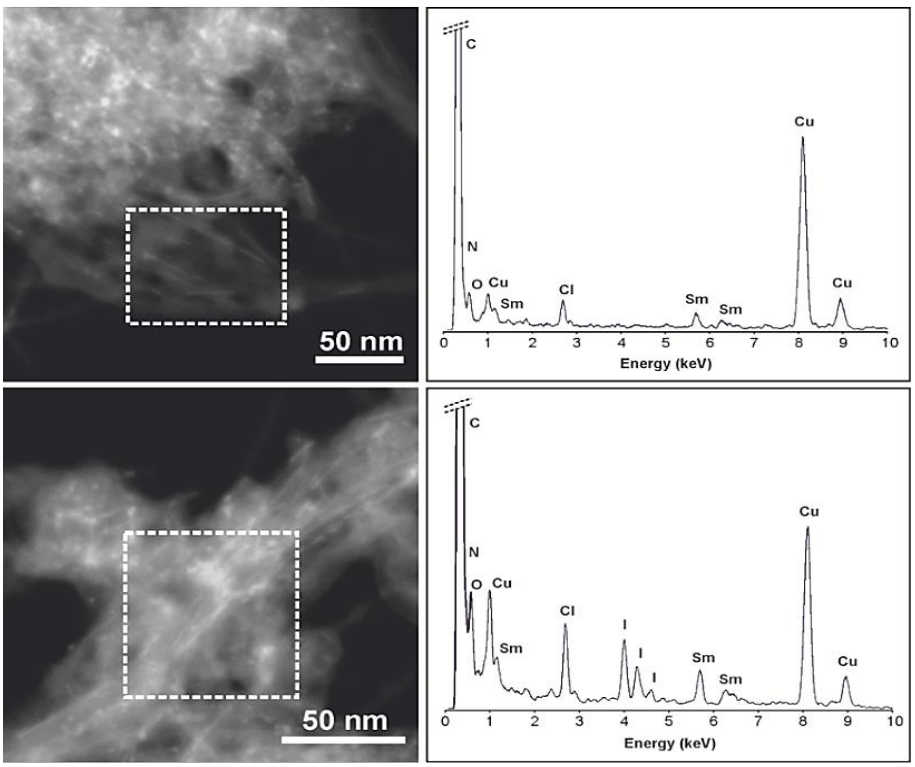

Figure 3.36 HAADF-STEM images of $SmCl_3$@SWCNTs-NH_2 (top) and $SmCl_3$@SWCNTs-I (bottom) and the corresponding EDX spectra from the areas marked by the dotted squares.

Additionally, we characterized antibody–SWCNT conjugates by electron microscopy after performing an immunostaining with a secondary antibody conjugated with gold nanoparticles (Au NPs) (**Figure 3.37 a, c**).

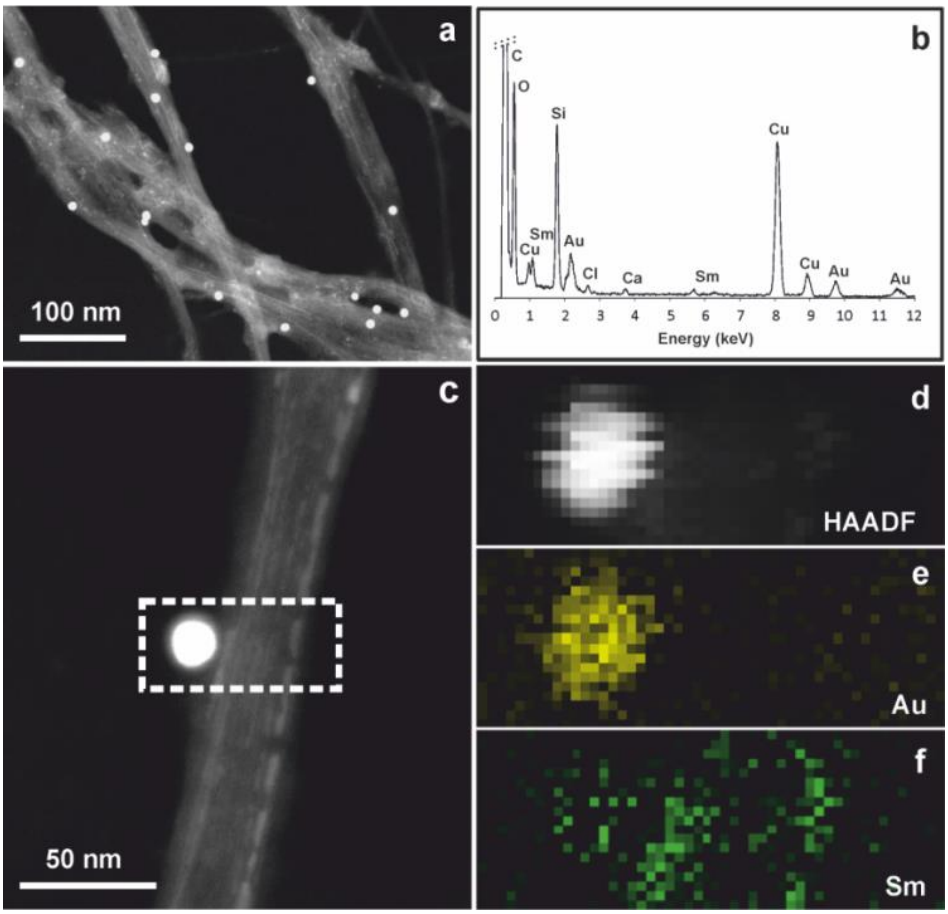

Figure 3.37 Analysis of the $SmCl_3$@SWCNTs-mAb conjugate; a) HAADF-STEM image of the conjugate after staining with an anti-human IgG/AuNPs, b) EDX analysis of the sample, c-f) HAADF-STEM-EDX mapping of the area of dotted square, d) HAADF-STEM image, e) Au EDX signal map and f) Sm EDX signal map.

This immunostaining experiment had the double goal of allowing visualisation of the Cetuximab attached to the nanotubes and to prove its ability to recognize a

specific antibody. The antibody-functionalized conjugate $SmCl_3$@SWCNT-mAb (**4a**) and the control complex $SmCl_3$@SWCNT/mAb (**5a**) were stained with an anti-human IgG linked with colloidal Au nanoparticles of 15 nm in diameter, able to recognize Cetuximab. The characterization of $SmCl_3$@SWCNT-mAb (4a) stained with anti-human IgG was performed by EDX analysis (**b**) and EDX elemental mapping, confirming the presence of both Au and Sm, and their location in the analysed area (**d-e**). We could therefore proof that Cetuximab was efficiently immobilized on the Sm-filled SWCNTs and that its affinity toward an appropriate secondary antibody was preserved upon conjugation [322].

To sum up, $SmCl_3$-filled and functionalized single-walled carbon nanotubes were characterized by HAADF-STEM imaging, EDX spectroscopy and mapping. The visualization of the organic moieties was possible through the attachment of the heavy element tag, namely I-rich molecule. A secondary antibody conjugated with Au nanoparticles allowed to visualize the Cetuximab along the CNT walls. Additionally, TGA was done for all of the samples at each step of functionalization.

3.5 Functionalized carbon nanotubes interacting with cells

Functionalized CNTs are known to be able to translocate across the plasma membranes and enter cells either passively by direct translocation across membranes or actively via endocytosis [323]. This fact makes them potential drug delivery carriers. Even without the therapeutic cargo, amine functionalized SWCNTs have shown intrinsic therapeutic action in stroke prevention *in vivo* [324]. Moreover, the successful delivery of caspase-3 siRNA by MWCNTs-NH_3^+ was also demonstrated. The administration of that complex resulted in reduced neuronal damage and enhanced motor function recovery in rat stroke model [186]. In another study, the delivery of CpG oligonucleotide (short single-stranded

synthetic DNA molecule containing a cytosine triphosphate deoxynucleotide ("C") followed by a guanine triphosphate deoxynucleotide ("G"), both connected by phosphodiester link ("p")) to brain glioma was enhanced using SWCNTs in a single intracranial injection [325]. However, none of these studies used systemic administration where crossing the blood brain barrier (BBB) may constitute a major obstacle to brain delivery. Even though the CNTs have shown the ability to permeate through biological membranes with evidence of membrane sealing due to their unique needle like structure [326], no reports on their ability to cross the BBB *in vitro* or *in vivo* were reported in the literature prior to our investigation.

Therefore, in this part we will discuss the results of the investigation on the ability of amino-functionalized MWCNTs (MWCNTs-NH_3^+) to cross the Blood-Brain Barrier (BBB) *in vitro* using a co-culture BBB model comprising primary porcine brain endothelial cells (PBEC) and primary rat astrocytes, and *in vivo* following a systematic administration of radiolabelled [^{111}In]DTPA-MWCNTs into mice.

The purpose of this subchapter is to show the capabilities that electron microscopy has in the investigation on biological samples. The delicate nature of biological samples is often an issue for electron microscopy examination. The cells are composed of light elements, are soft and fragile; they have to be embedded in resin and fine cut using ultramicrotone to obtain a sample with appropriate thickness for transmission electron microscopy (below ~100 nm). The resin and the cell are both unstable (easily breakable) under high voltage electron bombardment and thus the need of using a low voltage beam for general imaging and localization of CNTs in the cells. For this purpose, we have applied low voltage STEM imaging in the SEM with the HAADF or BF detector at 15 kV. However, to obtain high resolution images of MWCNTs to confirm their integrity, the compromise between the stability and resolution had to be met. Consequently, especially important for the STEM/TEM investigations in the TEM was to maintain the equilibrium between the accelerating voltage (the higher it is, the better the resolution) and the sample stability (lower voltage preferred). The compromise was

found for 120 kV beam acceleration voltage and low dose practice, where the beam is spread in order to provide lower dose to the imaged area.

The synthesis of the functionalized MWCNTs was as follows. First, pristine MWCNTs were functionalized by 1,3-dipolar cycloaddition as shown on **Figure 3.38**. The cycloaddition reaction was performed using Boc-protected amino acid and formaldehyde.

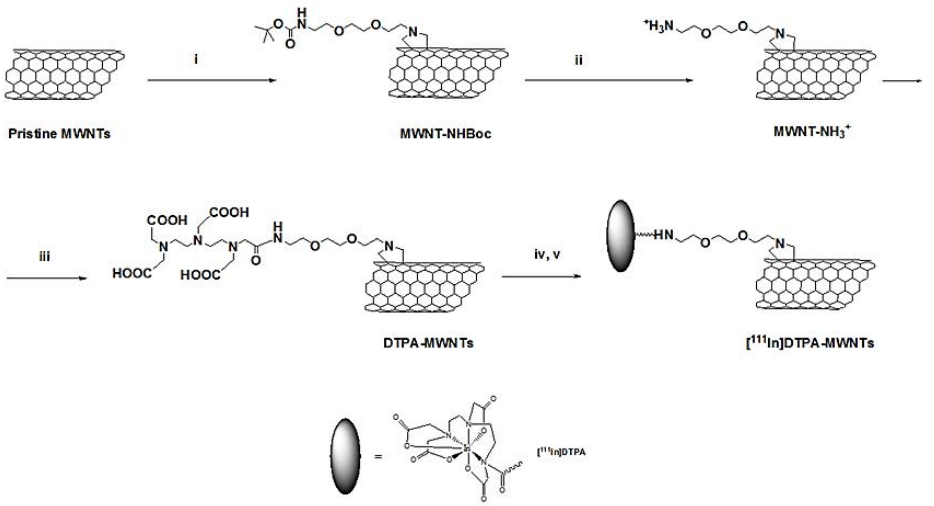

Figure 3.38 Synthesis of MWCNTs derivatives. (i) Boc-protected aminoacid $(CH_3)OCONH(CH_2CH_2O)_2$-$CH_2CH_2NHCH_2COOH$, HCHO, in DMF, 125 °C, 5 days. (ii) CF_3COOH in CH_2Cl_2, stirring, 24 h. (iii) DTPA, Et_3N in DMF, 60 °C, 48 h, N_2 atmosphere. (iv) $^{111}InCl_3$, at room temperature in 0.1 M ammonium acetate buffer (CH_3COONH_4) pH 5.5 for 30 min.

In the next step, the Boc-group was deprotected using acidic conditions yielding MWCNTs-NH_3^+. This construct was used in the *in vitro* studies on cell cultures for BBB crossing. After that, the ammonium groups of the MWCNT-NH_3^+ were neutralized using Et_3N to initiate the reaction with DTPA. DTPA-MWCNT constructs were radiolabelled with ^{111}Indium in the process of mixing with $^{111}InCl_3$ in a buffer solution of pH 5.5. These radiolabelled nanotubes were used for *in vivo* investigation of their biodistribution in mice.

In order to investigate the ability of f-MWCNTs to cross the PBEC monolayer, we used a co-culture BBB model of primary porcine endothelial cells and primary astrocytes. Co-culturing endothelial cells with astrocytes has previously been shown to improve the polarized BBB phenotype of brain endothelial cells in culture, especially important for complex processes such transcytosis [327, 328]. PBEC was allowed to form a monolayer on a porous polyester filter creating the main BBB interface that was supported by mediators released from primary astrocytes.

TEM imaging at 120 kV (**Figure 3.39 A**) showed the interaction of MWCNTs-NH_3^+ and the plasma membrane of the endothelial cells after 4 hours of incubation. It was shown the nanotubes were able to interact with the plasma membrane of PBEC and triggered the formation of lipid ruffles which initiated the endocytosis sequence to engulf MWCNTs-NH_3^+, as a first step of transcytosis.

Low-voltage (15 kV) BF/HAADF-STEM microscopy in the SEM after 24 h of incubation showed most of the MWCNTs-NH_3^+ were present within endoplasmic vesicles (EVs) and multi-vesicular bodies (MVBs) (**Figure 3.39 B** and **Figure 3.40**).

After 48 h of incubation, the release of the nanotubes from the cell was seen on the basal side of the chamber. The sealing of the membrane was confirmed by HRTEM imaging and is displayed on **Figure 3.40 A (iii)** and **B (iii)** where some of the MWCNTs-NH_3^+ appeared outside the cells with an intact plasma membrane indicating that the complete transcytosis of MWCNTs-NH_3^+ did not perturb the integrity of the plasma membrane.

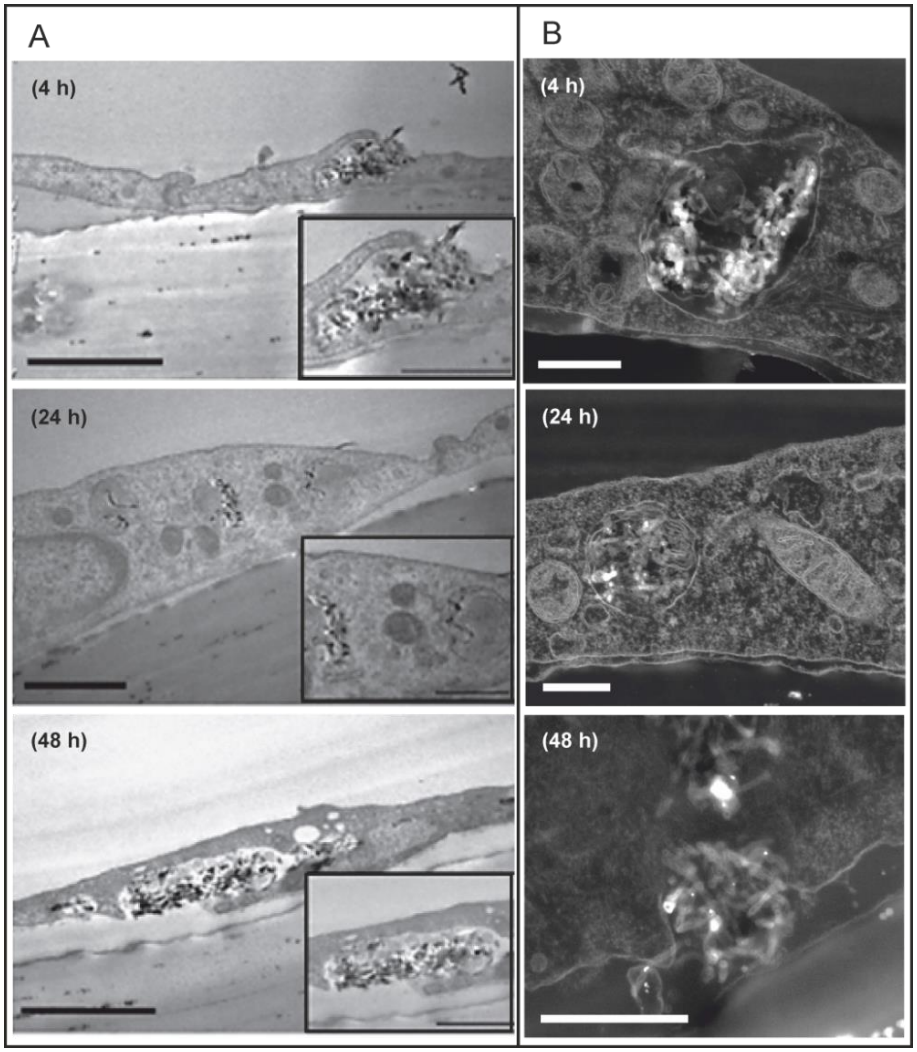

Figure 3.39 The transcytosis pattern of MWCNTs-NH_3^+ across PBEC monolayer following the incubation of MWCNTs-NH_3^+ with *in vitro* BBB model. MWCNTs-NH_3^+ were incubated with PBEC for (i) 4, (ii) 24 and (iii) 48 h. (A) Bright field TEM images of polyester filters showing the initial interaction of MWCNTs-NH_3^+ with PBEC. (B) Low voltage STEM (SEM) images of the polyester filter confirming the uptake and transcytosis of MWCNTs-NH_3^+ across PBEC monolayer. The scale bars are as follows: (A) 1 μm and 500 nm (insets); (B) 400 nm.

Further HRTEM imaging at 120 kV after 24 h confirmed that MWCNTs-NH_3^+ were on the basal side of PBEC or within partly opened vesicles facing the basal chamber (**Figure 3.40**). The intact tight junctions on micrographs suggested that the transcytosis of MWCNTs-NH_3^+ has no impact on BBB integrity. This is very important from the toxicological and drug delivery point of view as it shows the ability of MWCNTs-NH_3^+ to cross BBB *in vitro* without affecting the permeability and healthy function of the BBB.

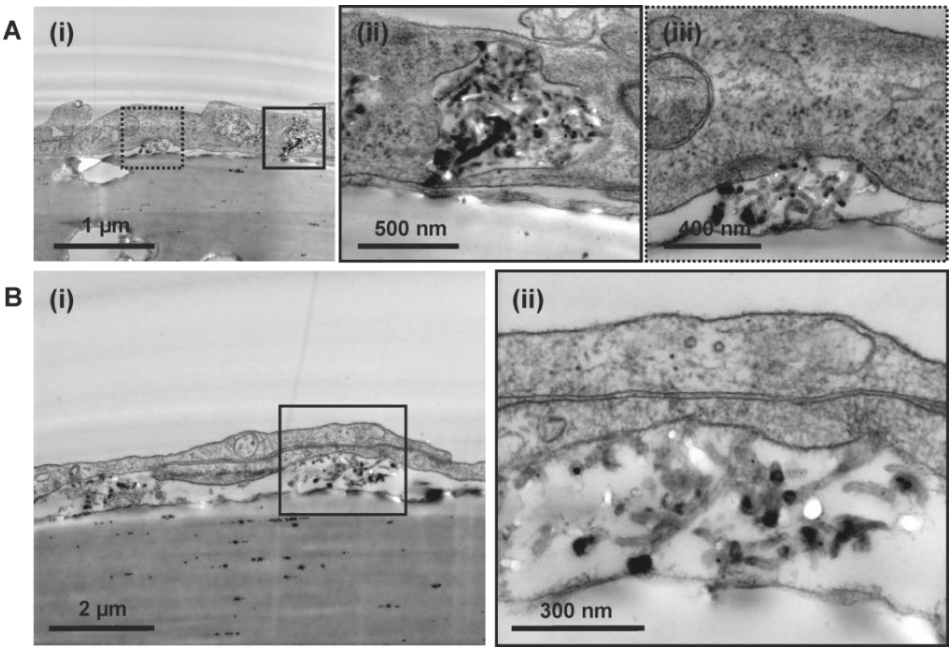

Figure 3.40 Mechanism of uptake of MWCNTs-NH_3^+ clusters across the PBEC monolayer. (A i-iii) Electron micrographs showing evidence of membrane fusion of the MWCNTs-NH_3^+-containing vesicles with the abluminal plasma membrane (solid square). Also, the images show a cluster of MWCNTs-NH_3^+ outside PBEC in the basal chamber, which appeared to have translocated across the PBEC monolayer after 24 hours of incubation (dashed square) (B i-ii) Electron micrographs providing further evidence on the complete translocation of MWCNTs-NH_3^+ across the *in vitro* BBB model. The MWCNTs-NH_3^+ appeared on the basal side of endothelial cells after 24 hours of incubation.

The stability of the structure of amino-functionalized carbon nanotubes following uptake was studied by HRTEM at 120 kV coupled with EELS spectroscopy (**Figure 3.41**).

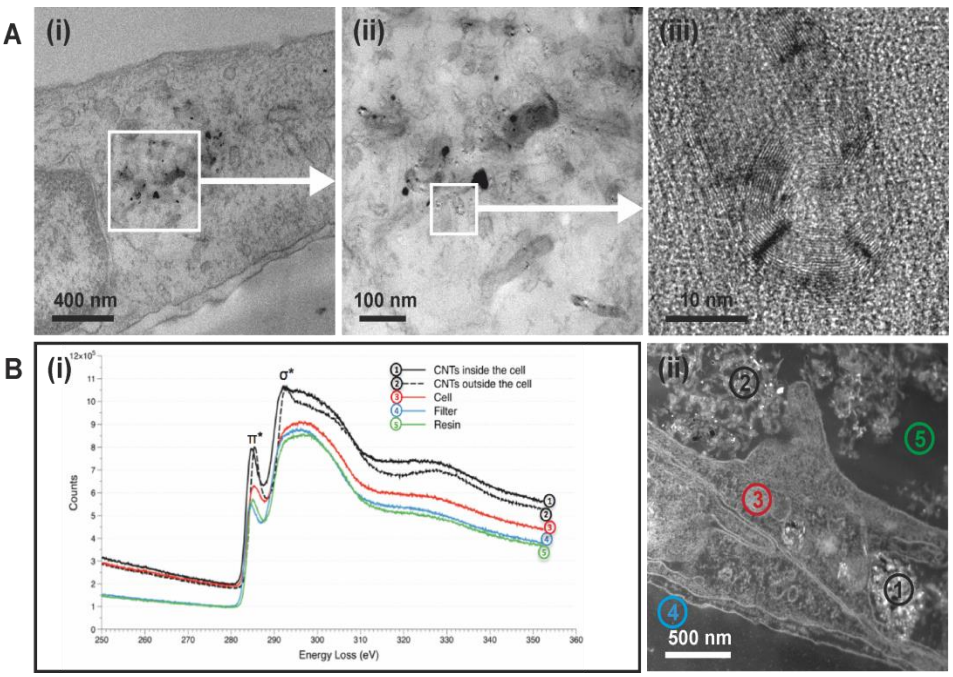

Figure 3.41 Integrity of the graphitic structure of MWNTs-NH_3^+ following uptake into endothelial cells. (A) HRTEM imaging showing the multi-walled structure of the MWCNTs-NH_3^+ was preserved. (B) Electron energy loss spectroscopy of MWNTs-NH_3^+ within and outside the endothelial cells. The HAADF-STEM image showed the measured points that included (1) MWCNTs-NH_3^+ within the cells, (2) MWCNTs-NH_3^+ outside the cells, (3) cell body, (4) polyester filter (used to grow cell on) and (5) the resin.

Indeed, HRTEM was able to confirm the integrity preservation of the MWCNTs-NH_3^+ within the cells, and therefore reflect the stability of these nanostructures against hydrolysing enzymes. The evaluation of the integrity of carbon nanotube constructs was done by measuring of the interlayer spacing between the walls on HRTEM micrograph (**Figure 3.41 A iii**) which gave a value of 0.34 nm, fitting

perfectly to the interlayer spacing of graphene layers in CNTs. Moreover, the analysis of carbon transitions of different points in the sample by EELS (**Figure 3.41 i, ii**) confirmed the graphitic structure of the MWCNTs-NH_3^+ as compared to amorphous carbon detected in the cell body, resin or filters. The relative intensity of the π^* peak from the MWCNTs-NH_3^+ (points 1 and 2) was higher than the signals of the cell, filter or resin (points 3, 4 and 5). More importantly, the MWCNTs spectra (points 1 and 2) showed a sharp σ^* peak, characteristic of graphitic material, which confirms the stability of the MWCNTs within the endothelial cells.

One of the advantages of using MWCNTs-NH_3^+ as nanocarriers is their ability to cross biological membranes. The needle shape, yet flexible structure allows them to cross plasma membranes without utilizing the cellular endocytic processes. Many studies have established the ability of MWNTs-NH_3^+ to cross biological membranes by direct translocation but none have explored BBB endothelial cells. During our investigation, low voltage STEM in the SEM revealed that small number of individual MWCNT-NH_3^+ were able to pierce the plasma membrane, and appeared to be crossing the membrane without any sign of membrane invagination (**Figure 3.42**).

The ability to move freely within the brain endothelial cells by crossing cellular membranes provides an unique internalization route for MWCNTs-NH_3^+ to evade the conventional transcytosis mechanisms used by other nanocarriers. This would be advantageous from a drug delivery point of view.

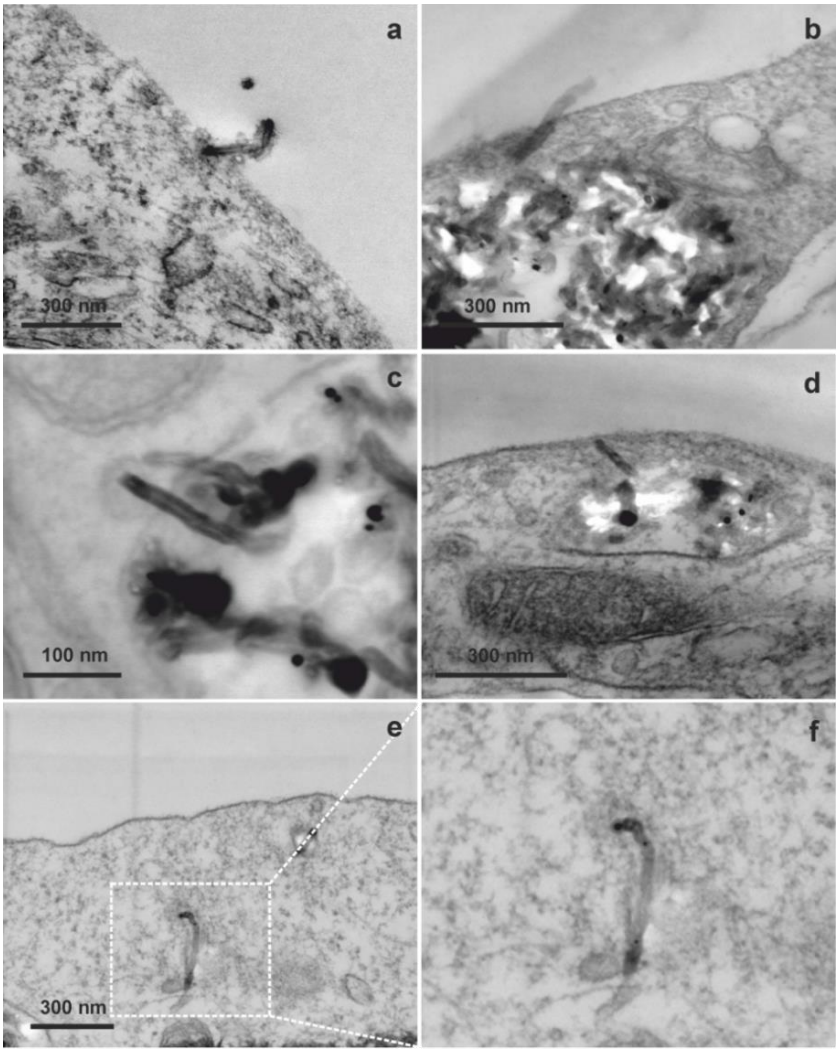

Figure 3.42 Translocation of individual MWCNTs-NH_3^+ across the PBEC membrane. Low voltage BF-STEM (15 kV): (a, b) single MWCNTs-NH_3^+ crossing the plasma membrane, (c, d) the transport of individual MWCNTs-NH_3^+ within the cell and (e, f) another single nanotube crossing the cell.

As showed before the entry of MWNTs-NH_3^+ into PBEC monolayer occurred mostly via vesicular uptake with the nanotube clusters being transported to the basal side of endothelial cell at 37 °C, temperature close to the human body temperature. However, we have also examined the effect of the temperature on the

transcytosis, incubating MWCNTs-NH_3^+ with cells at 4 ˚C during 4 h with the aim of inhibiting the energy-dependent route of uptake. Low voltage STEM imaging in the SEM confirmed that incubating the cells with nanotubes at low temperature (4 ˚C) resulted in the inhibition of vesicular uptake (**Figure 3.43**).

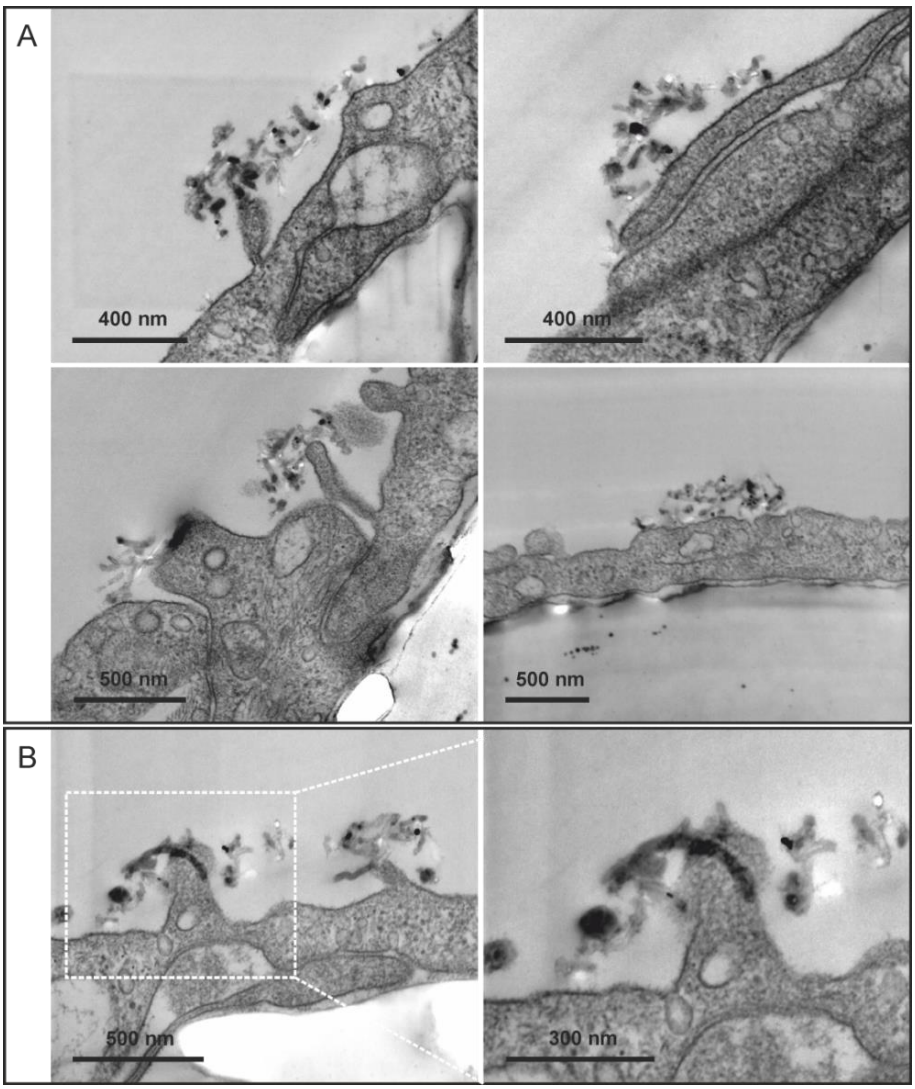

Figure 3.43 Inhibition of MWCNTs-NH_3^+ uptake into endothelial cells following the incubation at 4 ˚C for 4h. Low voltage bright field STEM images show (A) the

accumulation of MWCNTs-NH_3^+ outside the endothelial cells and (B) shows individual MWCNTs-NH_3^+ interacting with the endothelial extension.

At 4 °C the MWCNTs-NH_3^+ were not able to cross the membrane as vesicle formation was inhibited. This observation provides further evidence that the uptake of our structure is dependent on endocytosis mechanism. However, the MWCNTs-NH_3^+ clusters that were unable to enter the cell were observed at adjacent sites at the endothelial tight junctions showing some level of interaction with cellular extensions. Although no vesicular uptake was observed at 4 °C, few individual nanotubes were able to pierce the plasma membrane and thus the piercing mechanism seems to be energy-independent.

After the *in vitro* studies, the ability of [^{111}In]DTPA-MWCNTs to accumulate in mouse brain after systemic administration *in vivo* was studied using gamma counting. First, [^{111}In]DTPA-MWCNTs were injected into mice via intravenous administration and then the biodistribution in the major organs was monitored at specific time points (**Figure 3.44**). Mice were injected with [^{111}In]DTPA-MWCNTs (50 mg, 0.5 MBq) via the tail vein. At each time point (5 min, 30 min, 1 h, 4 h and 24 h) whole body perfusion with heparinized saline was performed and major organs were harvested for quantitative measurements of radioactivity by g-scintigraphy.

Figure 3.44 shows the biodistribution profile of [^{111}In]DTPA-MWCNTs in the major organs and in the blood. It is clearly visible the nanotubes accumulated mainly in lungs (26.5 ± 3.9 % ID) and liver (18.8 ± 0.7 % ID) 5 min after injection. The level of [^{111}In]DTPA-MWCNTs remained relatively high in the lung and liver after 24 h. The blood profile showed that 14.4 ± 0.4 % ID of nanotubes were circulating in the blood after 5 min, this level decreased over time to reach 1.3 ± 0.3 % ID after 24 h.

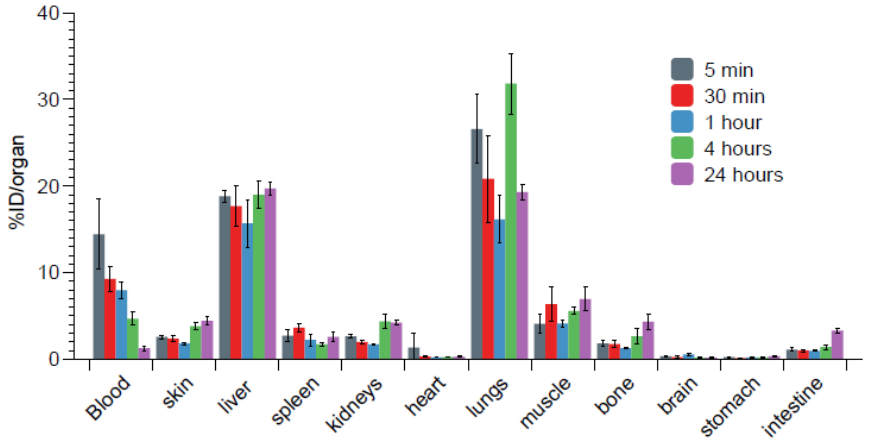

Figure 3.44 The accumulation of [^{111}In]DTPA-MWCNTs in the major organs at different time points.

Results presented here are the first evidence of f-MWCNTs translocation through BBB in an *in vitro* model. Additionally, the significant reduction in the transport of nanotubes across BBB at 4 ˚C confirmed that the uptake was driven by energy-dependant pathway.

3.6 Filled and functionalized carbon nanotubes interacting with cells

In the field of *in situ* imaging of biological tissues, X-ray fluorescence (XRF) [329] mapping permits observation of elemental distributions in a multichannel manner. However, this technique is not commonly used mostly due to the difficulties found in the interpretation of maps without an underlying cellular blueprint. To overcome this obstacle, the implementation of suitable contrast agents is desired. Since carbon nanotubes have large filling capacity and are easily functionalized with wide range of materials, they are ideal candidates to serve as a platform for creating such contrast agents. Besides their imaging capability, they may serve as targeting carriers.

XRF results from energy released when outer sphere electrons fall into holes in core atomic orbitals caused by ionization by lower energy end of hard X-ray radiation (**Figure 3.45**), from 2 – 20 keV [329].

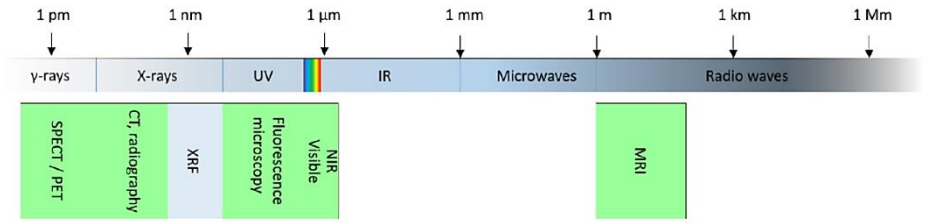

Figure 3.45 Use of the electromagnetic spectrum in medical/biological imaging.

Based on the suitable emission energies for biological use, barium ($L\alpha_1$ = 4.5 keV), lead ($L\alpha_1$ = 10.5 keV) and krypton ($L\alpha_1$ = 12.6 keV) were selected in our investigation as ideal candidates. Nevertheless, their global toxicity (Pb), neurotoxicity (Ba) and gaseous state (Kr) would ordinarily prohibit their use. Thus, their encapsulation into carbon nanotubes was performed providing sealed nanocapsules from where nothing larger than a proton can escape. As a result, any toxicity or other biological activity of the XRF tag elements is neutralized. Simultaneously, any loss, leaching or degradation of the encapsulated material is prevented [128]. Additionally, these filled CNTs were externally decorated with peptides to provide affinity for sub-cellular targets (**Figure 3.46**).

The synthetic strategy for filling of SWCNTs with BaI_2 and PbO was based on molten phase capillary wetting (technique described before in this chapter). In the case of gaseous Kr the strategy consisted in sealing SWCNTs into a silica ampoule under approximately atmospheric pressure of Kr, and then heating it up to 700 ˚C. In the process of slow cooling down the ends of the nanotubes were sealed, trapping the Kr gas in the interior cavities. Successful closing of the nanotubes tips was confirmed by HRTEM imaging as showed on **Figure 3.47 (a)** for Kr@SWCNTs. Furthermore, HAADF-STEM micrographs confirmed the positive filling of PbO and BaI_2 into SWCNTs. As required for biological use, prior to the

formation of nanocapsules, the SWCNTs were purified and shortened by steam method (process described before in this chapter), resulting in 400 – 450 nm long nanotubes. The as-filled SWCNTs were washed from the external residue to provide "clean" sidewalls.

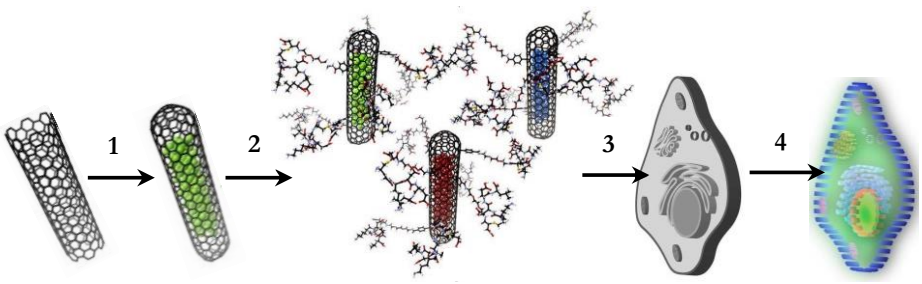

Figure 3.46 Design of XRF - contrast carrier systems to probe cellular organelles through XRF mapping: 1 – filling of SWCNT with elemental tags and sealing the ends; 2 – attaching targeting peptides; 3 – cellular uptake; 4 – XRF imaging (map of cellular features).

On **Figure 3.47 a** HAADF-STEM images show bright lines following the shape of carbon nanotubes and thus indicating filling with high Z species for PbO@SWCNT and BaI_2@SWCNT. Although the low density of Kr gas prevented observation of Kr in Kr@SWCNT in this way, the sealing of the nanocapsule ends was nonetheless confirmed in bright-field imaging (HRTEM). The difficulty of observing Kr by conventional methods, including TEM, is due to the low density of gases (~1000 times lower than for condensed phases). Nevertheless, Kr has provided a suitable signal in the XRF experiment, confirming its presence in the interior cavities of CNTs (**Figure 3.47 b**).

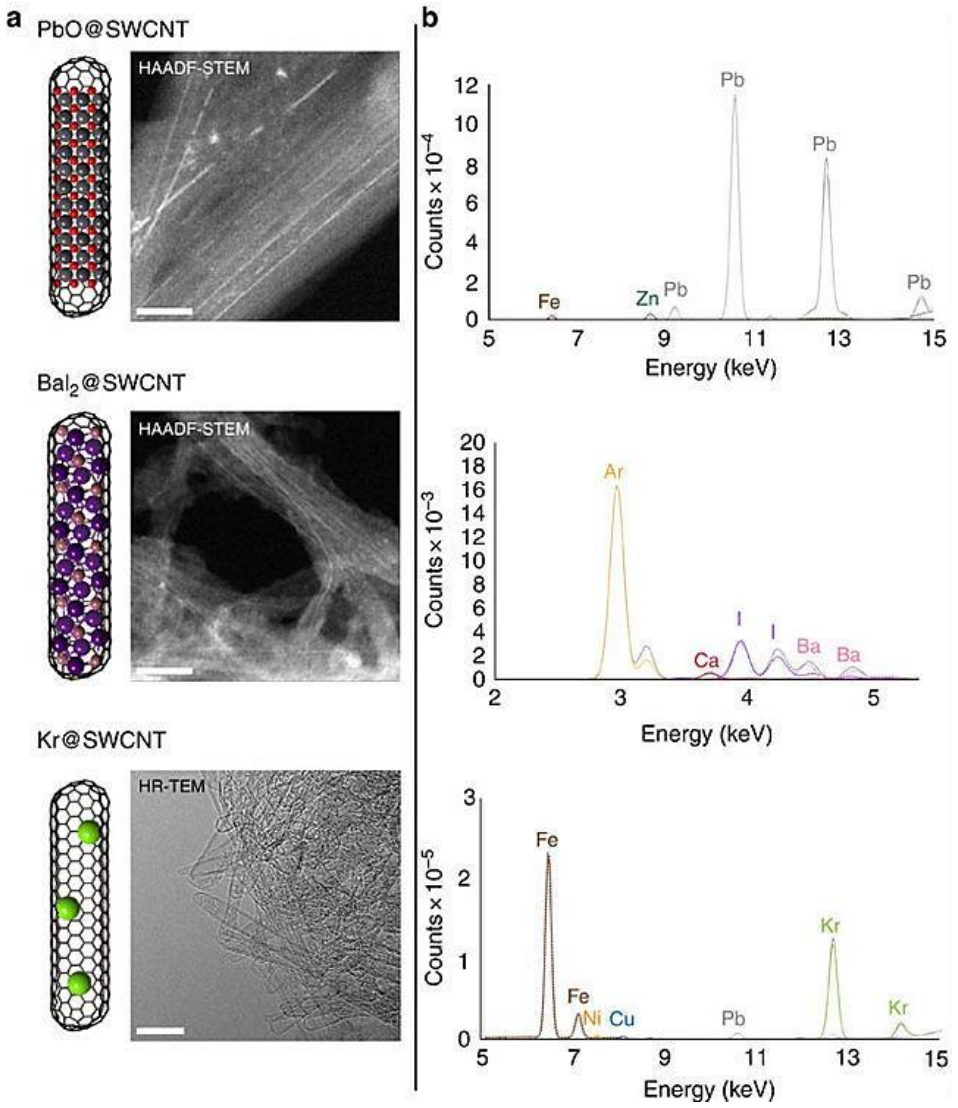

Figure 3.47 Characterization of filled SWCNTs and functionalization with targeting peptides. (a) TEM characterization of filled SWCNTs (scale bars, 10 nm). (b) XRF spectra of the filled tubes recorded using synchrotron radiation at excitation energies of 16, 6 and 15 keV for PbO, BaI_2 and Kr fillings, respectively, confirm the utility of not only Pb and Ba but also, strikingly, Kr.

Moreover, X-Ray Absorption (XAS) spectrum was acquired at synchrotron facility, which provided high signal-to-noise ratio for Kr signal, and ensured the encapsulation and preservation of the gas inside SWCNTs (**Figure 3.48**).

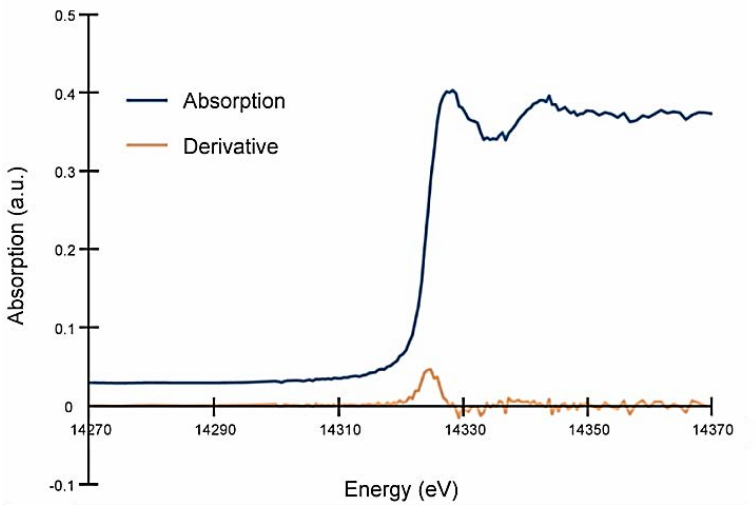

Figure 3.48 X-ray absorption edge of Kr enclosed in SWCNTs, measured using synchrotron radiation, confirming the elemental assignment. Measured: 14.325 keV, expected: 14.3256 keV.

In the last step of creating CNTs – based cellular imaging agents, the peptides were attached to the external walls by covalent bonding. The peptides were selected to be representative for specific cells allowing mapping of the trafficking of these agents at differing penetration depths into cells: RGD (Arg-Gly-Asp, cell surface adhesion), KDEL (Lys-Asp-Glu-Leu, endoplasmic reticulum (ER) targeting) and two nuclear localization sequences (NLSs) taken from the SV40 virus and the human protein IL-1α. A generalized bifunctional spacer was designed and synthesized to ensure sufficient functional accessibility of peptides to corresponding cellular receptors. This was attached to the side-walls of the filled SWCNTs through the selective reaction of the aniline-moiety terminus of the spacer as its diazonium [139], giving a usefully stable C – C linkage that leaves the opposite terminus of the linker free for further reaction [330].

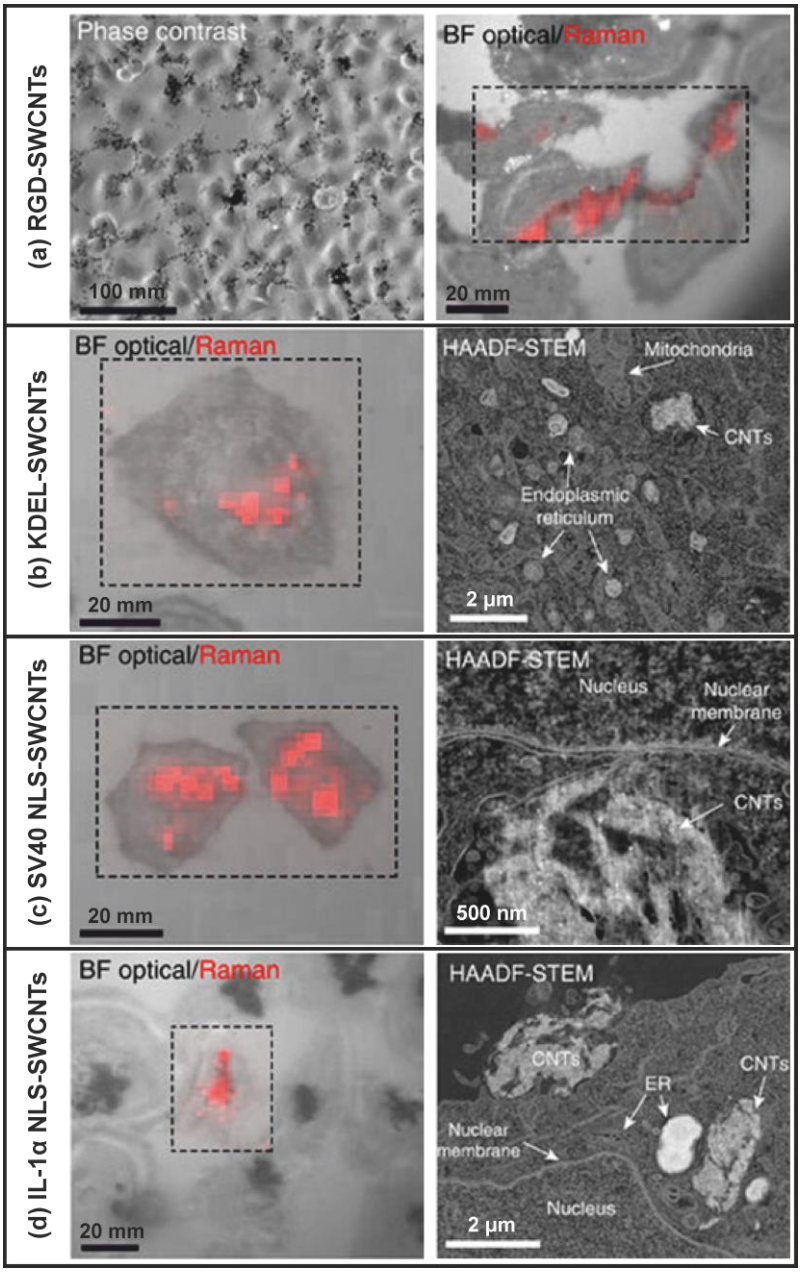

Figure 3.49 Intracellular tracking of peptide-functionalized SWCNT nanobottles. Maps of the SWCNT Raman G-band (1500–1650 cm^{-1}) were recorded within the dashed boxes. (a) RGD-functionalized SWNTs interacting with HeLa cells imaged by phase contrast, and bright-field microscopy with Raman mapping. (b) KDEL-

functionalized SWCNTs inside HeLa cells imaged by bright-field microscopy with Raman mapping and HAADF-STEM. (c) SV40 NLS-functionalized SWCNTs inside HeLa cells imaged by bright-field microscopy with Raman mapping and HAADF-STEM. (d) IL-1a NLS-functionalized SWCNTs inside HeLa cells imaged by bright-field microscopy with Raman mapping and HAADF-STEM.

The dynamic, cellular distribution of the prepared XRF contrast agents was monitored using dual modes of combined, simultaneous optical and Raman microscopy over a period of 24 h. Small aggregates of SWCNTs manifested as optically opaque regions aligned with high G-band Raman intensity (1,500 – 1,650 cm^{-1}) (**Figure 3.49**). With the use of SEM imaging in transmission mode (HAADF-STEM) the observations on the intracellularly targeted SWCNTs at higher magnification were conducted (**Figure 3.49** right-handed column, except for **a**). In all of the cases the aggregates of SWCNTs are visible on the micrographs as high contrast regions of fibrous texture in the cell regions consistent with Raman/optical results. Now we will discuss left-handed column of **Figure 3.49**. Consequently, in (**a**) SWCNTs are seen to follow the cell outline contours, consistent with the binding of RGD to cell-surface integrins. In (**b**) Raman mapping shows SWCNTs within the cells at locations consistent with the ER. Also, HAADF-STEM found SWCNT bundles close to the ER, but could not unambiguously show association. In the case of (**c**) Raman mapping showed SWCNTs within the cells, overlapping with the nuclei. On the HAADF-STEM the interactions with the nuclear membrane are revealed, as expected for the association of the SV40 peptide with the nuclear pore. Nuclear localization is clearly visible in (**d**) for the Raman maps. Additionally, HAADF-STEM uncovered cellular uptake of the SWCNTs and their trafficking towards the nucleus.

The observations of CNTs in the cells were confirmed by EELS spectroscopy, which revealed characteristic graphitic carbon peaks at ~292 eV (**Figure 3.50**).

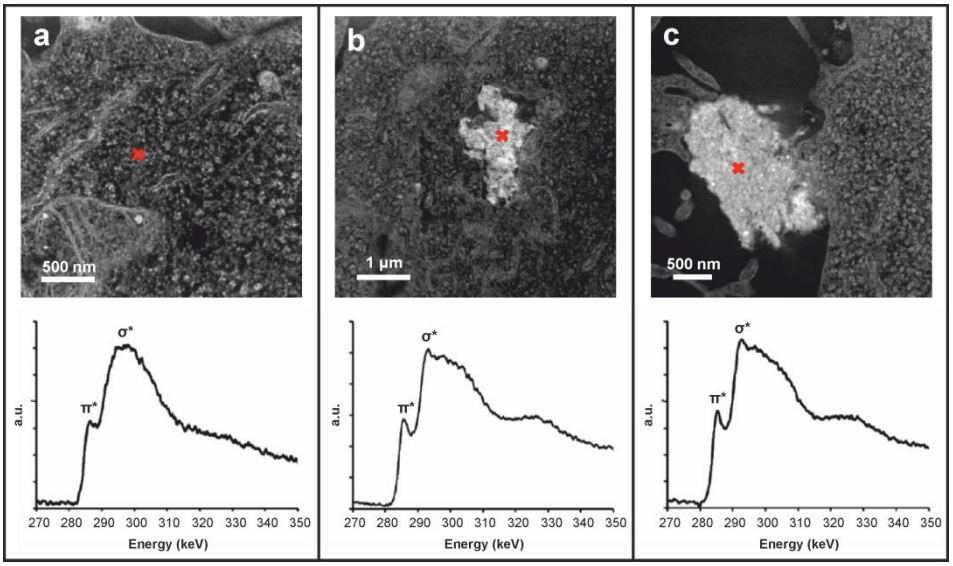

Figure 3.50 Carbon K-edge Electron Energy Loss spectrum (EELS) of the cells (left) SWCNT bundles inside (centre) and outside (right) cells.

The main features present on EELS spectra of **Figure 3.50** (**a-c**) are two peaks: a peak at 285 eV representing 1s to π* transition and a broad band at 290 – 310 eV representing σ*, both characteristic of amorphous carbon [331]. However, the fine structure of the σ* band, and in particular the sharp peak at 293 eV on (**b)** and (**c)**, is indicative of graphitic carbon [332]. The SWCNT bundles (**b, c**) can be visually recognised by their high contrast, fibrous texture, bright spots (iron nanoparticle impurities), and 'smearing' due to resistance to the microtome. In contrast to that on **a,** the lack of sharp peak in σ* band indicates the amorphous nature of the cell.

With the key aspects of cellular trafficking both confirmed and revealed using the peptide-functionalized nanocapsules, they were tested as designed XRF-contrast agents in the 'mapping' of a tissue-like cellular array in a proof of principle study (**Figure 3.51**). An X-ray excitation energy of 10 keV was sufficient to excite the 'Ba + I nanocapsule contents, as well as the biologically present elements, but for the Kr and Pb nanocapsules maps were compiled at 15 and 14 keV, respectively with

additional scans at 5 keV to provide adequate signal for the lower-Z biologically abundant elements.

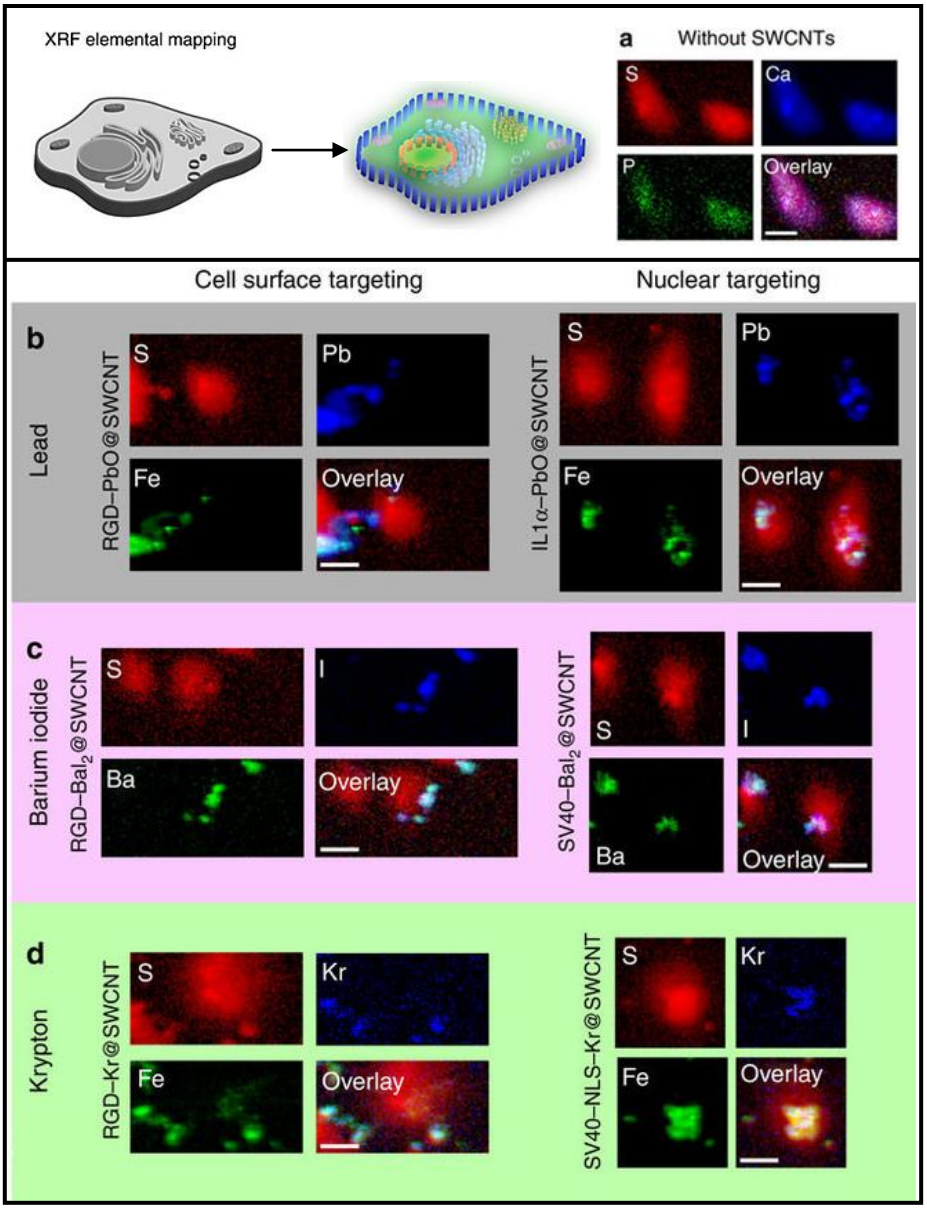

Figure 3.51 Use of filled and decorated SWCNTs as biological XRF contrast agents. (a) Elemental distribution maps of untreated HeLa cells. (b) XRF maps of cells treated with Pb@SWCNT-based contrast agents. (c) XRF maps of cells treated

with BaI_2@SWCNT-based contrast agents. (d) XRF maps of cells treated with Kr@SWCNT-based contrast agents. Scale bars are 20 mm.

Maps of untreated cells (**Figure 3.51 a**) showed the presence of biotic elements such as P, S and Cl. Of these, the best contrast was obtained for S, and hence the S map was chosen as a marker of the cell outline, which can be used to assess the location of the filled SWCNTs relative to the cell. Small levels of iron impurities are ubiquitous in SWCNTs, and advantageously could be used here as an additional co-localization marker of SWCNT positions [333] (for example, in green channel in **Figure 3.51 b, d**). Excitingly, the XRF maps of treated cells, through the unique elemental contents of the nanocapsules, revealed modes of uptake and trafficking consistent with those observed by optical, Raman, and electron microscopy imaging detailed above. Consequently, on **Figure 3.51**, three biologically relevant channels are presented to show the cell features. Sulphur was chosen as the best maker of cell morphology (**a**). Fe channel is included as a marker of SWCNT location, and correlates with Pb, showing the lack of escape of Pb from the SWCNTs (**b**). Colocation of Ba and I confirms secure encapsulation of the elements (**c**). Fe channel is included as a marker of SWCNT location, and correlates with Kr, showing the lack of escape of Kr from the SWCNTs (**d**).

In summary, three nanocapsules consisting of encapsulated salts of BaI_2 and PbO, and Kr gas into SWCNTs, which external walls were additionally functionalized with peptides, were created for XRF imaging of cells. The structures were characterized by electron microscopy imaging in STEM and HRTEM mode for the confirmation of successful encapsulation and closing of the ends. The Raman/optical imaging showed the distribution of nanocapsules in the cells. Furthermore, EELS spectroscopy confirmed the localization of CNTs inside the cells. Additionally, as a proof of concept they were used for XRF imaging resulting in expected distribution inside the cells.

3.7 Conclusions

In this chapter, we have introduced the sequence of preparation and characterization of functional carbon nanotubes for targeted delivery of radioactivity and/or imaging based on carbon nanotubes. All of the important steps and characterization techniques were described for each stage.

First of all, the purification and shortening of CNTs based on clean high temperature steam method was described. The optimization of the characterization methods for length distribution, purification and the integrity of CNTs was discussed. As-prepared, clean and shortened SW- and MW-CNTs (biologically compatible), were ready for further endo- and exo- functionalization.

Encapsulation of suitable inorganic salts into SWCNT and MWCNTs was discussed and included potentially radioactivable salts such as: $LuCl_3$, LuI_3, $SmCl_3$, $EuCl_3$, NaI, KI, CuI, CuBr, ZnI_2, CeI_3, $CeCl_3$, PbI_2 and $GdCl_3$. Filling yield, crystalline structure and possible forms were mainly assessed by HRTEM, STEM, EDX and TGA techniques.

Following that, the external functionalization with organic moieties was described. The addition of heavy elemental tags, such as Gd enabled the electron microscopy investigation of functionalization through Z-contrast imaging in HAADF-STEM mode. EDX spectroscopy provided for additional proof of functionalization of this kind. Two parallel constructs were created, Gd-DTPA-MWCNT-1 and Gd-DTPA-MWCNT-2. Both were proven as efficient MRI contrast agents.

Then, the simultaneous endo- and exo-functionalization of CNTs was reported. Few examples were related, the $SmCl_3$- filled SWCNTs functionalized with I-rich organic molecules and Au NPs, and the $GdCl_3$- and $SmCl_3$- filled MWCNTs, functionalized with N-rich linker. Iodine as relatively heavy element permitted for HAADF-STEM visualization of molecules in $SmCl_3$@SWCNTs, while nitrogen

was detected through EDX elemental analysis in $GdCl_3$@MWCNTs and $SmCl_3$@MWCNTs samples.

Additionally, we have studied the translocation capabilities of functionalized MWCNTs through blood-brain barrier (BBB) in an *in vitro* model. The first evidence of such translocation was given based on low voltage transmission electron microscopy. Furthermore, sealing of the cell membrane and the integrity of CNTs was confirmed through HRTEM imaging. Significant reduction in the transport of nanotubes across BBB at 4 °C was concluded and indicated an energy-dependant pathway of CNTs uptake.

In the last part of this chapter, three nanocapsules (PbO@SWCNTs, BaI_2@SWCNTs, Kr@SWCNTs) were presented. External walls of these filled-SWCNTs were functionalized with peptides and tested for XRF imaging of cells. All of the structures were characterized by HRTEM and/or STEM imaging. Moreover, Raman combined with optical imaging was used for the studies on the distribution of nanobottles in the cells. EELS spectroscopy confirmed the localization of CNTs inside the cells. Finally, the nanocapsules resulted to act as efficient agents for XRF imaging.

PART II

SINGLE-LAYERED INORGANIC NANOTUBES SHAPED BY CARBON NANOTUBES

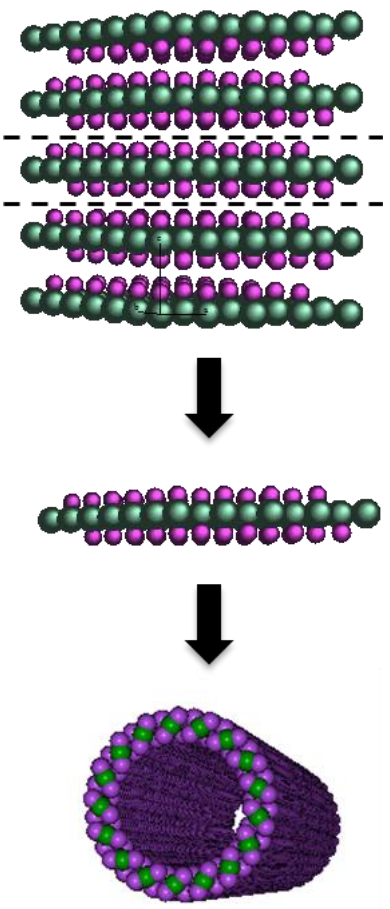

4 Sub-nanometer diameter single-layered lutetium halide nanotubes grown inside SWCNTs

In this chapter we present the formation and characterization of single-walled lutetium halide nanotubes of extremely low diameters encapsulated into single-walled carbon nanotubes.

$LuCl_3$@SWCNT

$LuBr_3$@SWCNT

LuI_3@SWCNT

4.1 Introduction

Recent advances in synthesis strategies have given rise to the formation of new low dimensional nanostructures [334-336]. Such nanomaterials are often characterized by novel and/or enhanced electrical, optical, magnetic, thermal, mechanical and/or chemical properties due to their high surface to volume ratio, frequently finding applications in technology and medicine [337, 338].

On one hand, carbon nanotubes [2] are often employed as template material for the formation of other nanostructures owing their internal cavity may be filled with a chosen payload and/or their external walls may be functionalized [339]. These functional carbon nanotube hybrids are studied for a wide variety of applications, from molecular electronics [340], to radiology [341], water confinement [342] and energy storage [343], just to mention some of them.

On the other hand, compounds with layered structures have strong in-plane bonding and weak out-of-plane interactions, which facilitate exfoliation of atomically thin two-dimensional layers. Wrapping seamlessly one layer into a cylinder results in a nanotube formation that combines characteristics of two-dimensional (2D) and one-dimensional (1D) nanomaterial. Although usually formation of multi-layered nanotubes is preferred [344], single-layered equivalents are also formed. Recently, single layer lead iodide nanotubes were reported to form in the interior cavities of multi-walled carbon nanotubes (MWCNTs) [345]. It was found that the diameter of the PbI_2 inorganic nanotube was merely dependent on the diameter of the CNT host, with a threshold at 3.5 nm, below which no PbI_2 nanotubes were found but only PbI_2 shaped as nanorods. Also, we have recently proved that other layered compounds can grow as single-layered nanotubes by using MWCNTs as templates for encapsulation of CeI_3, $CeCl_3$, $TbCl_3$ and ZnI_2, as discussed in section **1.2.1**. However, the use of SWCNTs for the template assisted growth of inorganic nanotubes has not been reported to date.

Due to their small internal cavity, single-walled carbon nanotubes [346] are perfect candidates to act as a template for the formation of narrow inorganic nanotubes. To explore this, we decided to encapsulate lutetium trihalides (LuX_3, X = Cl, Br, I), known to have a layered structure in the bulk, inside SWCNTs.

As a long half-life β-emitter, ^{177}Lutetium finds biomedical applications in radiopharmaceutical industry with its main use in the treatment of neuroendocrine tumors, but similarly studied for the treatment of other tumors, such as bone, colon, ovarian or prostate cancers [276, 347, 348]. The encapsulation and sealing of lutetium inside carbon nanotubes could possibly avoid the whole body exposure to Lu. Moreover, additional functionalization with biologically active molecules could provide targetable and biocompatible nanocapsules.

Besides their biomedical utility, lutetium halides, as other trivalent lanthanide trihalides, are used as scintillators and laser crystals owing their wide optical gaps of around 6 eV, 5 eV and 4 eV for $LuCl_3$, $LuBr_3$ and LuI_3, respectively [349]. The band gaps of layered materials may undergo a significant change when transferred from bulk to a monolayer [350]. Furthermore, a single layer rolled up into a tube inside a carbon nanotube will suffer a significant strain which may lead to the further band gap modification, especially due to the Van der Waals interaction between carbon and lutetium halide layers. Therefore, the synthesis of narrow diameters single-layered LuX_3 nanotubes is expected to result in a modulation of the optical properties of these materials.

The main drive for this work was to explore the formation of LuX_3 nanotubes into SWCNTs. Additionally, by keeping the cation but changing the halide (Cl, Br, I) we intended to get further insights on the role of the anion size for obtaining of these type of nanostructures.

4.2 Results and discussion

4.2.1 Synthesis of LuX_3@SWCNTs hybrids

LuX_3@SWCNTs hybrids were prepared by molten phase capillary wetting. Elicarb® SWCNTs (Thomas Swan & Co. Ltd) used in these studies were produced by chemical vapor deposition. As-received material contained iron catalyst coated with graphitic shells. Thus prior to the encapsulation experiments, SWCNTs were purified by steam treatment (4 h) and subsequent HCl washing following a previously reported protocol [36]. Then, as-purified SWCNTs were filled with three lutetium halides: $LuCl_3$, $LuBr_3$ and LuI_3 (anhydrous 99.9% purity, Sigma Aldrich). First, CNTs were mixed with the chosen payload in w/w ratio 1:10 and ground together in an argon-filled glovebox. The mixture was sealed under vacuum inside a silica tube. Then, samples were annealed in a horizontal furnace during 12 h. They were dwelled at different temperatures above their respective melting points, depending on selected payload: 960 °C, 1050 °C and 1100 °C for $LuCl_3$ ($T_{melting}$ = 905 °C), $LuBr_3$ ($T_{melting}$ = 1025 °C) and LuI_3 ($T_{melting}$ = 1050 °C), respectively. The excess of non-encapsulated material was removed by washing the samples with hot water (~80 °C).

4.2.2 Electron microscopy imaging and spectroscopy

Formation of LuX_3 nanotubes was first assessed by HRTEM and HAADF-STEM imaging on the FEI Tecnai F20 microscope at 200 kV. Representative low magnification STEM images of the samples are shown in the first row on **Figure 4.1.** Higher magnification images were acquired for better visualization of nanotubular structures (second row). Additionally, EDX spectra of bulk samples were acquired by coupled EDAX spectrometer for each hybrid material in HRTEM mode (third row).

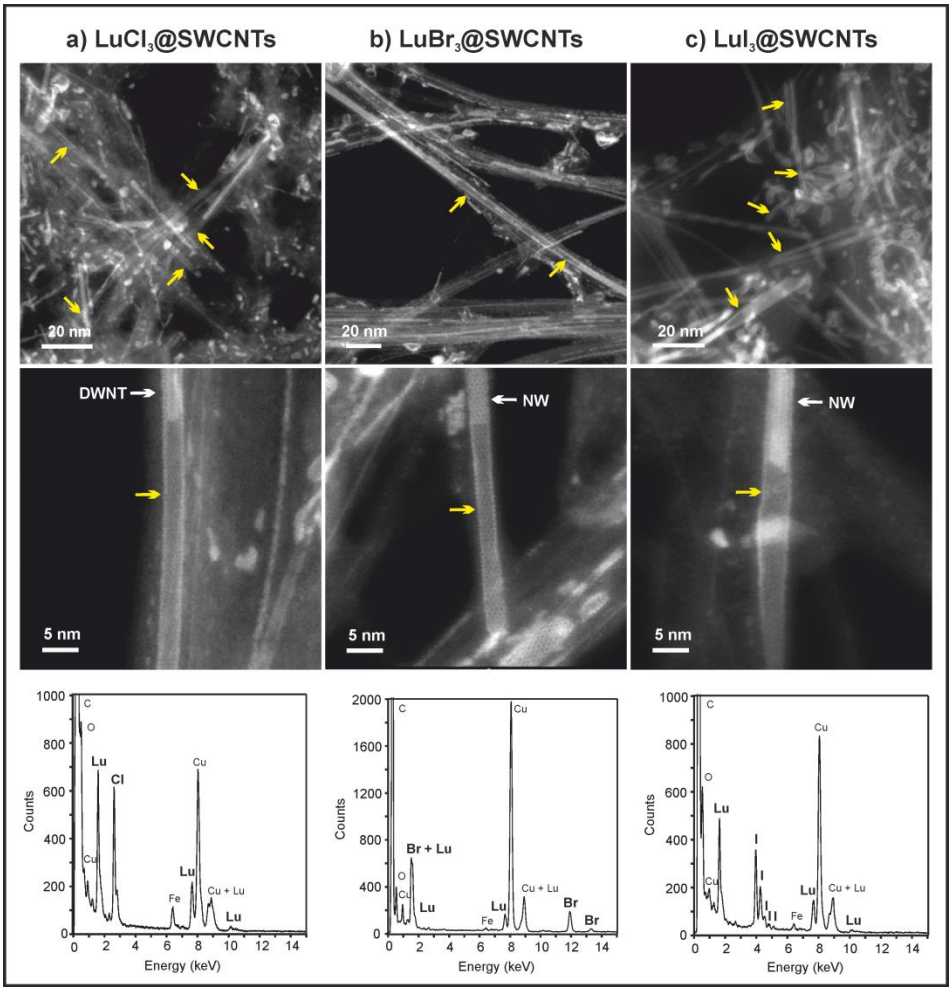

Figure 4.1 Low magnification HAADF-STEM imaging of LuX_3@SWCNT hybrids (first row), higher magnification micrographs (second row) and EDX spectra for each sample (third row). *Yellow arrows point to some of the inorganic nanotube structures, white arrows point to other structures, such double-walled NT (DWNT) and nanowire (NW).

In HAADF-STEM mode, high atomic number of lutetium makes it appear much brighter than carbon. As opposed to that, due to low atomic number of carbon, CNTs walls are usually hardly visible on the micrographs. Furthermore, LuX_3 filled in SWCNTs either in form of nanowires (NWs) or nanotubes (NTs) can be easily

appreciated on **Figure 4.1** (first and second row). Graphitic walls surrounding the payload are visible as gray halo around them. It should be noted that on the micrographs where the edges of the payload (LuX_3) are brighter than the interior a structure of tubular nature is present (some of them are indicated by yellow arrows). However, many nanowires are also present characterized by no contrast change through the hybrid diameter. The difference between NT and NW formation is clearly seen in the second row of **Figure 4.1** where a transition of NW to NT occurs for $LuBr_3$ and LuI_3. In the case of $LuCl_3$, the transition goes from double-layer nanotube to single-layer nanotube. In each column of the same figure, EDX spectrum (third row) is displayed for each corresponding compound. EDX elemental analyses confirmed the presence of carbon, lutetium and corresponding halide, (X = Cl, Br or I). Fe signal arises from the residual iron catalyst not removed during the purification step, whereas the Cu signal is related to the TEM support grid.

As already mentioned above, not only nanotubes of lutetium halides were formed inside CNTs but formation of nanowires was also observed. It was found that, of all filled CNTs, the LuX_3 crystallized as nanotubes (NTs) within: 19% in the case of $LuCl_3$, 24% for $LuBr_3$ and 22% for LuI_3 being the rest filled with nanowires (NWs), this is 81 % for $LuCl_3$, 76 % for $LuBr_3$ and 78 % for LuI_3. Statistical analyses of the diameter distribution of both forms (NT and NW) for all of the samples ($LuCl_3$, $LuBr_3$ and LuI_3) were performed based on electron micrographs. These results are displayed graphically on **Figure 4.2**. On the same figure, example images of nanotubes and nanowires of the payloads with exceptionally narrow diameters are displayed. Yet, there are two ways of measuring the diameters of nanotubes, we may either use the outer borders of the nanotube as a measure (d_{ext}) and thus compare it with a nanowire of the same or similar diameter or either use the middle point of both walls of a NT and take that number as a diameter (D). In all cases for D values sub-1 nm diameters were observed (**Figure 4.2 d**).

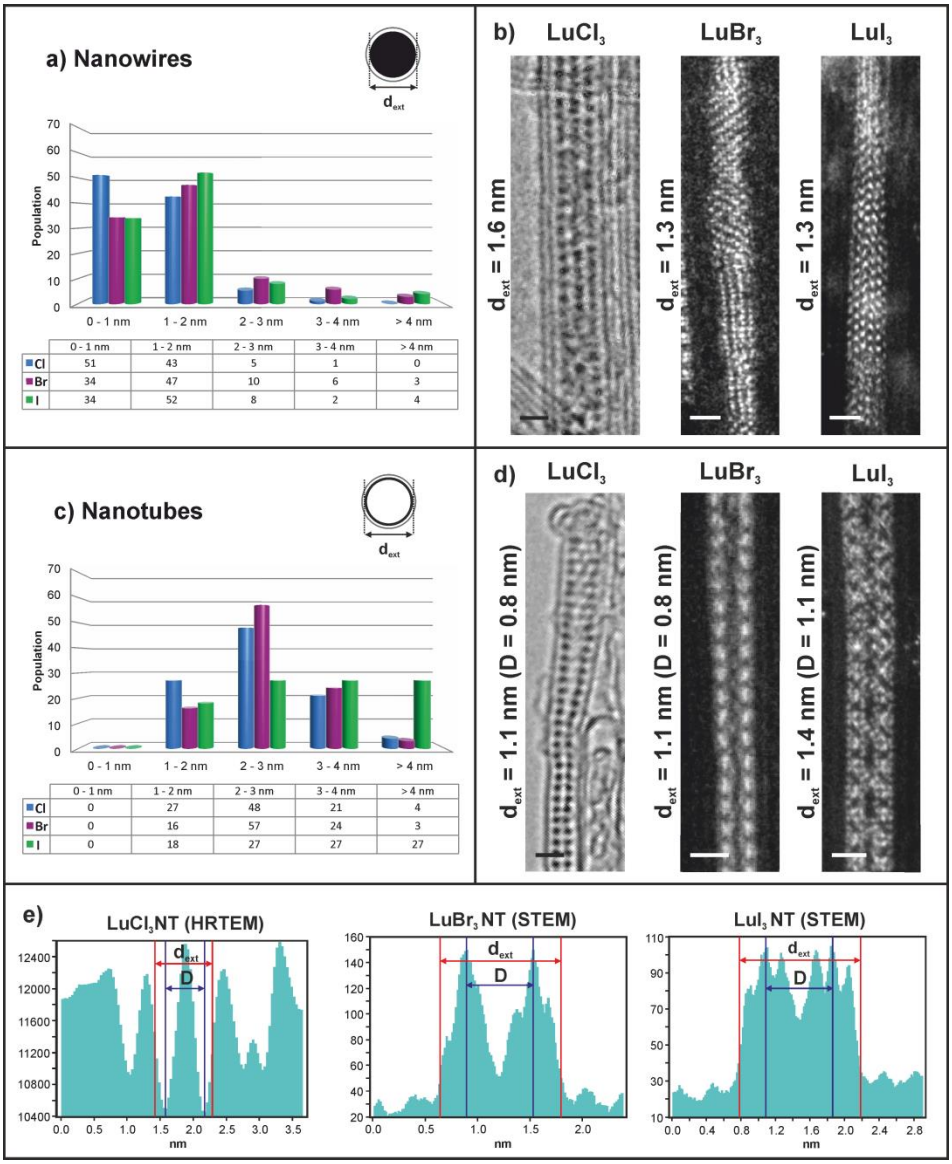

Figure 4.2 Statistical analyses of the distribution of the diameters for LuX_3@SWCNT hybrids: a) nanowires and c) nanotubes. On the right to the histograms: micrographs of $LuCl_3$ (HRTEM), $LuBr_3$ (STEM) and LuI_3 (STEM) structures with their corresponding diameters displayed next to each micrograph (nanowires: b, nanotubes: d). In (e) the intensity profiles drawn perpendicular to the nanotube main axes from (d) micrographs with explanation of the difference in d_{ext} and D values. All scale bars in (b) and (d) are 1 nm.

On **Figure 4.2** the distribution histograms of nanotubes and nanowires of trihalides are shown with the diameters measured as external diameters (d_{ext}) for NW and NT for more precise comparison. For all the samples, over 80 % of the NWs had external diameters below 2 nm. Contrary to that, most of the nanotubes were formed in the d_{ext} range between 2 and 3 nm for $LuCl_3$ and $LuBr_3$, while in the case of LuI_3 the amount of NTs was found to be stable above 2 nm up to 4 nm diameters. Interestingly, smaller anion/halide facilitated smaller nanotube formation. The highest amount of nanotubes was formed in d_{ext}=(1-2) nm range for chloride, d_{ext}=(2-3) nm range for bromide while in general, the largest nanotubes were found for iodide, above d_{ext}=(3 nm). Maximum external diameters observed for each compound were as follows: 3.1 nm, 4.9 nm and 4.9 nm for nanowires of $LuCl_3$, $LuBr_3$ and LuI_3, respectively, while for nanotubes maximum external diameters were: 4.7 nm, 4.4 nm and 5.7 nm for Cl, Br and I anions, respectively.

On the right of **Figure 4.2**, electron micrographs of narrow diameter NTs and NWs (d_{ext}=1.1 - 1.4 nm) of each halide are displayed. For $LuCl_3$, a HRTEM image of a nanotube of d_{ext}=1.1 nm is visually compared with a nanowire of the same external diameter. Both of them are enclosed within double-walled CNTs. The difference of the structure is clearly seen as the NT is characterized by dark edges close to the carbon walls while no difference between the edge and the interior is seen for the NW. Similarly, narrow diameter nanotubes are evident on aberration-corrected HAADF-STEM images for $LuBr_3$ (d_{ext}=1.1 nm) and for LuI_3 (d_{ext}=1.4 nm). The difference in the structure when compared with nanowires of similar diameters is clearly seen, as the nanotubes are characterized by bright edges close to the CNTs walls.

One should note that the above-mentioned diameter values are given by measuring the outermost walls of the LuX_3 nanotubes. If instead we consider the NT diameter as a distance between the center of the LuX_3 layer, even smaller values will be obtained (D values instead of d_{ext}), reaching extraordinarily narrow

diameters for all three halides. Hence, the calculated D values for $LuCl_3$ and $LuBr_3$ nanotubes of external 1.1 nm outermost diameters correspond to 0.8 nm diameters while the LuI_3 nanotube with 1.4 nm turns to 1.1 nm. These results are in good agreement with the theoretically calculated values for the thickness of a single layer of each halide (X). Single layer thicknesses were calculated by crystal structure refinement based on XRD results obtained with synchrotron radiation that will be shown in next section of this chapter on **Figure 4.7**. Thus, layer thicknesses for $LuCl_3$, $LuBr_3$ and LuI_3 were calculated to be 0.28 nm, 0.30 nm and 0.35 nm, respectively. This means the NTs presented on **Figure 4.2** are of the smallest diameters they can possibly get.

These exciting results led us to further investigate the structure of the synthesized LuX_3@SWCNT hybrids by aberration-corrected HAADF-STEM imaging. Hence, atomically resolved images were acquired on FEI´s QU-Ant STEM microscope operated at 300 kV allowing to confirm the crystallinity of the structures of LuX_3 nanotubes and their sub-nanometer diameters (D). Few examples of HAADF-STEM micrographs for each compound are displayed on **Figure 4.3**.

Consequently, on the HAADF-STEM images of **Figure 4.3**, three $LuCl_3$ nanotubes of D equal to 5.8 nm, 2.7 nm and 3.0 nm (a), three $LuBr_3$ nanotubes of D = 3.2, 1.9 nm, 0.8 nm and 3.1 nm (b) and three LuI_3 nanotubes of D = 4.6 nm, 3.3 nm and 1.6 nm (c) are presented. High crystallinity of the nanotubes is evident. For all hybrids we are presenting one closed-ended nanotube formation (marked with yellow arrow) that confirms ideal adaptation of their structures to the closed tips of enclosing single-walled carbon nanotubes.

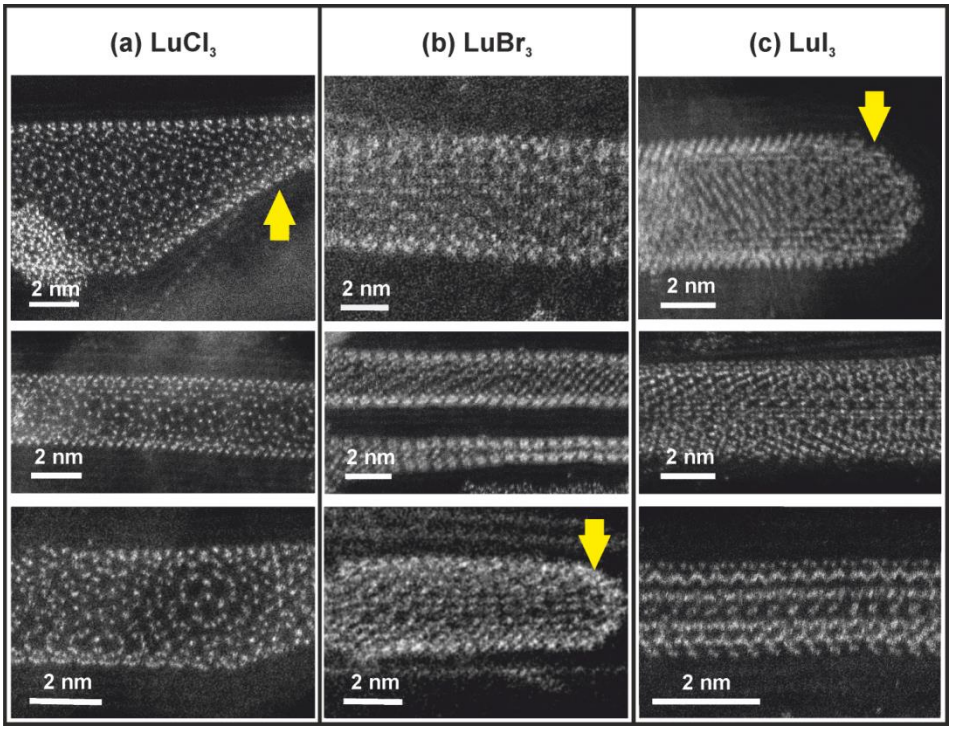

Figure 4.3 Aberration-corrected HAADF-STEM images of LuX_3 nanotubes acquired on FEI´s Qu-Ant STEM operated at 300 kV: a) $LuCl_3$ of D = 5.8 nm (top), D = 2.7 nm (middle) and D = 3.0 nm (bottom); b) $LuBr_3$ of D = 3.2 nm (top), D = 1.9 nm + D = 0.8 nm (middle) and D = 3.1 nm (bottom); C) LuI_3 of D = 4.6 nm (top), D = 3.3 nm (middle) and D = 1.6 nm (bottom). *Yellow arrows are pointing to the nanotubes with closed tips.

For the $LuCl_3$ NT of D = 5.8 nm, Fast Fourier Transformation (FFT) was performed which showed the reciprocal space reflections of the structure. After application of a mask on most of the reflections and performing Inverse Fast Fourier Transformation (IFFT), hexagonal structure of single layer lutetium trichloride nanotube was revealed (**Figure 4.4**). This structure results from the Moiré pattern due to superposition of the top and bottom structures.

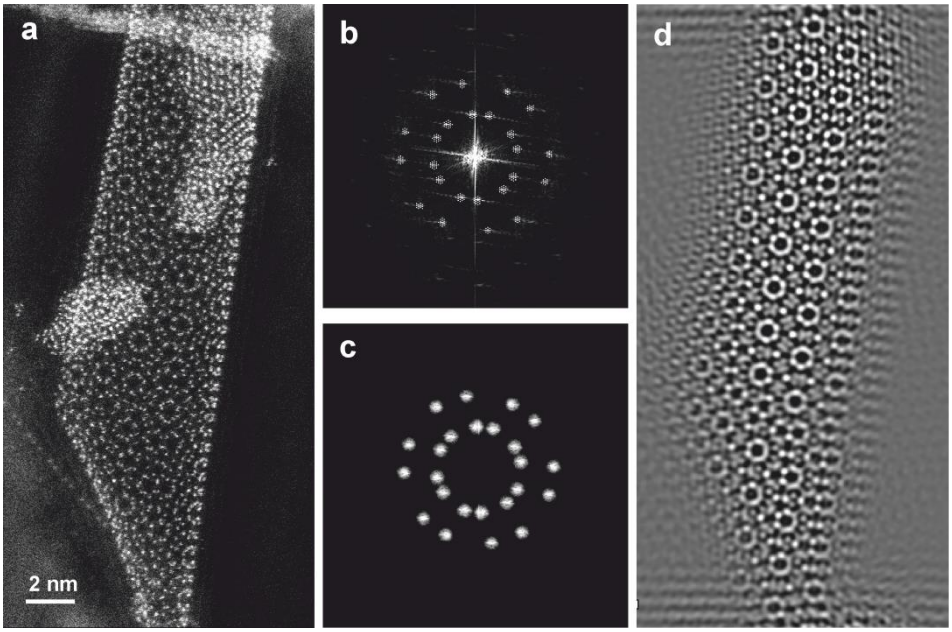

Figure 4.4 $LuCl_3$@SWCNT of D = 5.8 nm (a), its FFT (b), applied mask (c) and IFFT (d).

Although, in most of the cases single-layered nanotubes were formed during the molten phase process, when the diameter of the host SWCNT was sufficiently large, the formation of double-walled lutetium halide nanotubes (DWNTs) was observed. Accordingly, on **Figure 4.5** we present HAADF-STEM images of DWNTs of $LuCl_3$ (d_{ext}=5.2 nm), $LuBr_3$ (d_{ext}=6.3 nm) and LuI_3 of (d_{ext}=4.4 nm). It should be noted that formation of this kind of structure was quite rare and was only observed for SWCNT of diameters larger 4 nm.

On **Figure 4.5** in the three of the cases clear double layer nanotube is distinguished. Measured interlayer distance for $LuCl_3$, $LuBr_3$ and LuI_3 were found to be: 0.61 nm, 0.68 nm and 0.73 nm, respectively, and are close to the calculated interlayer thicknesses of LuX_3, which are 0.56 nm for $LuCl_3$, 0.60 nm for $LuBr_3$ and 0.70 nm for LuI_3.

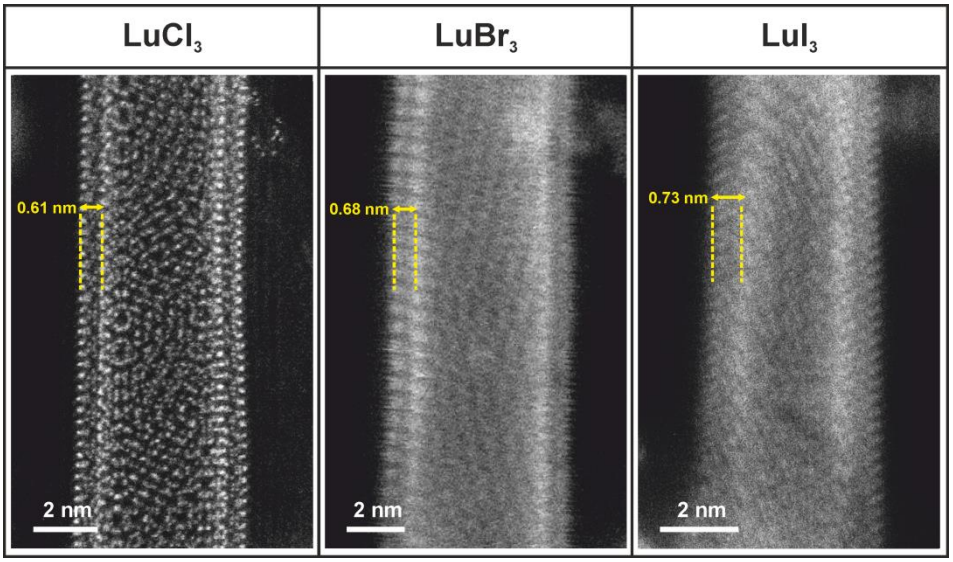

Figure 4.5 Double-walled lutetium halide nanotubes present in host SWCNTs. From left to right: $LuCl_3$, $LuBr_3$ and LuI_3. Measured inter-layer distances were: 0.61 nm, 0.68 nm and 0.73 nm for $LuCl_3$, $LuBr_3$ and LuI_3 NTs, respectively.

For the $LuBr_3$ DWNT showed above, we have additionally acquired EDX elemental maps to confirm its composition and spatial distribution of elements.

The EDX elemental mapping of $LuBr_3$@SWCNT hybrid was acquired on FEI's Tecnai Osiris microscope operated at 200 kV and equipped with EDX detector. Consequently, on **Figure 4.6**, a HAADF-STEM image (a), corresponding Lu+Br and C EDX maps (b,c) of a double-walled $LuBr_3$ nanotube enclosed in SWCNT are displayed showing more Lu and Br signal proceeding from the walls of $LuBr_3$ NT.

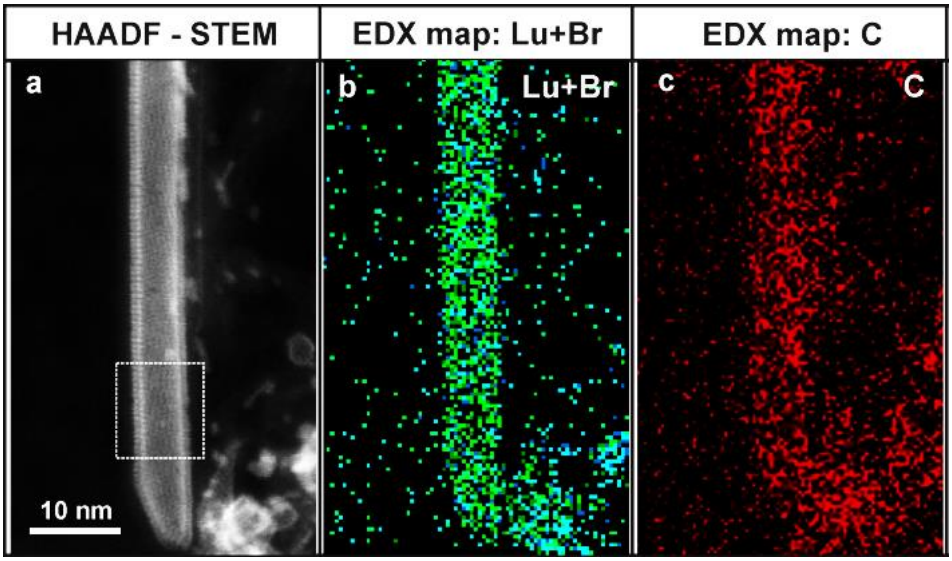

Figure 4.6 $LuBr_3$ double-walled nanotube. a) HAADF-STEM image of the hybrid. EDX maps representing Lu (blue) and Br (green) mixed signals (b) carbon map (c) of a hybrid displayed on (a).

4.2.3 Structural refinement and HAADF-STEM image simulations

Little crystallographic information for lutetium halides is available in the literature and therefore an X-Ray Diffraction (XRD) experiments were conducted on the starting materials (99.9 % pure $LuCl_3$, $LuBr_3$ and LuI_3 powders). As a result, a synchrotron based XRD measurements were obtained and crystallographic information extracted, after Rietveld refinment procedure. Subsequently, crystal structures were graphically represented (**Figure 4.7**) and the atomic position of elements in the crystal network determined (**Table 1**).

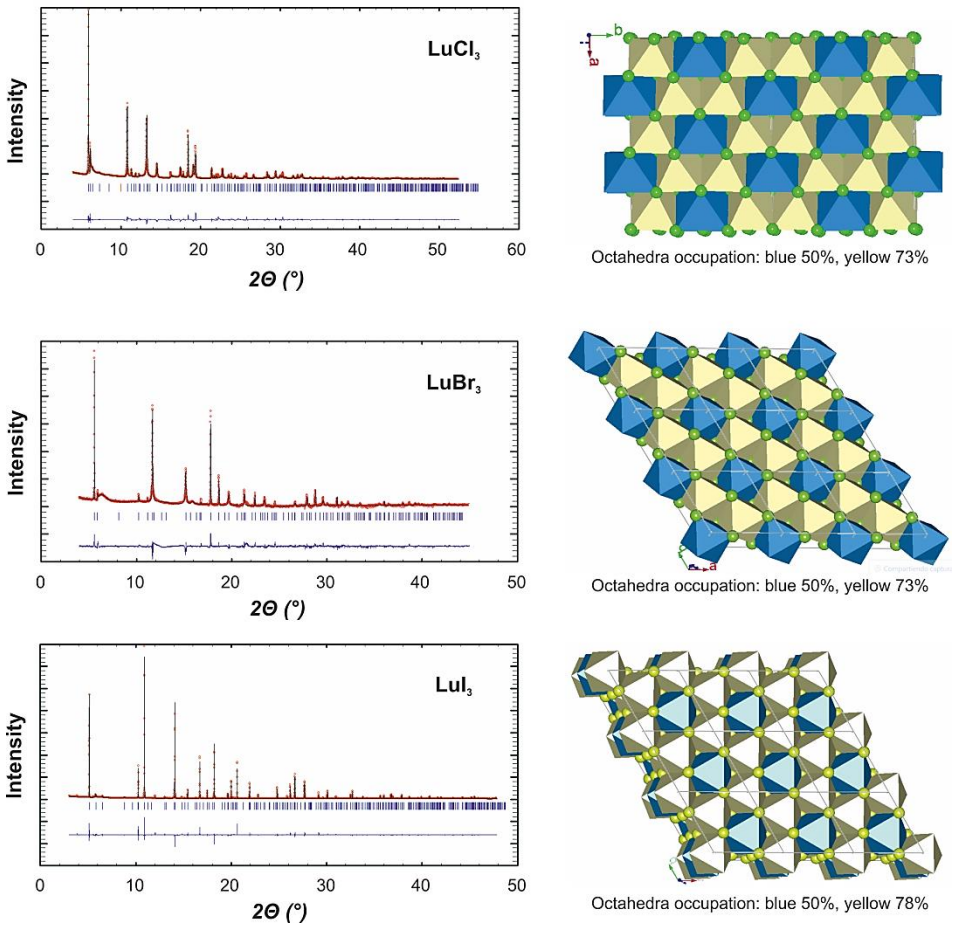

Figure 4.7 Synchrotron based XRD patterns with Rietveld refinement and crystal structure of $LuCl_3$ (first row); $LuBr_3$ (second row); LuI_3 (third row).

The XRD pattern of $LuCl_3$ reveals a monoclinic *C* 2/*m* (no. 12) crystal structure with cell parameters a = 6.7004(3) Å, b = 11.6072(6) Å, c = 6.3963(4) Å and β = 110.454(8) °. These values are in good agreement with those published in 1954 by Templeton and Carter but far more precise [351]. For $LuBr_3$ the XRD pattern reveals hexagonal *P* -3 (no. 147) crystal structure with cell parameters a = 6.9445(4) Å and c = 6.3704(8) Å. This is a differing result comparing to a hexahydrate structure reported by Brown, Fletcher, and Holah in 1968 [352]. The authors found based on XRD measurements that $LuBr_3$ hexahydrate belonged to a

monoclinic *P* 2/*n* space group with a = 9.902 Å, b = 6.678 Å, c = 8.024 Å and β = 93.42°. Lastly, the XRD pattern of LuI_3 reveals rhombohedral *R* -3 (no. 148) crystal structure with cell parameters a = 7.3871(2) Å and c = 20.7671(4) Å. These crystal parameters are in disagreement with results published by Astakhova and Goryushkin in 1992 where LuI_3, prepared by iodinating Lu with iodine vapor, resulted in hexagonal structure with a = 19.5800 Å and c = 20.7700 Å [353]. In spite of the different crystal systems and space groups defining the different lutetium halides, all can be described as layered structures consisting on sheets of partially-filled LuX_6 octahedra sharing edges. In all cases two subsets of octahedra are present in each sheet. One subset, with larger occupancies, form a honeycomb structure, and the second subset (with lower occupancy) is placed in the holes of the first one.

Table 3 Parameters of the crystal structure of all LuX_3 powders derived from the fitting of synchrotron based XRD measurements.

Compound	Atom	W.P.	x/a	y/b	z/c	Occ
$LuCl_3$	Lu1	4h	½	0.3229(9)	0	0.728(5)
	Lu2	2b	½	0	0	0.544(10)
	Cl1	8j	0.219(8)	0.181(5)	0.745(5)	1
	Cl2	4m	0.219(16)	0	0.198(9)	1
$LuBr_3$	Lu1	2d	1/3	2/3	0.515(6)	0.729(10)
	Lu2	1b	0	0	0.5	0.540(20)
	Br1	6g	0.005(7)	0.663(7)	0.263(29	1
LuI_3	Lu1	6c	0	0	0.166(5)	0.780(2)
	Lu2	3b	0	0	1/2	0.438(6)
	I	18f	0.333(2)	0.005(2)	0.0834(8)	1

Based on high resolution HAADF-STEM micrographs and as-obtained crystallographic data, we performed simulations of HAADF-STEM micrographs for all of the LuX_3 structures. This may be a complex task if you think of this kind of structures. The simplest method is to imagine a single atomic layer of any material rolled up into a tube. First of all, there are many ways of doing that,

arranging the net around any selected axis (any chirality). Second of all, depending on the point of view of as prepared tube a different Moiré pattern may be revealed. This is exactly what is happening when simulating micrographs of LuX_3 nanotubes.

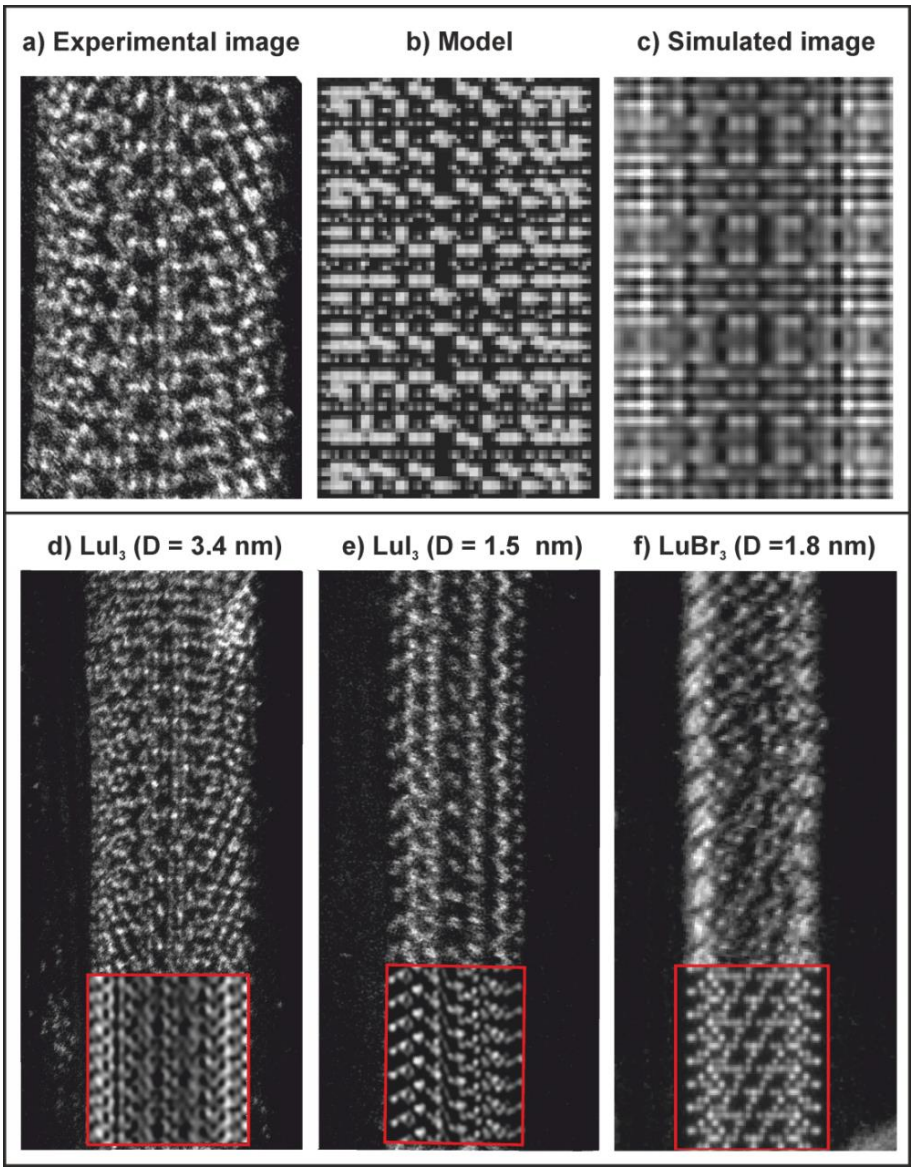

Figure 4.8 HAADF-STEM experimental image (a) of LuI_3 (D = 3.3 nm) compared with a created model (b) and simulation of a nanotube of the same diameter in STEM_CELL program (c). Experimental images with their respective simulated

micrographs for LuI_3 of D=3.3 nm (d) simulated at 25° tilt along the y axis followed by LuI_3 of D=1.6 nm and $LuBr_3$ of D=1.9 nm (f), both simulated at 0° tilt along the y axis.

The structural models of the inorganic LuX_3 nanotubes used as input for the TEM simulations were obtained by taking the coordinates and cell parameters of the bulk material resolved by the X-Ray measurements, isolating a monolayer and rolling it up to form a tubular structure. We generated models for nanotubes whose axis are oriented along the x- and y-crystal axis of the bulk orthorhombic unit cell. In the case of LuI_3 we also carried out a careful structure optimization of the cell vectors and of the atomic positions within density-functional theory, using the Siesta code [354] and a standard conjugate gradient algorithm, finding negligible deviations from the X-ray data (i.e. less than 0.05 Å).

A careful choice of a rolling axis and tilt angle of the chosen structure for simulations can give a good fit with experimentally acquired image, shown on **Figure 4.8 d-f**. However, even after a careful selection of the tilt bringing nicely fitted model there may be some surprises, like this example showed in the first row of the same figure. The model created for LuI_3 NT structure at 0° tilt (b) seems to fit very well the experimental image (a) but the resulting simulated image (c) is not the best approximation of it.

For all of our simulations we used STEM_CELL program developed by V. Grillo [355]. After many trials and careful selection of right parameters, the best fit was obtained for LuI_3 nanotube with D = 3.3 nm and 25° tilt in y (d), other LuI_3 NT of D = 1.6 nm and 0° tilt (e) and for $LuBr_3$ NT of D = 1.9 nm and 0° tilt (f), all showed on **Figure 4.8**. We simulated images employing the same electron voltage as experimentally acquired micrographs (300 kV).

4.2.4 Evidencing tubular structure formation by tilt series

To further prove the tubular nature of the halides present in the interior cavity of SWCNTs, a tilt series of a single LuI_3@SWCNT hybrid of 3.0 nm in external diameter was acquired on aberration-corrected FEI´s Qu-Ant-STEM at 120 kV (shown on **Figure 4.9**).

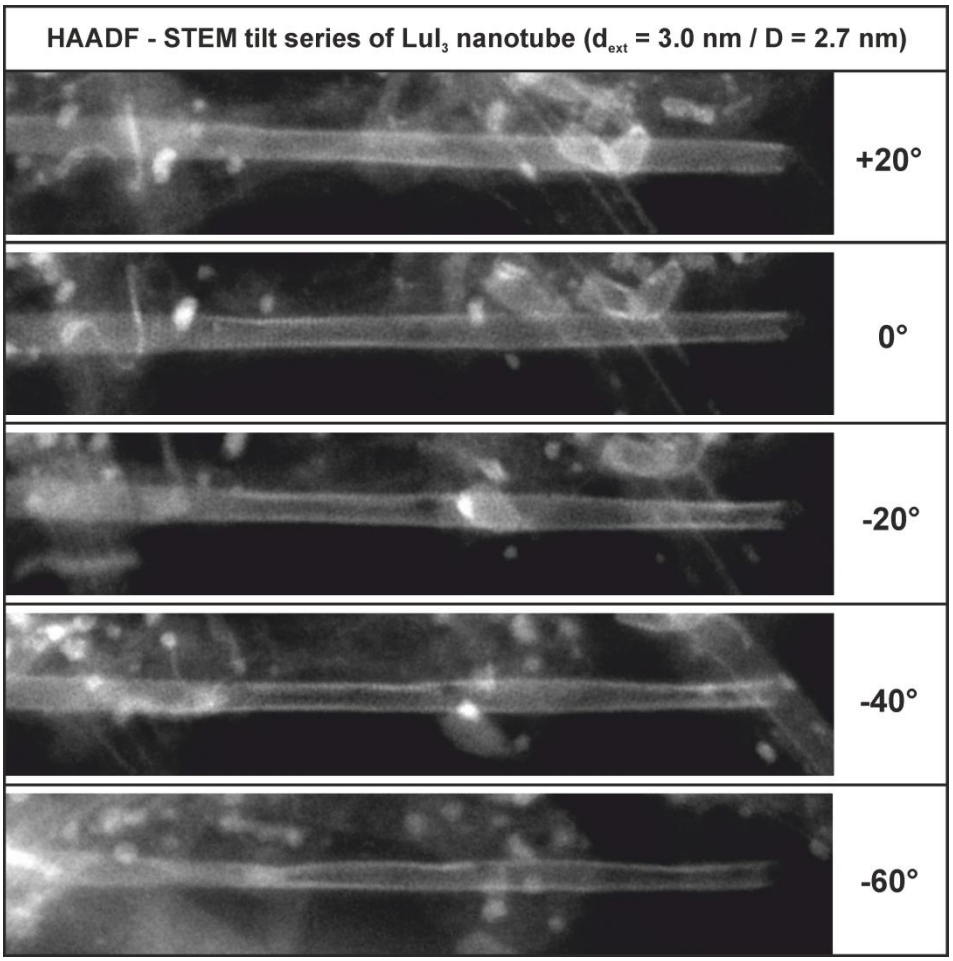

Figure 4.9 Tilt series of LuI_3 nanotube enclosed in SWCNT in HAADF-SEM mode. Images were taken every 20° from +20° to -60° (top to bottom).

HAADF-STEM images were acquired in the tilt range of +20° to -60° using a specialized Fischione 2020 single tilt holder. The images obtained at different tilts

show the same pattern, the brighter edges of the structure at each tilt step indicating a tubular structure is formed and thus confirming our claim. Further tilting of the structure was not possible due to the beam damage causing breakage of the nanotube, hence preventing us to perform a complete electron tomography experiment. In the case of nanotube of D = 2.7 nm its tubular structure is obvious for us even on a single 2D image. However, for the narrow diameter nanotube it is not so evident. Therefore, another tilt series (from +10° to -10°) was acquired, this time for LuI_3 nanotube of much smaller diameter, this is D = 0.9 nm. The results are displayed on **Figure 4.10**.

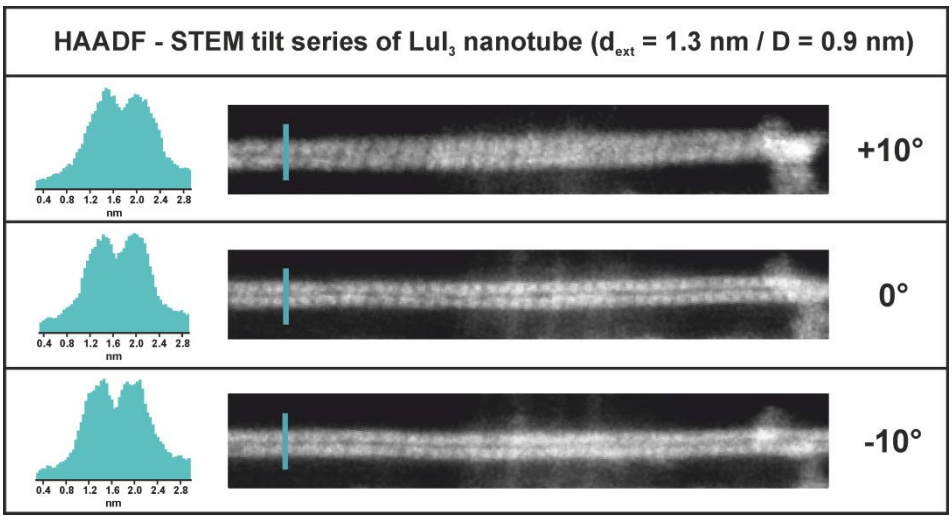

Figure 4.10 Tilt series of narrow diameter LuI_3 nanotube enclosed in SWCNT acquired in HAADF-STEM on FEI´s Titan Cubed at 120 kV from +10° to -10° every 10.

Three HAADF-STEM images were acquired with a 10° step from +10° to -10°. As before, it is clear on each image the edges of the structures appear brighter. For better visualization intensity profiles were drawn along a green line perpendicular to the structure on each micrograph. The intensity profiles are shown on the left side of each micrograph presenting a clear change between the edges where the intensity reaches its maximum and the interior of the structure, where it drops

substantially. This behavior is only possible with tubular structures and serves as further confirmation of nanotube formation of extremely narrow diameter (D = 0.9 nm).

4.3 Conclusions

To summarize, high quality lutetium trihalide single layer nanotubes of narrow (even sub-nanometer) diameters were formed in the interior cavity of single-walled carbon nanotubes used as a host and modelling platform. Inorganic nanotubes were produced by simple, solvent-free, high temperature method.

Statistical analysis, based on low magnification STEM imaging, of the formation of nanotubes against nanowires revealed that most of the NW were formed for smaller diameters (below 2 nm) while NT were formed for bigger range of diameters (up to 6 nm). However, the formation of sub-nanometer diameter NT for all lutetium halides was observed. It was shown there is a preferential distribution of diameters depending on the anion size, with preferential formation of bigger nanotubes for iodide while chloride and bromide would have the highest population at lower diameters (between d_{ext} = 2 to 3 nm). The structures of LuX_3 nanotubes were confirmed mainly by aberration corrected electron microscopy imaging, EDX mapping and tilt experiments. Valuable crystallographic information was extracted from synchrotron based XRD measurements for $LuCl_3$, $LuBr_3$ and LuI_3 compounds.

Simulations of HAADF-STEM micrographs provided a further proof of the correct analysis of the tubular nature of our samples, showing a good agreement between the experimentally acquired and simulated images based on the structural refinement data from XRD synchrotron based experiments on the bulk materials.

All of the information included here may pave a road for the synthesis of new nanomaterials of interesting structures possibly characterized by novel and/or

enhanced physical properties. The investigation into practical applications of LuX_3@SWCNT hybrids should also be followed.

5 Single-layered lead iodide nanotubes enrolled on multi-walled carbon nanotubes

In this chapter we present the synthesis, structural characterization and optical properties of nano-hybrid single-layered lead iodide nanotubes (PbI_2) enrolled on the external walls of arc-discharge multi-walled carbon nanotubes.

MWCNT@PbI_2

5.1 Introduction

In recent years, two dimensional nanomaterials have received increasing attention due to their enhanced properties emerging from high surface-to-volume ratio and quantum confinement effects that make them suitable candidates for applications in electronic and optical devices. Combining characteristics of one and two dimensional materials, nanotubes are part of this group of nanostructures [356-360]. Theoretically, any crystalline structure able to form a thin film can be rolled up into a tube. Lead iodide (PbI_2) has a laminar Van der Waals structure which is easily exfoliated into atomically thin two-dimensional layers. Moreover, lead iodide has been widely studied due to its optical and electrical properties, electroluminescence, photoluminescence and non-linear effects [361-364]. Considerable focus is put into its application in room temperature X-Ray [365-367] and γ-Ray [368] detectors. Likewise, lead iodide based perovskites are studied for field-effect transistors [369], light emitting diodes [364] and high performance solar cells [370-373]. In this context, many lead iodide nanostructures [374, 375] have been synthesized and thin films exfoliated or grown on substrates, such as silicon wafers [376, 377].

One of the most motivating forms of all lead iodide systems is a monolayer, a structure of the highest surface-to-volume ratio. Interestingly, bulk PbI_2 is a direct bandgap semiconductor which becomes indirect when transforming into a monolayer due to low-dimensional effects [377-379]. The bulk optical band gap was reported to be at 2.41 eV [380]. However with decreasing thickness the PL peak would blue-shift achieving 2.47 eV for a monolayer [380]. Thickness dependence of the band gap properties is therefore related to changes in photoluminescence and optoelectronic properties of PbI_2. This was previously observed in other systems of reduced dimensionality including carbon nanotubes and other nanostructured materials [22, 381]. Nevertheless, theoretical calculations

on monolayer PbI_2 predicted the red shift of the absorption edge when deposited on top of graphene forming a Van der Waals heterostructure [378].

Furthermore, tubular structures of lead iodide were also recently studied. After the first report on the formation of multi-layered nanotubes of PbI_2 using WS_2 nanotubes as template [382], formation of single-layered PbI_2 nanotubes inside CVD grown multi-walled carbon nanotubes (PbI_2@MWCNTs) was succeeded [67]. In this work, calculated band gaps for free standing PbI_2 nanotubes (NTs) after removal of the CNT template, were reported. According to the calculations there is a little difference in the energy of the band gap of monolayer PbI_2 NTs when compared with the bulk material (~2.5 eV for NTs compared with 2.4 eV for bulk).

The template material has therefore a crucial impact on the PbI_2 structures that are produced. To further investigate its effect, we decided to employ CNTs from a different source, namely arc-discharge MWCNTs, as templates for the growth of PbI_2-CNT hybrids.

In this chapter, we report on the formation of a new nano-hybrid material, composed of single layer lead iodide (PbI_2) enrolled on the external walls of arc-discharge multi-walled carbon nanotubes with extremely high yield. Additionally, we describe its optical properties by photoluminescence and cathodoluminescence.

5.2 Results and discussion

5.2.1 Characterization of arc-discharge MWCNT template material

The synthesis procedure for the template assisted growth of PbI_2 nanostructures was adapted from Cabana et al. [67] with the main difference in using a different source of MWCNT templates. While SWAN´s CVD-grown CNTs were chosen for the first study, for the current work we selected arc-discharge produced and

chemically purified nanotubes supplied by n-tec®. A comparison of both types of tubes is shown in **Table 1**. The most important dissimilarities between the two are the lack of metal impurities and extremely high degree of straightness of the latter, as can be observed on **Figure 5.1**.

Table 1 Properties of CVD- and arc discharge-grown MWCNTs.

Property	SWAN® MWCNTs	n-tec® MWCNTs
Production method	Chemical Vapor Deposition	Arc Discharge
Purified	No	Yes
Metal nanoparticles	Yes (Fe)	No
Amorphous and graphitic carbon	Yes	Yes
Typical length	1 μm	2 μm
Typical diameter	~20 nm	5 – 70 nm
Shape	Curved	Straight
Thermal stability in air	Up to 600°C	Up to 650°C

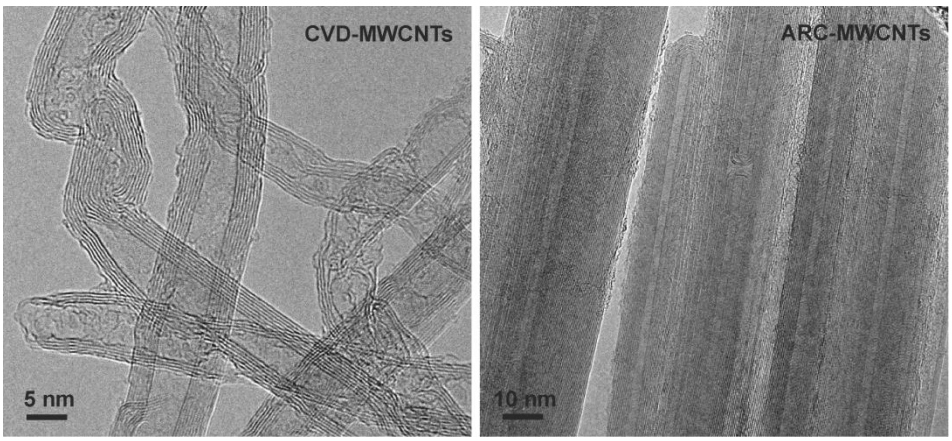

Figure 5.1 CVD-grown MWCNTs from SWAN® compared to arc discharge-grown MWCNTs from n-tec®.

On **Figure 5.1** a clear difference in the straightness of CVD- and arc discharge-grown NTs is seen. It is worth to mention that the latter are also characterized by being composed by many more layers, narrower internal cavities and larger external diameters. The diameters of MWCNTs used for the synthesis are of importance as they determine the diameters of grown PbI_2 nanostructures. Hence, statistical analysis of the diameters of starting MWCNTs was performed and is displayed on **Figure 5.2**.

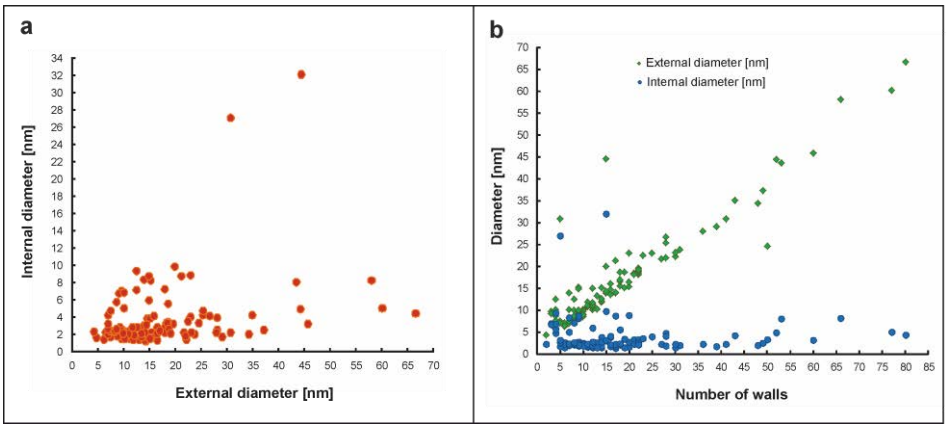

Figure 5.2 a) External and internal diameters of starting MWCNTs; b) Number of walls correlated with the diameter of MWCNTs.

In general, with the increasing nanotube´s diameter the number of walls was found to be increasing. While the external diameter changed linearly with the number of walls from 5 to 66 nm (median value = 13.5 nm, average = 17.2 nm), the internal diameters were found to be (with very few exceptions) in the narrow range of 1 to 10 nm (median value = 2.5 nm, average = 3.7 nm) (**Figure 5.2 b**).

Prior to the synthesis of hybrid material the n-tec® MWCNTs were steam-treated for 2 h or 12 h in order to open the tips of the nanotubes. The experimental details of steam treatment are described elsewhere [43]. After steam purification the samples showed a larger amount of open tips together with the removal of most of the graphitic nanoparticle impurities. The amount of open-ended nanotubes was

doubled within 2 h of steam (from 22% to 43% of all CNTs) but did not show any further improvement after additional 10 h (**Figure 5.3**). Therefore, 2h steam treated MWCNTs were selected for further synthesis steps.

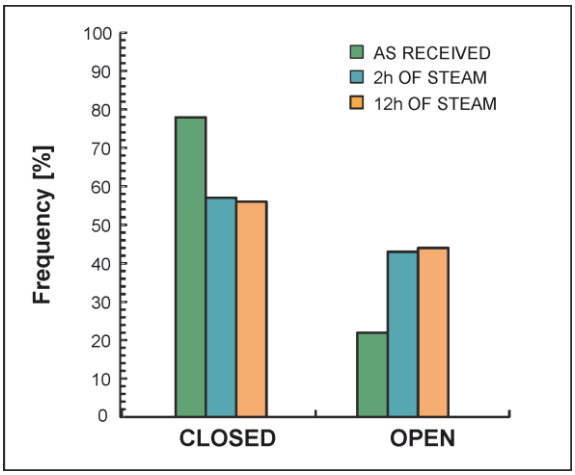

Figure 5.3 Statistical analyses of open/closed ends of: as-received MWCNTs and after 2h, and 12h of steam treatment.

5.2.2 Synthesis and structural characterization of PbI_2-MWCNT hybrids

Steam-treated MWCNTs (n-tec®) were ground with PbI_2 (Aldrich, 99.999%) in the w/w ratio of 1:23 (MWCNTs:PbI_2) in a glove-box and then transferred into a quartz tube under argon. The quartz tube was closed and sealed, then inserted into a tubular oven. The oven was heated ~100 °C above the melting point of PbI_2 (500 °C) and upheld at this temperature for 12 hours. Slow cooling rate (5 °C/min) permitted highly crystalline layers of PbI_2 to be formed on the outer walls of MWCNTs with 99% of success. We will refer to these hybrids as MWCNTs@PbI_2. On **Figure 5.4 a**, a HAADF-STEM image showing a high yield of coverage is presented. The bright contrast of PbI_2 makes the MWCNTs@PbI_2 nanohybrids look bright. The smooth layers of lead iodide covering the whole surface of straight carbon nanotubes are seen as they follow the CNTs´ shape. We

speculate that the successful coverage with such an extraordinary yield is due to the high straightness of the initial multi-walled carbon nanotubes.

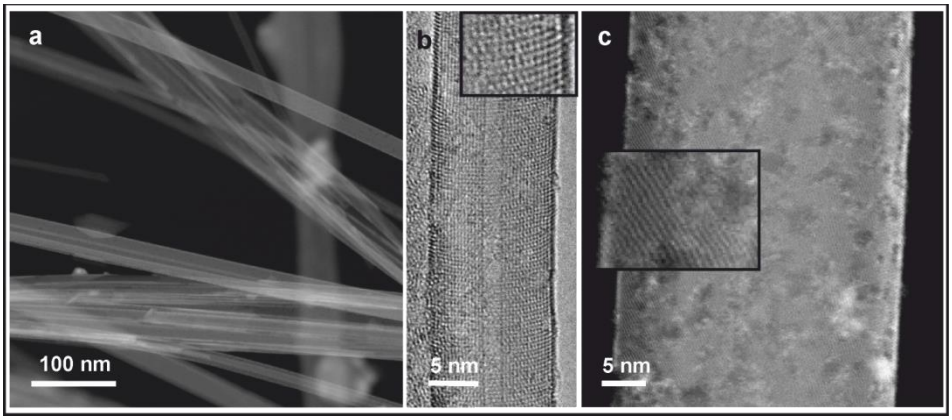

Figure 5.4 MWCNTs@PbI_2: a) HAADF-STEM image showing the yield of coverage = 99%; b) HRTEM image of a single hybrid. In the inset a zoom-in into atomic structure of the layer; c) HAADF-STEM image of a single hybrid. Zoom-in into the structure of the PbI_2 layer in the inset.

In order to get an insight into the atomic structure of the layer, HRTEM images were acquired at 200 kV. An example image is displayed on **Figure 5.4 b**. Dark contrast lines are visible in close contact with the outmost external wall of the MWCNT and can be attributed to the single-layered PbI_2 nanotube. Interestingly, it was observed that no multi-layered structures of PbI_2 are formed. In the inset of the HRTEM image, the zoom-in into the atomic structure is presented where the distinctive curvature of the formed PbI_2 nanotube can be directly appreciated. The highly crystalline layer formation was further confirmed by aberration-corrected STEM imaging (**Figure 5.4 c**).

Moreover, the open-ended carbon nanotubes permitted additional formation of nanotubes and nanowires of lead iodide in the interior cavity of MWCNTs (**Figure 5.5**). Such structures will be referred in this work as **t**PbI_2@MWCNTs@PbI_2, for lead iodide nanotubes on the inside and outside of MWCNTs; and **w**PbI_2@MWCNTs@PbI_2, for lead iodide nanowires filled in the

internal cavity of MWCNTs covered by lead iodide nanotubes. Moreover, a fourth configuration is possible, which is a mix between **t**PbI_2@MWCNT@PbI_2 and **w**PbI_2@MWCNT@PbI_2 where internal lead iodide nanotube converts into nanowire and then again into nanotube followed by nanowire and so on. This kind of structure was common in our sample.

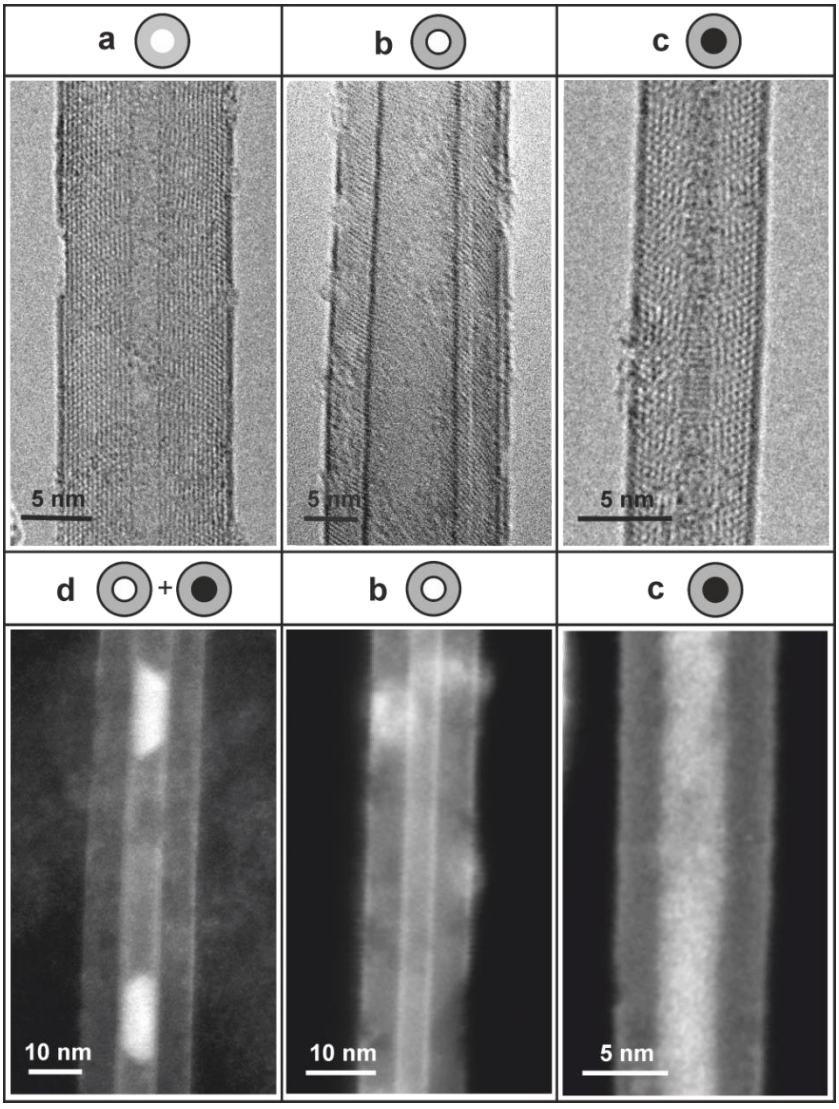

Figure 5.5 Different possible hybrids found in as-synthesized sample: a) MWCNT covered by a tube of PbI_2 (MWCNT@PbI_2); b) a tube of PbI_2 inside MWCNT

covered by a tube of PbI_2 ($tPbI_2$@MWCNT@PbI_2); c) a wire of PbI_2 inside MWCNT covered by a tube of PbI_2 ($wPbI_2$@MWCNT@PbI_2); d) mixed $tPbI_2$@MWCNT@PbI_2 and $wPbI_2$@MWCNT@PbI_2. First row: HRTEM, second row: HAADF-STEM; all acquired on FEI´s Tecnai F20 at 200 kV. *Black circles represent PbI_2 nanotubes; black filled circles PbI_2 nanowires, grey areas represent CNTs.

Additionally, the single-layer nature of the PbI_2 was corroborated by analyzing the thickness of the layer. In bulk PbI_2 crystal an interlayer spacing of 0.6986 nm has been reported [383]. However, for a single layer a smaller thickness is expected. In already mentioned work on single-layered PbI_2 inside carbon nanotubes [67] a thickness of 0.4 nm was informed. The same value for the external layer was measured in our study based on electron micrographs. Herein, we are confident of the PbI_2 monolayer formation.

In order to further investigate the structure of prepared hybrids, X-Ray diffraction studies were performed. Bulk lead iodide belongs to the *P -3m1* crystal structure. It is a layered material, with hexagonal unit cell where each lead atom is sandwiched between two iodine atoms. It is characterized by strong intra-layer bonding and weak Van der Waals inter-layer interactions [384]. The XRD patterns of the starting materials (MWCNTs, bulk PbI_2) and the final product are shown on **Figure 5.6**.

In the case of bulk PbI_2 a set of reflection peaks corresponding to hexagonal *P -3m1* crystal structure was confirmed. Apart from the reflections of pure bulk, a small quantity of impurities was present (marked with asterisk (*)) and assigned to lead iodide mixed oxides. The reflections of starting MWCNTs were assigned to graphitic hexagonal structure. Lastly, the XRD of the product (MWCNTs@PbI_2) showed strong preferred orientation. According to the DFT calculations the lowest energy surface in PbI_2 is the (001) surface, with the surface energy of 0.428 J/m^2, much lower than that for the other crystal surfaces [380]. Indeed, it was shown that the lead iodide monolayer in MWCNTs@PbI_2 sample crystallized in the low

energy (001) surface. The peaks of the highest intensities are those belonging to the (00l) group of reflections, this is: (001), (003) and (004). This is consistent with delamination of PbI_2 sheets perpendicular to the c axis.[385] Additionally, presence of residual lead oxides was assigned to low intensity peaks (white circles, ○). The presence of oxides is due to the low stability of lead iodide that gradually decomposes in air.

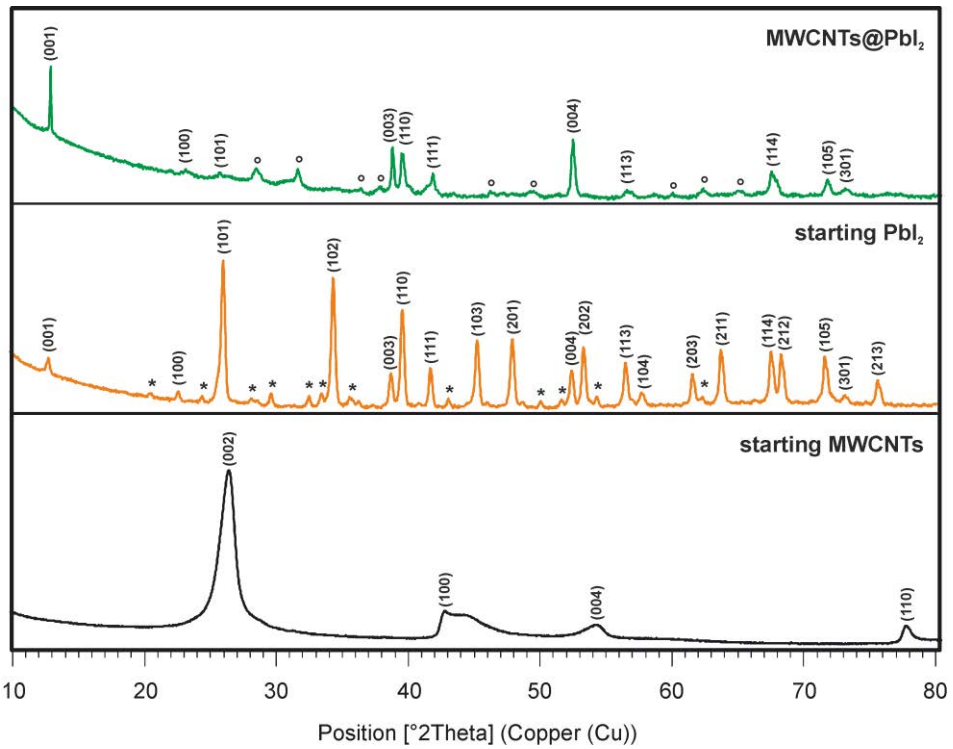

Figure 5.6 X-Ray diffraction patterns of (from top to down): MWCNTs@PbI_2 hybrids; starting bulk PbI_2 used for the synthesis and starting MWCNTs.

5.2.3 Study of the composition

Spectroscopic techniques were used to validate the composition of MWCNT@PbI_2 sample and the absence of impurities. A representative EDX spectrum of a single MWCNT@PbI_2 hybrid shown in **Figure 5.7** includes peaks confirming the presence of lead (M lines) and iodide (L lines). The carbon peak (K

line) corresponds mainly to the MWCNT with some contribution from the lacey carbon film covering the TEM grid. The copper peaks, K and L lines, matched the grid composition.

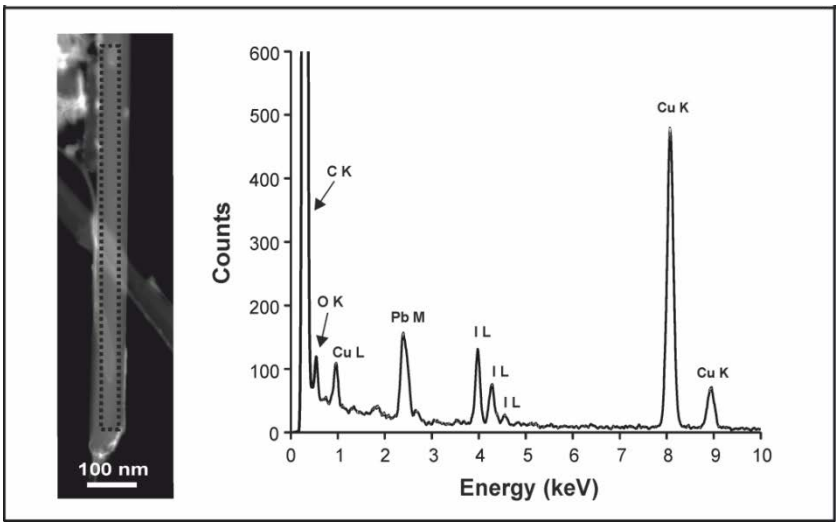

Figure 5.7 EDX spectrum of a single MWCNT@PbI_2 structure. The spectrum was acquired in STEM mode from the area of the tube marked on the image (inset) as a black rectangle. *The carbon peak (max. at 7000 counts) was cut off from the scale for better visibility of lower intensity peaks.

In addition, the spatial distribution of the elements was achieved with EDX mapping technique in STEM mode, performed on a single MWCNT@PbI_2 hybrid (**Figure 5.8**). This experiment was performed at lower voltage (120 kV) in order to prevent the electron damage caused to the lead iodide layer during the analysis. Spectral imaging gave us the confidence an elementally uniform and evenly spread layer of lead iodide was wrapped around MWCNT. It is clearly seen on the EDX maps that the C signal emerges from the interior of the hybrid while Pb and I signals give a higher density signal at the edges of the hybrid. The signals of Pb and I are weaker than carbon since it originates from a single-layer lead iodide nanotube wrapped around a multi-layered CNT.

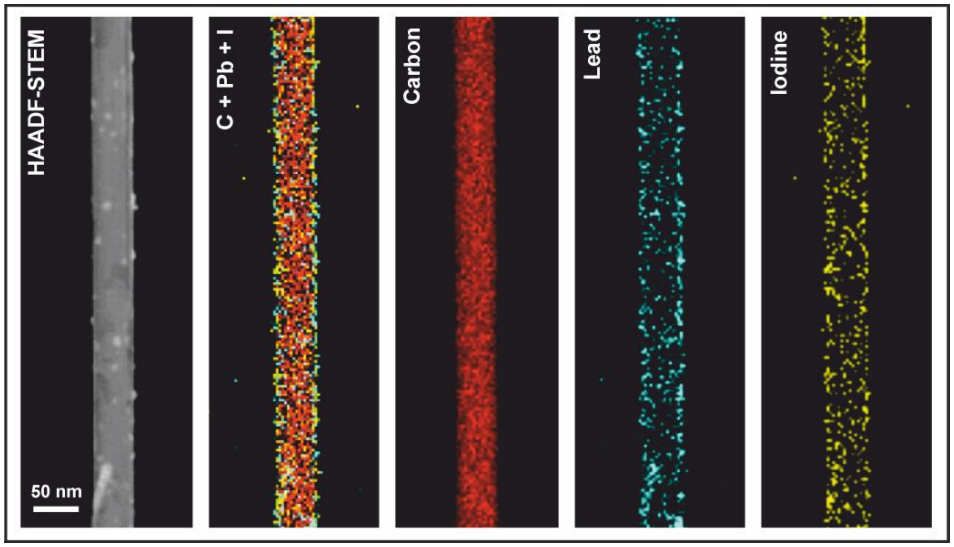

Figure 5.8 EDX maps in STEM mode of single MWCNT@PbI_2; from left to right: HAADF image of selected area, mixed EDX signals: Carbon (red) + Lead (blue) + Iodine (yellow), Carbon signal, Lead signal and Iodine signal.

5.2.4 Electron tomography

Standard TEM images are projections of three dimensional (3D) objects into two dimensions (2D) and therefore the real 3D structure may be misconstructed in the mind of the viewer. Thus, with the purpose of confirmation of film continuity along the carbon nanotube walls, a 3D visualization reconstructed from a series of 2D HAADF-STEM images was performed for MWCNT@PbI_2 hybrid (**Figure 5.9**) and mixed internal nanowire/nanotube (**w/t**PbI_2@MWCNT@PbI_2) hybrid (**Figure 5.10**). The acquisition of 2D images was executed in a wide range of tilt angles using specialized Fischione 2020 single tilt holder. The procedure consisted of acquiring series of HAADF-STEM images on aberration corrected FEI´s Qu-Ant EM microscope operating at 120 kV of both structures: MWCNT@PbI_2 and **w/t**PbI_2@MWCNT@PbI_2, tilting the holder from -72° to +76° with an increment of 4° for the first one and tilting from -70° to +74° every 4° for the latter. The reconstructions were carried out in Inspect 3D program. Projection images of

these reconstructions are displayed on the right side of **Figure 5.9** and **Figure 5.10** with corresponding orthoslices a-c showing the cross sections of the hybrids.

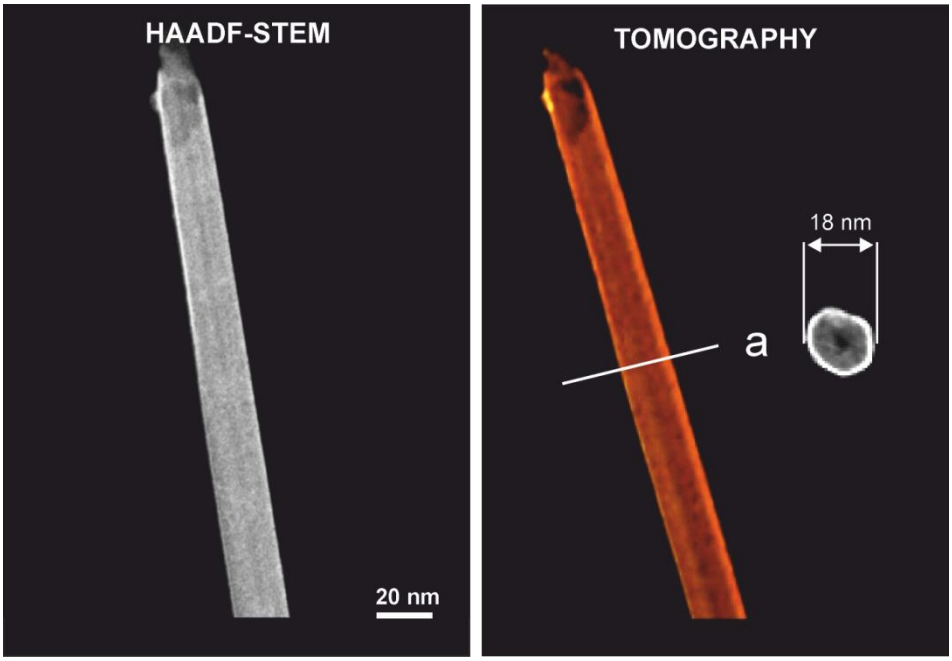

Figure 5.9 HAADF-STEM image of MWCNT@PbI_2 (left) before tomography acquisition and single projection image (right) from tomography of MWCNT@PbI_2. Orthoslice (a) clearly shows MWCNT (dim grey disk) covered by a single layer of lead iodide (bright edge).

Certainly, the PbI_2 monolayer was found to be continuous and to cover the entire surface of carbon nanotube. The projection image on the right side of **Figure 5.9** represents a single MWCNT@PbI_2 hybrid with no endothelial filling. MWCNT is appearing on the orthoslice (a) as dim gray disk surrounded by an edge of high brightness (PbI_2 layer) and is clearly an example of multi-layer CNT with narrow internal diameter.

On the other hand, on **Figure 5.10** we observe a single t/wPbI_2@MWCNT@PbI_2 hybrid covered by a continuous and smooth single layer of PbI_2 but also endohedrally filled with lead iodide nanotube and nanowire structures

interchanging along the hybrid. It is clearly seen on orthoslice (b) and (c). While (b) is composed of two bright circles corresponding to the exterior and interior layers of lead iodide, on (c) we may observe that besides of the external layer, the interior of the hybrid is fully filled forming a nanowire of lead iodide.

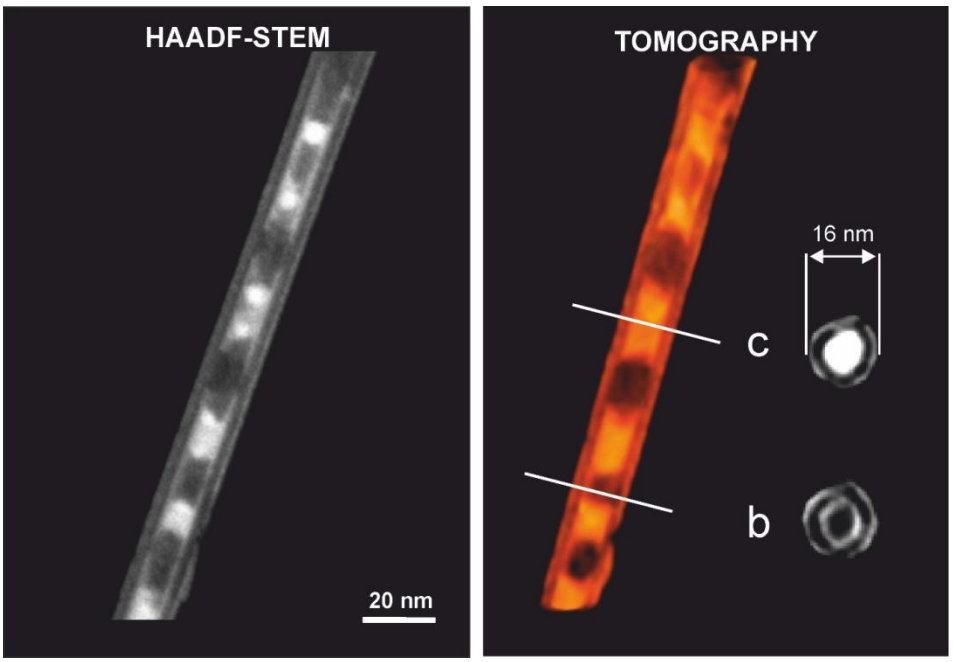

Figure 5.10 HAADF-STEM image of single t/wPbI$_2$@MWCNT@PbI$_2$ hybrid (left) before tomography acquisition and projection image from tomography of the same hybrid (right). Orthoslice (b) shows a region of the hybrid where lead iodide nanotubes are present on the inside and on the outside of MWCNT. Orthoslice (c) shows a region of the hybrid for which internal nanowire and external nanotube are present.

5.2.5 Optical properties

Photoluminescence spectroscopy is an accurate technique to study the optical characteristics of materials and thus has been used in many studies concerning lead iodide [367, 374-377, 386]. For the purpose of our study we combined

photoluminescence (PL) and cathodoluminescence (CL) in order to get an insight into optical properties of the as-prepared material.

First, PL was acquired exciting our sample with a laser of 473 nm and compared with the bulk material, namely starting lead iodide used for the synthesis of our hybrid. **Figure 5.11** shows the photoluminescence (PL) spectra of MWCNTs@PbI_2 sample (red line) and bulk PbI_2 (brown line).

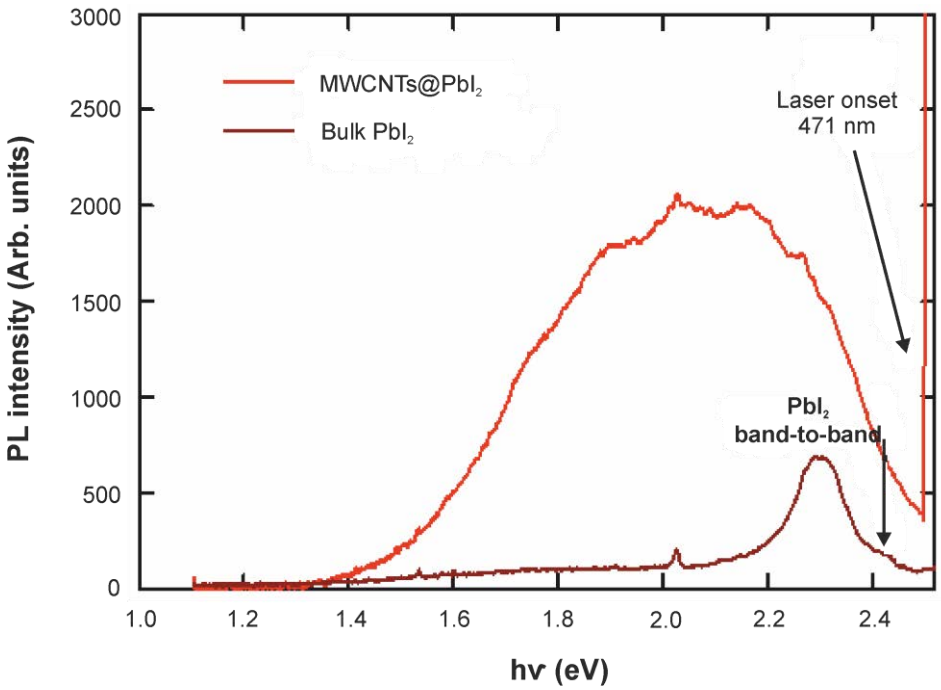

Figure 5.11 Photoluminescence spectra of MWCNTs@PbI_2 sample and bulk PbI_2 acquired with 473 nm laser.

The samples where excited at 473 nm and the emission was measured in the range of 1240 to 500 nm (1.0 eV to 2.5 eV). The emission spectrum of the bulk shows the intrinsic band-to-band emission at 2.41 eV followed by extrinsic components: an intense line centered at 2.30 eV and low intensity broad band centered at about 2.0 eV. As the absorption coefficient of PbI_2 is large for 473 nm, the excitation light is absorbed closer to the grain surface and thus the extrinsic features

dominate the PL spectrum. Their emission intensities are related to the quality of the PbI_2 crystal, where the 2.30 eV band (called D band) is related to the traps in the bulk material and the 2.0 eV band (called G band) is related to the surface qualities [376, 387]. The origin of these bands is ascribed to the radiative recombination of carriers (electron-hole pairs) that are trapped in the bulk and on surface defects, respectively. On top of it, the intrinsic band-to-band of PbI_2 appears at 2.41 eV, as a shoulder of the 2.30 eV peak.

The PL spectrum of MWCNTs@PbI_2 sample (red line) is much more intense and consists of a broad band centered at around 2.0 eV (G band) and therefore it is more extrinsic in nature and related to radiative recombination of excitons and photo-carriers trapped at the crystal surface. Additionally, at the high energy side the PL is clearly shifted to higher photon energies suggesting a blue-shift of the band gap. Unfortunately the onset of the laser is blocking this part of spectrum but if we extrapolate the high energy tail of PL signal of MWCNTs@PbI_2 it is clear that it would exceed the energy of the band-to-band transition to around 2.50 eV.

In order to further examine the optical properties of our sample we employed a laser of higher energy, namely pulsed laser of 266 nm in normal beam configuration (**Figure 5.12**). High excitation conditions (266 nm laser) used for acquisition of time-dependent PL spectra of our sample enhance the intrinsic band-to-band photoluminescence, as defects can only capture a part of photo-excited electron-hole pairs. This effect is clearly observed where the intrinsic peak at 2.41 eV is far more intense than in the reference PbI_2 spectrum.

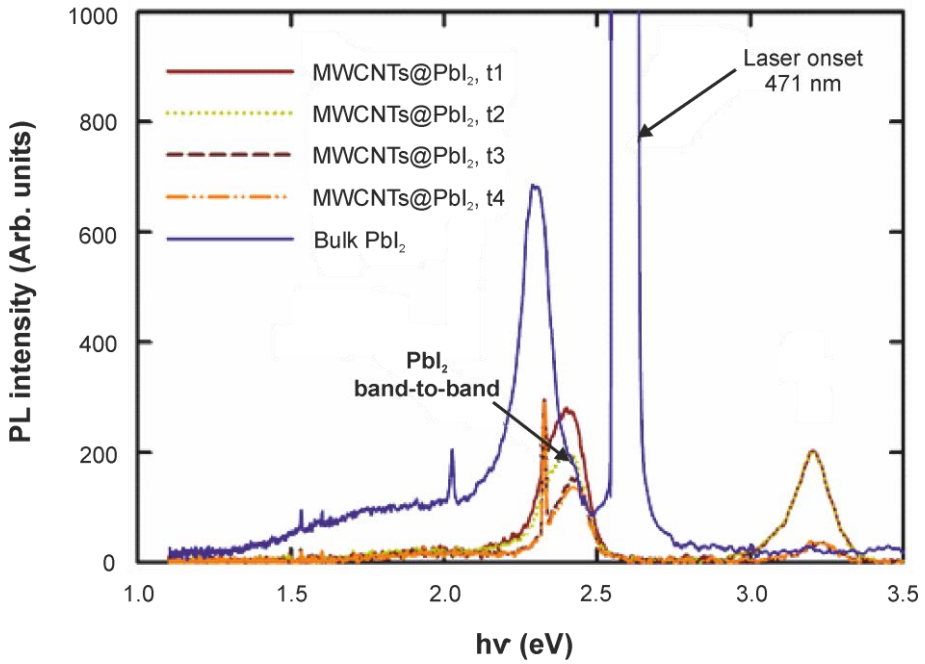

Figure 5.12 Time-dependent PL of MWCNTs@PbI_2 sample acquired with pulsed 266 nm laser (normal beam). PL spectra were acquired at t1 to t4 time points.

It should be noted the PL spectrum of bulk PbI_2 displayed on **Figure 5.12** was acquired at 473 nm laser due to the difficulty of obtaining a signal at 266 nm and is only displayed for comparison with MWCNT@PbI_2. Forr PbI_2-MWCNT hybrids a new peak centered at around 3.20 eV appeared when using high excitation energy. This peak may be due to high energy transitions when narrow PbI_2 nanotubes or nanowires are formed inside MWCNTs and thus suffer from confinement effects, known to shift the energy of the band to higher values. More investigation is needed in order to confirm the origin of this band and will be completed in near future. Especially low-temperature PL experiments would provide a better way to understand the intrinsic material properties due to suppressed nonradiative electron-hole recombination processes at low temperatures.

It was noticed that, when the laser is used without any attenuation, the sample is degraded (a slow decrease of the PL intensity with time is observed). However, the degradation is not observed when the excitation laser is attenuated (**Figure 5.13**).

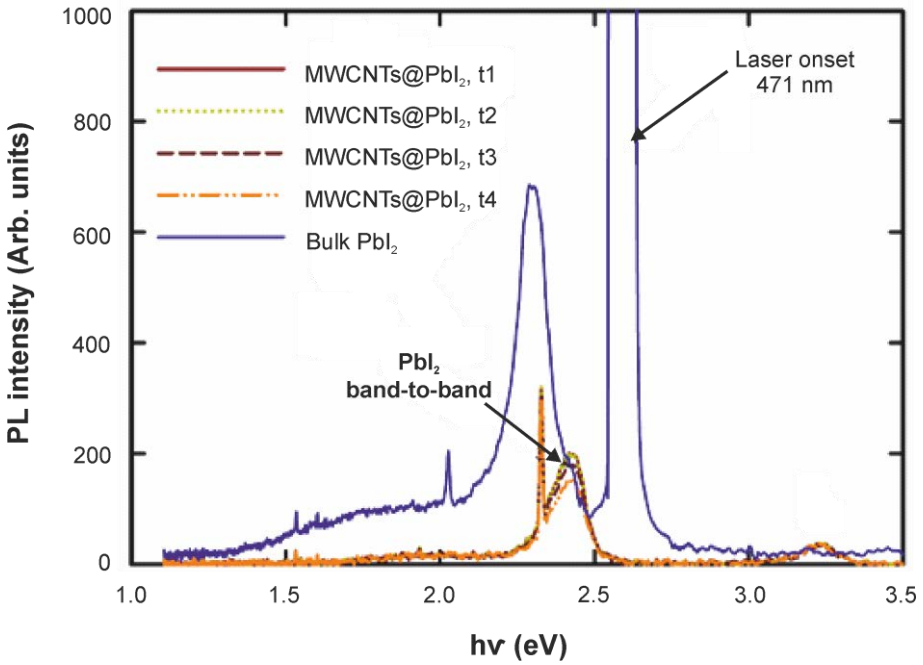

Figure 5.13 Time-dependent PL of MWCNTs@PbI_2 acquired with 266 nm pulsed laser (expanded beam). PL spectra were acquired at t1 to t4 time points.

Cathodoluminescence (CL) is valuable and complementary technique to PL. In a CL experiment highly energetic electrons are used as a source of excitation. Combining STEM with CL enables to collect high sensitivity data with high spatial resolution. Essentially, CL spectrum is characterized by emission lines of characteristic wavelengths from a material under study. Such STEM – CL experimental setup allowed us to obtain information on band-to-band transitions from individual MWCNTs@PbI_2 hybrids as may be seen on **Figure 5.14**. This is particularly useful for the studies on our hybrid material since the sample is composed not only of the MWCNT@PbI_2 but also **t/w**PbI_2@MWCNTs@PbI_2 structures and some excess of bulk PbI_2 used for the synthesis. Hence, we selected

an individual MWCNT@PbI_2 hybrid, measured its CL signal and compared it with that of bulk PbI_2, as showed on **Figure 5.14**.

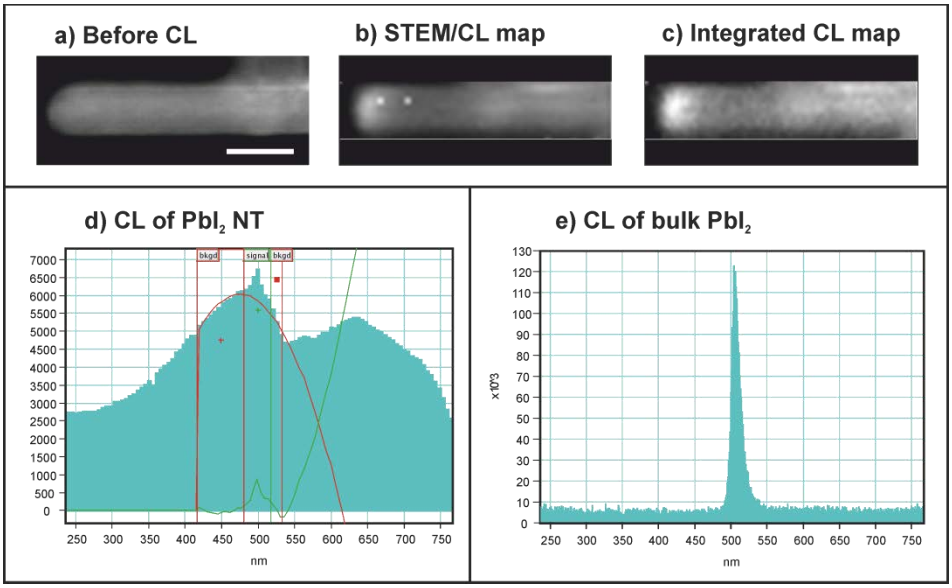

Figure 5.14 Cathodoluminescence (CL) in STEM mode of single MWCNT@PbI_2 hybrid. (a) HAADF-STEM image of the hybrid before the CL acquisition; (b) STEM/CL map; (c) CL map after signal integration and removal of the background; d) CL signal integrated over the background and e) CL signal of the bulk material.

Remarkably, cathodoluminescence signal was obtained from individual MWCNT@PbI_2 hybrid of 33.8 nm in diameter (**Figure 5.14 a**). The emission band originating from the hybrid was centered at 495 nm (2.50 eV), what corresponds to a slight shift of the band-to band transition when compared to bulk PbI_2 (**e**) which CL signal was centered at 505 nm (2.45 eV). These results are consistent with the same shift measured by PL.

5.2.6 Stability studies

During long exposures when performing electron microscopy imaging and elemental analysis we noticed that lead iodide monolayers underwent

decomposition leading to the formation of nanoparticles on the walls of MWCNTs (**Figure 5.15**).

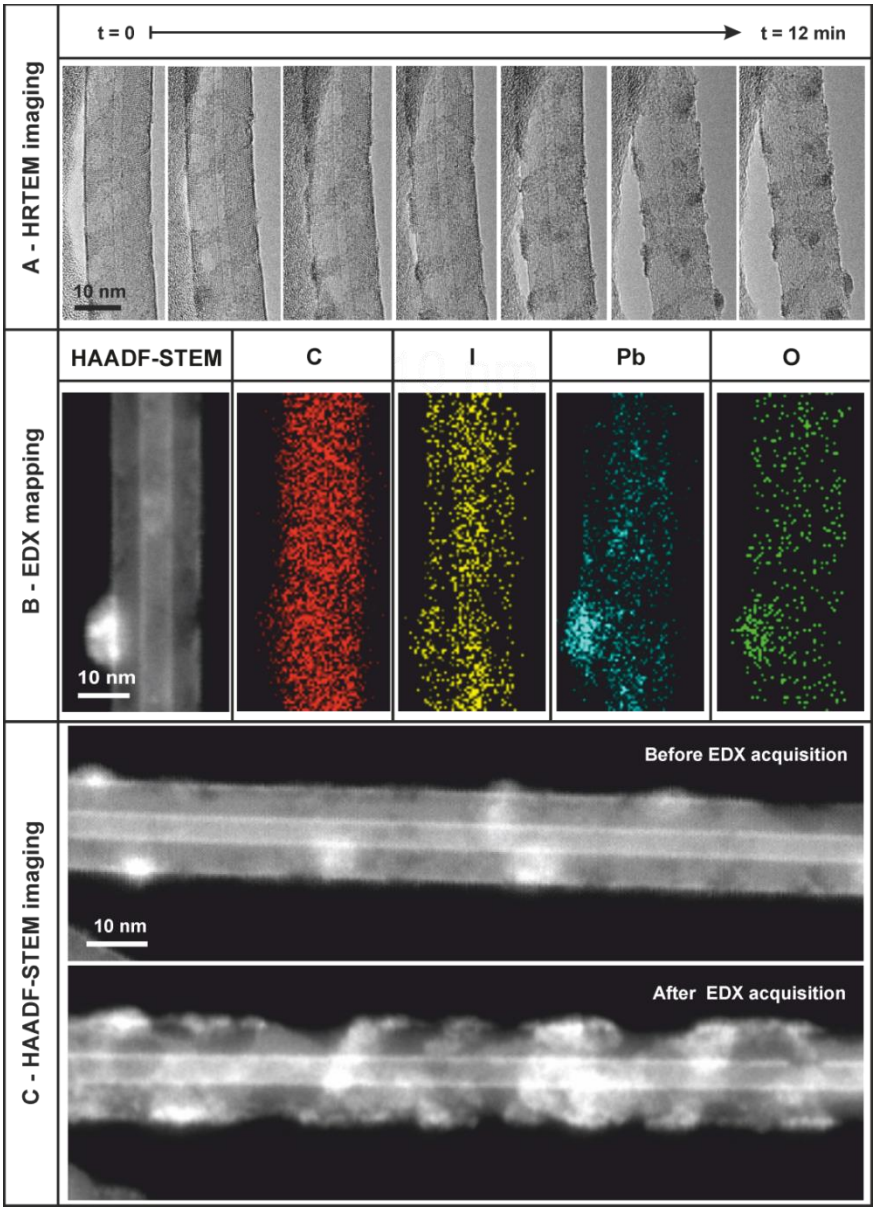

Figure 5.15 Electron beam induced decomposition of the outer layer of PbI_2: A) HRTEM imaging of the process of decomposition of PbI_2 nanotube and formation of nanoparticles; B) EDX mapping of $tPbI_2$@MWCNT@$tPbI_2$ hybrid with attached

nanoparticle (lead and oxygen rich); C) HAADF-STEM images of single $tPbI_2$@MWCNT@$tPbI_2$ hybrid before (top) and after (bottom) EDX map acquisition.

This effect was attributed to the highly energetic beam of electrons interacting with the sample and inducing decomposition of lead iodide. As may be seen on **Figure 5.15 panel A**, a complete decomposition of the outer layer of lead iodide and formation of nanoparticles occurred in HRTEM mode in only 12 min of exposure (Tecnai F20 at 200 kV). In panel **B**, the EDX mapping of a $tPbI_2$@MWCNTs@PbI_2 hybrid already shows some indications of destruction, what is confirmed in panel **C** where the comparison between HAADF-STEM images before and after map acquisition are shown with visible damage caused on the surface (Tecnai Osiris at 120 kV). Interestingly, the internal PbI_2 nanotube seems to be intact after the EDX mapping, which means carbon nanotubes are effective in preventing its destruction.

The same behaviour was seen for the samples left on the bench and consequently exposed to sunlight. The photodecomposition occurred with time leading to the formation of nanoparticles on the external walls of CNTs (**Figure 5.16**). It can be seen on HRTEM image acquired at 200 kV (on the left of panel **A**), PbI_2 nanotube and PbI_2 nanowire are intact in the interior cavity of MWCNTs while on the exterior wall nanoparticles are present. The nanoparticles were found to be composed of PbO, as confirmed by HRTEM on **Figure 5.16 A** (right panel) and by EDX elemental mapping on **Figure 5.15 B**. It should be noted, when stored in dark, the MWCNT@PbI_2 hybrids were found to be stablet even after 4 months.

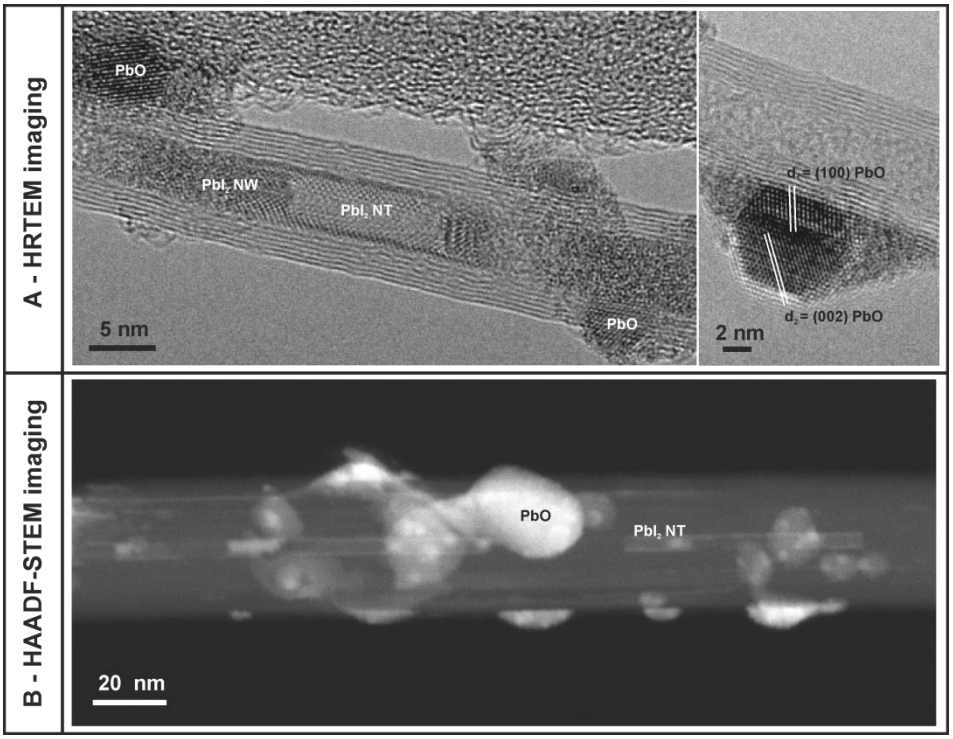

Figure 5.16 Photodecomposition of lead iodide external nanotubes in MWCNTs@PbI_2 due to storage conditions: A) HRTEM images of as formed PbO nanoparticles. The internal structures, i.e. PbI_2 nanowire (NW) and PbI_2 nanotube (NT) remained intact after 4 months on the bench (directly exposed to sunlight); B) HAADF-STEM image of as formed PbO nanoparticles and the internal PbI_2 NT.

5.3 Conclusions

To summarize, a simple method was used to prepare a unique structure composed of lead iodide single layers enrolled on top of multi-walled carbon nanotubes with extremely high efficiency (99%). Extensive characterization by electron microscopy imaging, spectroscopy and X-Ray diffraction was performed showing smooth, highly crystalline monolayers of PbI_2 spread along MWCNTs. In some cases PbI_2 nanotubes and/or nanowires were contained in the interior cavity of MWCNTs, giving rise to more complex hybrid structures.

The sample composed of hybrids with wide range of diameters resulted in blue shifted band-to-band component of photoluminescence signal when compared with bulk. Moreover a wide band centered at ~2.0 eV and assigned to radiative recombination of electron-hole pairs at surface defects was described at lower laser energy (473 nm). At higher laser excitation energy (266 nm) the 2.0 eV band decreased substantially while intrinsic band-to-band transition was enhanced showing a slight blue shift when compared with bulk PbI_2. Additionally, a high energy transition centered at 3.2 eV was tentatively attributed to narrow diameter lead iodide NTs or NWs confined in the interior cavities of MWCNTs. Further studies at low temperature are planned to get a better insight to the intrinsic properties of our hybrids.

Cathodoluminescence of individual MWCNT@PbI_2 hybrid showed the band-to-band transition was centered at 2.50 eV while for the bulk PbI_2 it was centered at 2.45 eV. Therefore a slight shift to higher energy was confirmed and was found to fit well with PL results and literature. Based on used materials and techniques the development of new heterostructures of akin nature may be achieved and adapted for applications in optoelectronic devices, solar cells, photovoltaics and others.

6 General conclusions

The main achievements of this Thesis can be summarized as follows:

Part I: "Nanocapsules for imaging and targeted delivery"

- Individual SWCNTs can be can be imaged by means of surface sensitive HRSEM at 2 kV by employing orthodichlorobenzene as a dispersing agent and TEM carbon coated Cu grids as support. By using these parameters, we have been able to study the shortening of SWCNTs by steam treatment. Short nanotubes (ca. 200 nm median length) are obtained after 10 h of steam, and their length does not change significantly even after 25 h of steam treatment.

- The efficiency of the filling and washing steps has been established for a myriad of potentially radioactivable inorganic salts, including $LuCl_3$, LuI_3, $SmCl_3$, $EuCl_3$, NaI, KI, CuI, CuBr, ZnI_2, CeI_3, $CeCl_3$, PbI_2 and $GdCl_3$. The most suitable protocol for the washing of the external material has been shown to be the combination of Soxhlet and dialysis procedures.

- The encapsulated materials adopt different structures once filled into the CNTs. Nanowires, nanoparticles, nanosnakes and nanotubes have been observed. Nanotubes are present when the encapsulated material has a layered structure. We have determined that the yield of nanotubes is enhanced when increasing the synthesis temperature.

- Visualization of the organic moieties attached on the external walls of CNTs has been possible by attachment of functional groups with heavy element tags, such as Gd and I. In addition, successful immobilization of antibody Cetuximab along the CNT walls has been proved by imaging gold nanoparticles conjugated to an immunostained secondary antibody.

- Low voltage STEM has proved useful to visualize the interaction of MWCNT-NH_3^+ with brain endothelial cells, providing the first evidence of translocation capabilities of functionalized MWCNTs through blood-brain barrier

(BBB) in an *in vitro* model. Significant reduction in the transport of nanotubes across BBB has been observed at 4 °C, an indication of the energy-dependent pathway of CNTs uptake.

- Cellular uptake of peptide-functionalized SWCNTs filled with PbO, BaI_2 or Kr into HeLa cells and their trafficking towards the nucleus has been observed by low voltage STEM featuring higher spatial resolution than Raman and optical microscopies.

Part II: "Single-layered inorganic nanotubes shaped by carbon nanotubes"

- Subnanometer single-layered lutetium halide nanotubes have been successfully synthesized by using the interior cavities of SWCNTs as hosts for their growth. There is a preferential distribution of diameters depending on the size of the lutetium halide anion. Larger nanotubes are formed for iodide while chloride and bromide present the highest population at lower diameters. Aberration corrected STEM combined with image simulations has provided an unambiguous proof of the tubular structure of the encapsulated lutetium halides.

- Lead iodide single-layered nanotubes can be obtained on the external walls of CNTs with 99% yield by using straight arc-discharge MWCNTs as templates. We have confirmed their structure by aberration-corrected STEM and electron tomography, as well as their composition by STEM-EDX mapping. The optical signal of these hybrids is blue-shifted with respect to that of PbI_2 in bulk. Remarkably, detection of cathodoluminescence from an individual hybrid has been successfully achieved by STEM-CL.

7 Publications

1. "Sub-nanometer diameter single-layer lutetium halide nanotubes grown inside SWCNTs" Elzbieta Pach, Magdalena Kierkowicz, Mert Kurttepeli, Carlos Frontera, Riccardo Rurali, Sara Bals, Gustaaf van Tendeloo, Gerard Tobias, Belén Ballesteros, to be submitted

2. "Single-layer lead iodide nanotubes enrolled on multi-walled carbon nanotubes" Elzbieta Pach, Laura Cabana, Mert Kurttepeli, Alfredo Segura, Mathieu Kociak, Sara Bals, Gustaaf van Tendeloo, Gerard Tobias, Belén Ballesteros, to be submitted

3. "Charge transfer in steam purified arc discharge single walled carbon nanotubes filled with lutetium halides" Ana Santidrián, Magdalena Kierkowicz , Elzbieta Pach , Denisa Darvasiová, Belén Ballesteros, Gerard Tobias, Martin Kalbáč, to be submitted

4. "Encapsulation of two-dimensional materials inside carbon nanotubes: towards an enhanced synthesis of single-layered metal halides" Stefania Sandoval, Elzbieta Pach, Belén Ballesteros, Gerard Tobias, in revision *Carbon*

5. "Filling Single-Walled Carbon Nanotubes with Lutetium Chloride: A Sustainable Production of Nanocapsules Free of Non-Encapsulated Material" Magdalena Kierkowicz, Jose Miguel Gonzalez-Dominguez, Elzbieta Pach, Stefania Sandoval, Belen Ballesteros, Tatiana Da Ros, Gerard Tobias, *ACS Sustainable Chemistry and Engineering* **2017**, 5 (3), pp 2501-2508, doi: 10.1021/acssuschemeng.6b02850

6. "Evaluation of the immunological profile of antibody-functionalized metal-filled single-walled carbon nanocapsules for targeted radiotherapy" Aritz Perez Ruiz de Garibay, Cinzia Spinato, Rebecca Klippstein, Maxime Bourgognon, Markus Martincic, Elzbieta Pach, Belén Ballesteros, Cécilia

Ménard-Moyon, Khuloud T. Al-Jamal, Gerard Tobias, and Alberto Bianco, *Scientific Reports* **2017**, 7: 42605, doi: 10.1038/srep42605

7. "Carbon nanotubes allow capture of krypton, barium and lead for multichannel biological X-ray fluorescence imaging" J. Serpell, Reida N. Rutte, Kalotina Geraki, Elzbieta Pach, Markus Martincic, Magdalena Kierkowicz, Sonia De Munari, Kim Wals, Ritu Raj, Belen Ballesteros, Gerard Tobias, Daniel C. Anthony, Benjamin G. Davis Christopher, *Nature Communications* **2016**, 7: 13118, doi: 10.1038/ncomms13118

8. "Synthesis of dry $SmCl_3$ from Sm_2O_3 revisited. Implications for the encapsulation of samarium compounds into carbon nanotubes" Markus Martincic, Carlos Frontera, Elzbieta Pach, Belén Ballesteros, Gerard Tobias, *Polyhedron* **2016**, Vol. 116, pp 116-121, doi: 10.1016/j.poly.2016.03.045

9. "Gadolinium-functionalised multi-walled carbon nanotubes as a T_1 contrast agent for MRI cell labelling and tracking" Ania Servant, Igor Jacobs, Cyrill Bussy, Chiara Fabbro, Tatiana Da Ros, Elzbieta Pach, Belen Ballesteros, Maurizio Prato, Klaas Nicolay, Kostas Kostarelos, *Carbon* **2016**, Vol. 97, pp. 126-133, doi: 10.1016/j.carbon.2015.08.051

10. "Effect of Steam-Treatment Time on the Length and Structure of Single-Walled and Double-Walled Carbon Nanotubes" Magdalena Kierkowicz, Elzbieta Pach, Ana Santidrián, Ester Tobías-Rossell, Martin Kalbáč, Belén Ballesteros, Gerard Tobias, *ChemNanoMat* **2016**, Vol. 2, Issue 2, pp. 108-116, doi: 10.1002/cnma.201500207

11. "Design of antibody-functionalized carbon nanotubes filled with radioactivable metals towards a targeted anticancer therapy" Cinzia Spinato, Aritz Perez Ruiz de Garibay, Magdalena Kierkowicz, Elzbieta Pach, Markus Martincic, Rebecca Klippstein, Maxime Bourgognon, Julie

Tzu-Wen Wang, Cécilia Ménard-Moyon, Khuloud T. Al-Jamal, Belén Ballesteros, Gerard Tobias, Alberto Bianco, *Nanoscale* **2016**, 8, pp. 12626-12638, doi: 10.1039/C5NR07923C

12. "The interaction of carbon nanotubes with an *in vitro* blood-brain barrier model and mouse brain *in vivo*" Houmam Kafa, Julie Tzu-Wen Wang, Noelia Rubio, Kerrie Venner, Glenn Anderson, Elzbieta Pach, Belén Ballesteros, Jane E Preston, N Joan Abbott, Khuloud T Al-Jamal, *Biomaterials* **2015**, Vol. 53, pp. 437-452, doi: 10.1016/j.biomaterials.2015.02.083

13. "Quantitative monitoring of the removal of non-encapsulated material external to filled carbon nanotube samples" Markus Martincic, Elzbieta Pach, Belén Ballesteros, Gerard Tobias, *Physical Chemistry Chemical Physics* **2015**, 17, pp. 31662-31669, doi: 10.1039/C5CP04664E

14. "Production of Water-Soluble Few-Layer Graphene Mesosheets by Dry Milling with Hydrophobic Drug" Noelia Rubio, Rui Serra-Maia, Houmam Kafa, Kuo-Ching Mei, Elzbieta Pach, William Luckhurst, Mire Zloh, Frederic Festy, Jonathan P. Richardson, Julian R. Naglik, Belén Ballesteros, and Khuloud T. Al-Jamal, *Langmuir* **2014**, 30 (49), pp. 14999-15008, doi: 10.1021/la5038475

15. "Covalent Functionalization of Multi-walled Carbon Nanotubes with a Gadolinium Chelate for Efficient T_1-Weighted Magnetic Resonance Imaging" Iris Marangon, Cécilia Ménard-Moyon, Jelena Kolosnjaj-Tabi, Marie Lys Béoutis, Lénaic Lartigue, Damien Alloyeau, Elzbieta Pach, Belén Ballesteros, Gwennhael Autret, Tsedev Ninjbadgar, Dermot F. Brougham, Alberto Bianco and Florence Gazeau, *Advanced Functional Materials* **2014**, Vol. 24, Issue 45, pp. 7173-7186, doi: 10.1002/adfm.201402234

8 Bibliography

1. Kroto, H.W., et al., *C60: Buckminsterfullerene.* Nature, 1985. **318**(6042): p. 162-163.
2. Iijima, S., *Helical microtubules of graphitic carbon.* Nature, 1991. **354**(6348): p. 56-58.
3. Moisala, A., A.G. Nasibulin, and E.I. Kauppinen, *The role of metal nanoparticles in the catalytic production of single-walled carbon nanotubes—a review.* Journal of Physics: Condensed Matter, 2003. **15**(42): p. S3011-S3035.
4. Maser, W.K., et al., *Production of high-density single-walled nanotube material by a simple laser-ablation method.* Chemical Physics Letters, 1998. **292**(4-6): p. 587-593.
5. Journet, C., et al., *Large-scale production of single-walled carbon nanotubes by the electric-arc technique.* Nature, 1997. **388**(6644): p. 756-758.
6. Treacy, M.M.J., T.W. Ebbesen, and J.M. Gibson, *Exceptionally high Young's modulus observed for individual carbon nanotubes.* Nature, 1996. **381**(6584): p. 678-680.
7. Krishnan, A., et al., *Young's modulus of single-walled nanotubes.* Physical Review B, 1998. **58**(20): p. 14013-14019.
8. Falvo, M.R., et al., *Bending and buckling of carbon nanotubes under large strain.* Nature, 1997. **389**(6651): p. 582-4.
9. Poncharal, P., *Electrostatic Deflections and Electromechanical Resonances of Carbon Nanotubes.* Science, 1999. **283**(5407): p. 1513-1516.
10. Peng, H., et al., *Sidewall carboxylic acid functionalization of single-walled carbon nanotubes.* J Am Chem Soc, 2003. **125**(49): p. 15174-82.
11. Hamada, N., S. Sawada, and A. Oshiyama, *New one-dimensional conductors: Graphitic microtubules.* Phys Rev Lett, 1992. **68**(10): p. 1579-1581.
12. Saito, R., et al., *Electronic structure of graphene tubules based onC60.* Physical Review B, 1992. **46**(3): p. 1804-1811.
13. Wilder, J.W.G., et al., Nature, 1998. **391**(6662): p. 59-62.
14. Lieber, C.M., et al., Nature, 1998. **391**(6662): p. 62-64.
15. de Heer, W.A., A. Ch telain, and D. Ugarte, *A Carbon Nanotube Field-Emission Electron Source.* Science, 1995. **270**(5239): p. 1179-1180.
16. Dai, H., E.W. Wong, and C.M. Lieber, *Probing Electrical Transport in Nanomaterials: Conductivity of Individual Carbon Nanotubes.* Science, 1996. **272**(5261): p. 523-526.
17. Ebbesen, T.W., et al., *Electrical conductivity of individual carbon nanotubes.* Nature, 1996. **382**(6586): p. 54-56.
18. Liang, S.-D., *Intrinsic properties of electronic structure in commensurate double-wall carbon nanotubes.* Physica B: Condensed Matter, 2004. **352**(1-4): p. 305-311.
19. Yanagi, K., et al., *Transport mechanisms in metallic and semiconducting single-wall carbon nanotube networks.* ACS Nano, 2010. **4**(7): p. 4027-32.
20. O'Connell, M.J., et al., *Band gap fluorescence from individual single-walled carbon nanotubes.* Science, 2002. **297**(5581): p. 593-6.
21. Bachilo, S.M., et al., *Structure-assigned optical spectra of single-walled carbon nanotubes.* Science, 2002. **298**(5602): p. 2361-6.

22. Wang, F., et al., *The optical resonances in carbon nanotubes arise from excitons.* Science, 2005. **308**(5723): p. 838-41.
23. Green, A.A. and M.C. Hersam, *Processing and properties of highly enriched double-wall carbon nanotubes.* Nat Nanotechnol, 2009. **4**(1): p. 64-70.
24. Tsyboulski, D.A., et al., *Structure-dependent fluorescence efficiencies of individual single-walled carbon nanotubes.* Nano Lett, 2007. **7**(10): p. 3080-5.
25. Yang, S., et al., *Photoluminescence from inner walls in double-walled carbon nanotubes: some do, some do not.* Nano Lett, 2011. **11**(10): p. 4405-10.
26. Ando, T., *Excitons in Carbon Nanotubes.* Journal of the Physics Society Japan, 1997. **66**(4): p. 1066-1073.
27. Strano, M.S., et al., *Assignment of (n,m) Raman and Optical Features of Metallic Single-Walled Carbon Nanotubes.* Nano Letters, 2003. **3**(8): p. 1091-1096.
28. Benedict, L.X., S.G. Louie, and M.L. Cohen, *Heat capacity of carbon nanotubes.* Solid State Communications, 1996. **100**(3): p. 177-180.
29. Yi, W., et al., *Linear specific heat of carbon nanotubes.* Physical Review B, 1999. **59**(14): p. R9015-R9018.
30. Pop, E., et al., *Thermal conductance of an individual single-wall carbon nanotube above room temperature.* Nano Lett, 2006. **6**(1): p. 96-100.
31. Berber, S., Y.K. Kwon, and D. Tomanek, *Unusually high thermal conductivity of carbon nanotubes.* Phys Rev Lett, 2000. **84**(20): p. 4613-6.
32. Pettes, M.T. and L. Shi, *Thermal and Structural Characterizations of Individual Single-, Double-, and Multi-Walled Carbon Nanotubes.* Advanced Functional Materials, 2009. **19**(24): p. 3918-3925.
33. Chiang, I.W., et al., *Purification and Characterization of Single-Wall Carbon Nanotubes.* The Journal of Physical Chemistry B, 2001. **105**(6): p. 1157-1161.
34. Tohji, K., et al., *Purifying single-walled nanotubes.* Nature, 1996. **383**(6602): p. 679-679.
35. Tobias, G., et al., *Purification and opening of carbon nanotubes using steam.* J Phys Chem B, 2006. **110**(45): p. 22318-22.
36. Ballesteros, B., et al., *Steam purification for the removal of graphitic shells coating catalytic particles and the shortening of single-walled carbon nanotubes.* Small, 2008. **4**(9): p. 1501-6.
37. Shen, K., et al., *Single-walled carbon nanotube purification, pelletization, and surfactant-assisted dispersion: a combined TEM and resonant micro-raman spectroscopy study.* J Phys Chem B, 2005. **109**(10): p. 4455-63.
38. Dujardin, E., et al., *Purification of Single-Shell Nanotubes.* Advanced Materials, 1998. **10**(8): p. 611-613.
39. Xu, Y.Q., et al., *Controlled multistep purification of single-walled carbon nanotubes.* Nano Lett, 2005. **5**(1): p. 163-8.
40. Fang, H.-T., et al., *Purification of Single-Wall Carbon Nanotubes by Electrochemical Oxidation.* Chemistry of Materials, 2004. **16**(26): p. 5744-5750.

41. Murphy, R., et al., *High-Yield, Nondestructive Purification and Quantification Method for Multiwalled Carbon Nanotubes.* The Journal of Physical Chemistry B, 2002. **106**(12): p. 3087-3091.
42. Liu, J., et al., *Fullerene pipes.* Science, 1998. **280**(5367): p. 1253-6.
43. Kierkowicz, M., et al., *Effect of Steam-Treatment Time on the Length and Structure of Single-Walled and Double-Walled Carbon Nanotubes.* ChemNanoMat, 2016. **2**(2): p. 108-116.
44. Zheng, M., et al., *DNA-assisted dispersion and separation of carbon nanotubes.* Nat Mater, 2003. **2**(5): p. 338-42.
45. Chen, R.J., et al., *Noncovalent functionalization of carbon nanotubes for highly specific electronic biosensors.* Proc Natl Acad Sci U S A, 2003. **100**(9): p. 4984-9.
46. Besteman, K., et al., *Enzyme-Coated Carbon Nanotubes as Single-Molecule Biosensors.* Nano Letters, 2003. **3**(6): p. 727-730.
47. Moore, V.C., et al., *Individually Suspended Single-Walled Carbon Nanotubes in Various Surfactants.* Nano Letters, 2003. **3**(10): p. 1379-1382.
48. Tobias, G. and E. Flahaut, *CHAPTER 16. Smart Carbon Nanotubes.* 2013. **2**: p. 90-116.
49. Leonhardt, A., et al., *Synthesis, Properties, and Applications of Ferromagnetic-Filled Carbon Nanotubes.* Chemical Vapor Deposition, 2006. **12**(6): p. 380-387.
50. Hampel, S., et al., *Growth and characterization of filled carbon nanotubes with ferromagnetic properties.* Carbon, 2006. **44**(11): p. 2316-2322.
51. Zhang, X., et al., *Rapid growth of well-aligned carbon nanotube arrays.* Chemical Physics Letters, 2002. **362**(3-4): p. 285-290.
52. Deck, C.P. and K. Vecchio, *Growth mechanism of vapor phase CVD-grown multi-walled carbon nanotubes.* Carbon, 2005. **43**(12): p. 2608-2617.
53. Kunadian, I., et al., *Growth kinetics of MWCNTs synthesized by a continuous-feed CVD method.* Carbon, 2009. **47**(2): p. 384-395.
54. Müller, C., et al., *Growth studies, TEM and XRD investigations of iron-filled carbon nanotubes.* physica status solidi (a), 2006. **203**(6): p. 1064-1068.
55. Müller, C., et al., *Iron filled carbon nanotubes grown on substrates with thin metal layers and their magnetic properties.* Carbon, 2006. **44**(9): p. 1746-1753.
56. Seraphin, S., et al., *Yttrium carbide in nanotubes.* Nature, 1993. **362**(6420): p. 503-503.
57. Satishkumar, B.C., et al., *Novel experiments with carbon nanotubes: opening, filling, closing and functionalizing nanotubes.* Journal of Physics B: Atomic, Molecular and Optical Physics, 1996. **29**(21): p. 4925-4934.
58. Monthioux, M., *Filling single-wall carbon nanotubes.* Carbon, 2002. **40**(10): p. 1809-1823.
59. Tasis, D., et al., *Chemistry of carbon nanotubes.* Chem Rev, 2006. **106**(3): p. 1105-36.
60. Tobias, G., B. Ballesteros, and M.L.H. Green, *Carbon nanocapsules: blocking materials inside carbon nanotubes.* Physica Status Solidi (C), 2010. **7**(11-12): p. 2739-2742.

61. Gautam, U.K., et al., *Recent developments in inorganically filled carbon nanotubes: successes and challenges.* Science and Technology of Advanced Materials, 2016. **11**(5): p. 054501.
62. Chancolon, J., et al., *Filling of carbon nanotubes with selenium by vapor phase process.* J Nanosci Nanotechnol, 2006. **6**(1): p. 82-6.
63. Fröhlich, T., et al., *Insertion of C60 into multi-wall carbon nanotubes—a synthesis of C60@MWCNT.* Carbon, 2004. **42**(12-13): p. 2759-2762.
64. Fedotov, P.V., et al., *Optical properties of single-walled carbon nanotubes filled with CuCl by gas-phase technique.* physica status solidi (b), 2014. **251**(12): p. 2466-2470.
65. Baaziz, W., et al., *High-Density Monodispersed Cobalt Nanoparticles Filled into Multiwalled Carbon Nanotubes.* Chemistry of Materials, 2012. **24**(9): p. 1549-1551.
66. Kharlamova, M.V., et al., *Study of the electronic structure of single-walled carbon nanotubes filled with cobalt bromide.* JETP Letters, 2010. **91**(4): p. 196-200.
67. Cabana, L., et al., *Synthesis of PbI_2 single-layered inorganic nanotubes encapsulated within carbon nanotubes.* Advanced Materials, 2014. **26**(13): p. 2016-21.
68. Keller, N., et al., *Carbon nanotubes as a template for mild synthesis of magnetic CoFe2O4 nanowires.* Carbon, 2004. **42**(7): p. 1395-1399.
69. Sutter, E. and P. Sutter, *Au-Induced Encapsulation of Ge Nanowires in Protective C Shells.* Advanced Materials, 2006. **18**(19): p. 2583-2588.
70. Sutter, E., et al., *Assembly of ordered carbon shells on GaN nanowires.* Applied Physics Letters, 2007. **90**(9): p. 093118.
71. Dyke, C.A. and J.M. Tour, *Overcoming the insolubility of carbon nanotubes through high degrees of sidewall functionalization.* Chemistry, 2004. **10**(4): p. 812-7.
72. Wu, H.-C., et al., *Chemistry of carbon nanotubes in biomedical applications.* J. Mater. Chem., 2010. **20**(6): p. 1036-1052.
73. Monthioux, M., et al., *Sensitivity of single-wall carbon nanotubes to chemical processing: an electron microscopy investigation.* Carbon, 2001. **39**(8): p. 1251-1272.
74. Hamon, M.A., et al., *End-group and defect analysis of soluble single-walled carbon nanotubes.* Chemical Physics Letters, 2001. **347**(1-3): p. 8-12.
75. Luksirikul, P., et al., *Sidewall functionalisation of carbon nanotubes by addition of diarylcarbene derivatives.* Journal of Materials Chemistry, 2011. **21**(47): p. 19080.
76. Chen, J., *Solution Properties of Single-Walled Carbon Nanotubes.* Science, 1998. **282**(5386): p. 95-98.
77. Holzinger, M., et al., *Sidewall Functionalization of Carbon Nanotubes This work was supported by the European Union under the 5th Framework Research Training Network 1999, HPRNT 1999-00011 FUNCARS.* Angewandte Chemie International Edition, 2001. **40**(21): p. 4002.
78. Khabashesku, V.N., W.E. Billups, and J.L. Margrave, *Fluorination of Single-Wall Carbon Nanotubes and Subsequent Derivatization Reactions.* Accounts of Chemical Research, 2002. **35**(12): p. 1087-1095.

79. Boul, P.J., et al., *Reversible sidewall functionalization of buckytubes.* Chemical Physics Letters, 1999. **310**(3-4): p. 367-372.
80. Saini, R.K., et al., *Covalent sidewall functionalization of single wall carbon nanotubes.* J Am Chem Soc, 2003. **125**(12): p. 3617-21.
81. Umek, P., et al., *Addition of Carbon Radicals Generated from Organic Peroxides to Single Wall Carbon Nanotubes.* Chemistry of Materials, 2003. **15**(25): p. 4751-4755.
82. Balaban, T.S., et al., *Polyacylation of Single-Walled Nanotubes under Friedel–Crafts Conditions: An Efficient Method for Functionalizing, Purifying, Decorating, and Linking Carbon Allotropes.* Advanced Materials, 2006. **18**(20): p. 2763-2767.
83. Chen, S., et al., *A new approach to the functionalization of single-walled carbon nanotubes with both alkyl and carboxyl groups.* Chemical Physics Letters, 2005. **402**(4-6): p. 312-317.
84. Banerjee, S. and S.S. Wong, *Demonstration of Diameter-Selective Reactivity in the Sidewall Ozonation of SWNTs by Resonance Raman Spectroscopy.* Nano Letters, 2004. **4**(8): p. 1445-1450.
85. Yudasaka, M., et al., *Effect of an organic polymer in purification and cutting of single-wall carbon nanotubes.* Applied Physics A: Materials Science & Processing, 2000. **71**(4): p. 449-451.
86. Koshio, A., et al., *A Simple Way to Chemically React Single-Wall Carbon Nanotubes with Organic Materials Using Ultrasonication.* Nano Letters, 2001. **1**(7): p. 361-363.
87. Coleman, J.N., et al., *High Performance Nanotube-Reinforced Plastics: Understanding the Mechanism of Strength Increase.* Advanced Functional Materials, 2004. **14**(8): p. 791-798.
88. Shaffer, M.S.P. and K. Koziol, *Polystyrene grafted multi-walled carbon nanotubes.* Chemical Communications, 2002(18): p. 2074-2075.
89. Qin, S., et al., *Solubilization and Purification of Single-Wall Carbon Nanotubes in Water by in Situ Radical Polymerization of Sodium 4-Styrenesulfonate.* Macromolecules, 2004. **37**(11): p. 3965-3967.
90. Viswanathan, G., et al., *Single-step in situ synthesis of polymer-grafted single-wall nanotube composites.* J Am Chem Soc, 2003. **125**(31): p. 9258-9.
91. Vaisman, L., H.D. Wagner, and G. Marom, *The role of surfactants in dispersion of carbon nanotubes.* Adv Colloid Interface Sci, 2006. **128-130**: p. 37-46.
92. Rastogi, R., et al., *Comparative study of carbon nanotube dispersion using surfactants.* J Colloid Interface Sci, 2008. **328**(2): p. 421-8.
93. Foldvari, M. and M. Bagonluri, *Carbon nanotubes as functional excipients for nanomedicines: I. Pharmaceutical properties.* Nanomedicine, 2008. **4**(3): p. 173-82.
94. Staii, C., et al., *DNA-decorated carbon nanotubes for chemical sensing.* Nano Lett, 2005. **5**(9): p. 1774-8.

95. Zhang, X., L. Meng, and Q. Lu, *Cell behaviors on polysaccharide-wrapped single-wall carbon nanotubes: a quantitative study of the surface properties of biomimetic nanofibrous scaffolds.* ACS Nano, 2009. **3**(10): p. 3200-6.
96. Weizmann, Y., D.M. Chenoweth, and T.M. Swager, *Addressable terminally linked DNA-CNT nanowires.* J Am Chem Soc, 2010. **132**(40): p. 14009-11.
97. Klumpp, C., et al., *Functionalized carbon nanotubes as emerging nanovectors for the delivery of therapeutics.* Biochim Biophys Acta, 2006. **1758**(3): p. 404-12.
98. Sun, Y., S.R. Wilson, and D.I. Schuster, *High Dissolution and Strong Light Emission of Carbon Nanotubes in Aromatic Amine Solvents.* Journal of the American Chemical Society, 2001. **123**(22): p. 5348-5349.
99. Kong, J. and H. Dai, *Full and Modulated Chemical Gating of Individual Carbon Nanotubes by Organic Amine Compounds.* The Journal of Physical Chemistry B, 2001. **105**(15): p. 2890-2893.
100. Guo, Z., P.J. Sadler, and S.C. Tsang, *Immobilization and Visualization of DNA and Proteins on Carbon Nanotubes.* Advanced Materials, 1998. **10**(9): p. 701-703.
101. Arnold, M.S., et al., *Encapsulation of Carbon Nanotubes by Self-Assembling Peptide Amphiphiles.* Langmuir, 2005. **21**(10): p. 4705-4709.
102. Prakash, S., et al., *Polymeric nanohybrids and functionalized carbon nanotubes as drug delivery carriers for cancer therapy.* Adv Drug Deliv Rev, 2011. **63**(14-15): p. 1340-51.
103. Peng, X., et al., *Carbon nanotube-nanocrystal heterostructures.* Chem Soc Rev, 2009. **38**(4): p. 1076-98.
104. Jiang, L. and L. Gao, *Fabrication and characterization of ZnO-coated multi-walled carbon nanotubes with enhanced photocatalytic activity.* Materials Chemistry and Physics, 2005. **91**(2-3): p. 313-316.
105. Coleman, K.S., et al., *Functionalization of single-walled carbon nanotubes via the Bingel reaction.* J Am Chem Soc, 2003. **125**(29): p. 8722-3.
106. Li, C., et al., *Seed-Mediated Growth of ZnO Nanorods on Multiwalled Carbon Nanotubes.* Journal of Nanoscience and Nanotechnology, 2008. **8**(9): p. 4441-4446.
107. Liu, L., et al., *Self-assembly of gold nanoparticles to carbon nanotubes using a thiol-terminated pyrene as interlinker.* Chemical Physics Letters, 2003. **367**(5-6): p. 747-752.
108. Han, L., et al., *A Direct Route toward Assembly of Nanoparticle−Carbon Nanotube Composite Materials.* Langmuir, 2004. **20**(14): p. 6019-6025.
109. Planeix, J.M., et al., *Application of Carbon Nanotubes as Supports in Heterogeneous Catalysis.* Journal of the American Chemical Society, 1994. **116**(17): p. 7935-7936.
110. Georgakilas, V., et al., *Decorating carbon nanotubes with metal or semiconductor nanoparticles.* Journal of Materials Chemistry, 2007. **17**(26): p. 2679.
111. Juárez, B.H., et al., *Quantum Dot Attachment and Morphology Control by Carbon Nanotubes.* Nano Letters, 2007. **7**(12): p. 3564-3568.

112. Gu, F., C. Li, and S. Wang, *Solution-chemical synthesis of carbon nanotube/ZnS nanoparticle core/shell heterostructures.* Inorg Chem, 2007. **46**(13): p. 5343-8.
113. Han, W.-Q. and A. Zettl, *Coating Single-Walled Carbon Nanotubes with Tin Oxide.* Nano Letters, 2003. **3**(5): p. 681-683.
114. Zhang, Y. and H. Dai, *Formation of metal nanowires on suspended single-walled carbon nanotubes.* Applied Physics Letters, 2000. **77**(19): p. 3015.
115. Zhang, Y., et al., *Metal coating on suspended carbon nanotubes and its implication to metal–tube interaction.* Chemical Physics Letters, 2000. **331**(1): p. 35-41.
116. Huang, W., H. Chen, and J.M. Zuo, *One-dimensional self-assembly of metallic nanostructures on single-walled carbon-nanotube bundles.* Small, 2006. **2**(12): p. 1418-21.
117. Li, C., et al., *Decorating multiwalled carbon nanotubes with zinc oxide nanoparticles by thermally decomposing Zn-oleate in an organic medium.* Science in China Series E: Technological Sciences, 2008. **52**(5): p. 1254-1257.
118. Yu, H., et al., *TiO2−Multiwalled Carbon Nanotube Heterojunction Arrays and Their Charge Separation Capability.* The Journal of Physical Chemistry C, 2007. **111**(35): p. 12987-12991.
119. Kong, B.-S., et al., *Single-Walled Carbon Nanotube Gold Nanohybrids: Application in Highly Effective Transparent and Conductive Films.* The Journal of Physical Chemistry C, 2007. **111**(23): p. 8377-8382.
120. Vairavapandian, D., P. Vichchulada, and M.D. Lay, *Preparation and modification of carbon nanotubes: review of recent advances and applications in catalysis and sensing.* Anal Chim Acta, 2008. **626**(2): p. 119-29.
121. Sun, Z., et al., *Fabrication of Ruthenium-Carbon Nanotube Nanocomposites in Supercritical Water.* Advanced Materials, 2005. **17**(7): p. 928-932.
122. Lee, H., et al., *In-situ growth of copper sulfide nanocrystals on multiwalled carbon nanotubes and their application as novel solar cell and amperometric glucose sensor materials.* Nano Lett, 2007. **7**(3): p. 778-84.
123. Li, C., et al., *Controllable preparation and properties of composite materials based on ceria nanoparticles and carbon nanotubes.* Journal of Solid State Chemistry, 2008. **181**(10): p. 2620-2625.
124. Du, N., et al., *Porous Indium Oxide Nanotubes: Layer-by-Layer Assembly on Carbon-Nanotube Templates and Application for Room-Temperature NH3 Gas Sensors.* Advanced Materials, 2007. **19**(12): p. 1641-1645.
125. Rao, C.N.R., B.C. Satishkumar, and A. Govindaraj, *Zirconia nanotubes.* Chemical Communications, 1997(16): p. 1581-1582.
126. Li, J., et al., *Preparation of nanocomposites of metals, metal oxides, and carbon nanotubes via self-assembly.* J Am Chem Soc, 2007. **129**(30): p. 9401-9.
127. R.Rüdiger R. Meyer, J.S., Rafal E. Dunin-Borkowski, Angus I. Kirkland, Miles C. Novotny, Sam R. Bailey, John L. Hutchison, Malcolm L. H. Green, *Discrete Atom Imaging of One-Dimensional Crystals Formed Within Single-Walled Carbon Nanotubes.* Science, 2000. **289**(5483): p. 1324-1326.
128. Hong, S.Y., et al., *Filled and glycosylated carbon nanotubes for in vivo radioemitter localization and imaging.* Nat Mater, 2010. **9**(6): p. 485-90.

129. Lin, N., et al., *Scanning tunneling microscopy and spectroscopy of a carbon nanotube.* Carbon, 1996. **34**(10): p. 1295-1297.
130. Hassanien, A. and M. Tokumoto, *The electronic properties of suspended single wall carbon nanotubes.* Carbon, 2004. **42**(12-13): p. 2649-2653.
131. Kim, P., et al., *STM study of single-walled carbon nanotubes.* Carbon, 2000. **38**(11-12): p. 1741-1744.
132. Gimenez-Lopez Mdel, C., et al., *Encapsulation of single-molecule magnets in carbon nanotubes.* Nat Commun, 2011. **2**: p. 407.
133. Yase, K., et al., *Angular-resolved EELS of a carbon nanotube.* Thin Solid Films, 1996. **273**(1-2): p. 222-224.
134. Goode, A.E., et al., *Mapping functional groups on oxidised multi-walled carbon nanotubes at the nanometre scale.* Chem Commun (Camb), 2014. **50**(51): p. 6744-7.
135. Amama, P.B., et al., *XPS and Raman characterization of single-walled carbon nanotubes grown from pretreated Fe2O3nanoparticles.* Journal of Physics D: Applied Physics, 2008. **41**(16): p. 165306.
136. Droppa, R., et al., *Incorporation of nitrogen in carbon nanotubes.* Journal of Non-Crystalline Solids, 2002. **299-302**: p. 874-879.
137. Bahr, J.L., et al., *Functionalization of Carbon Nanotubes by Electrochemical Reduction of Aryl Diazonium Salts: A Bucky Paper Electrode.* Journal of the American Chemical Society, 2001. **123**(27): p. 6536-6542.
138. Dresselhaus, M.S., et al., *Single Nanotube Raman Spectroscopy.* Accounts of Chemical Research, 2002. **35**(12): p. 1070-1078.
139. Bahr, J.L. and J.M. Tour, *Highly Functionalized Carbon Nanotubes Using in Situ Generated Diazonium Compounds.* Chemistry of Materials, 2001. **13**(11): p. 3823-3824.
140. Kuzmany, H., et al., *Vibrational spectra of single wall carbon nanotubes.* Carbon, 1998. **36**(5-6): p. 709-712.
141. Cherukuri, P., et al., *Mammalian pharmacokinetics of carbon nanotubes using intrinsic near-infrared fluorescence.* Proc Natl Acad Sci U S A, 2006. **103**(50): p. 18882-6.
142. Hogele, A., et al., *Photon antibunching in the photoluminescence spectra of a single carbon nanotube.* Phys Rev Lett, 2008. **100**(21): p. 217401.
143. Barone, P.W., et al., *Near-infrared optical sensors based on single-walled carbon nanotubes.* Nat Mater, 2005. **4**(1): p. 86-92.
144. Njuguna, J., O.A. Vanli, and R. Liang, *A Review of Spectral Methods for Dispersion Characterization of Carbon Nanotubes in Aqueous Suspensions.* Journal of Spectroscopy, 2015. **2015**: p. 1-11.
145. Grossiord, N., et al., *Time-dependent study of the exfoliation process of carbon nanotubes in aqueous dispersions by using UV-visible spectroscopy.* Anal Chem, 2005. **77**(16): p. 5135-9.
146. Ryabenko, A.G., T.V. Dorofeeva, and G.I. Zvereva, *UV–VIS–NIR spectroscopy study of sensitivity of single-wall carbon nanotubes to chemical processing*

and Van-der-Waals SWNT/SWNT interaction. Verification of the SWNT content measurements by absorption spectroscopy. Carbon, 2004. **42**(8-9): p. 1523-1535.
147. Toshimitsu, F. and N. Nakashima, *Facile Isolation of Adsorbent-Free Long and Highly-Pure Chirality-Selected Semiconducting Single-Walled Carbon Nanotubes Using A Hydrogen-bonding Supramolecular Polymer.* Sci Rep, 2015. **5**: p. 18066.
148. Lauret, J.S., et al., *Bandgap photoluminescence of semiconducting single-wall carbon nanotubes.* Physica E: Low-dimensional Systems and Nanostructures, 2004. **21**(2-4): p. 1057-1060.
149. Cambedouzou, J. and P. Launois, *X-Ray Diffraction for Structural Studies of Carbon Nanotubes and their Insertion Compounds.* 2013: p. 81-127.
150. Kociak, M., et al., *How accurate can the determination of chiral indices of carbon nanotubes be?* The European Physical Journal B - Condensed Matter, 2003. **32**(4): p. 457-469.
151. Briones-Leon, A., et al., *Orbital and spin magnetic moments of transforming one-dimensional iron inside metallic and semiconducting carbon nanotubes.* Physical Review B, 2013. **87**(19).
152. Sun, K.J., R.A. Wincheski, and C. Park, *Magnetic property measurements on single wall carbon nanotube polyimide composites.* Journal of Applied Physics, 2008. **103**(2): p. 023908.
153. Grechnev, G.E., et al., *Magnetic properties of N-doped multi-walled carbon nanotubes.* Materialwissenschaft Und Werkstofftechnik, 2013. **44**(2-3): p. 136-138.
154. Bonavolontà, C., et al., *Non-destructive testing of a carbon-nanotube-reinforced composite using HTS-SQUID and electromagnetic techniques.* Superconductor Science and Technology, 2009. **22**(9): p. 095001.
155. Robati, D., S. Bagheriyan, and M. Rajabi, *Raman spectroscopy and TGA studies for the synthesis of multi-walled carbon nanotube-functionalized thiol (MWCNT-SH) nanocomposites: study of effect of concentration.* International Nano Letters, 2015. **5**(3): p. 179-182.
156. Ballesteros, B., et al., *Quantitative Assessment of the Amount of Material Encapsulated in Filled Carbon Nanotubes.* Journal of Physical Chemistry C, 2009. **113**(7): p. 2653-2656.
157. Vittorio, O., V. Raffa, and A. Cuschieri, *Influence of purity and surface oxidation on cytotoxicity of multiwalled carbon nanotubes with human neuroblastoma cells.* Nanomedicine, 2009. **5**(4): p. 424-31.
158. Dong, J. and Q. Ma, *Advances in mechanisms and signaling pathways of carbon nanotube toxicity.* Nanotoxicology, 2015. **9**(5): p. 658-76.
159. Dumortier, H., *When carbon nanotubes encounter the immune system: desirable and undesirable effects.* Adv Drug Deliv Rev, 2013. **65**(15): p. 2120-6.
160. Bhattacharya, K., et al., *Biological interactions of carbon-based nanomaterials: From coronation to degradation.* Nanomedicine, 2016. **12**(2): p. 333-51.
161. Park, E.J., et al., *Single-walled carbon nanotubes disturbed the immune and metabolic regulation function 13-weeks after a single intratracheal instillation.* Environ Res, 2016. **148**: p. 184-95.

162. Vietti, G., et al., *Towards predicting the lung fibrogenic activity of nanomaterials: experimental validation of an in vitro fibroblast proliferation assay.* Part Fibre Toxicol, 2013. **10**: p. 52.
163. Poland, C.A., et al., *Carbon nanotubes introduced into the abdominal cavity of mice show asbestos-like pathogenicity in a pilot study.* Nat Nanotechnol, 2008. **3**(7): p. 423-8.
164. Pantarotto, D., et al., *Synthesis, structural characterization, and immunological properties of carbon nanotubes functionalized with peptides.* J Am Chem Soc, 2003. **125**(20): p. 6160-4.
165. Huczko, A. and H. Lange, *Carbon Nanotubes: Experimental Evidence for a Null Risk of Skin Irritation and Allergy.* Fullerene Science and Technology, 2001. **9**(2): p. 247-250.
166. Shi Kam, N.W., et al., *Nanotube molecular transporters: internalization of carbon nanotube-protein conjugates into Mammalian cells.* J Am Chem Soc, 2004. **126**(22): p. 6850-1.
167. Pantarotto, D., et al., *Functionalized carbon nanotubes for plasmid DNA gene delivery.* Angew Chem Int Ed Engl, 2004. **43**(39): p. 5242-6.
168. !!! INVALID CITATION !!!
169. Palomaki, J., et al., *Long, needle-like carbon nanotubes and asbestos activate the NLRP3 inflammasome through a similar mechanism.* ACS Nano, 2011. **5**(9): p. 6861-70.
170. Wang, P., et al., *Multiwall carbon nanotubes mediate macrophage activation and promote pulmonary fibrosis through TGF-beta/Smad signaling pathway.* Small, 2013. **9**(22): p. 3799-811.
171. Liu, Y., et al., *Understanding the toxicity of carbon nanotubes.* Acc Chem Res, 2013. **46**(3): p. 702-13.
172. Case, B.W., et al., *Applying definitions of "asbestos" to environmental and "low-dose" exposure levels and health effects, particularly malignant mesothelioma.* J Toxicol Environ Health B Crit Rev, 2011. **14**(1-4): p. 3-39.
173. Kagan, V.E., et al., *Direct and indirect effects of single walled carbon nanotubes on RAW 264.7 macrophages: role of iron.* Toxicol Lett, 2006. **165**(1): p. 88-100.
174. Murray, A.R., et al., *Oxidative stress and inflammatory response in dermal toxicity of single-walled carbon nanotubes.* Toxicology, 2009. **257**(3): p. 161-71.
175. Lam, C.W., et al., *Pulmonary toxicity of single-wall carbon nanotubes in mice 7 and 90 days after intratracheal instillation.* Toxicol Sci, 2004. **77**(1): p. 126-34.
176. Mercer, R.R., et al., *Distribution and fibrotic response following inhalation exposure to multi-walled carbon nanotubes.* Part Fibre Toxicol, 2013. **10**: p. 33.
177. Mercer, R.R., et al., *Alteration of deposition pattern and pulmonary response as a result of improved dispersion of aspirated single-walled carbon nanotubes in a mouse model.* Am J Physiol Lung Cell Mol Physiol, 2008. **294**(1): p. L87-97.
178. Carrero-Sanchez, J.C., et al., *Biocompatibility and toxicological studies of carbon nanotubes doped with nitrogen.* Nano Lett, 2006. **6**(8): p. 1609-16.

179. Lacerda, L., et al., *Tissue histology and physiology following intravenous administration of different types of functionalized multiwalled carbon nanotubes.* Nanomedicine (Lond), 2008. **3**(2): p. 149-61.
180. Bardi, G., et al., *Pluronic-coated carbon nanotubes do not induce degeneration of cortical neurons in vivo and in vitro.* Nanomedicine, 2009. **5**(1): p. 96-104.
181. Taylor, A.J., et al., *Atomic layer deposition coating of carbon nanotubes with aluminum oxide alters pro-fibrogenic cytokine expression by human mononuclear phagocytes in vitro and reduces lung fibrosis in mice in vivo.* PLoS One, 2014. **9**(9): p. e106870.
182. De Volder, M.F., et al., *Carbon nanotubes: present and future commercial applications.* Science, 2013. **339**(6119): p. 535-9.
183. Chen, D., et al., *Theranostic applications of carbon nanomaterials in cancer: Focus on imaging and cargo delivery.* J Control Release, 2015. **210**: p. 230-45.
184. Bhirde, A.A., et al., *Targeted killing of cancer cells in vivo and in vitro with EGF-directed carbon nanotube-based drug delivery.* ACS Nano, 2009. **3**(2): p. 307-16.
185. Kam, N.W., et al., *Carbon nanotubes as multifunctional biological transporters and near-infrared agents for selective cancer cell destruction.* Proc Natl Acad Sci U S A, 2005. **102**(33): p. 11600-5.
186. Al-Jamal, K.T., et al., *Functional motor recovery from brain ischemic insult by carbon nanotube-mediated siRNA silencing.* Proc Natl Acad Sci U S A, 2011. **108**(27): p. 10952-7.
187. Sacchetti, C., et al., *Polyethylene-glycol-modified single-walled carbon nanotubes for intra-articular delivery to chondrocytes.* ACS Nano, 2014. **8**(12): p. 12280-91.
188. Kostarelos, K., et al., *Cellular uptake of functionalized carbon nanotubes is independent of functional group and cell type.* Nat Nanotechnol, 2007. **2**(2): p. 108-13.
189. Liu, Z., K. Yang, and S.-T. Lee, *Single-walled carbon nanotubes in biomedical imaging.* J. Mater. Chem., 2011. **21**(3): p. 586-598.
190. Robinson, J.T., et al., *In vivo fluorescence imaging in the second near-infrared window with long circulating carbon nanotubes capable of ultrahigh tumor uptake.* J Am Chem Soc, 2012. **134**(25): p. 10664-9.
191. Chen, M.L., et al., *Quantum dots conjugated with Fe3O4-filled carbon nanotubes for cancer-targeted imaging and magnetically guided drug delivery.* Langmuir, 2012. **28**(47): p. 16469-76.
192. Wu, H., et al., *Prostate stem cell antigen antibody-conjugated multiwalled carbon nanotubes for targeted ultrasound imaging and drug delivery.* Biomaterials, 2014. **35**(20): p. 5369-80.
193. De la Zerda, A., et al., *Carbon nanotubes as photoacoustic molecular imaging agents in living mice.* Nat Nanotechnol, 2008. **3**(9): p. 557-62.
194. Wang, C., et al., *RGD-conjugated silica-coated gold nanorods on the surface of carbon nanotubes for targeted photoacoustic imaging of gastric cancer.* Nanoscale Res Lett, 2014. **9**(1): p. 264.

195. Liu, Z., et al., *Multiplexed multicolor Raman imaging of live cells with isotopically modified single walled carbon nanotubes.* J Am Chem Soc, 2008. **130**(41): p. 13540-1.
196. Wang, X., et al., *Noble metal coated single-walled carbon nanotubes for applications in surface enhanced Raman scattering imaging and photothermal therapy.* J Am Chem Soc, 2012. **134**(17): p. 7414-22.
197. Ruggiero, A., et al., *Imaging and treating tumor vasculature with targeted radiolabeled carbon nanotubes.* Int J Nanomedicine, 2010. **5**: p. 783-802.
198. Al Faraj, A., A.P. Shaik, and A.S. Shaik, *Magnetic single-walled carbon nanotubes as efficient drug delivery nanocarriers in breast cancer murine model: noninvasive monitoring using diffusion-weighted magnetic resonance imaging as sensitive imaging biomarker.* Int J Nanomedicine, 2015. **10**: p. 157-68.
199. Das, M., et al., *Augmented anticancer activity of a targeted, intracellularly activatable, theranostic nanomedicine based on fluorescent and radiolabeled, methotrexate-folic Acid-multiwalled carbon nanotube conjugate.* Mol Pharm, 2013. **10**(7): p. 2543-57.
200. Liang, C., et al., *Tumor metastasis inhibition by imaging-guided photothermal therapy with single-walled carbon nanotubes.* Adv Mater, 2014. **26**(32): p. 5646-52.
201. Yinghuai, Z., et al., *Substituted carborane-appended water-soluble single-wall carbon nanotubes: new approach to boron neutron capture therapy drug delivery.* J Am Chem Soc, 2005. **127**(27): p. 9875-80.
202. Singh, R. and S.V. Torti, *Carbon nanotubes in hyperthermia therapy.* Adv Drug Deliv Rev, 2013. **65**(15): p. 2045-60.
203. Janib, S.M., A.S. Moses, and J.A. MacKay, *Imaging and drug delivery using theranostic nanoparticles.* Adv Drug Deliv Rev, 2010. **62**(11): p. 1052-63.
204. Lee, K., et al., *Progress in the synthesis of carbon nanotube- and nanofiber-supported Pt electrocatalysts for PEM fuel cell catalysis.* Journal of Applied Electrochemistry, 2006. **36**(5): p. 507-522.
205. Wildgoose, G.G., C.E. Banks, and R.G. Compton, *Metal nanoparticles and related materials supported on carbon nanotubes: methods and applications.* Small, 2006. **2**(2): p. 182-93.
206. Malek Abbaslou, R.M., et al., *Iron catalysts supported on carbon nanotubes for Fischer–Tropsch synthesis: effect of pore size.* 2009. **1**: p. 147-156.
207. Ashkarran, A.A., et al., *TiO2 nanoparticles immobilized on carbon nanotubes for enhanced visible-light photo-induced activity.* Journal of Materials Research and Technology, 2015. **4**(2): p. 126-132.
208. Suryawanshi, A., et al., *Doubling of photocatalytic H2 evolution from g-C3N4 via its nanocomposite formation with multivall carbon nanotubes: Electronic and morphological effects.* International Journal of Hydrogen Energy, 2012. **37**(12): p. 9584-9589.
209. Dai, L., et al., *Carbon nanomaterials for advanced energy conversion and storage.* Small, 2012. **8**(8): p. 1130-66.
210. Köhler, A.R., et al., *Studying the potential release of carbon nanotubes throughout the application life cycle.* Journal of Cleaner Production, 2008. **16**(8-9): p. 927-937.

211. Gong, K., et al., *Nitrogen-doped carbon nanotube arrays with high electrocatalytic activity for oxygen reduction.* Science, 2009. **323**(5915): p. 760-4.
212. Le Goff, A., et al., *From hydrogenases to noble metal-free catalytic nanomaterials for H2 production and uptake.* Science, 2009. **326**(5958): p. 1384-7.
213. Wang, L., et al., *Carbon nanotube-based heterostructures for solar energy applications.* Chem Soc Rev, 2013. **42**(20): p. 8134-56.
214. Trancik, J.E., S.C. Barton, and J. Hone, *Transparent and catalytic carbon nanotube films.* Nano Lett, 2008. **8**(4): p. 982-7.
215. Hu, L., et al., *Light-Induced Charge Transfer in Pyrene/CdSe-SWNT Hybrids.* Advanced Materials, 2008. **20**(5): p. 939-946.
216. Robel, I., B.A. Bunker, and P.V. Kamat, *Single-Walled Carbon Nanotube-CdS Nanocomposites as Light-Harvesting Assemblies: Photoinduced Charge-Transfer Interactions.* Advanced Materials, 2005. **17**(20): p. 2458-2463.
217. Dockendorf, C.P.R., et al., *Individual carbon nanotube soldering with gold nanoink deposition.* Applied Physics Letters, 2007. **90**(19).
218. Jurkschat, K., et al., *Multiwalled carbon nanotubes with molybdenum dioxide nanoplugs--new chemical nanoarchitectures by electrochemical modification.* Small, 2006. **2**(1): p. 95-8.
219. Huang, C.-S., et al., *Field emission properties of CNT–ZnO composite materials.* Diamond and Related Materials, 2009. **18**(2-3): p. 452-456.
220. Chaudhary, S., et al., *Fluorescence Microscopy Visualization of Single-Walled Carbon Nanotubes Using Semiconductor Nanocrystals.* Nano Letters, 2004. **4**(12): p. 2415-2419.
221. Liu, S., et al., *Mirror-image photoswitching of individual single-walled carbon nanotube transistors coated with titanium dioxide.* Angew Chem Int Ed Engl, 2009. **48**(26): p. 4759-62.
222. Star, A., et al., *Gas sensor array based on metal-decorated carbon nanotubes.* J Phys Chem B, 2006. **110**(42): p. 21014-20.
223. Mubeen, S., et al., *Palladium Nanoparticles Decorated Single-Walled Carbon Nanotube Hydrogen Sensor.* The Journal of Physical Chemistry C, 2007. **111**(17): p. 6321-6327.
224. Kumar, A., et al., *Ferroelectric-carbon nanotube memory devices.* Nanotechnology, 2012. **23**(16): p. 165702.
225. Kim, H.S., et al., *Hydrogen storage in ni nanoparticle-dispersed multiwalled carbon nanotubes.* J Phys Chem B, 2005. **109**(18): p. 8983-6.
226. Vernon-Parry, K.D., *Scanning electron microscopy: an introduction.* III-Vs Review, 2000. **13**(4): p. 40-44.
227. Joy, D.C., *Scanning electron microscopy for materials characterization.* Current Opinion in Solid State and Materials Science, 1997. **2**(4): p. 465-468.
228. Bogner, A., et al., *A history of scanning electron microscopy developments: towards "wet-STEM" imaging.* Micron, 2007. **38**(4): p. 390-401.
229. Knoll, M., *Aufladepotentiel und sekundäremission elektronenbestrahlter körper.* Zeitschrift für technische Physik 1935. **16**: p. 467-475.

230. McMullan, D., *Scanning electron microscopy 1928-1965*. Scanning, 2006. **17**(3): p. 175-185.
231. Oatley, C.W., *The early history of the scanning electron microscope*. Journal of Applied Physics, 1982. **53**(2): p. R1.
232. Williams, D.B. and C.B. Carter, 2009.
233. Bloch, F., *Uber die Quantenmechanik der Elektronen in Kristallgittern*. Zeitschrift fur Physik, 1929. **52**(7-8): p. 555-600.
234. Gazalet, J., et al., *A tutorial survey on waves propagating in periodic media: Electronic, photonic and phononic crystals. Perception of the Bloch theorem in both real and Fourier domains*. Wave Motion, 2013. **50**(3): p. 619-654.
235. Kafa, H., et al., *The interaction of carbon nanotubes with an in vitro blood-brain barrier model and mouse brain in vivo*. Biomaterials, 2015. **53**: p. 437-52.
236. Zach, J., *Chromatic correction: a revolution in electron microscopy?* Philos Trans A Math Phys Eng Sci, 2009. **367**(1903): p. 3699-707.
237. Haider, M., et al., *Current and future aberration correctors for the improvement of resolution in electron microscopy*. Philos Trans A Math Phys Eng Sci, 2009. **367**(1903): p. 3665-82.
238. Pennycook, S.J., et al., *Aberration-corrected scanning transmission electron microscopy: from atomic imaging and analysis to solving energy problems*. Philos Trans A Math Phys Eng Sci, 2009. **367**(1903): p. 3709-33.
239. Saghi, Z. and P.A. Midgley, *Electron Tomography in the (S)TEM: From Nanoscale Morphological Analysis to 3D Atomic Imaging*. Annual Review of Materials Research, 2012. **42**(1): p. 59-79.
240. Midgley, P.A. and R.E. Dunin-Borkowski, *Electron tomography and holography in materials science*. Nat Mater, 2009. **8**(4): p. 271-80.
241. Shindo, D. and T. Oikawa, *Energy Dispersive X-ray Spectroscopy*. 2002: p. 81-102.
242. Fultz, B. and J. Howe, *Transmission Electron Microscopy and Diffractometry of Materials*. 2013: p. 181-236.
243. Egerton, R.F., *Electron Energy-Loss Spectroscopy in the Electron Microscope*. Springer, 2011. **3rd Edition**.
244. Mahfoud, Z., et al., *Cathodoluminescence in a Scanning Transmission Electron Microscope: A Nanometer-Scale Counterpart of Photoluminescence for the Study of II–VI Quantum Dots*. The Journal of Physical Chemistry Letters, 2013. **4**(23): p. 4090-4094.
245. Shinde, K.N., et al., *Basic Mechanisms of Photoluminescence*. 2012. **174**: p. 41-59.
246. Yuan, L. and L. Huang, *Exciton dynamics and annihilation in WS2 2D semiconductors*. Nanoscale, 2015. **7**(16): p. 7402-8.
247. Eckert, M., *Max von Laue and the discovery of X-ray diffraction in 1912*. Annalen der Physik, 2012. **524**(5): p. A83-A85.
248. Fauth, F., et al., *The new Material Science Powder Diffraction beamline at ALBA Synchrotron*. Powder Diffraction, 2013. **28**(S2): p. S360-S370.

249. Ballesteros, B.n., et al., *Quantitative Assessment of the Amount of Material Encapsulated in Filled Carbon Nanotubes.* The Journal of Physical Chemistry C, 2009. **113**(7): p. 2653-2656.
250. Araujo, P.T., et al., *Resonance Raman Spectroscopy of the Radial Breathing Modes in Carbon Nanotubes.* Physica E: Low-dimensional Systems and Nanostructures, 2010. **42**(5): p. 1251-1261.
251. Kalbac, M. and L. Kavan, *Influence of the Resonant Electronic Transition on the Intensity of the Raman Radial Breathing Mode of Single Walled Carbon Nanotubes during Electrochemical Charging.* The Journal of Physical Chemistry C, 2009. **113**(37): p. 16408-16413.
252. Paolucci, D., et al., *Singling out the Electrochemistry of Individual Single-Walled Carbon Nanotubes in Solution.* Journal of the American Chemical Society, 2008. **130**(23): p. 7393-7399.
253. Fagaly, R.L., *Superconducting quantum interference device instruments and applications.* Review of Scientific Instruments, 2006. **77**(10): p. 101101.
254. Pulskamp, K., S. Diabate, and H.F. Krug, *Carbon nanotubes show no sign of acute toxicity but induce intracellular reactive oxygen species in dependence on contaminants.* Toxicol Lett, 2007. **168**(1): p. 58-74.
255. Ali-Boucetta, H., et al., *Asbestos-like pathogenicity of long carbon nanotubes alleviated by chemical functionalization.* Angew Chem Int Ed Engl, 2013. **52**(8): p. 2274-8.
256. Donaldson, K., et al., *Pulmonary toxicity of carbon nanotubes and asbestos - similarities and differences.* Adv Drug Deliv Rev, 2013. **65**(15): p. 2078-86.
257. Wang, Y., et al., *Etching and cutting of multi-walled carbon nanotubes in molten nitrate.* Corrosion Science, 2011. **53**(11): p. 3764-3770.
258. Rubio, N., et al., *Ball-milling modification of single-walled carbon nanotubes: purification, cutting, and functionalization.* Small, 2011. **7**(5): p. 665-74.
259. Lustig, S.R., et al., *Lithographically Cut Single-Walled Carbon Nanotubes: Controlling Length Distribution and Introducing End-Group Functionality.* Nano Letters, 2003. **3**(8): p. 1007-1012.
260. Jeong, S.-H., et al., *Preparation of Aligned Carbon Nanotubes with Prescribed Dimensions: Template Synthesis and Sonication Cutting Approach.* Chemistry of Materials, 2002. **14**(4): p. 1859-1862.
261. Banhart, F., J. Li, and M. Terrones, *Cutting single-walled carbon nanotubes with an electron beam: evidence for atom migration inside nanotubes.* Small, 2005. **1**(10): p. 953-6.
262. Liu, J., *Fullerene Pipes.* Science, 1998. **280**(5367): p. 1253-1256.
263. Shuba, M.V., et al., *Soft cutting of single-wall carbon nanotubes by low temperature ultrasonication in a mixture of sulfuric and nitric acids.* Nanotechnology, 2012. **23**(49): p. 495714.
264. Lin, C.C., et al., *Electron transport behavior of individual zinc oxide coated single-walled carbon nanotubes.* Nanotechnology, 2009. **20**(10): p. 105703.
265. Brukh, R. and S. Mitra, *Mechanism of carbon nanotube growth by CVD.* Chemical Physics Letters, 2006. **424**(1-3): p. 126-132.

266. Terranova, M.L., V. Sessa, and M. Rossi, *The World of Carbon Nanotubes: An Overview of CVD Growth Methodologies.* Chemical Vapor Deposition, 2006. **12**(6): p. 315-325.
267. Kumar, M. and Y. Ando, *Chemical Vapor Deposition of Carbon Nanotubes: A Review on Growth Mechanism and Mass Production.* Journal of Nanoscience and Nanotechnology, 2010. **10**(6): p. 3739-3758.
268. Sloan, J., et al., *Integral atomic layer architectures of 1D crystals inserted into single walled carbon nanotubes.* Chemical Communications, 2002(13): p. 1319-1332.
269. Monthioux, M. and E. Flahaut, *Meta- and hybrid-CNTs: A clue for the future development of carbon nanotubes.* Materials Science and Engineering: C, 2007. **27**(5-8): p. 1096-1101.
270. Kalbac, M., et al., *Sexithiophene encapsulated in a single-walled carbon nanotube: an in situ Raman spectroelectrochemical study of a peapod structure.* Chemistry, 2010. **16**(38): p. 11753-9.
271. El-Gendy, A.A., et al., *Tuneable magnetic properties of carbon-shielded NiPt-nanoalloys.* RSC Adv., 2016. **6**(57): p. 52427-52433.
272. Bajpai, A., et al., *The filling of carbon nanotubes with magnetoelectric Cr2O3.* Carbon, 2012. **50**(4): p. 1706-1709.
273. del Carmen Giménez-López, M., et al., *Encapsulation of single-molecule magnets in carbon nanotubes.* Nature Communications, 2011. **2**: p. 407.
274. Vyalikh, A., et al., *A carbon-wrapped nanoscaled thermometer for temperature control in biological environments.* Nanomedicine (Lond), 2008. **3**(3): p. 321-7.
275. Martincic, M. and G. Tobias, *Filled carbon nanotubes in biomedical imaging and drug delivery.* Expert Opin Drug Deliv, 2015. **12**(4): p. 563-81.
276. Lyra, M.E., et al., *Radionuclides Used in Nuclear Medicine Therapy – From Production to Dosimetry.* Current Medical Imaging Reviews, 2013. **9**(1): p. 51-75.
277. Ting, G., C.H. Chang, and H.E. Wang, *Cancer nanotargeted radiopharmaceuticals for tumor imaging and therapy.* Anticancer Research, 2009. **29**(10): p. 4107-18.
278. McDevitt, M.R., et al., *PET imaging of soluble yttrium-86-labeled carbon nanotubes in mice.* PLoS One, 2007. **2**(9): p. e907.
279. Deng, X., et al., *A generally adoptable radiotracing method for tracking carbon nanotubes in animals.* Nanotechnology, 2008. **19**(7): p. 075101.
280. Liu, Z., et al., *In vivo biodistribution and highly efficient tumour targeting of carbon nanotubes in mice.* Nat Nanotechnol, 2007. **2**(1): p. 47-52.
281. Niccoli Asabella, A., et al., *The copper radioisotopes: a systematic review with special interest to 64Cu.* Biomed Res Int, 2014. **2014**: p. 786463.
282. Jorgensen, J.T., et al., *High tumor uptake of (64)Cu: implications for molecular imaging of tumor characteristics with copper-based PET tracers.* Nucl Med Biol, 2013. **40**(3): p. 345-50.
283. Hamoudeh, M., et al., *Radionuclides delivery systems for nuclear imaging and radiotherapy of cancer.* Adv Drug Deliv Rev, 2008. **60**(12): p. 1329-46.

284. Mitra, A., et al., *Nanocarriers for Nuclear Imaging and Radiotherapy of Cancer.* Current Pharmaceutical Design, 2006. **12**(36): p. 4729-4749.
285. Reilly, R.M., et al., *Preclinical pharmacokinetic, biodistribution, toxicology, and dosimetry studies of 111In-DTPA-human epidermal growth factor: an auger electron-emitting radiotherapeutic agent for epidermal growth factor receptor-positive breast cancer.* J Nucl Med, 2006. **47**(6): p. 1023-31.
286. Chen, P., et al., *Antitumor effects and normal tissue toxicity of 111In-labeled epidermal growth factor administered to athymic mice bearing epidermal growth factor receptor-positive human breast cancer xenografts.* J Nucl Med, 2003. **44**(9): p. 1469-78.
287. Grigsby, P.W., K. Baglan, and B.A. Siegel, *Surveillance of patients to detect recurrent thyroid carcinoma.* Cancer, 1999. **85**(4): p. 945-951.
288. Yeong, C.H., M.H. Cheng, and K.H. Ng, *Therapeutic radionuclides in nuclear medicine: current and future prospects.* J Zhejiang Univ Sci B, 2014. **15**(10): p. 845-63.
289. Sethi, R., Y. Mackeyev, and L.J. Wilson, *The Gadonanotubes revisited: A new frontier in MRI contrast agent design.* Inorganica Chimica Acta, 2012. **393**: p. 165-172.
290. Sitharaman, B., et al., *Magnetic resonance imaging studies on gadonanotube-reinforced biodegradable polymer nanocomposites.* J Biomed Mater Res A, 2010. **93**(4): p. 1454-62.
291. van der Zande, M., et al., *In vivo magnetic resonance imaging of the distribution pattern of gadonanotubes released from a degrading poly(lactic-co-glycolic Acid) scaffold.* Tissue Eng Part C Methods, 2011. **17**(1): p. 19-26.
292. Anderson, P., *Samarium for osteoblastic bone metastases and osteosarcoma.* Expert Opin Pharmacother, 2006. **7**(11): p. 1475-86.
293. Wartenberg, N., et al., *Radioactive Europium-Chelate-Based Silica Nanoparticles as a Probe for Stability, Incorporation Efficiency and Trace Analysis.* European Journal of Inorganic Chemistry, 2013. **2013**(9): p. 1493-1498.
294. Samuel, J., et al., *Lanthanide-chelate silica nanospheres as robust multicolor Vis-NIR tags.* Chem Commun (Camb), 2010. **46**(15): p. 2647-9.
295. Philippot, C., et al., *Doped silica nanoparticles containing two-photon luminescent Eu(iii) complexes for the development of water stable bio-labels.* Journal of Materials Chemistry, 2011. **21**(46): p. 18613.
296. Xu, C., et al., *1D lanthanide halide crystals inserted into single-walled carbon nanotubes.* Chemical Communications, 2000(24): p. 2427-2428.
297. Das, T. and S. Banerjee, *Theranostic Applications of Lutetium-177 in Radionuclide Therapy.* Current Radiopharmaceuticals, 2015. **9**(1): p. 94-101.
298. Bal, C., et al., *Pharmacokinetic, Dosimetry and Toxicity Study of ^{177}Lu-EDTMP in Patients: Phase 0/I study.* Current Radiopharmaceuticals, 2015. **9**(1): p. 71-84.
299. Das, M., et al., *Auto-catalytic ceria nanoparticles offer neuroprotection to adult rat spinal cord neurons.* Biomaterials, 2007. **28**(10): p. 1918-25.

300. Celardo, I., et al., *Ce(3)+ ions determine redox-dependent anti-apoptotic effect of cerium oxide nanoparticles.* ACS Nano, 2011. **5**(6): p. 4537-49.
301. Yang, L., et al., *Intrinsically radiolabeled multifunctional cerium oxide nanoparticles for in vivo studies.* Journal of Materials Chemistry B, 2013. **1**(10): p. 1421.
302. Martincic, M., et al., *Synthesis of dry SmCl3 from Sm2O3 revisited. Implications for the encapsulation of samarium compounds into carbon nanotubes.* Polyhedron, 2016.
303. Martincic, M., et al., *Quantitative monitoring of the removal of non-encapsulated material external to filled carbon nanotube samples.* Phys Chem Chem Phys, 2015. **17**(47): p. 31662-9.
304. Kierkowicz, M., et al., *Filling Single-Walled Carbon Nanotubes with Lutetium Chloride: A Sustainable Production of Nanocapsules Free of Nonencapsulated Material.* ACS Sustainable Chemistry & Engineering, 2017. **5**(3): p. 2501-2508.
305. Marangon, I., et al., *Covalent Functionalization of Multi-walled Carbon Nanotubes with a Gadolinium Chelate for EfficientT1-Weighted Magnetic Resonance Imaging.* Advanced Functional Materials, 2014. **24**(45): p. 7173–7186.
306. Servant, A., et al., *Gadolinium-functionalised multi-walled carbon nanotubes as a T1 contrast agent for MRI cell labelling and tracking.* Carbon, 2016. **97**: p. 126-133.
307. Bianco, A., K. Kostarelos, and M. Prato, *Making carbon nanotubes biocompatible and biodegradable.* Chem Commun (Camb), 2011. **47**(37): p. 10182-8.
308. Tran, L.A., et al., *The use of gadolinium-carbon nanostructures to magnetically enhance stem cell retention for cellular cardiomyoplasty.* Biomaterials, 2014. **35**(2): p. 720-6.
309. Ma, Q., et al., *The gadonanotubes: structural origin of their high-performance MRI contrast agent behavior.* Journal of Materials Chemistry B, 2013. **1**(42): p. 5791.
310. Sahoo, N.G., et al., *Functionalized carbon nanomaterials as nanocarriers for loading and delivery of a poorly water-soluble anticancer drug: a comparative study.* Chem Commun (Camb), 2011. **47**(18): p. 5235-7.
311. Shi, X., et al., *Multifunctional dendrimer-modified multiwalled carbon nanotubes: synthesis, characterization, and in vitro cancer cell targeting and imaging.* Biomacromolecules, 2009. **10**(7): p. 1744-50.
312. Herrero, M.A., et al., *Synthesis and characterization of a carbon nanotube-dendron series for efficient siRNA delivery.* J Am Chem Soc, 2009. **131**(28): p. 9843-8.
313. Kam, N.W., Z. Liu, and H. Dai, *Functionalization of carbon nanotubes via cleavable disulfide bonds for efficient intracellular delivery of siRNA and potent gene silencing.* Journal of The American Chemical Society, 2005. **127**(36): p. 12492-3.
314. Samori, C., et al., *Enhanced anticancer activity of multi-walled carbon nanotube-methotrexate conjugates using cleavable linkers.* Chem Commun (Camb), 2010. **46**(9): p. 1494-6.

315. Wu, W., et al., *Targeted delivery of amphotericin B to cells by using functionalized carbon nanotubes.* Angew Chem Int Ed Engl, 2005. **44**(39): p. 6358-62.
316. Grandis, J.R., et al., *Levels of TGF- and EGFR Protein in Head and Neck Squamous Cell Carcinoma and Patient Survival.* JNCI Journal of the National Cancer Institute, 1998. **90**(11): p. 824-832.
317. Owonikoko, T.K., S.Y. Sun, and S.S. Ramalingam, *The role of cetuximab in the management of non-small-cell lung cancer.* Clin Lung Cancer, 2009. **10**(4): p. 230-8.
318. Egloff, A.M. and J.R. Grandis, *Targeting epidermal growth factor receptor and SRC pathways in head and neck cancer.* Semin Oncol, 2008. **35**(3): p. 286-97.
319. Ciardiello, F. and G. Tortora, *A novel approach in the treatment of cancer: targeting the epidermal growth factor receptor.* Clin Cancer Res, 2001. **7**(10): p. 2958-70.
320. Lee, P.C., et al., *Targeting colorectal cancer cells with single-walled carbon nanotubes conjugated to anticancer agent SN-38 and EGFR antibody.* Biomaterials, 2013. **34**(34): p. 8756-65.
321. Marega, R., et al., *Functionalized Fe-Filled Multiwalled Carbon Nanotubes as Multifunctional Scaffolds for Magnetization of Cancer Cells.* Advanced Functional Materials, 2013. **23**(25): p. 3173-3184.
322. Spinato, C., et al., *Design of antibody-functionalized carbon nanotubes filled with radioactivable metals towards a targeted anticancer therapy.* Nanoscale, 2016. **8**(25): p. 12626-38.
323. Bianco, A., K. Kostarelos, and M. Prato, *Applications of carbon nanotubes in drug delivery.* Curr Opin Chem Biol, 2005. **9**(6): p. 674-9.
324. Lee, H.J., et al., *Amine-modified single-walled carbon nanotubes protect neurons from injury in a rat stroke model.* Nat Nanotechnol, 2011. **6**(2): p. 121-5.
325. Zhao, D., et al., *Carbon nanotubes enhance CpG uptake and potentiate antiglioma immunity.* Clin Cancer Res, 2011. **17**(4): p. 771-82.
326. Al-Jamal, K.T., et al., *Cellular uptake mechanisms of functionalised multi-walled carbon nanotubes by 3D electron tomography imaging.* Nanoscale, 2011. **3**(6): p. 2627-35.
327. Candela, P., et al., *Physiological pathway for low-density lipoproteins across the blood-brain barrier: transcytosis through brain capillary endothelial cells in vitro.* Endothelium, 2008. **15**(5-6): p. 254-64.
328. Skinner, R.A., et al., *Transport of interleukin-1 across cerebromicrovascular endothelial cells.* Br J Pharmacol, 2009. **156**(7): p. 1115-23.
329. Pushie, M.J., et al., *Elemental and chemically specific X-ray fluorescence imaging of biological systems.* Chem Rev, 2014. **114**(17): p. 8499-541.
330. Quintana, M. and M. Prato, *Supramolecular aggregation of functionalized carbon nanotubes.* Chem Commun, 2009(40): p. 6005-7.
331. Kocbach, A., et al., *Physicochemical characterisation of combustion particles from vehicle exhaust and residential wood smoke.* Part Fibre Toxicol, 2006. **3**: p. 1.

332. Zhou, W., S.J. Pennycook, and J.C. Idrobo, *Probing the electronic structure and optical response of a graphene quantum disk supported on monolayer graphene.* J Phys Condens Matter, 2012. **24**(31): p. 314213.
333. Bussy, C., et al., *Carbon nanotubes in macrophages: imaging and chemical analysis by X-ray fluorescence microscopy.* Nano Lett, 2008. **8**(9): p. 2659-63.
334. Liang, H.W., S. Liu, and S.H. Yu, *Controlled synthesis of one-dimensional inorganic nanostructures using pre-existing one-dimensional nanostructures as templates.* Advanced Materials, 2010. **22**(35): p. 3925-37.
335. Fan, H.J., P. Werner, and M. Zacharias, *Semiconductor nanowires: from self-organization to patterned growth.* Small, 2006. **2**(6): p. 700-17.
336. Xia, Y., et al., *One-Dimensional Nanostructures: Synthesis, Characterization, and Applications.* Advanced Materials, 2003. **15**(5): p. 353-389.
337. Wang, Q.H., et al., *Electronics and optoelectronics of two-dimensional transition metal dichalcogenides.* Nature Nanotechnology, 2012. **7**(11): p. 699-712.
338. Osada, M. and T. Sasaki, *Two-dimensional dielectric nanosheets: novel nanoelectronics from nanocrystal building blocks.* Advanced Materials, 2012. **24**(2): p. 210-28.
339. Eder, D., *Carbon nanotube-inorganic hybrids.* Chemical Reviews, 2010. **110**(3): p. 1348-85.
340. Gimenez-Lopez Mdel, C., et al., *Encapsulation of single-molecule magnets in carbon nanotubes.* Nature Communications, 2011. **2**: p. 407.
341. Hong, S.Y., et al., *Filled and glycosylated carbon nanotubes for in vivo radioemitter localization and imaging.* Nature Materials, 2010. **9**(6): p. 485-90.
342. Maniwa, Y., et al., *Water-filled single-wall carbon nanotubes as molecular nanovalves.* Nature Materials, 2007. **6**(2): p. 135-41.
343. Mohana Reddy, A.L., et al., *Hybrid nanostructures for energy storage applications.* Advanced Materials, 2012. **24**(37): p. 5045-64.
344. Rao, C.N.R. and A. Govindaraj, *Synthesis of Inorganic Nanotubes.* Advanced Materials, 2009. **21**(42): p. 4208-4233.
345. Cabana, L., et al., *Synthesis of PbI(2) single-layered inorganic nanotubes encapsulated within carbon nanotubes.* Advanced Materials, 2014. **26**(13): p. 2016-21.
346. Iijima, S. and T. Ichihashi, *Single-shell carbon nanotubes of 1-nm diameter.* Nature, 1993. **363**(6430): p. 603-605.
347. Hakimi, A., et al., *Production, quality control, biological evaluation and biodistribution modeling of Lutetium-177 maltolate as a viable bone pain palliative in skeletal metastasis.* Journal of Radioanalytical and Nuclear Chemistry, 2014. **303**(1): p. 1-10.
348. Ting, G., C.H. Chang, and H.E. Wang, *Cancer nanotargeted radiopharmaceuticals for tumor imaging and therapy.* Anticancer Res, 2009. **29**(10): p. 4107-18.
349. Rogers, E., P. Dorenbos, and E. van der Kolk, *Systematics in the optical and electronic properties of the binary lanthanide halide, chalcogenide and pnictide compounds: an overview.* New Journal of Physics, 2011. **13**(9): p. 093038.

350. Dumcenco, D., et al., *Large-Area Epitaxial Monolayer MoS2.* ACS Nano, 2015. **9**(4): p. 4611-20.
351. Templeton, D.H. and G.F. Carter, *The Crystal Structures of Yttrium Trichloride and Similar Compounds.* The Journal of Physical Chemistry, 1954. **58**(11): p. 940-944.
352. Brown, D., S. Fletcher, and D.G. Holah, *The preparation and crystallographic properties of certain lanthanide and actinide tribromides and tribromide hexahydrates.* Journal of the Chemical Society A: Inorganic, Physical, Theoretical, 1968: p. 1889.
353. Astakhova, I.S. and V.F. Goryushkin, *X-ray diffraction study of lutetium iodide.* Russian Journal of Inorganic Chemistry, 1992. **37**.
354. Soler, J.M., et al., *The SIESTA method forab initioorder-Nmaterials simulation.* Journal of Physics: Condensed Matter, 2002. **14**(11): p. 2745-2779.
355. Grillo, V. and E. Rotunno, *STEM_CELL: a software tool for electron microscopy: part 1 simulations.* Ultramicroscopy, 2013. **125**: p. 97-111.
356. Goldberger, J., R. Fan, and P. Yang, *Inorganic nanotubes: a novel platform for nanofluidics.* Acc Chem Res, 2006. **39**(4): p. 239-48.
357. Amara, M.S., et al., *Hybrid, Tunable-Diameter, Metal Oxide Nanotubes for Trapping of Organic Molecules.* Chemistry of Materials, 2015. **27**(5): p. 1488-1494.
358. Kang, D.Y., et al., *Dehydration, dehydroxylation, and rehydroxylation of single-walled aluminosilicate nanotubes.* ACS Nano, 2010. **4**(8): p. 4897-907.
359. Radisavljevic, B., et al., *Single-layer MoS2 transistors.* Nat Nanotechnol, 2011. **6**(3): p. 147-50.
360. Hong, X., et al., *Ultrafast charge transfer in atomically thin MoS(2)/WS(2) heterostructures.* Nat Nanotechnol, 2014. **9**(9): p. 682-6.
361. Arnold M. Guloy, Z.T., Paulo B. Miranda, and Vojislav I. Srdanov, *A New Luminescent Organic-Inorganic Hybrid Compound With Large Optical Linearity.* Adv Mater, 2001. **13**(11): p. 833-837.
362. Wu, L.M., X.T. Wu, and L. Chen, *Structural overview and structure-property relationships of iodoplumbate and iodobismuthate.* Coordination Chemistry Reviews, 2009. **253**(23-24): p. 2787-2804.
363. Shkir, M., et al., *Effect of thickness on the structural, optical and electrical properties of thermally evaporated PbI2 thin films.* Journal of Physics and Chemistry of Solids, 2012. **73**(11): p. 1309-1313.
364. Tan, Z.K., et al., *Bright light-emitting diodes based on organometal halide perovskite.* Nat Nanotechnol, 2014. **9**(9): p. 687-92.
365. Kasap, S.O. and J.A. Rowlands, *Review X-ray photoconductors and stabilized a-Se for direct conversion digital flat-panel X-ray image-detectors.* Journal of Materials Science: Materials in Electronics, 2000. **11**(3): p. 179-198.
366. Caldeira Filho, A.M. and M. Mulato, *Characterization of thermally evaporated lead iodide films aimed for the detection of X-rays.* Nuclear Instruments and Methods in Physics Research Section A: Accelerators, Spectrometers, Detectors and Associated Equipment, 2011. **636**(1): p. 82-86.

367. Condeles, J.F. and M. Mulato, *Polycrystalline lead iodide films produced by solution evaporation and tested in the mammography X-ray energy range.* Journal of Physics and Chemistry of Solids, 2016. **89**: p. 39-44.
368. Chaudhary, S.K., *Lead Iodide Crystals as Input Material for Radiation Detectors.* Crystal Structure Theory and Applications, 2012. **01**(03): p. 21-24.
369. Chin, X.Y., et al., *Lead iodide perovskite light-emitting field-effect transistor.* Nat Commun, 2015. **6**: p. 7383.
370. Lee, M.M., et al., *Efficient hybrid solar cells based on meso-superstructured organometal halide perovskites.* Science, 2012. **338**(6107): p. 643-7.
371. Jeng, J.Y., et al., *CH3NH3PbI3 perovskite/fullerene planar-heterojunction hybrid solar cells.* Adv Mater, 2013. **25**(27): p. 3727-32.
372. Chen, Q., et al., *Controllable self-induced passivation of hybrid lead iodide perovskites toward high performance solar cells.* Nano Lett, 2014. **14**(7): p. 4158-63.
373. Sharenko, A. and M.F. Toney, *Relationships between Lead Halide Perovskite Thin-Film Fabrication, Morphology, and Performance in Solar Cells.* J Am Chem Soc, 2016. **138**: p. 463-470.
374. Finlayson, C.E. and P.J.A. Sazio, *Highly efficient blue photoluminescence from colloidal lead-iodide nanoparticles.* Journal of Physics D: Applied Physics, 2006. **39**(8): p. 1477-1480.
375. Liu, X., et al., *Whispering gallery mode lasing from hexagonal shaped layered lead iodide crystals.* ACS Nano, 2015. **9**(1): p. 687-95.
376. Sheng, C.X., et al., *Laser action and photoexcitations dynamics in PbI_2 films.* Optical Materials Express, 2015. **5**(3): p. 530.
377. Toulouse, A.S., et al., *Frenkel-like Wannier-Mott excitons in few-layerPbI2.* Physical Review B, 2015. **91**(16).
378. Zhou, M., et al., *Single layer lead iodide: computational exploration of structural, electronic and optical properties, strain induced band modulation and the role of spin-orbital-coupling.* Nanoscale, 2015. **7**(37): p. 15168-74.
379. Ugeda, M.M., et al., *Giant bandgap renormalization and excitonic effects in a monolayer transition metal dichalcogenide semiconductor.* Nat Mater, 2014. **13**(12): p. 1091-5.
380. Zhong, M., et al., *Large-scale 2D PbI2 monolayers: experimental realization and their indirect band-gap related properties.* Nanoscale, 2017. **9**(11): p. 3736-3741.
381. Scholes, G.D. and G. Rumbles, *Excitons in nanoscale systems.* Nat Mater, 2006. **5**(9): p. 683-96.
382. Kreizman, R., et al., *Core-shell PbI2@WS2 inorganic nanotubes from capillary wetting.* Angew Chem Int Ed Engl, 2009. **48**(7): p. 1230-3.
383. B Palosz, W.S.a.H.S., *The structure of PbI2 polytypes 2H and 4H: a study of the 2H-4H transition.* Journal of Physics: Condensed Matter, 1990. **2**(24): p. 5285-5295.
384. Tubbs, M.R., *The optical properties and chemical decomposition of halides with layer structures. I. crystal structures, optical properties, and electronic structure.* Physica Status Solidi (b), 1972. **49**(1): p. 11-50.

385. Flahaut, E., et al., *Crystallization of 2H and 4H PbI2in Carbon Nanotubes of Varying Diameters and Morphologies.* Chemistry of Materials, 2006. **18**(8): p. 2059-2069.
386. Condeles, J.F., T.G. Netto, and M. Mulato, *Lead iodide films as X-ray sensors tested in the mammography energy region.* Nuclear Instruments & Methods in Physics Research Section a-Accelerators Spectrometers Detectors and Associated Equipment, 2007. **577**(3): p. 724-728.
387. Baltog, I., M. Baibarac, and S. Lefrant, *Quantum well effect in bulk PbI(2) crystals revealed by the anisotropy of photoluminescence and Raman spectra.* J Phys Condens Matter, 2009. **21**(2): p. 025507.